Constitutive modelling of fine-grained soils containing gas bubbles

Hongjian Cai

2022

James Watt School of Engineering
University of Glasgow

Submitted in fulfilment of the requirement for the degree of Doctor of Philosophy

Declaration

I declare that this thesis is a record of original work carried out by myself under the supervision of Dr Zhiwei Gao and Prof. Simon Wheeler in the Infrastructure & Environment Research Division of the James Watt School of Engineering at the University of Glasgow, United Kingdom. This research was undertaken during the period of Oct 2018 to Sep 2022. The copyright of this thesis belongs to the author under the terms of the United Kingdom Copyright Acts. Due acknowledgement must always be made of the use of any material contained in, or derived from, this thesis. The thesis has not been presented elsewhere in consideration for a higher degree.

Parts of the work have been published under joint authorship with the supervisor.

Gao Z.W., Cai H.J. (2021). "Effect of total stress path and gas volume change on undrained shear strength of gassy clay." *Int. J. Geomech.* 21(11). http://doi.org/10.1061/(ASCE) GM.1943-5622. 0002198.

Gao Z.W., Cai H.J., Hong Y, Lu D.C. (2021). "A critical state constitutive model for gassy clay." *Canadian Geotechnical Journal.* http://doi.org/ 10.1139/cgj-2020-0754. ("Editor's Choice" paper for 2022).

Cai H.J., Gao Z.W., Hong Y., Zhang J.F., Lu D.C. (2023). "Constitutive Modelling of Overconsolidated gassy clay." 9th International SUT OSIG Conference "Innovative Geotechnologies for Energy Transition", London, UK,12-14 September 2023 (under review).

Acknowledgement

I would like to take this opportunity to express my sincere gratitude to all those who have supported me during my four-year research study at the University of Glasgow.

My deepest gratitude goes first and foremost to my supervisor, Dr. Zhiwei Gao, for his constant encouragement and instructive advice. Dr. Gao has walked me through all stages of the process of my research. He has given me a lot of helpful suggestions not only on research but also on the plan for my career. Without his support, the research and thesis would have not reached the present form. Secondly, I would like to thank Prof. Simon Wheeler, my second supervisor, who has instructed and helped me a lot in my research. He has made significant contribution in deriving the new upper and lower bounds of undrained shear strength.

I am also deeply grateful to Dr. Yi Hong and his students from Zhejiang University. They offered me great help with the experimental study.

I want to say thank you to all my friends in Glasgow for their company and encouragement. It is a memorable time for all of us. Thanks are also due to my friends in China for their support and praise.

Last but not least, I owe my thanks to my family for their always support and most selfless love.

Abstract

Fine-grained marine sediments containing free gas bubbles can be frequently encountered in the seabed worldwide, which can cause large-scale submarine landslides and offshore foundation failures. This soil has a unique composite structure with gas bubbles fitting within the saturated soil matrix. Therefore, its mechanical behaviour cannot be described using conventional unsaturated soil mechanics. The gas cavities have a detrimental effect on the soil stiffness and strength when they are filled with undissolved gas because gas has low bulk modulus and shear stiffness. The cavities can be filled with gas and pore water due to 'bubble flooding'. Bubble flooding has a beneficial effect on the soil stiffness and undrained shear strength because it makes the saturated soil matrix partially drained under a globally undrained condition. The critical state constitutive modelling approach for fine-grained soils containing gas bubbles (FGS) is presented, which accounts for the composite structure of the soil and bubble flooding.

The new lower and upper bounds for the undrained shear strength of FGS are derived firstly by considering the effect of total stress path and plastic hardening of the saturated soil matrix. For the upper bound, it is assumed that there is only bubble flooding, and the shear strength of an unsaturated soil sample is the same as that of the saturated soil matrix. Bubble flooding makes the saturated soil matrix partially drained and increases the undrained shear strength. The amount of bubble flooding is calculated using the Modified Cam-Clay model and Boyle's law for ideal gas. The lower bound is derived based on the assumption that the entire soil fails without bubble flooding and the gas cavity size evolves due to plastic hardening of the saturated soil matrix. Compared to Wheeler's upper and lower bounds which do not consider plastic hardening of the saturated soil matrix, the new theoretical results give a better prediction of the undrained shear strength of FGS, especially for the upper bound. Implications for constitutive modelling of FGS is discussed based on the new research outcomes.

A constitutive model for normally consolidated FGS is then proposed based on the new bounds. The cavities are assumed to have a detrimental effect on the plastic hardening of the saturated soil matrix because they damage the soil structure. The variable found in the new upper and lower bounds is introduced to capture this detrimental effect of gas bubbles. Some of the bubbles can be flooded by pore water from the saturated soil matrix, increasing the soil stiffness and strength. The new model uses stress quantities which can be readily measured, and only one parameter is introduced (as compared to the MCC model) to describe the effect of gas bubbles on the mechanical behaviour of FGS, making it easy to calibrate and use. The soil response in triaxial compression and isotropic compression is considered in the model. However, there are limitations for the conventional elastoplastic constitutive model to describe the mechanical behaviour of overconsolidated FGS. A constitutive model for overconsolidated FGS is derived based on the structure of that of the normally consolidated FGS. The bounding surface and the dilatancy relation are considered to describe the response of the overconsolidated FGS matrix. The model has been validated by the results of a series of tests. Finally, the comparisons of predictions from three models with test data are shown to indicate a progressive relationship among the models proposed in the thesis.

Contents

List of Figures

List of Tables

List of Symbols

C_a	Concentration of a specific gas in the aqueous phase
C_{gl}	Compressibility of the liquid/gas mixture
e	Global void ratio
e_0	Initial void ratio
e_m	Matrix void ratio
e_{m0}	Initial void ratio for the saturated soil matrix
e_{mf}	Void ratio of matrix when complete bubble flooding occurs
F	Yield function
f	Volume fraction of gas
f_0	Initial volume fraction of gas
f_f	Gas volume fraction at failure
G_m	Elastic shear modulus of the saturated soil matrix
h	Henry's constant
K_H	Modulus for Henry's law
$K_{H,inv}$	Modulus for Henry's law
K_m	Elastic bulk modulus of the saturated soil matrix
K_p	Plastic modulus for the saturated soil matrix
$\bar{K}_p$	plastic modulus at the image stress point
L	Loading index
P_g	Partial pressure of the specific gas in the gas phase
p	Total stress
$\bar{p}$	Mean stress at the image stress point
$\bar{p}_0$	Size of the bounding surface
p'	Mean effective stress
p'_c	Preconsolidation pressure
p'_0	Initial mean effective stress

p'_f	Mean effective stress at failure
p_a	Atmospheric pressure
p_m	Total effective stress of the saturated clay matrix
p'_m	Mean effective stress of the saturated clay matrix
q	Deviator stress
$\bar{q}$	Deviator stress at the image stress point
q_f	Deviator stress at failure
q_m	Deviator stress of the saturated clay matrix
q_y	Deviator stress at yield condition
S_r	Degree of saturation
S_{r0}	Initial degree of saturation
s_u	Undrained shear strength
s_u^s	Undrained shear strength of the saturated soil
u_g	Gas pressure
u_{g0}	Initial gas pressure
u_w	Pore water pressure
u_{w0}	Initial gas pressure
u_{wf}	Pore water pressure at failure
u_{w0_ref}	Reference u_{w0}
V	Total specific soil volume
V_c	Specific volume of the cavity
V_f	Specific volume of bubble flooding
V_g	Specific volume of gas bubbles
V_g^0	The initial specific volume of free gas
V_g^f	Specific volume of gas at failure
V_m	Specific volume of the saturated soil matrix
V_m^0	The initial specific volume of the saturated soil matrix

V_m^f	Specific volume of the saturated soil matrix at failure
V_v	Specific volume of void
V_w	Specific volume of pore water
λ	Slope of normal consolidation line
κ	Slope of swelling line
M	Critical state stress ratio
M_c	Critical state stress ratio
M_d	Dilatancy stress ratio
M_v	Virtual peak stress ratio
N	Value of V_m at unit mean effective stress for the normal compression line in the $V_m - \ln p'$ space
Γ	Value of V_m at unit mean effective stress for the critical state line in the $V_m - \ln p'$ space
OCR	Overconsolidation ratio
R	Reciprocal of overconsolidation ratio
a	Slope of total stress path
ε_a	Axial strain
ε_r	Radial strain
ε_q	Shear strain
ε_v	Volumetric strain
ε_v^c	Volumetric strain of gas cavities
ε_v^m	Volumetric strain of saturated soil matrix
ε_v^b	Volumetric strain of water flow at the boundary
ε_v^f	Volumetric strain due to bubble flooding
ε_q^m	Shear strain of saturated soil matrix
ε_q^c	Shear strain of gas cavities
ε_v^{me}	Elastic volumetric strain of saturated soil matrix

ε_v^{mp}	Plastic volumetric strain of saturated soil matrix
ε_q^{me}	Elastic shear strain of saturated soil matrix
ε_q^{mp}	Plastic shear strain of saturated soil matrix
σ_3	Minor principal stress
σ_y	Yield stress of matrix
σ_a	Total axial strain
σ_r	Total radial strain
α	Parameter for bounding surface
m	Parameter for dilatancy stress ratio
n	Parameter for virtual peak stress ratio
a_H	Parameter for hardening law of constitutive model for normally consolidated gassy soil
γ	Parameter for hardening law of constitutive model for over-consolidation gassy soil
ω	Functions of cavities' volume fraction
ϖ	Functions of cavities' volume fraction
X and ξ	X and ξ are two material constants for scaling the effects of u_{w0} and ψ_0 on the dilatancy of the gassy soil in the model proposed by Hong et al 2020; X and ξ can render the rate of bubble flooding in the model proposed by Gao et al., 2020
ϑ and μ	Parameters can be used to determine the shape of yield surface
κ	swelling index
ν	Poisson's ratio

Chapter 1 Introduction

Fine-grained soils containing large gas bubbles can be widely seen in the seabed throughout the world (Esrig and Kirby 1977; Jommi et al., 2019; Richardson et al., 2001; Sultan and Garziglia, 2014; Whelan et al., 1976; Whelan and Lester, 1980; Wu and Jeng, 2019). For instance, the gas-charged seabed has been found in the Bristol Channel, North Sea, Gulf of Mexico, Gulf of Guinea, offshore western Africa, and Eastern China Sea (Fig. 1.1). The gas is typically methane produced biogenically or thermochemically (Barden and Sides, 1970; Fleischeret al.,2001; Sills et al., 1991; Sills and Wheeler, 1992; Sills and Thomas, 2002; Sultan et al., 2012; Tjelta et al., 2007; Wheeler et al., 1990). Free gas can dramatically influence the mechanical behaviour of soils and is considered a major hazard for offshore ground engineering (Amaratunga and Grozic, 2009; Dittrich et al., 2010; Houlsby and Byrne, 2005; Kvenvolden, 1988; Milich, 1999; Nisbet and Piper, 1998; Rebata-Landa and Santamarina, 2012; Riboulot et al., 2013; Rowe and Mabrouk, 2012; Sills and Gonzalez, 2001; Sultan et al., 2012). Some failures of offshore foundations and large-scale submarine landslides have occurred due to detrimental effect of gas bubbles on soil stiffness and shear strength (Locat and Lee, 2002; Riboulot et al., 2013). Gas venting (mainly methane) was encountered during a deep excavation in southwestern Ontario, Canada and it shows that the gas exsolved from gassy soil can have effect during excavation (Mabrouk and Rowe, 2011). Meanwhile, the presence of gas bubbles can influence the consolidation behaviour due to its compressibility (Puzrin et al., 2011). Methane in dredging sludge may lead to expansion of sludge layers, partly or even completely counterbalancing consolidation (van Kessel and van Kesteren, 2002). A typical example includes the world’s largest submarine slides (i.e., Storegga Slide), which was partly triggered by the presence of gas within the marine sediments (Sultan et al., 2004). To mitigate the geotechnical risks associated with gassy soils, it is vital to have a proper understanding of the mechanical behaviour of this soil.

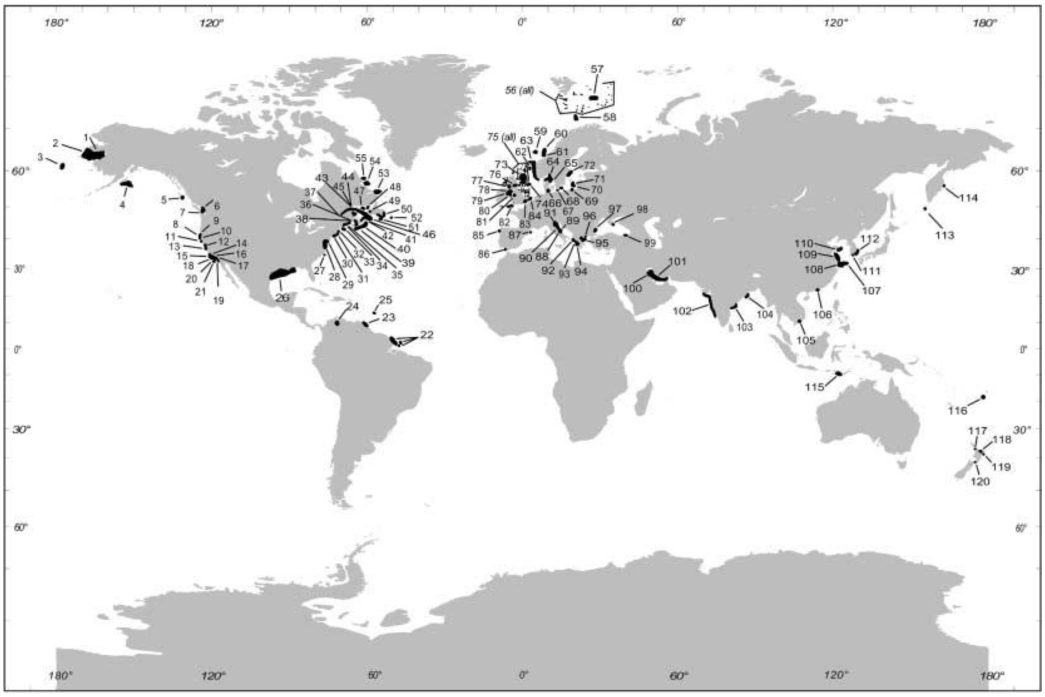

Fig. 1.1 Worldwide distribution of gassy sediments in the sea. Numbers correspond to references indexed in Fleischer et al. (2001)

The structure of soils containing gas bubbles can vary considerably, depending on the relative sizes of the bubbles and soil particles. Terzaghi (1943) was careful to distinguish between small and large bubbles, which he referred to as “gas bubbles” and “gas voids”, respectively. If the gas bubbles are smaller than the particle size, the soil structure is likely to be as illustrated in Fig. 1.3 (Anderson and Hampton, 1980; Wheeler, 1986; Boudreau et al., 2005). The bubbles fit within the normal void spaces without distortion of the soil structure. The radius of curvature of each gas-water interface, which controls the difference between gas pressure and water pressure, is equal to the radius of the bubble. If the gas bubbles are much larger than the normal particle size, the soil skeleton is pushed back by the gas, leaving a large gas-filled void (Fig. 1.4). It should be noticed that though the gas bubble is larger in this case, the volume of gas is still small due to its low solubility. The gas-water interfaces are formed by a large number of small menisci, which bridge the gaps between the particles. When the gas bubbles fit inside the saturated soil matrix, rather than the pore water, the gas phase is discontinuous, and the water phase is continuous (Fig. 1.4). The conventional unsaturated soil mechanics is not suitable for describing the response of gassy soils because it has been developed for soils with the continuous gas phase and discontinuous water phase, like soils on the embankment slopes (in Fig. 1.5).

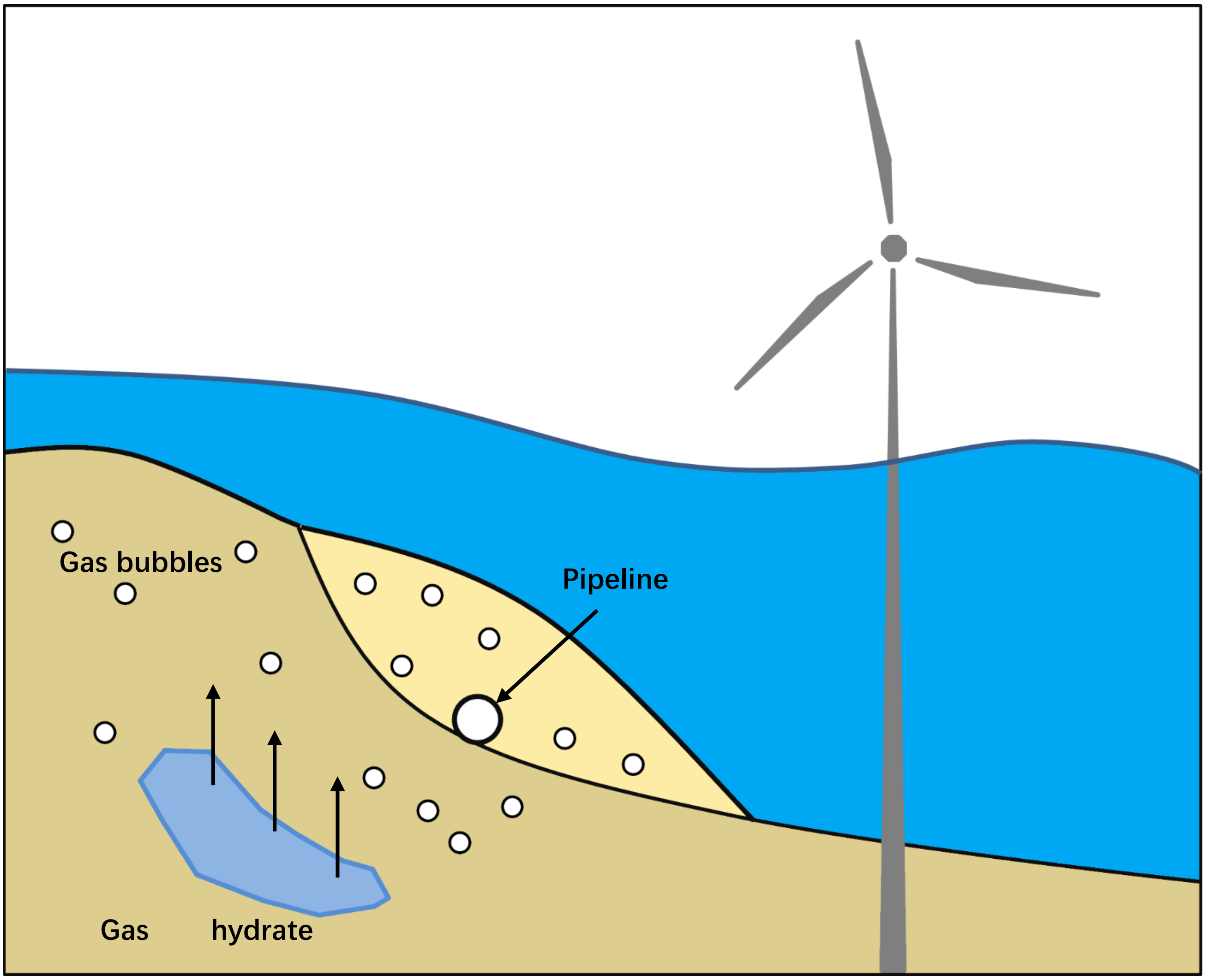

Fig. 1.2 Submarine landslides in gassy fine-grained soils and the impact on offshore infrastructure

Fine-grained gassy soils are essentially composite materials with three phases: the soil skeleton, pore water and gas bubbles (Wheeler, 1986). The interaction between gas bubbles and saturated soil matrix governs the stress-strain relationship of the soil. Generally, the gas bubbles increase the compressibility of gassy soils due to their low bulk modulus (Thomas, 1987; Wheeler, 1986; Hong et al., 2017; Wroth and Houlsby, 1985). Nevertheless, they can either increase or decrease the undrained strength of gassy clay which is associated with the unique internal structure of the soil. The gas bubbles are much larger than the soil particles and fit within the saturated soil matrix as shown in Fig. 1.4. The gas bubbles occupy the entire cavities when there is no bubble flooding (Wheeler, 1986). In this case, these bubbles are like the cavities in solids (e.g., concrete or steel), which have a damaging effect on the soil strength. In some cases, however, the pore water can drain into the cavities when the difference between the pore water pressure and pore gas pressure reaches a critical value, which is called 'bubble flooding' (Wheeler, 1986; Wheeler, 1988a, 1988b; Sills et al., 1991). Bubble flooding makes the saturated soil matrix partially drained in a globally undrained test. In an undrained test for FGS, there is no water flow in or out of the sample at the boundary, but the sample volume can change due to 'bubble flooding' and gas volume change with variation in total mean stress.

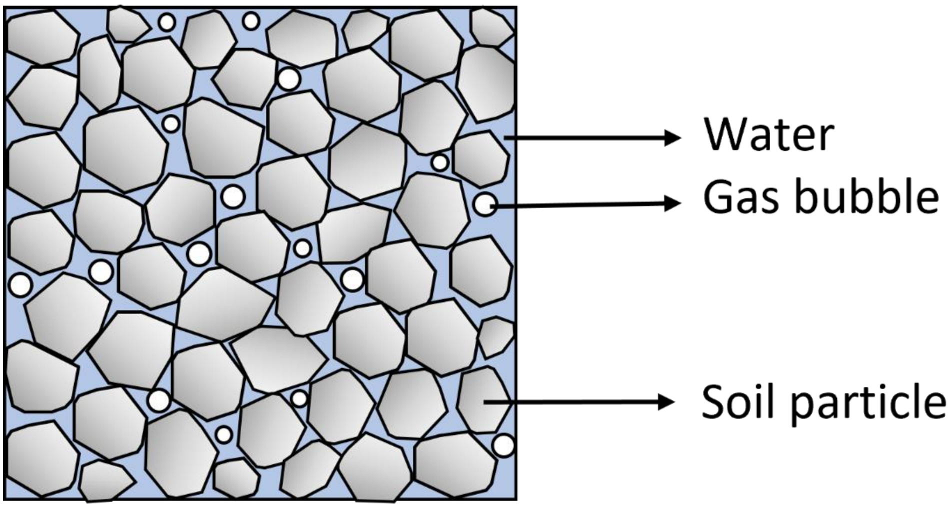

Fig. 1.3 Gas bubbles much smaller than soil particles (gassy sand)

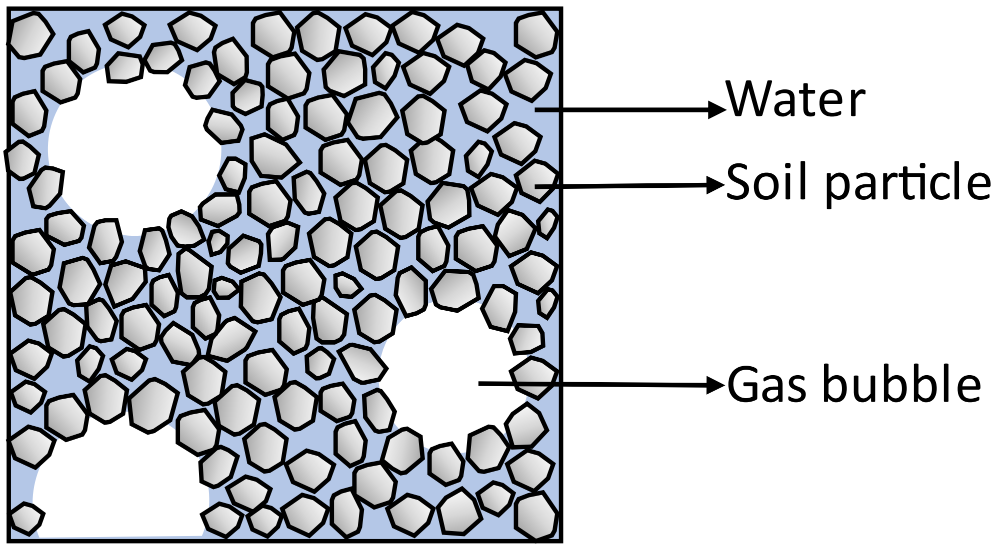

Fig. 1.4 Gas bubbles much larger than soil particles (gassy soils in the seabed)

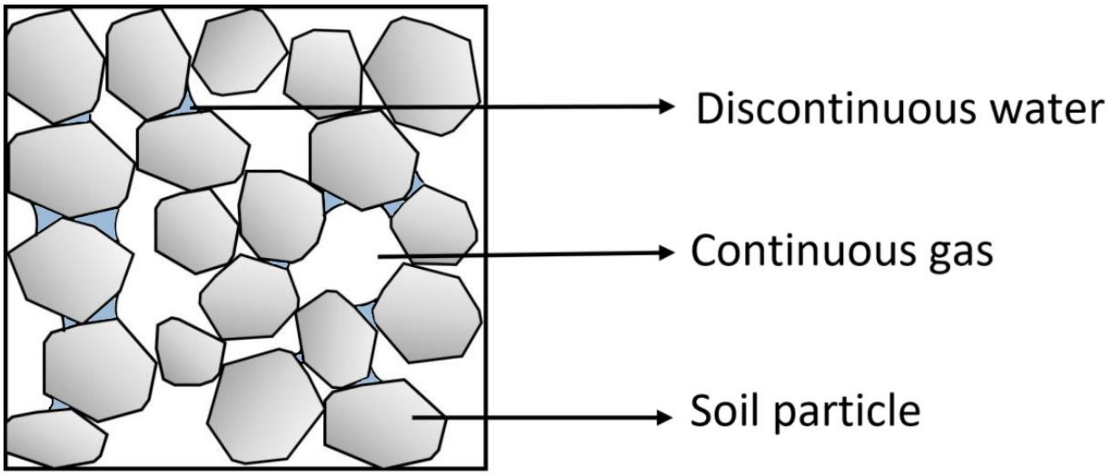

Fig. 1.5 Unsaturated soil onshore (discontinuous water phase and continuous gas phase)

There have been extensive experimental and theoretical studies on the behaviour of gassy soils (Sills et al., 1991; Sultan et al., 2012; Wheeler et al., 1990; Gao et al., 2021). Wheeler (1986) demonstrated that gassy soil has a unique composite structure with saturated soil matrix and gas cavities which can be filled with gas or water and gas. Based on this, Wheeler (1986) has derived the upper and lower bounds for the undrained shear strength of gassy soils. This research has laid the foundation for research on the constitutive modelling of gassy soils (Gao et al., 2020; Gao et al., 2021; Grozic et al., 2005; Hong et al., 2020; Pietruszczak and Pande, 1996). Progress has been made in modelling the constitutive relationship of gassy soils based on these early studies. Grozic et al. (2005) have derived a constitutive model for gassy soil by considering the gas bubbles as the part of the pore water, which has limitations on representing the actual internal structure of gassy soil. Based on extensive laboratory studies, Hong et al. (2020) proposed a constitutive model for gassy soils by considering the effect of free gas on the dilatancy and yield surface shape. Gao et al. (2020) have developed a composite approach for constitutive modelling of gassy soils. These recent models can describe the detrimental and beneficial effects of gas bubbles on the stiffness and strength of gassy soils. But the model parameters are not easy to determine.

Meanwhile, naturally deposited soils in the seabed or lakebed can become overconsolidated due to water pressure variation, sediment movement, submarine landslides and cyclic loading, which makes the current mean effective stress smaller than the past maximum (Gao et al., 2017). Research on the mechanical behaviour of overconsolidated gassy soils is also carried out. The overconsolidation can have effect on the dilatancy behaviour of soils, which can be found in both drained tests and undrained tests. The dilatancy behaviour of overconsolidated soil has a significant influence on the interaction between the saturated soil matrix and gas bubbles, which has been reported in some undrained triaxial test results on lightly overconsolidated gassy soils by Sham (1989). In this case, the undrained shear strength can also be affected. The constitutive model for describing the stress-strain relationship of both normally consolidated and overconsolidated gassy soil is worth researching.

Six chapters will be included in this study, and they are organised as below:

Chapter 1 presents a brief introduction to fine-grained soils containing gas bubbles.

Chapter 2 gives a review of the existing research on FGS, with a focus on the theoretical study.

Chapter 3 presents the new upper and lower bounds of the undrained shear strength of FGS. For the upper bound, it is assumed that there is only bubble flooding, but complete bubble flooding is not possible based on fundamental physics. The amount of bubble flooding depends on the stress path. For the lower bound, bubble compression is considered which makes the volume fraction of gas bubbles smaller during loading. A new state variable that is suitable for modelling the undrained shear strength of FGS is identified. The new upper and lower bounds are validated using experimental test data in the literature.

Chapter 4 presents a new constitutive model of the normally consolidated FGS. The new state variable found in Chapter 3 is used to capture the effect of gas bubbles on FGS behaviour. The model is based on the MCC. Only one extra parameter is needed to model the effect of free gas on soil behaviour. The model is validated by tests in the literature. Comparison is made by the new bounds and the prediction of model in Chapter 4 with test data, it is evident that the model prediction of Chapter 4 is within the two bounds.

Chapter 5 presents a new constitutive model of the overconsolidated FGS. The model is derived based on the framework of the model in Chapter 4. A new dilatancy relation and a new plastic modulus (both of which are related to the overconsolidation ratio) are introduced. The model is validated using the test results on three FGS samples reported in the literature. Comparison is made by the new bounds and the predictions of models in Chapter 4 and Chapter 5 with test data. The new upper and lower bounds can simulate the undrained shear strength better in most cases and the model in Chapter 5 can give a closer prediction with test data. Meanwhile, the overconsolidated model gives better prediction for the stress-strain relationship, effective stress path and undrained shear strength. The comparison shows good predictions of models with test data.

Chapter 7 includes the conclusion and recommendations for further research.

Chapter 2 Literature review

FGS is a unique unsaturated soil with a composite structure. Fine-grained soil can be either clay or silt. Its mechanical behaviour (compressibility, elastic stiffness, and shear strength) is governed by the soil-gas interaction. Early studies on FGS have used clay (s), and a recent study on gassy silt has shown that it shows similar response to that of FGS (Hong et al.). In this chapter, a review of past research on this soil is presented. This includes the geotechnical problems associated with this soil, the internal structure of the soil, laboratory tests (equipment and results), and theoretical studies (compressibility, undrained shear strength and constitutive modelling). The main knowledge gaps in the constitutive modelling of this soil are identified.

2.1 Geotechnical problems associated with FGS

FGS are considered a major geohazard for offshore ground engineering and oil/gas exploration (Atigh and Byrne, 2004; Locat and Lee, 2002; Sultan et al., 2012; Wheeler, 1986). The presence of gas bubbles could obviously influence the volume change behaviour of the soils due to their high compressibility (Nageswaran, 1983). A number of researchers have reported unusually low values of shear strength, which may be partly responsible for submarine landslides on very low-angle slopes (Bea and Arnold, 1973; Coleman and Prior, 1978; Prior and Suhayda, 1979; Whelan et al., 1977). Besides, the excess water pressure could be caused directly by the process of gas generation, or it could be due to the gas bubbles reducing the soil permeability, which could hinder the dissipation of pore water set up during the deposition of the soil. Escape of gas from the seabed can cause erosion features, such as seabed pockmarks, which could raise the violent gas eruptions and affect the siting and design of the offshore structures (Hovland and Judd, 1988; King and MacLean, 1970). First, the stability and serviceability of infrastructures such as piles and suction caissons built in the sea can be affected by gas bubbles (Wheeler, 1988; Sills et al., 1991). Secondly, in some cases, gas bubbles can reduce the strength of submarines, which can trigger large-scale submarine landslides, and then can cause significant damage to subsea cables, pipelines and foundations (Locat and Lee, 2002; Grozic et al., 2005). Thus, a better understanding of the behaviour of fine-grained soils containing gas bubbles is considerable for the offshore construction industry, and proper methods for characterising the gassy soil response are desirable.

2.2 Internal structure of FGS

Fig. 2.1 shows the unique internal structure of FGS. The gas bubbles fit inside the saturated clay matrix rather than the pore water. Therefore, the gas phase is discontinuous, and the water phase is continuous. The conventional unsaturated soil mechanics is not suitable for describing the response of FGS because it has been developed for soils with a continuous gas phase and discontinuous water phase, like soils on embankment slopes (Fig. 1.5). FGS are essentially composite materials with three phases: the soil skeleton, pore water and gas bubbles (Wheeler, 1986). The relationship between soil stress and strain is controlled by the interaction of gas bubbles with saturated soil matrix.

The gas bubbles can have a significant influence on the mechanical response of soils, including compressibility, stiffness and undrained shear strength, which must be properly considered in a geotechnical design (Sills et al., 1991; Sultan et al., 2012; Vega-Posada et al., 2014). Puzrin et al. (2011) have focused on increasing the compressibility of the pore fluid, by introducing gas bubbles through in situ microbial gas production. This method can shift about 50% of the total settlement from primary consolidation settlement to immediate settlement (Puzrin et al., 2011). Due to their high compressibility, undissolved gas bubbles make fine-graded soils more compressible (Nageswaran, 1983, Thomas, 1987). Depending on the stress state, pore water pressure, and pore gas pressure of soil, the gas bubbles can either increase or decrease the undrained shear strength of the soil. The upper and lower bounds have been proposed by Wheeler (1986) based on a series of laboratory tests on FGS. It is found that the pore gas pressure and the gas volume fraction are the key factors that control the bounds of the undrained shear strength (Wheeler, 1986; Sham, 1989). The compression and solution of gas is considered as the primary reason for the increased undrained shear strength of FGS (Grozic et al., 2005a; Grozic et al., 2005b). A series of tests on gassy silt with different pore water pressure have been carried out by Hong et al. (2017). It is found that gassy silt and clay show similar mechanical response.

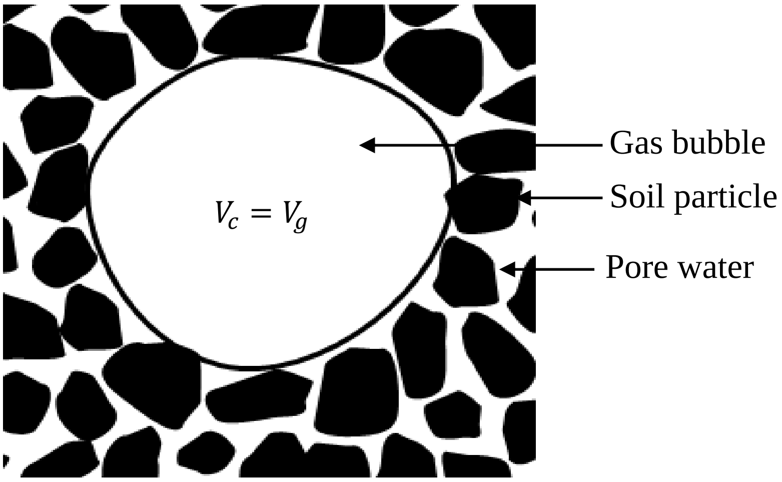

(a)

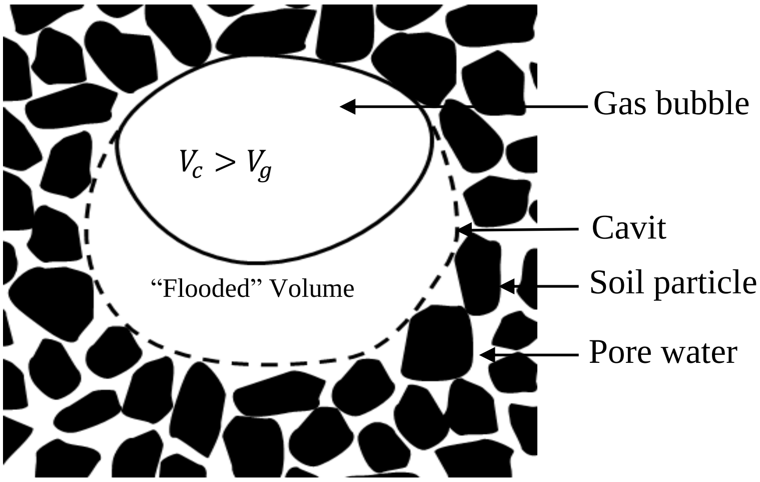

(b)

Fig. 2.1 Gas cavities filled by (a) free gas and (b) free gas and pore water (Gao, et al, 2021)

2.3 Experimental study of FGS

In this section, some of the experimental studies on FGS are introduced. The zeolite molecular sieve technique developed by Nageswaean (1983) is first introduced. The method can produce uniform gas bubble distribution in the soil. Then the double-cell triaxial apparatuses for the experimental study of FGS used by Bishop et al. (1961) and Wheeler (1986) are presented and some of the test results are shown. Some recent tests on gassy silt by Hong et al. (2020) are also introduced. In addition, the oedometer tests carried out by Thomas (1987) are discussed.

2.3.1 Sample preparation for experimental study on soils containing gas bubbles

Reconstituted gassy specimens have been used in the experiments due to the difficulties in getting intact gassy samples from the field because of gas expansion upon unloading (Lunne et al., 2001; Sham 1989; Sultan et al., 2012; Wheeler 1988b). Methane is most frequently encountered in FGS in the seabed and has been used by Wheeler (1987). Helium was used in the tests for safety reasons by Sham (1989).

The bubbles of gas in the sample are produced by using the zeolite molecular sieve technique (Nageswaean, 1983; Wheeler,1986; Hong et al., 2017). Zeolites are a group of inert chemicals with an extreme affinity for polar molecules such as water. For zeolite crystal, if the water of hydration is removed by heating, other molecules of appropriate size can be incorporated into the zeolite crystal while maintaining its original structure. If a gas-impregnated dried zeolite is mixed with the soil slurry, the zeolite will absorb the water from the soil slurry instead of the gas, which is released to generate bubbles. Zeolite is available in numerous natural and manufactured varieties. The zeolite will be chosen by contrasting the molecular diameter of the selected gas. The zeolite powder is dried for 24 hours at 105°C for the purpose of removing the moisture. The majority of the air is then removed from the crystal structure of the dried zeolite by putting it in an evacuated chamber for 24 hours at a pressure of -70 to -80 kPa. The zeolite is then exposed to nitrogen for more than 10 hours at a pressure of 100 kPa. After being mixed with soil slurry, the gas-filled zeolite absorbed the water from the slurry rather than the gas, which was released to create gas bubbles. It is essential that the different samples with different gas components, have the same volume of zeolite particles due to the fact that the physical characteristics of the soil and zeolite are not the same (Nageswaran, 1983). A zeolite-soil slurry is made by mixing the gassy zeolite with the slurry of the chosen soil. The slurry will be placed into 38 mm diameter moulds for initial one-dimensional consolidation after being stirred as quickly as possible to avoid gas escape.

2.3.2 Triaxial test apparatus for FGS

In most cases, the undrained condition is considered because this is more common for offshore geotechnical engineering. In addition, it is very time-consuming to carry out drained tests on clay. In undrained triaxial tests, the volume change is caused by the compression of the gas in the unsaturated soil. The volumetric strain of gassy soil cannot be measured simply by the water flow from the soil sample in triaxial tests. Research has been conducted to resolve this issue.

Bishop and Donald (1961) have developed a double cell triaxial test system as shown in Fig. 2.2. Mercury was injected inside the sample cell. A stainless-steel ball floating in the mercury is used as the cathetometer sighting point to detect the vertical displacement of the mercury surface. The cell pressure was delivered to both sides of an interior jacket that contained mercury. Due to this configuration, the level of the mercury surface was unaffected by any variations in cell volume brought on by changes in cell pressure. In the following few decades, this approach for measuring the volume change of soil samples was extensively employed for experimental research on unsaturated soils. Some of the test results are shown in Fig. 2.3. The changes in pore air and pore water pressure under an increasing cell pressure are shown in Fig. 2.3 (a) for a sample of the Talybont boulder clay compacted at two water contents. Mercury cell has been used to prevent air diffusion through the rubber membrane and time has been given for equilibrium under each pressure. Values for cell pressure are plotted against water pressure. The initial air pressure in samples sealed soon after compaction appears generally not to be atmospheric, but the negative values are rather small (Fig. 2.3 (b)). Fig. 2.4 shows the result of $(\sigma_1 - \sigma_3)$ and deviator strain with a constant water content on partly saturated loose silt.

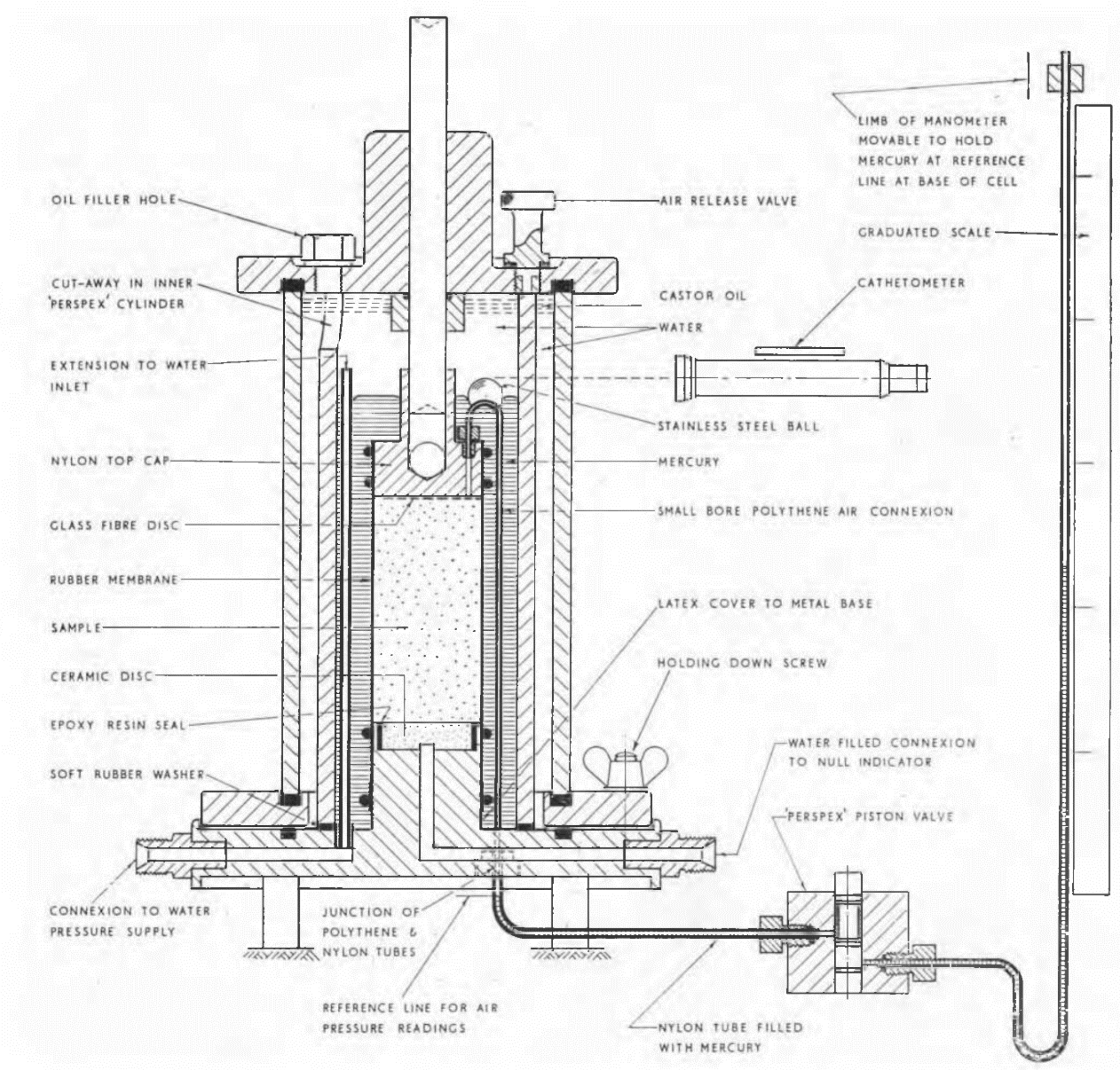

Fig. 2.2 Modification of triaxial cell to surround rubber membrane with mercury, diagrammatic section (Bishop, 1961).

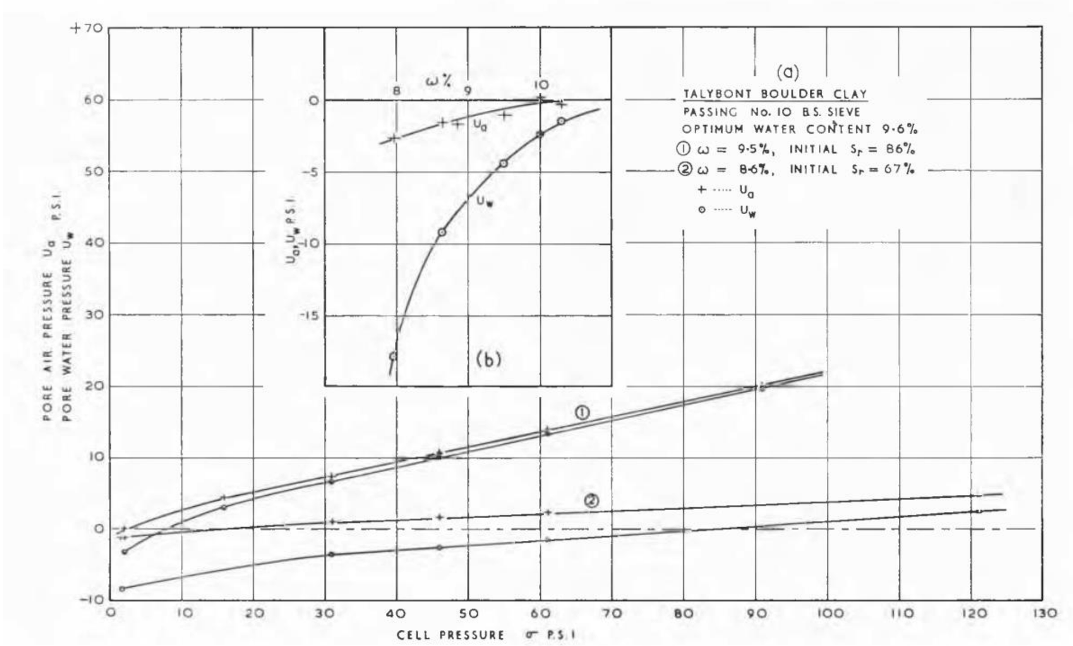

Fig 2.3 (a) Changes of pore air and pore water pressure in compacted soil under undrained conditions using mercury cell; (b) Initial pore air and pore water pressures in sealed specimens (Bishop et al., 1961)

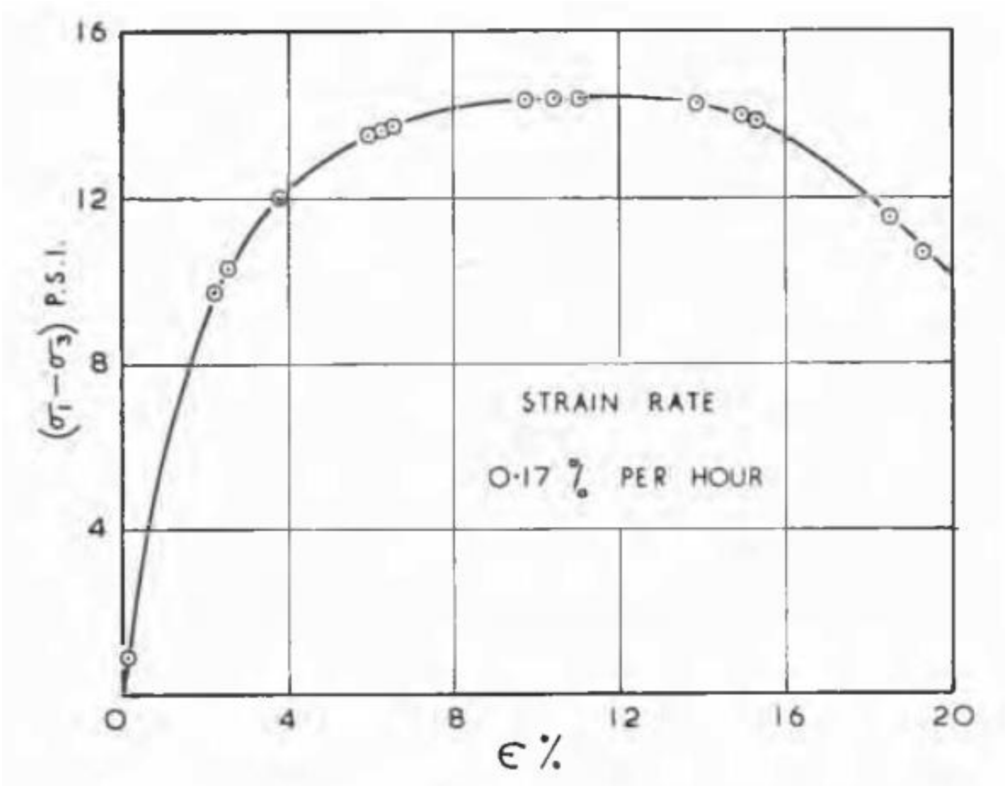

Fig. 2.4 Constant water content test with controlled air pressure on partly saturated loose silt (Bishop et al., 1961)

Wheeler (1986) has carried out a series of triaxial tests on FGS. The double-cell triaxial equipment has been improved. The improvements are all related to measuring the volume change independently of the water flow from the soil sample. The cell is entirely filled with water, and the flow into the cell was measured with a burette rather than partially filling the cell with mercury and then measuring the displacement of the mercury surface as Bishop did. As a fluid interface is no longer necessary, this improvement can eliminate the need for two cell fluids. Additionally, the measurement accuracy is improved, as the mercury surface in Bishop and Donald's apparatus shows far less displacement than the meniscus in the burette. The modified apparatus is shown in Fig. 2.5.

Some of the test results are shown in Figs. 2.6 to 2.8. Fig. 2.6 shows the deviator stress and pore water pressure plotted against the axial strain. Fig. 2.7a shows three curves with different degree of saturation relating the overall void ratio after consolidation to the consolidation pressure. Fig. 2.7b shows there is a unique relationship between the void ration of soil matrix to the consolidation pressure. The general shape of the stress-strain curves during the shearing stage is unaffected by the presence of gas bubbles based on the tests carried out by Wheeler (1986). This implies that the gas bubbles have no bearing on the overall failure. Gas bubbles, however, can have a significant impact on the undrained shear strength. Consolidation pressure and back pressure both have an influence on how gas bubbles affect the undrained shear strength (Fig 2.8). The test results are used to propose the upper and lower bounds in Wheeler’s study (Wheeler, 1986).

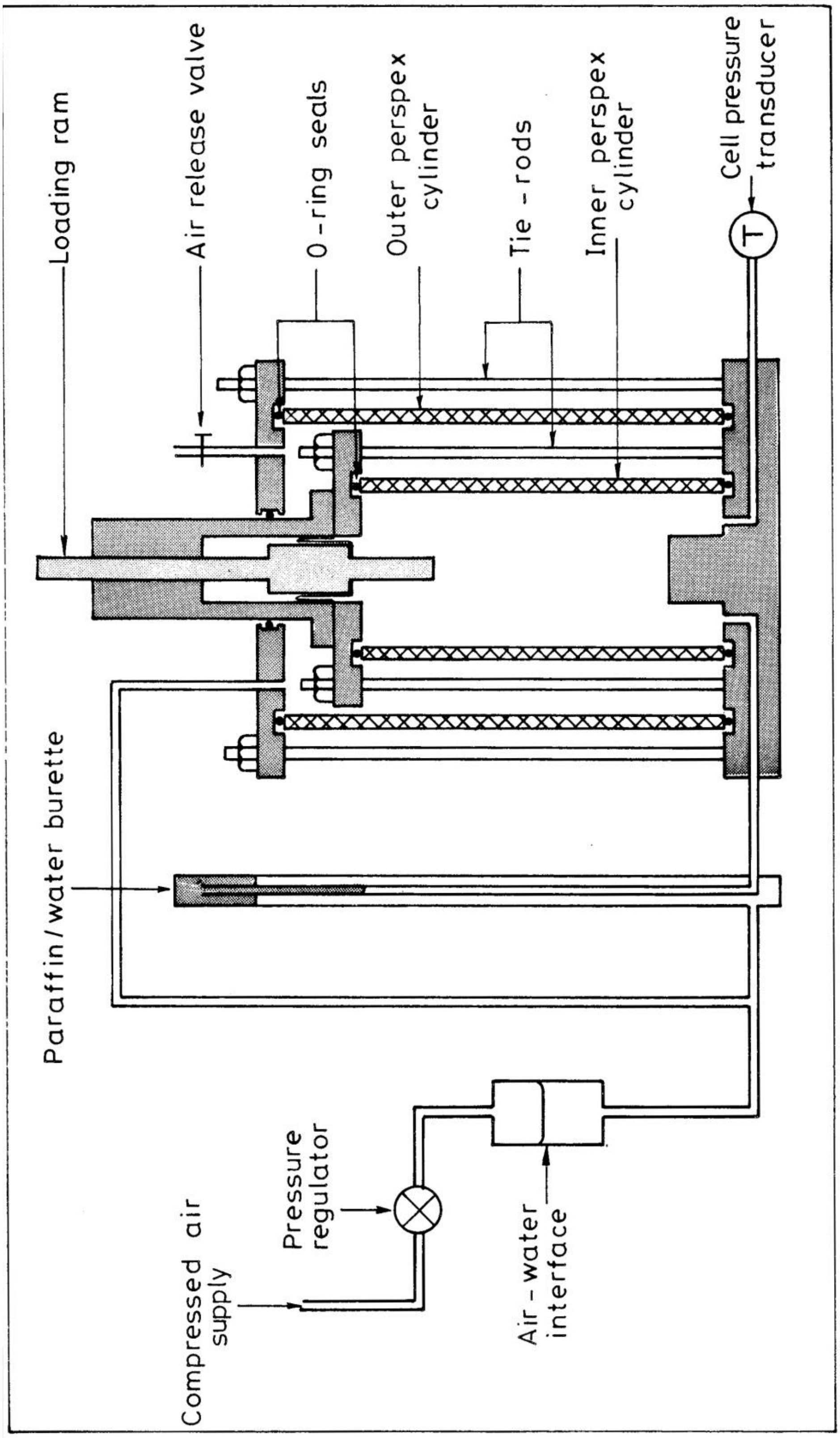

Fig. 2.5 Modified double cell triaxial apparatus (Wheeler, 1986)

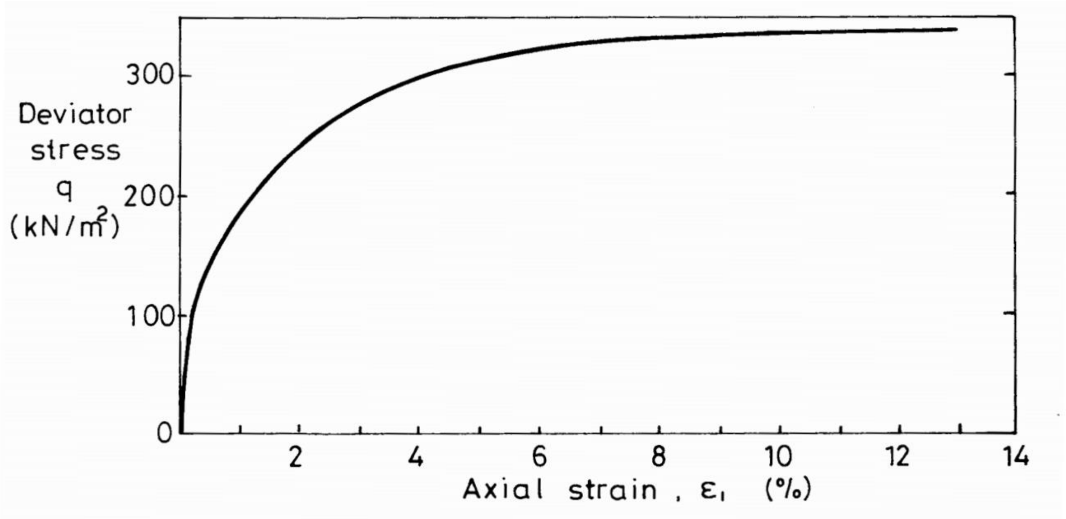

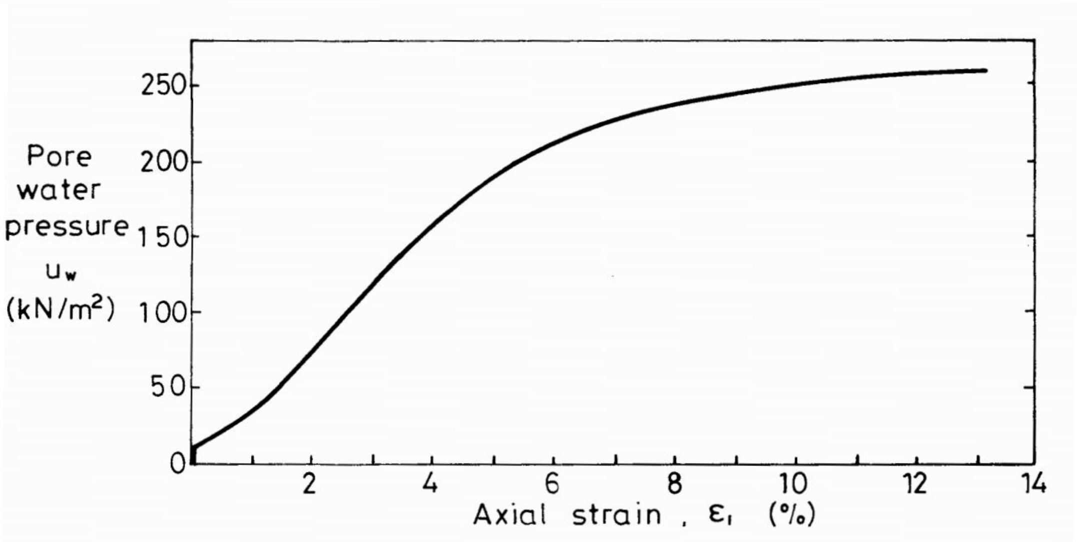

Fig.2.6 Typical behaviour under shearing with consolidation pressure is 400 kPa, initial pore water pressure (u_{w0}) = 0 and degree of saturation (Sr) = 0.95 (Wheeler, 1986)

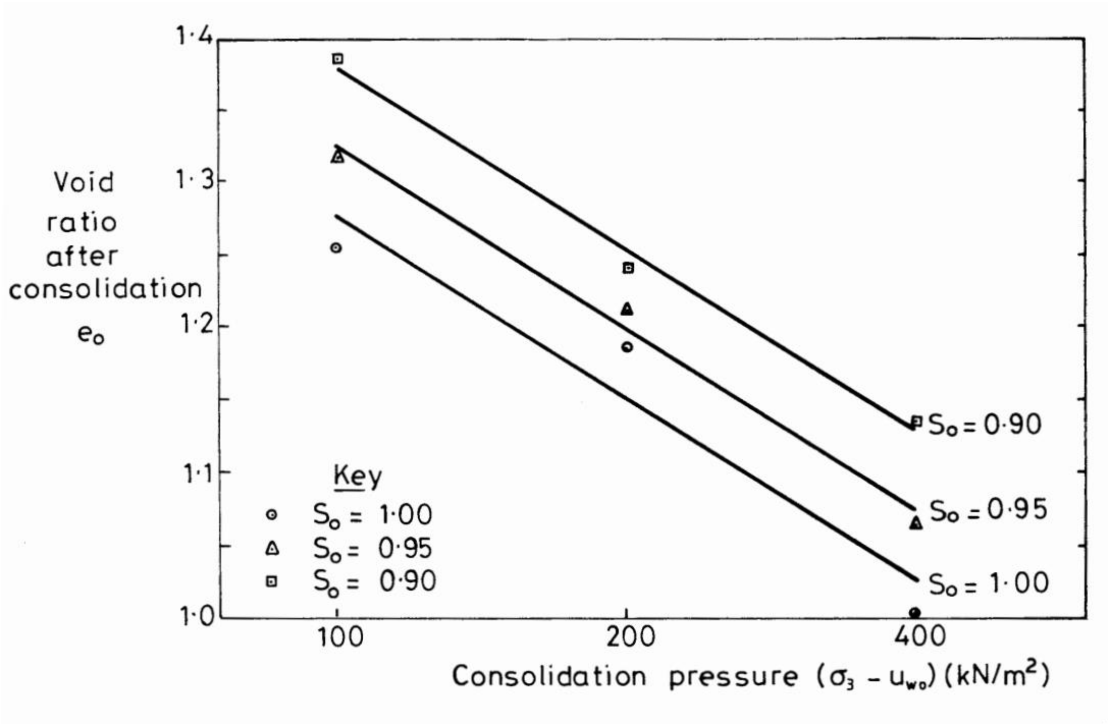

(a)

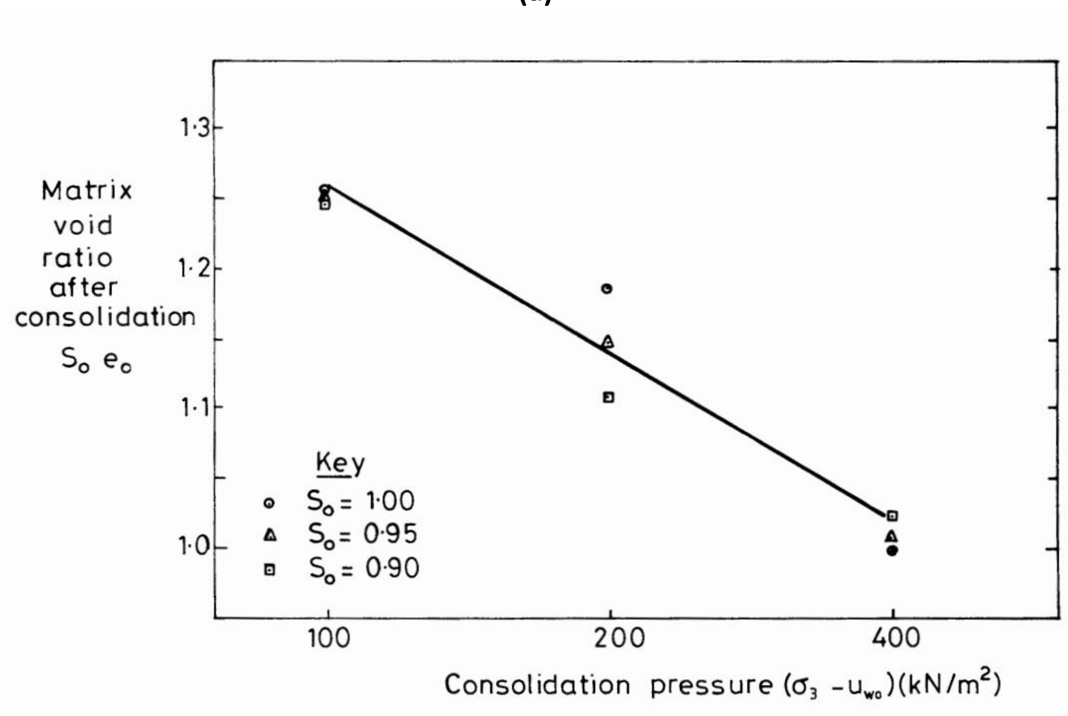

(b)

Fig. 2.7 Test result of isotropic consolidation (Wheeler, 1986)

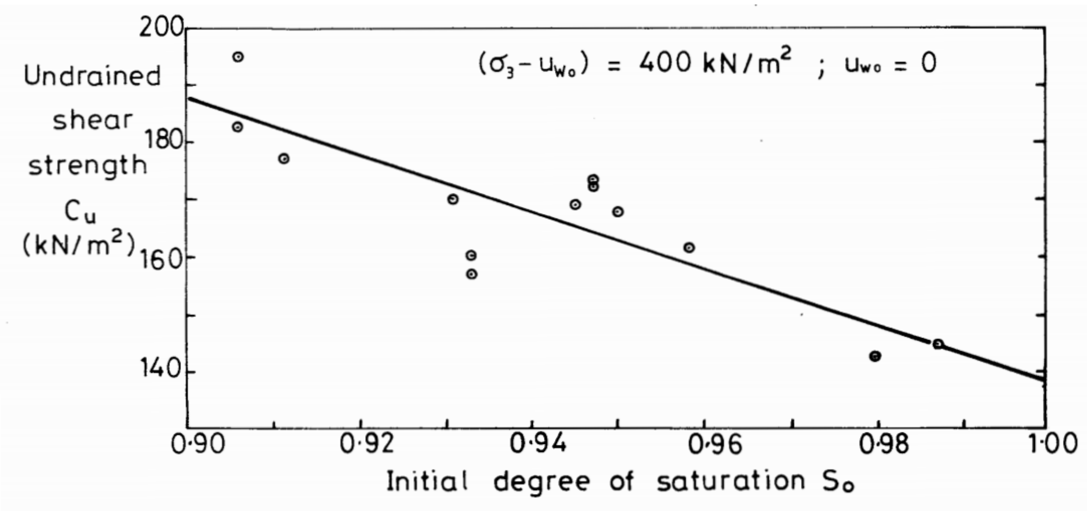

(a)

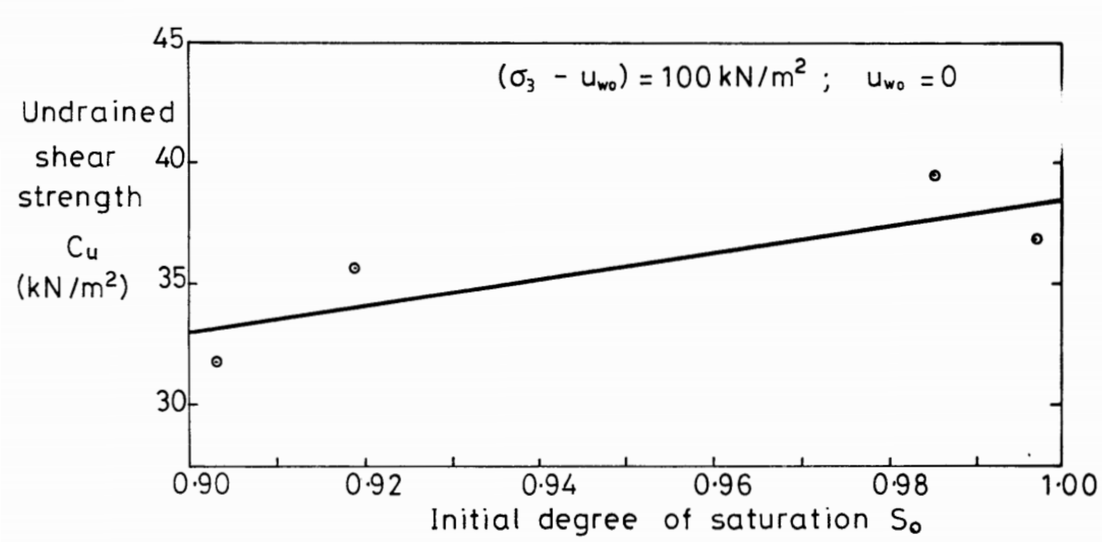

(b)

Fig. 2. 8 Test result of Undrained shear strength with initial degree of saturation (Wheeler, 1986)

Some triaxial tests of gassy Malaysian Kaolin soil were carried out in Zhejiang University, including two groups on FGS containing the same amount of gas with different initial pore water pressure and one group on saturated clay (Hong et al., 2020). The tests are all under undrained conditions and the same pre-consolidation pressure ($p_c' = 200\ \mathrm{kPa}$) was used in all the tests. For overconsolidated tests, the samples were first consolidated to p_c' and then unloaded to $p_{oc}' = p_c'/\mathrm{OCR}$, where OCR is the overconsolidation ratio. Only lightly overconsolidated clay samples have been used because they are more commonly seen in the seabed or lakebed. This study represents a mature method of experimental study for fine-grained FGS. Some of the test results of the shear strength have been shown in Figs. 2.9 to 2.11. With the higher degree of overconsolidation, the shear strength, which is half of the deviator stress, is getting lower based on the observation of the test data.

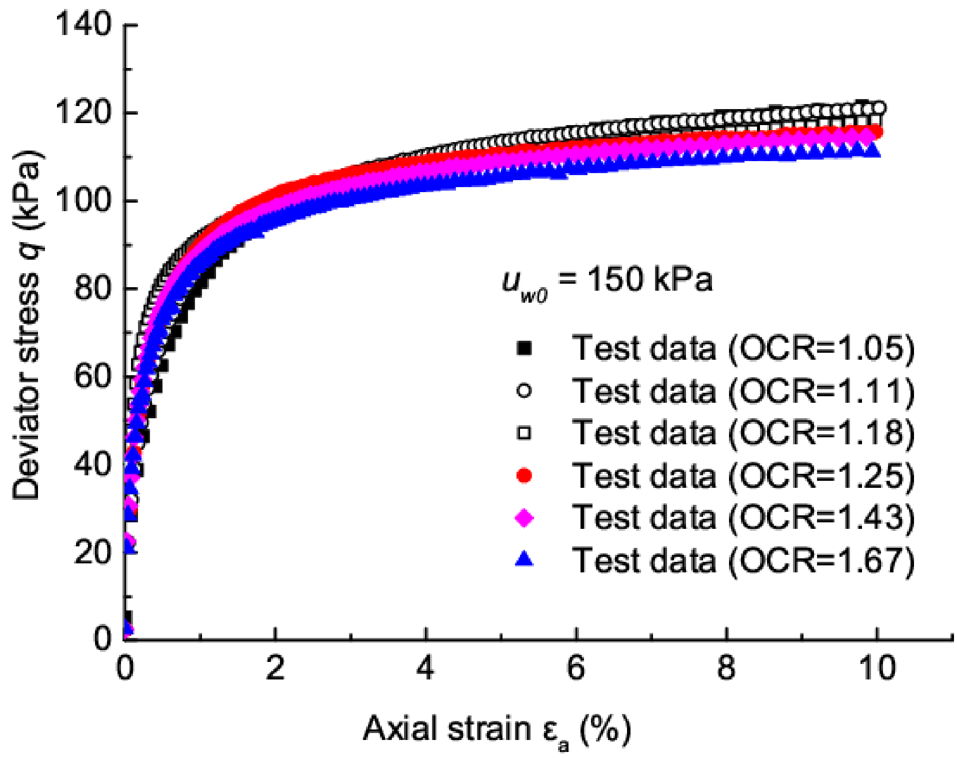

(a)

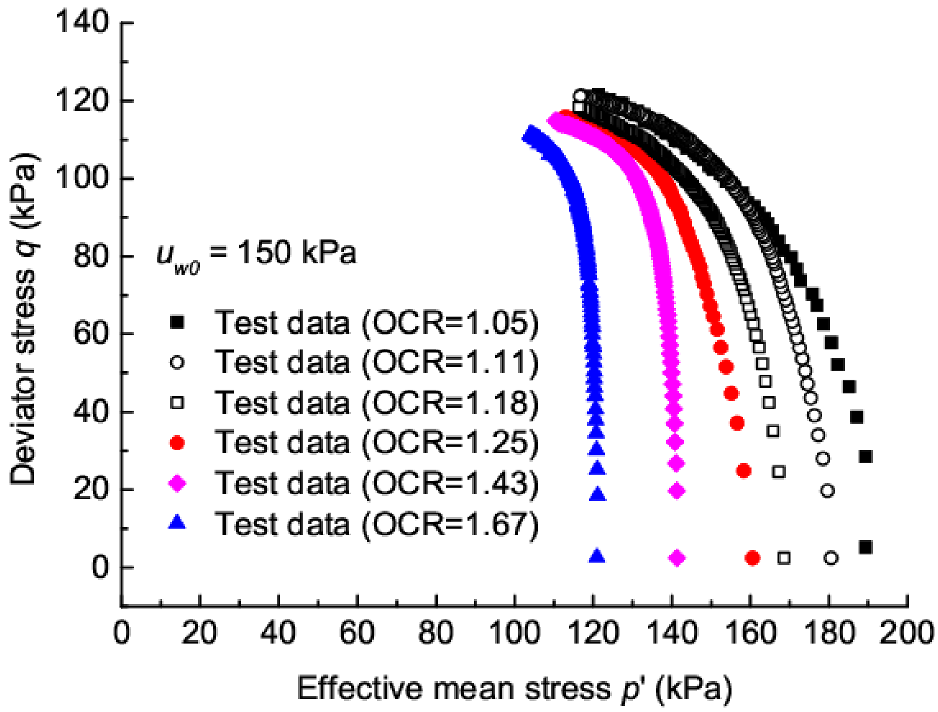

(b)

Fig. 2.9 Results of undrained triaxial compression tests on overconsolidated gassy Malaysian Kaolin with $p'_c = 200$ kPa, $u_{w0} = 150$ kPa, $S_{r0} = 0.94$ and different OCR: (a) the $\varepsilon_a - q$ relationship; (b) the effective stress path

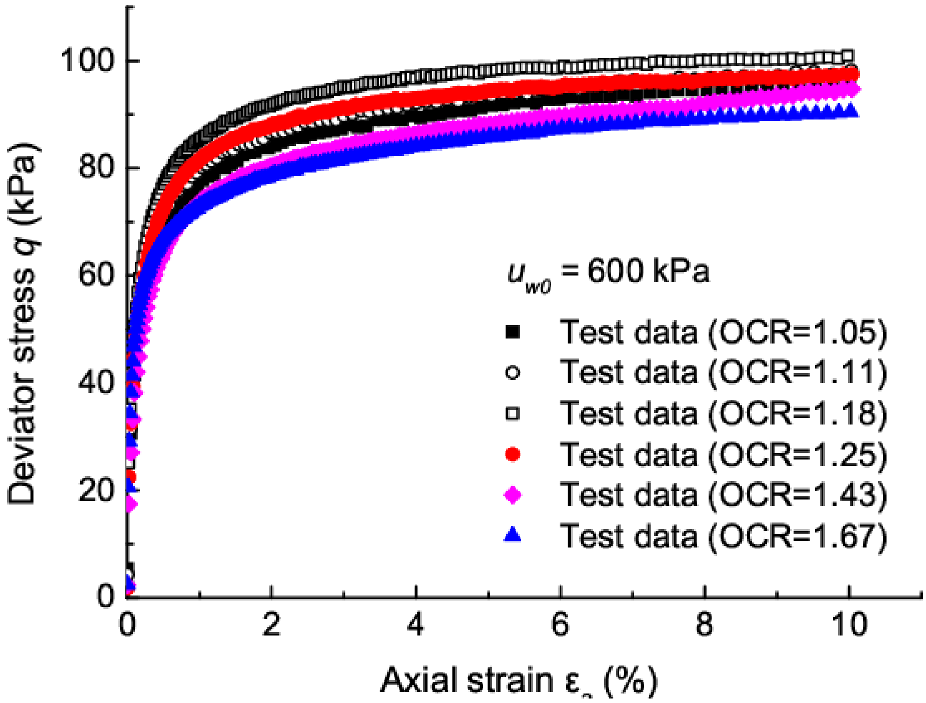

(a)

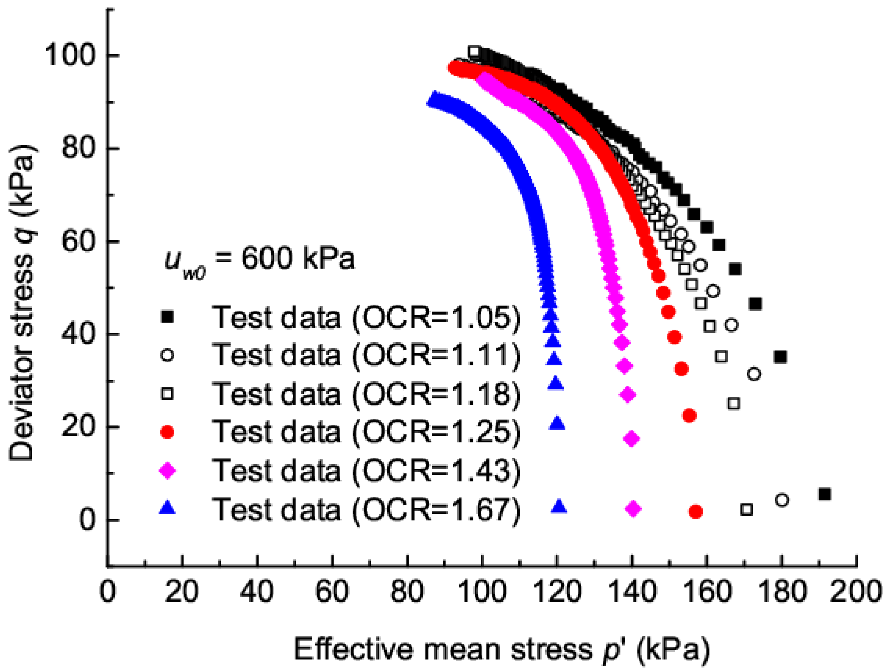

(b)

Fig. 2.10 Results of undrained triaxial compression tests on overconsolidated gassy Malaysian Kaolin with $p_c' = 200$ kPa, $u_{w0} = 600$ kPa, $S_{r0} = 0.96$ and different OCR: (a) the $\varepsilon_a - q$ relationship; (b) the effective stress path

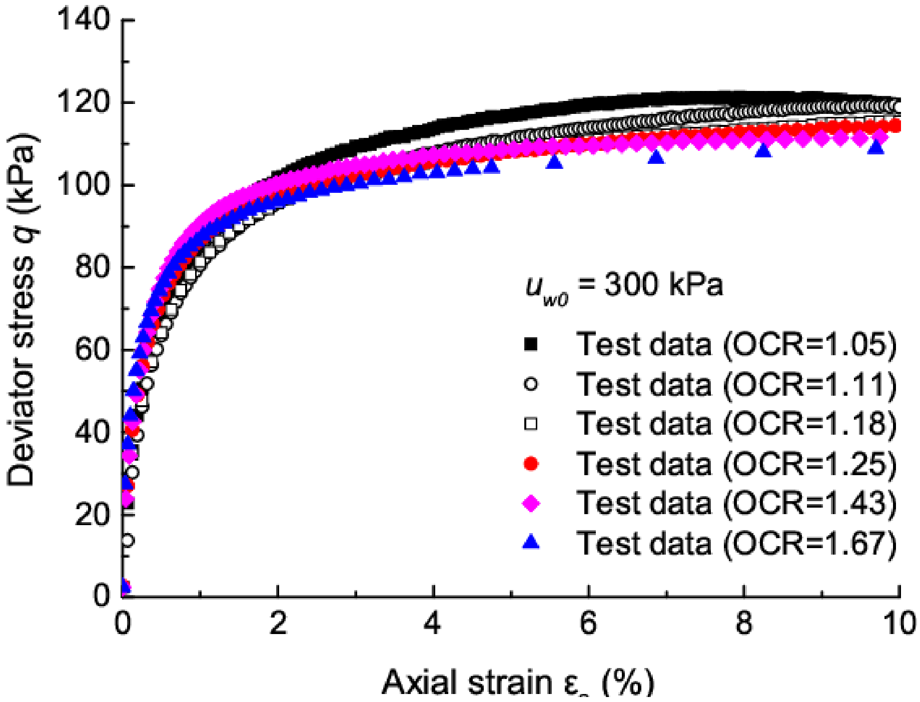

(a)

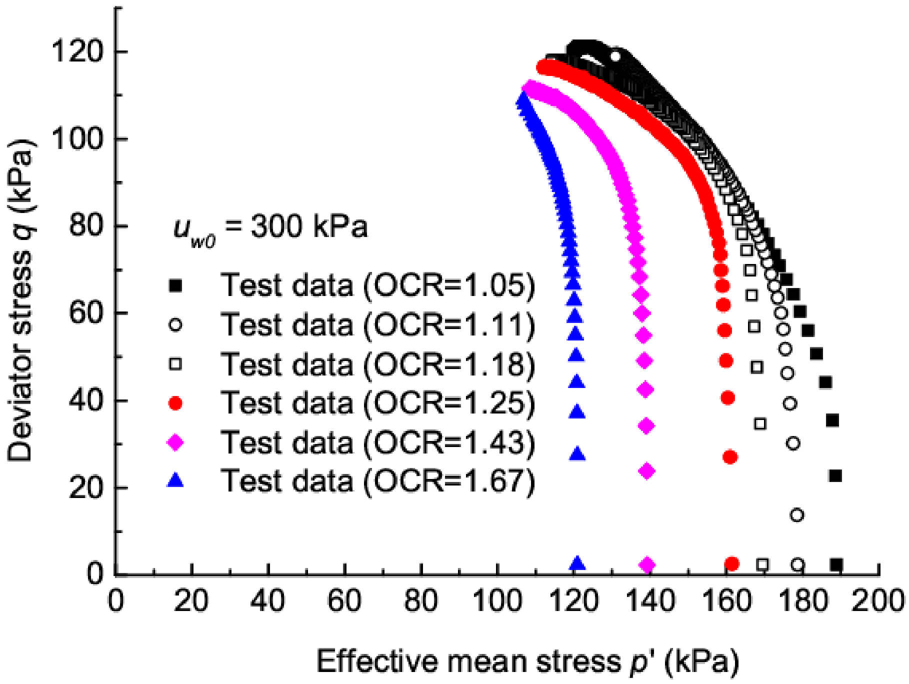

(b)

Fig. 2.11 Results of triaxial compression tests on overconsolidated gassy Malaysian Kaolin with $p'_c = 200$ kPa, $u_{w0} = 300$ kPa, $S_{r0} = 1.0$ and different OCR: (a) the $\varepsilon_a - q$ relationship; (b) the effective stress path

2.3.3 Oedometer tests on FGS

A specially designed oedometer cell was introduced to consolidate soil samples by Thomas (1987). The oedometer cell apparatus was initially developed by Nageswaran (1983), and numerous modifications have been made. However, the main structure of the apparatus remained the same, and a schematic description of the oedometer apparatus is presented in Fig. 2.12. The following measurements can be realised in this study (Thomas, 1987):

(a) Measurement of total vertical stress on the soil sample.
(b) Measurement of pore water pressure on the undrained face.
(c) Capability to consolidate soil from the slurry.
(d) Capability to separate the free gas from the pore fluid drains from the sample on consolidation.
(e) Independent evaluation of the volumes of each of the three phases (solid, water and free gas) throughout the consolidation test.
(f) Measurement of total horizontal stresses.

To calibrate the oedometer, de-aired water was firstly soaked into the cell, top cap, and sintered bronze disc. A rise in the water pressure beneath the piston was employed to gradually pressurise the cell up to 500kPa. The objective of the calibration was to assess how the apparatus responded to an increase in cell pressure in terms of compliance.

Two groups of consolidation tests have been carried out by Thomas (1987) in the University of Oxford. In the first series of tests, the total stress is applied in small, equal increments to allow for drainage and consolidation as the load is increased. In the second series of tests, the load is applied in three daily increments, with pore water pressure dissipation to atmospheric back pressure occurring after each increment. The results of the first series of tests demonstrate that there is no particular relationship between the vertical consolidation stress and the total void ratio for soils with different gas contents. The second series of tests illustrate that the only volume change that occurs in undrained conditions is caused by gas compression and dissolution. For the second series of tests, the results of the soil permeability evaluation involve first calculating the coefficient of consolidation and then the coefficient of volume change. It has been discovered that the relationship between soil permeability and gas content was unaffected. Some of the test results are shown in Figs. 2.13 and 2.14. The test SDTA6 in Fig. 2.13 is the sixth consolidated sample of soils with linear increase of total stress. The tests SDTB2 to 5 in Fig. 2.14 are four consolidated samples containing varying gas content with three-stage loading of total stress. Details of the text series can be found in Thomas (1987). It can be seen that there is a definite relationship between the gas content and the vertical stress for each test in Fig. 2.13. In Fig 2. 14, there are test results of different phase of void ratio with time and it shows the apparatus in this study can make independent evaluation of the volumes of each of the three phases throughout the consolidation test.

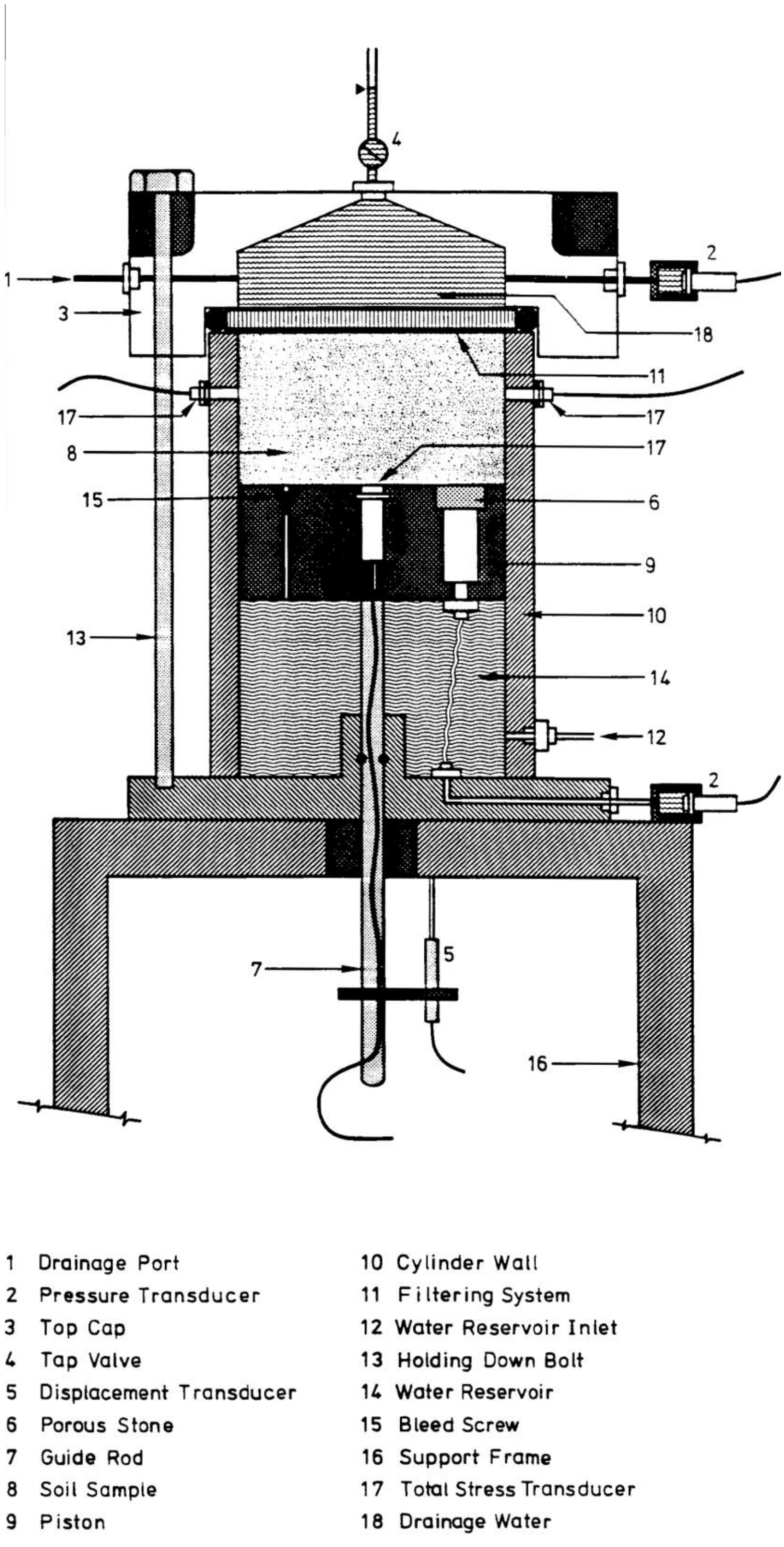

Fig. 2.12 Schematic description of oedometer apparatus (Thomas, 1987)

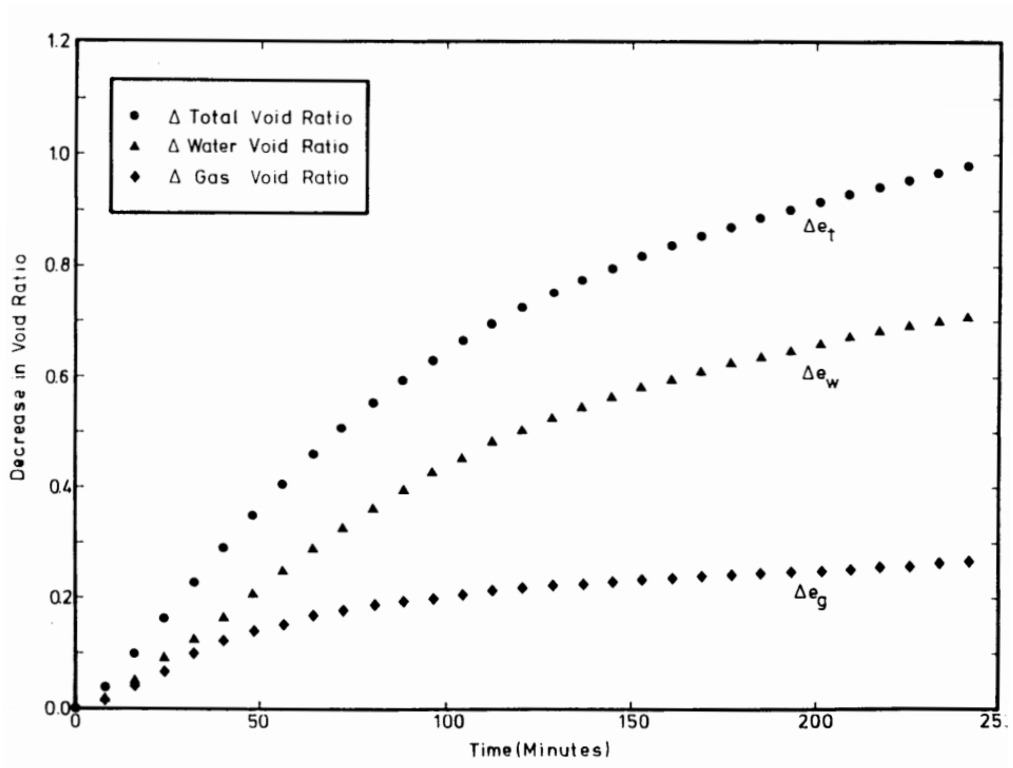

Fig. 2.13 Change in void ratio with time for SDTA6 (Thomas, 1987)

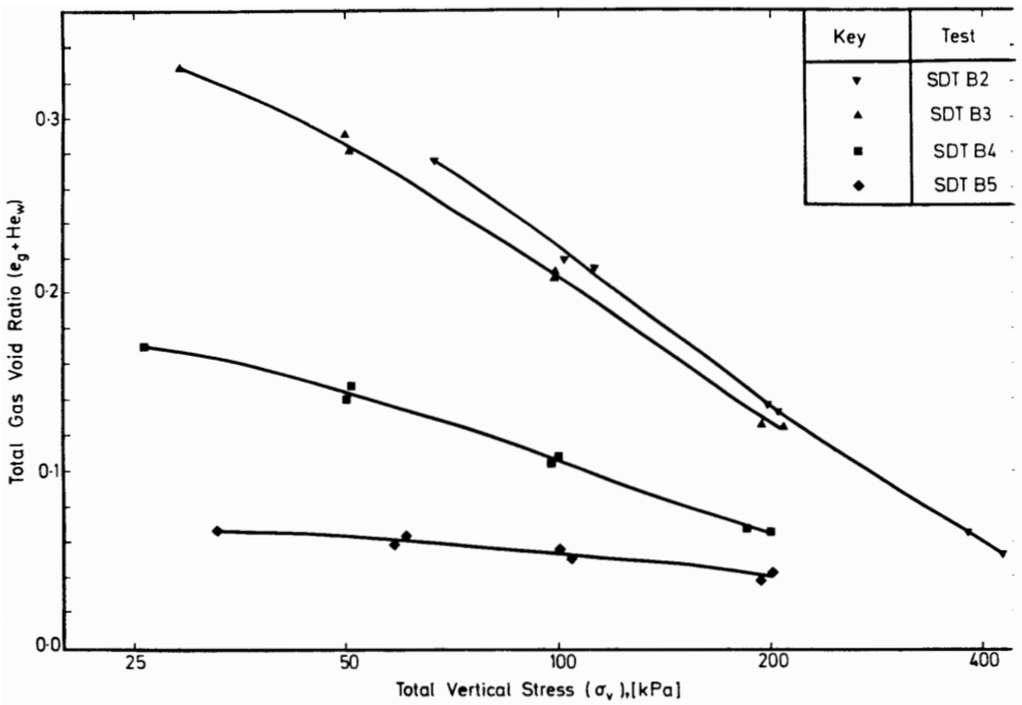

Fig. 2.14 Total gas void ratio versus total vertical stress for test series SDT B2-B5 (Thomas, 1987)

2.4 Previous research on constitutive modelling of normally consolidated fine-grained soils containing gas bubbles

Based on the experimental study on the soils containing gas bubbles, theoretical studies have been carried out by many researchers. Theoretical studies on FGS will be introduced in this section, with a primary focus on the undrained shear strength and constitutive modelling. The undrained condition is considered because this is more common for offshore geotechnical engineering.

2.4.1 Upper and lower bounds of the undrained shear strength of FGS

The upper and lower bounds of the undrained shear strength of FGS have been presented by Wheeler (1986). The upper bound relies on the assumption that all gas bubbles flood with pore water and that the cavity size of the bubbles stays constant throughout shearing. The assumption of constant cavity size is to eliminate the detrimental effect of gas cavities on soil strength. For the lower bound, it is assumed that bubble flooding does not occur, and the entire saturated soil matrix reaches failure. There is no water flow out of the soil boundary when the saturated soil sample is under undrained test. However, the volume can change due to bubble flooding in this case.

The lower bound proposed by Wheeler is based on the theory by Green (1972), who has proposed a model which can be used to predict the yield behaviour of a rigid-perfectly plastic von Mises type matrix containing empty spherical cavities. The model is simply a function with two stress invariants, p and q (with the assumption that any dependence on the third stress invariant could be ignored), and the volume fraction of cavities f. The function of the yield curve is

$$\omega q^2 + \varpi p^2 = {\sigma_y}^2 \tag{2.1}$$

ω and ϖ are functions of f and $\omega \geq 1, \varpi \geq 0$, σ_y is yield stress of matrix.

Eq. (2.1) illustrates a spheroidal yield surface in principal stress space and the yield can occur under an isotropic stress state since it depends on the mean stress p. So, Eq. (2.1) is the same as von Mises' yield function when $\omega = 1, \varpi = 0$.

Assumptions have been made for the expressions for ω and ϖ. Green (1972) made the assumption that the gas cavities were arranged in a cubic close-packed formation and the matrix material was in a state of plastic flow. So, the expression of ω is

$$\omega = \left[\frac{3-2f^{1/4}}{3(1-f^{1/3})}\right]^2 \tag{2.2}$$

The expression of ϖ is derived based on the condition under hydrostatic pressure. The thick spherical shell is selected as the matrix material, and the matrix encloses a single cavity. In Wheeler's study, the yield function of von Mises to the matrix material is employed, and the volume occupied by the cavity is equal to the volume fraction of cavities. The expression of ϖ is derived as below:

$$\varpi = \left(\frac{3}{2\log_e f}\right)^2 \tag{2.3}$$

Combining Eqs. (2.1), (2.2) and (2.3), the yield function derived by Green is

$$\left[\frac{3-2f^{1/4}}{3(1-f^{1/3})}\right]^2 q^2 + \left(\frac{3}{2\log_e f}\right)^2 p^2 = {\sigma_y}^2 \tag{2.4}$$

In this equation, it is assumed that the pressure in cavities is 0. However, there will be gas pressure if the bubble is large in the soil. In this case, the stress difference $(p-u_g)$ should be used instead of mean stress p. The modified expression of the yield function by Green is

$$\left[\frac{3-2f^{1/4}}{3(1-f^{1/3})}\right]^2 q^2 + \left(\frac{3}{2\log_e f}\right)^2 (p-u_g)^2 = {\sigma_y}^2 \tag{2.5}$$

The mean stress p can be expressed using the deviator stress q and the lateral stress σ_3 in triaxial compression condition

$$p = \sigma_3 + q/3 \tag{2.6}$$

When the deviator stress q reaches the yield conditions, the modified yield function is

$$\left[\frac{3-2f^{1/4}}{3(1-f^{1/3})}\right]^2 {q_y}^2 + \left(\frac{3}{2\log_e f}\right)^2 (\sigma_3 - u_g + q_y/3)^2 = {\sigma_y}^2 \tag{2.7}$$

As the values of f and u_g will remain constant in Weeler's assumption. Therefore Eq. (2.7) can be expressed as below

$$\left[\frac{3-2{f_0}^{1/4}}{3(1-{f_0}^{1/3})}\right]^2 \left(\frac{q_f}{\sigma_y}\right)^2 + \left(\frac{3}{2\log_e f_0}\right)^2 \left[\frac{\sigma_3-u_{g0}}{\sigma_y} + \frac{1}{3}\left(\frac{q_f}{\sigma_y}\right)\right]^2 = 1 \tag{2.8}$$

The yield stress has been normalised by σ_y. When the term $\frac{\sigma_3-u_{g0}}{\sigma_y}$ is increased, there is a more detrimental effect on the deviator stress at yield state as $\frac{q_f}{\sigma_y}$ decrease in Eq. (2.8). The yield function developed by Green can be used to predict the lower bound of the undrained shear stress of FGS as the value is a half of the deviator stress at the yield state.

Since the soil is considered as a rigid-perfectly-plastic material, the lower bound can underestimate the soil strength when there is considerable compression of gas bubbles during loading (Sultan et al., 2012). Compression of gas bubbles reduces the volume fraction of free gas in the soil. Higher gas volume fraction causes more damage to the soil structure and leads to lower undrained shear strength.

The pore water pressure increases dramatically under a normal consolidated undrained triaxial test. On the contrary, the gas pressure will change very slightly because the gas has high compressibility. in some circumstances, when the pressure difference between gas pressure and pore water pressure reaches a critical value, the saturated soil matrix can be partially drained by pore water draining into the gas cavities from the saturated soil matrix in a globally undrained shearing test. The matrix void ratio e_m will become smaller and the strength of soil matrix will increase. Due to the difficulty in calculating the specific amount of flooded bubbles, it is exceedingly difficult to determine the beneficial effect of bubble flooding. Additionally, the process of flooding might be affected by the changes of bubble size, which are challenging to measure. Wheeler (1989) assumed that all the bubbles were flooded by water, and the cavities sizes remain unchanged during shearing. In this case, an upper bound of the undrained shear strength for bubble flooding can be defined. The maximum value of stiffness can therefore be calculated once a minimum void ratio at failure e_{mf} for the soil matrix is provided.

The initial void ratio of the matrix e_{m0} and the initial volume fraction of bubbles f_0 can be utilised to calculate the void ratio of the soil matrix e_{mf} when complete bubble flooding occurs (Wheeler, 1986)

$$e_{mf} = e_{m0} - \frac{(1+e_{m0})f_0}{1-f_0} \tag{2.9}$$

The change of matrix void ratio will change the strength of matrix. It can be calculated by using the critical state concept with the stresses and the void ratio at failure. Fig. 2.15 shows shows the critical state line in the $e-p$ space with a slope of λ. Based on the critical state concept, the relationship between p'_{ff} and p'_f can be expressed as

$$p'_{ff} = p'_f \; exp(\frac{e_{m0}-e_{mf}}{\lambda}) \tag{2.10}$$

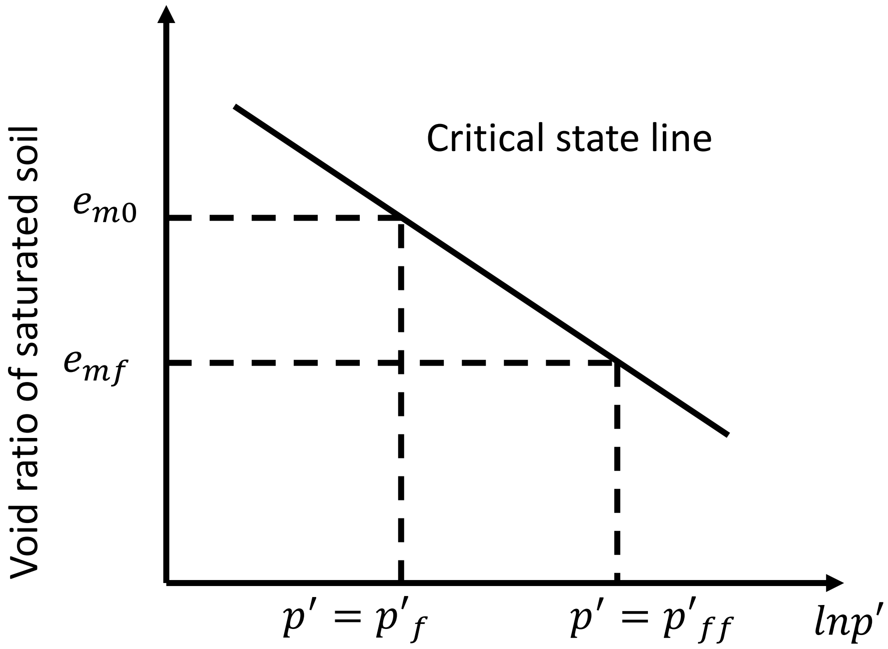

Fig. 2.15 Failure conditions for saturated soi matrix

If the soil matrix void ratio is constant at e_{m0}, the mean effective stress of the soil matrix will be p'_f. When the void ratio of the soil matrix becomes a smaller value of e_{mf}, the mean effective stress of the soil matrix at failure will be p'_{ff} (Fig. 2.15). The theory of critical state concept shows that the deviator stress at failure is related to the mean effective stress at failure for the saturated soil with $q = Mp'$. Thus, the yield stress of the soil matrix from an initial σ_{y0} to a final σ_{yf} can be expressed as:

$$\frac{\sigma_{yf}}{\sigma_{y0}} = \frac{p'_{ff}}{p'_f} \tag{2.11}$$

$$\sigma_{yf} = \sigma_{y0}\, exp(\frac{(1+e_{m0})f_0}{\lambda(1-f_0)}) \tag{2.12}$$

The total volume of the soil matrix will decrease when the water flows into the cavities. Given that it is assumed that the size of cavities cannot change during bubble flooding, the volume fraction of cavities will thus increase. So the volume fraction of cavities after complete bubble flooding can be expressed

$$f_f = f_0/(1 - f_0) \tag{2.13}$$

An upper bound of the undrained shear strength for FGS can be presented when complete bubble flooding occurs and no cavity contraction

$$\left[\frac{3-2f_f^{1/4}}{3(1-f_f^{1/3})}\right]^2\left(\frac{q_f}{\sigma_{yf}}\right)^2+\left(\frac{3}{2\log_e f_f}\right)^2\left[\frac{\sigma_3-u_{wf}}{\sigma_{yf}}+\frac{1}{3}\left(\frac{q_f}{\sigma_{yf}}\right)\right]^2=1 \quad (2.14)$$

Then f_f can be replaced by Eq (2.13) and q_f is twice of the undrained shear strength of saturated soils. Also, the pore water pressure at failure can be simply calculated by maximising $\frac{q_f}{\sigma_{yf}}$

$$u_{wf}=\sigma_3+q_f/3 \quad (2.15)$$

Combining Eqs. (2.9), (2.13), (2.14), and (2.15), the final upper bound can be expressed

$$\frac{C_u}{(C_u)_{sat}}=\frac{3(1-(f_0/(1-f_0))^{1/3})}{3-2(f_0/(1-f_0))^{1/4}}\exp\left[\frac{(1+e_{m0})f_0}{\lambda(1-f_0)}\right] \quad (2.16)$$

In Eq. (2.16), C_u and $(C_u)_{sat}$ are the undrained shear strength and the saturated undrained shear strength in wheeler, 1986 and in the following chapters, s_u and $(s_u)_{sat}$ are used instead. Fig. 2.16 shows the theoretical and experimental results of Wheeler's upper and lower bounds for the undrained shear strength of Combwich mud containing methane. The upper bound is inclined to overestimate the beneficial effect of gas bubbles on the soil strength due to the impossibility of complete bubble flooding if the gas dissolution in pore water is negligible. When the gas cavities are completely flooded, the gas volume becomes zero, and the gas pressure will reach infinite if the free gas does not dissolve in the pore water. Additionally, the total stress path is not taken into account while determining the upper and lower bounds. However, the total stress path has a direct effect on the evolution of pore water pressure u_w which affects the undrained shear strength. Indeed, the pore water pressure u_w is an important variable for modelling the lower bound of undrained shear strength, as the gas pressure u_g is closely related to u_w (Wheeler, 1986; Sham, 1989; Hong et al., 2020; Gao et al., 2020).

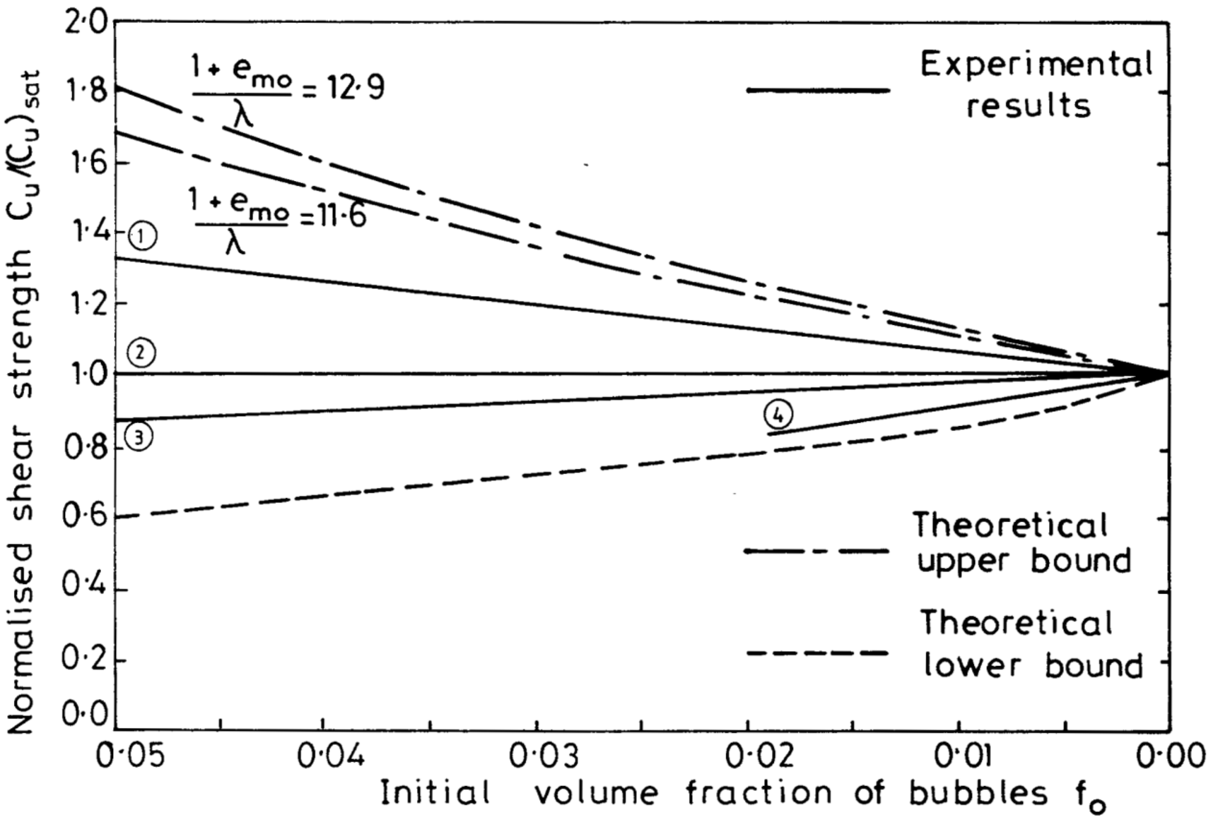

Fig. 2.16 Theoretical and experimental values of the undrained shear strength (Wheeler,1986)

2.4.2 Constitutive relations for partially saturated soils containing gas bubbles by Pietruszczak and Pande (1996)

An approach for constitutive modelling of FGS based on micromechanical analysis has been developed by Pietruszczak and Pande (1996). In the constitutive model, the average pore size is included as a material parameter, and gassy soil is modelled as a three-phase medium. It is assumed that the liquid and gas phases are separated by curved boundaries. Based on volume averaging, which is applied to both stress and strain measurements within each phase, the macroscopic mechanical properties of soil are determined. The average response is a function of each phrase's mechanical properties and volume contributions. The method demonstrates that the reaction of unsaturated soil may be viewed as a combination of the mechanical properties of elements, their corresponding volume fractions, and the kind of soil microstructure.

2.4.3 Constitutive model for FGS by Grozic et al. (2005)

Based on these preliminary studies, some attempts have been made to simulate the entire stress-strain relationship of FGS. Grozic et al. (2005) have proposed a constitutive model for this soil by considering the gas as part of the pore fluid. Henry's law has been used in the gassy soil model. It can be defined as the mass of gas dissolved in a fixed amount of liquid at a constant temperature, which is directly proportional to the absolute pressure of the gas above the solution. It means the solubility is dependent on the pressure, temperature, and salinity of the pore water. Henry's law can be expressed as below

$$K_H = \frac{C_a}{P_g} \text{ or } K_H = \frac{55.3}{K_{H,inv}} \tag{2.17}$$

where C_a is the concentration of a specific gas in the aqueous phase and P_g is the partial pressure of the specific gas in the gas phase (Fredlund and Rahardjo, 1993). Often the reciprocal value, $K_{H,inv}$ is used where K_H is in mol/l and $K_{H,inv}$ is in atm.

The volume of the pore fluids will alter due to their compressibility, which is a combination of the compression of the liquid and the compressibility of the free gas. The total stress, which is related to the compressibility of a gas mixture liquid, can be expressed as below

$$C_{gl} = SC_l(\frac{\mathrm{d}u_l}{\mathrm{d}\sigma}) + (1 - S_0 + hS_0)C_g(\frac{\mathrm{d}u_g}{\mathrm{d}\sigma}) \tag{2.18}$$

where C_{gl} is the compressibility of the gas mixture liquid, S is the degree of saturation, h is the Henry's constant, $\frac{\mathrm{d}u_l}{\mathrm{d}\sigma}$ represents the change in liquid pressure in relation to a change in total stress, $\frac{\mathrm{d}u_g}{\mathrm{d}\sigma}$ is the gas pressure change in relation to a total stress change, and σ is the total stress in the study of Grozic et al. (2005).

Eq. (2.18) will be used to calculate the volume change due to the compression and solution of gas by introducing the change of void ratio

$$\Delta e = (\frac{\Delta\bar{u}_g}{u_{g0}+\Delta\bar{u}_g})(1 - S_0 + K_H S_0)e_0 \tag{2.19}$$

Eq. (2.19) can be introduced into the modified Cam-Clay (MCC) model for considering the effect of gas in the soils. For each increment of axial strain applied, the MCC model is used to calculate the change of pore water pressure firstly due only to the applied strain. The corresponding void ratio change, and the degree of saturation inducted by the pore water pressure can then be determined. The predictions and measured results are shown as follows.

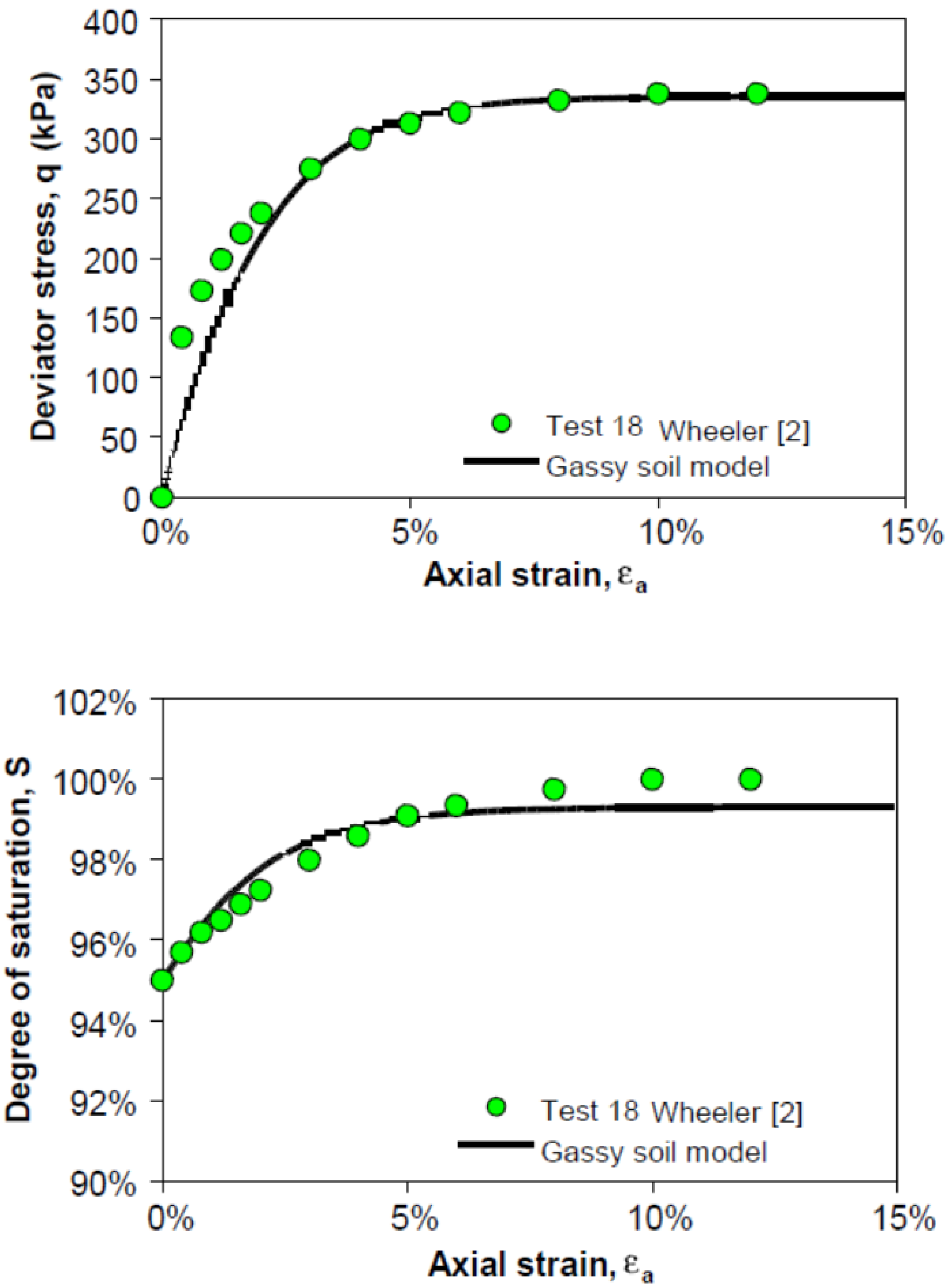

Fig. 2.17 Calibration of the gassy soil model. Gassy soil predictions and test results (Grozic et al., 2005)

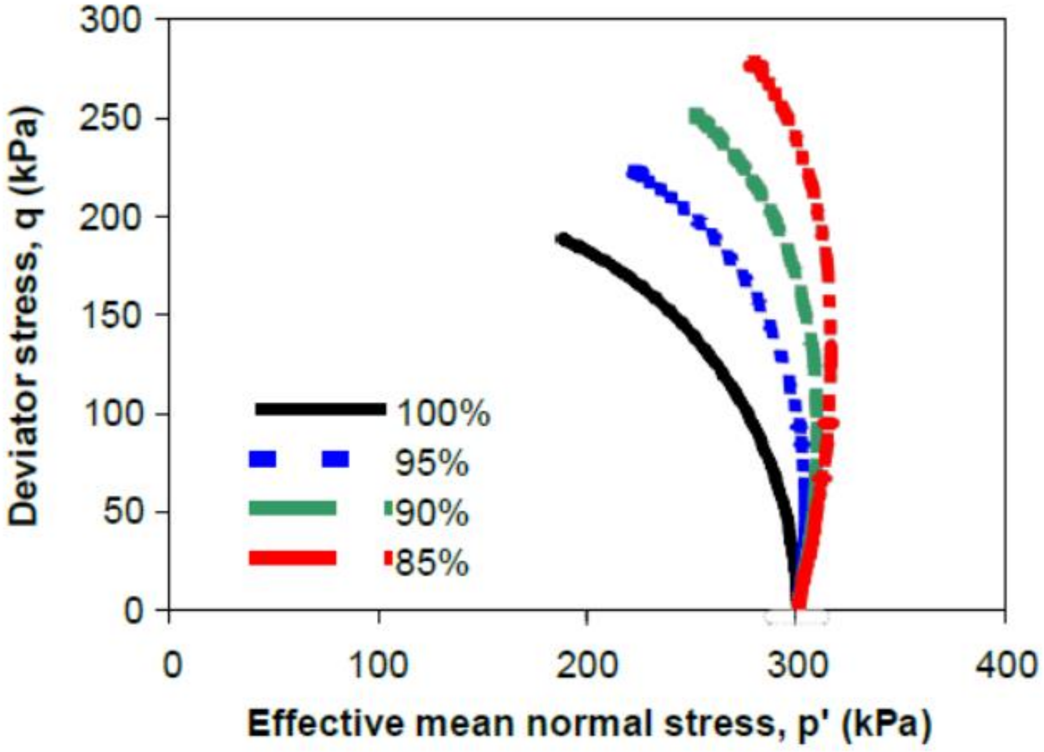

Fig. 2.18 prediction of the effect of initial gas volume from 100% to 85% (Grozic et al., 2005)

2.4.4 Constitutive model for FGS by Hong et al. (2020)

Based on extensive laboratory studies, Hong et al. (2020) proposed a constitutive model for FGS by considering the effect of free gas on the dilatancy and yield surface shape. Four additional parameters have been contributed to the constitutive model, which is constructed on the framework of the MCC model. A function D which can capture the stress-dilatancy relation was developed in the model

$$D = \frac{d\varepsilon_v^p}{d\varepsilon_q^p} = \left[1 + \xi \frac{u_{w0} - u_{w0\_ref}}{p_0'} \exp(-\frac{\chi}{\psi_0})\right] \frac{M^2 - \eta^2}{2\eta} \tag{2.20}$$

where u_{w0_ref} is the reference initial pore water pressure u_{w0} at which the stress–dilatancy of a gassy soil is similar to its saturated equivalent. X and ξ are two material constants for describing the effects of u_{w0} and initial gas volume fraction ψ_0 on the dilatancy of the FGS; and η is the stress ratio, p_0' is the effective mean stress and q is the deviator stress.

The yield function derived by Lagioia et al (1996) was used in this elastoplastic model

$$F = \frac{p'}{p'_0} - \frac{(1+\frac{\eta}{MK_2})^{\frac{K_2}{(1-\mu)(K_1-K_2)}}}{1+\frac{\eta}{MK_1}^{\frac{K_1}{(1-\mu)(K_1-K_2)}}} = 0 \tag{2.21}$$

where p'_0 is the preconsolidation pressure and K_1 and K_2 are given as below

$$K_{1/2} = \frac{\mu(1-\theta)}{\theta(1-\mu)}(1 \pm \sqrt{1 - \frac{4\theta(1-\mu)}{\mu(1-\theta)^2}}) \tag{2.22}$$

μ and θ are the parameters that can be used to determine the shape of yield surface.

The yield function F and the dilatancy function D are independently formulated, as shown by Eq. (2.20) and (2.21). A non-associated flow rule is adopted in this constitutive model

$$d\varepsilon_q^p = \langle L \rangle \frac{\partial F}{\partial q} \tag{2.23}$$

$$d\varepsilon_v^p = \langle L \rangle \frac{\partial F}{\partial q} D \tag{2.24}$$

where L is the loading index. The McCauley brackets $\langle \quad \rangle$ operate in the way of $\langle L \rangle = L$ if $L > 0$; otherwise, $\langle L \rangle = 0$.

The behaviour can be derived using Boyle's law

$$(u_g + p_a)V_g = (u_g + p_a + \mathrm{d}u_g)(V_g + \mathrm{d}\, V_g) = n_g RT = C \tag{2.25}$$

where u_g, p_a, $V_{g,}$ n_g, R and T are the pore gas pressure, atmospheric pressure, gas volume, number of the mole of the gas, ideal gas constant, and absolute temperature, respectively; and $\mathrm{d}u_g$ and $\mathrm{d}V_g$ are increments of gas pressure and gas volume, respectively. C can be stated by introducing the initial pore gas pressure u_{g0} and the initial gas volume V_{g0}

$$(u_{g0} + p_a)V_{g0} = C \tag{2.26}$$

The initial gas pressure is hard to measure, and it can be defined by initial pore water pressure and the initial total stress (Sham,1989)

$$u_{g0} = u_{w0} + \delta(p_0 - u_{w0}) \tag{2.27}$$

where δ is the model parameter which is from 0 to 1.

The volumetric strain of the gas bubble can then be expressed by combining Eqs. (2.25) - (2.27)

$$d\varepsilon_v^g = \frac{dV_g}{V} = \frac{dp(u_{w0}+p_a)(2p_0+p_a-u_{w0})\psi_0}{(u_g+p_a+dp)(u_g+p_a)(p_0+p_a)} \tag{2.28}$$

The formations were developed for calculating the volumetric strain and gas pressure of gas bubbles. In comparison to the MCC model, the model can predict the behaviour of fine-grained soils containing gas bubbles using four additional parameters (Fig. 2.19).

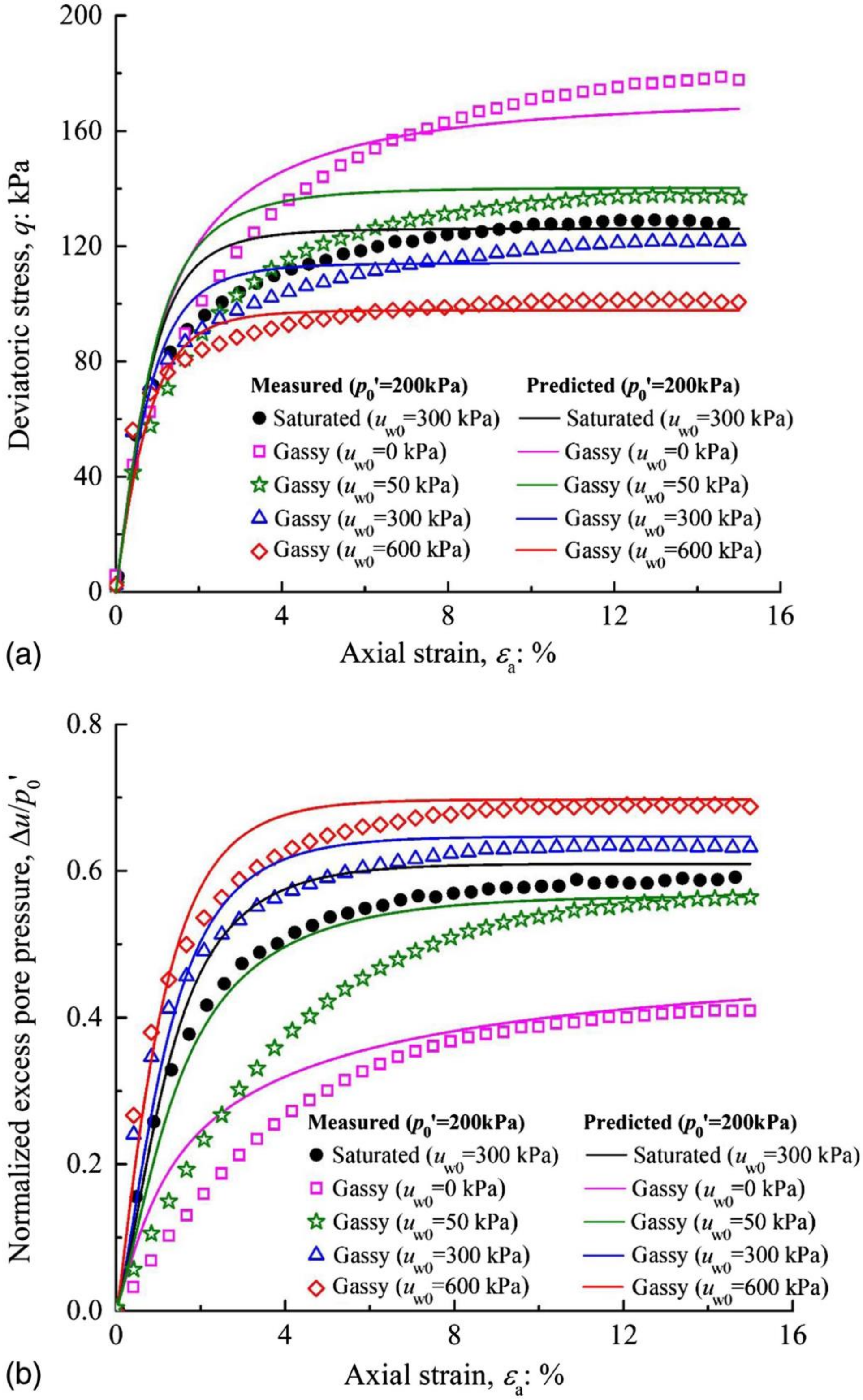

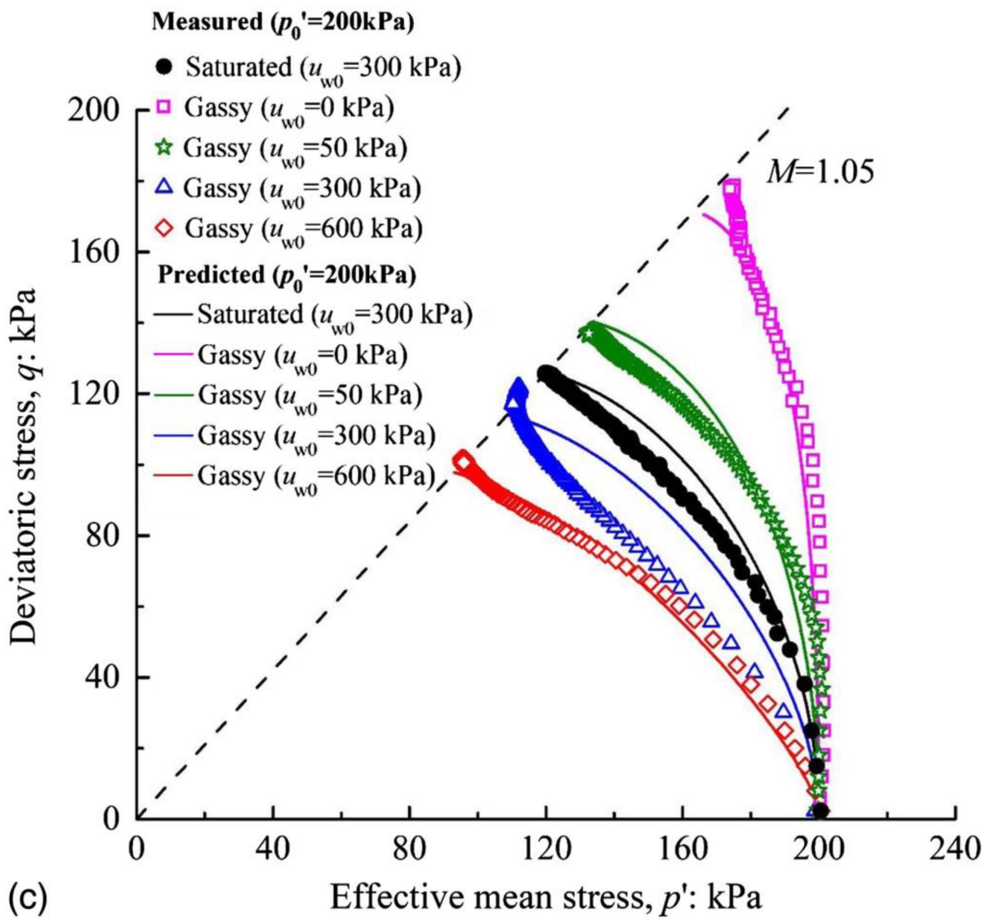

Fig. 2.19 Comparison between the predicted and measured shear behaviour of gassy Malaysia Kaolin silt: (a) stress–strain relation; (b) pore pressure response; and (c) effective stress path. (Data from Hong et al., 2019a)

2.4.5 Constitutive model for FGS by Gao et al. (2020)

A composite approach for constitutive modelling of FGS has been developed by Gao et al. (2020). For the fine-grained gassy soil, there are four components in the model: gas, water in cavities, water in the saturated soil matrix, and soil particles. The degree of saturation and void ratio can be used to describe the volume, including the volume fraction of gas bubbles. In this model, the mean effective stress and deviator stress can be expressed by the total effective stress of the soil matrix, mean effective stress of the soil matrix, the deviator stress of the soil matrix, gas pressure and pore water pressure.

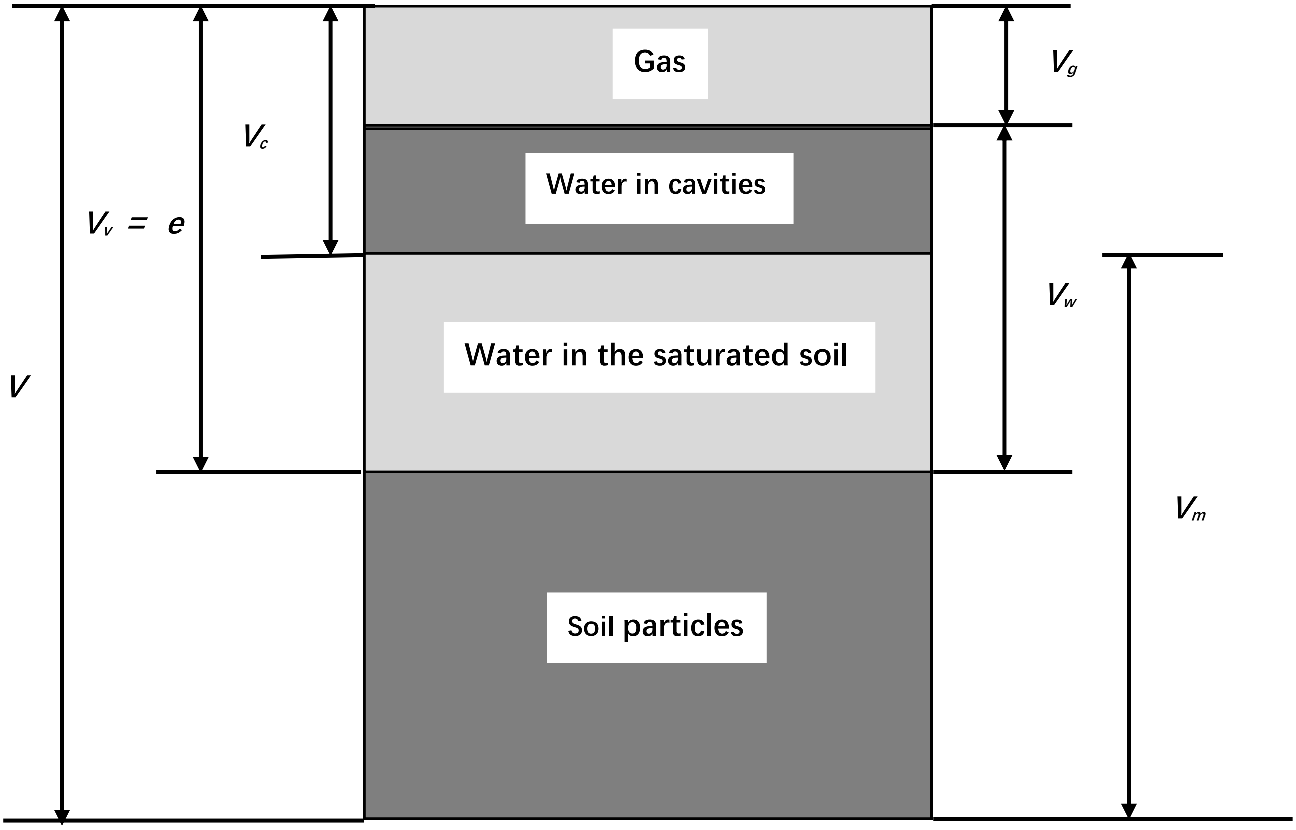

Fig. 2.20 Phase diagram for fine-grained soil containing gas bubbles (water in both the saturated matrix and cavities.

The yield function of MCC model is used in this model, and a modified hardening law is introduced as below

$$dp_0' = \langle L\rangle r_{pc} = \langle L\rangle(r_1 - r_2) = \langle L\rangle \frac{(1+e_0)p_0'}{\lambda-\kappa}\frac{\partial F}{\partial p'}\left[1 - a\sqrt{f}\,\frac{\eta}{\mathrm{M}}\left(\frac{u_g+p_a}{p_0'}\right)^{\xi}\right] \quad (2.29)$$

$$r_1 = \langle L\rangle \frac{(1+e_0)p_0'}{\lambda-\kappa}\frac{\partial F}{\partial p'} \quad (2.30)$$

$$r_2 = \langle L\rangle \frac{(1+e_0)p_0'}{\lambda-\kappa}\frac{\partial F}{\partial p'}\left[a\sqrt{f}\,\frac{\eta}{\mathrm{M}}\left(\frac{u_g+p_a}{p_0'}\right)^{\xi}\right] \quad (2.31)$$

where p_0' indicates the size of MCC yield surface, L is the loading index, e_0 is the initial value of the saturated matrix void ratio e_m, $\eta\ (= q/p')$ is the stress ratio, λ is the compression index, κ is the swelling index, p_a is the atmospheric pressure, $\langle\ \ \rangle$ are the McCauley brackets [$\langle L\rangle = L$ for $L > 0$ and $\langle L\rangle = 0$ otherwise] and ξ is a new model parameter. a is used to describe the detrimental effect of gas bubbles on plastic hardening and shear strength. r_1 and r_2 represent the variables in the hardening law. r_1 is the same as that for the MCC model and the term r_2 is used to model the detrimental effect of gas bubbles on plastic hardening and shear strength. When the volume fraction of the gas bubble is 0, $r_2 = 0$, it means the hardening law is identical to that of the original modified Cam clay model.

For strain variables, the summation of the volumetric strain of the saturated soil matrix and the volumetric strain of the cavity can be employed to decompose the total strain of the fine-grained FGS. (Tsai and Hahn, 1980; Pietruszczak and Pande, 1996; Diambra et al., 2010). It is evident that the volume fraction of the gas bubbles is associated with the volumetric strain of the cavity. The volumetric variation of water flow into and out of the matrix at the boundary of the saturated soil matrix and bubble flooding determines the volumetric strain increment of the saturated soil matrix. When bubble flooding occurs, the change of volumetric strain of bubble flooding can be described as below

$$d\varepsilon_v^f = Adu_w = (1 - s_r)(\frac{p_0'}{u_g+p_a})^{\xi}\exp(1 - \frac{u_g-u_w}{\chi p_0'})\ \frac{\langle du_w \rangle}{u_g+p_a} \tag{2.32}$$

In the equation, χ and ξ are two introduced parameters. There is complete bubble flooding when the degree of saturation is 1 and in this case, there is no change of volumetric strain of bubble flooding. Additionally, the magnitude of the bubble flooding will increase as the gas pressure decreases. ξ is one of the new model parameters which can reflect the rate of bubble flooding, and it will change with the p_0' based on the experiment results. χ is also used to calculate the rate of bubble flooding, and it can decrease the rate as the difference between gas pressure and pore water pressure increase.

The model also derived a method to calculate the initial gas pressure by assuming that the value is related to the initial total stress and initial pore water pressure

$$u_{gi} = u_{wi} + \delta(p_i - u_{wi}) = u_{wi} + \frac{u_{wi}+p_a}{p_i+p_a}(p_i - u_{wi}) \tag{2.33}$$

As the initial pore water increases, the initial gas pressure increases as well, eventually approaching the initial total stress.

The increment of pore water pressure is introduced in the elasto-plastic relation in the model. The pore gas pressure, volume change of cavities and gas should be updated based on the evolution of p', q and u_w. Details can be found in Gao et al. (2020). The constitutive equation of the model can be simply shown as

$$\begin{bmatrix} dp' \\ dq \\ du_w \end{bmatrix} = \begin{bmatrix} D_{11} & D_{12} & 0 \\ D_{21} & D_{22} & 0 \\ 0 & 0 & K_w \end{bmatrix} \begin{bmatrix} d\varepsilon_v \\ d\varepsilon_q \\ d\varepsilon_v^w \end{bmatrix} \tag{2.34}$$

Comparison between the measured data (from Hong et al.,2020) and predictions of the constitutive model are shown as Fig. 2.21. The recent two models (Hong et al., 2020, Gao et al.,2020) are capable of describing the detrimental and beneficial effect of free gas on the stiffness and strength of FGS (Ehlers and Blome, 2003; Ehlers et al., 2004; de Boer, 2003). But in addition to the classic critical state model for saturated clay, the two models have introduced at least two additional parameters. Some of which might be difficult to get through regular triaxial tests. Besides, the gas pressure is employed as an internal variable in the model proposed by Gao et al., 2020, making it difficult to use the model. Firstly, the gas pressure in FGS is incredibly difficult to measure, both in the lab and outdoors. Secondly, additional equations are needed to calculate the initial gas pressure and the evolution of the gas pressure during loading. Finally, when the gas pressure is used as a state variable, the constitutive equations must be derived using the elastic bulk modulus of water (Gao et al., 2020).

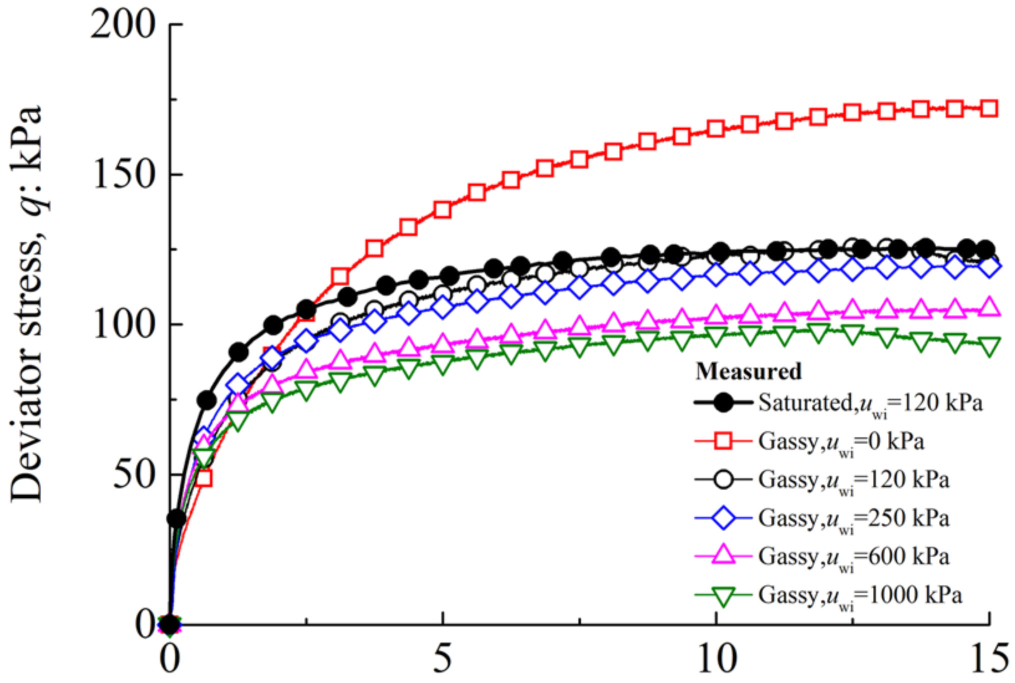

(a)

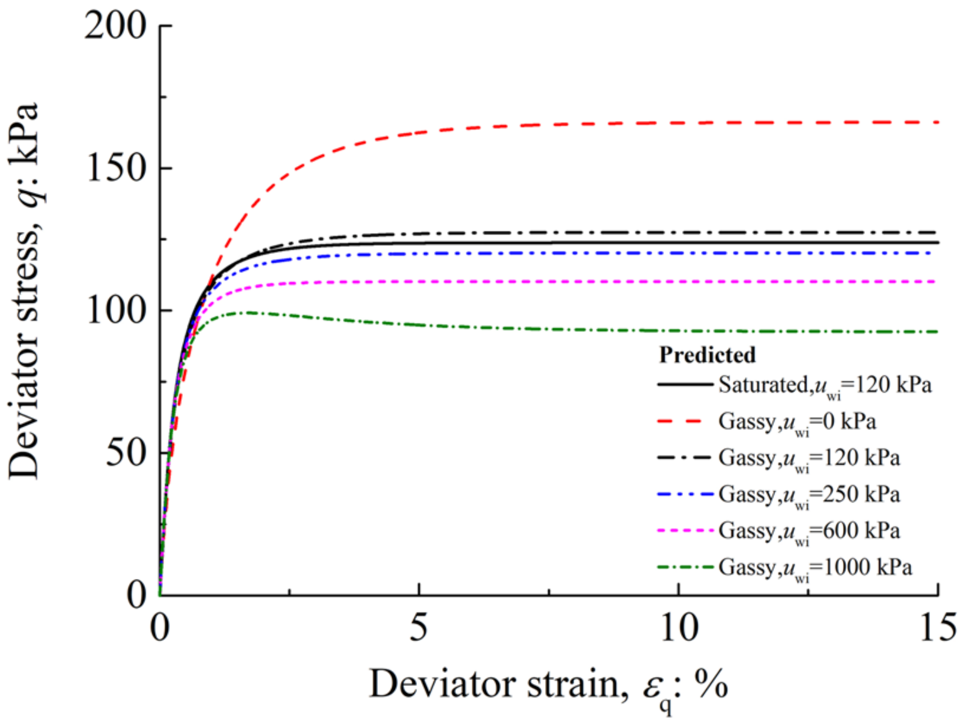

(b)

Fig. 2.21 Comparison between the measured data and predictions of Malaysian Kaolin in undrained compression: (a) test data; (b) model predictions (Gao et al., 2020)

2.4.6 Bounding surface model for overconsolidated saturated soils (Gao et al., 2017)

The majority of past research has concentrated on the behaviour of normally consolidated FGS. However, naturally deposited clay in the seabed or lakebed can become overconsolidated due to water pressure variation, sediment movement or submarine landslides. Bounding surface models (Dafalias, 1986) are widely used to describe the response of overconsolidated clay. A conventional plasticity model gives purely elastic response when the stress state is inside the yield surface, which is not realistic.

A bounding surface model has been derived to capture the dilatancy behaviour of the overconsolidated saturated soils. A dilatancy relation has been developed as below by Gao et al. (2017),

$$D = \frac{d\varepsilon_v^p}{\left|d\varepsilon_q^p\right|} = \frac{M_d^2 - \eta^2}{2\eta} \tag{2.35}$$

where $d\varepsilon_v^p$ and $d\varepsilon_q^p$ denote the plastic volumetric and shear strain increment for the saturated soil matrix, respectively

$$M_d = M_c R^m \tag{2.36}$$

m should be calibrated based on the test results on overconsolidated clay. R is the ratio of the 'image' and current stress state (Gao et al., 2017) and it is the reciprocal of overconsolidation ratio in the study. The variation of m typically ranges from 0 to 0.6 based on the experience (Gao et al., 2017), which has no significant influence on the prediction for the stress-strain relation base on the experimental investigation. m can be determined by fitting the $p' - q$ relations in undrained cases.

The bounding surface model with state-dependent dilatancy for overconsolidated clay is applied for the saturated soil matrix. The bounding surface is defined as (Collins, 2005)

$$\bar{F} = \frac{(\bar{p}\prime - \alpha\bar{p}_0/2)^2}{[(1-\alpha)\bar{p}\prime + \alpha\bar{p}_0/2]^2} + \frac{\bar{q}^2}{M_c^2[(1-\alpha)\bar{p}\prime + \alpha\bar{p}_0/2]^2} - 1 = 0 \tag{2.37}$$

where $\bar{p}_0$ is the size of the current yield surface, α is a model parameter and M_c is the critical state stress ratio in triaxial compression. The mapping centre for the bounding surface is the origin of the stress space.

Under undrained triaxial compression/extension loading conditions, the model gives the following relation

$$p_f/p_i = (\mathrm{OCR} \cdot \alpha/2)^{(\lambda-\kappa)/\lambda} \tag{2.38}$$

where p_f is mean effective stress at critical state and p_i is initial confining pressure. α can be evaluated from Eq. (2.38) directly because λ and κ are known. It is recommended to use the test results on normally consolidated clay since it is simpler to determine the critical state. The suggested range of parameter α is 0 to 1.8, ensuring that the bounding surface remains convex. The MCC yield surface is recovered when α=1.

The plastic modulus at the image stress point, $\overline{K}_p$ can be determined as below

$$\overline{K}_p = -\frac{\partial F}{\partial \bar{p}_0}\frac{\partial \bar{p}_0}{\partial \varepsilon_v^{mp}}\frac{\partial \bar{F}}{\partial \bar{q}}\overline{D} = -\frac{(1+e_0)\bar{p}_0}{\lambda-\kappa}\frac{\partial F}{\partial \bar{p}_0}\frac{\partial F}{\partial \bar{q}}\frac{M_c^2-\eta^2}{2\eta} \tag{2.39}$$

The relationship between $\overline{K}_p$, which can represent the increase of stiffness and peak stress ratio of clay with the degree of overconsolidation, and the plastic modulus at the current stress state, K_p is crucial to the performance of the bounding surface model (Dafalias and Herrmann, 1986; Pestana and Whittle. 1999). In the previous bounding surface models, K_p is typically assumed to be an interpolation function of $\overline{K}_p$ and a shape-hardening function (Dafalias and Herrmann 1986; Ling et al. 2002) or reference modulus (Banerjee and Yousif 1986; Pestana and Whittle 1999). To avoid excessive complication, the expression for K_p in this study is simply assumed to be of the identical form of $\overline{K}_p$ by simply replacing M_c with a virtual peak stress ratio M_v.

Therefore the plastic modulus for the saturated matrix is

$$K_p = -\frac{(1+e_0)\bar{p}_0}{\lambda-\kappa}\frac{\partial F}{\partial \bar{p}_0}\frac{\partial F}{\partial \bar{q}}\frac{M_v^2-\eta^2}{2\eta} \tag{2.40}$$

$$M_v = M_c R^{-n} \tag{2.41}$$

where M_v is related to R according to Eq. (2.41), and n is the nonnegative model parameter (Zervoyanis, 1982; Nakai and Hinokio, 2004; Mita et al., 2004). Typically, greater n results in a stiffer response because both M_v and K_p are increasing functions of n for $R \le 1$, which means OCR ≥ 1. Parameter n can then be determined through fitting stress-strain relations in undrained cases by setting parameter $m = 0$.

The bounding surface model can have a good prediction only for the overconsolidated saturated soils. Sham (1989) has reported some undrained triaxial test results on lightly overconsolidated FGS. It is shown that the overconsolidation affects the soil-gas interaction and the undrained shear strength. But a constitutive model for describing the stress-strain relationship of overconsolidated FGS has not been developed.

2.5 Limitations of Existing Constitutive Models

There have been developments in existing constitutive models for fine-grained soils containing gas bubbles. However, there are limitations which make these models not able to capture the mechanical behaviour of FGS very well.

- It is assumed that the gas and water existed as a single compressible pore fluid by Nageswaran (1983). This is valid for modelling the soil response under consolidation but not shear, because 'bubble flooding' can occur.
- The upper and lower bounds proposed by Wheeler (1986) have not considered the total stress path, which can influence the change of pore water pressure. The upper bound tends to overestimate the beneficial effect of gas bubbles on the soil stiffness due to complete bubble flooding is assumed in Wheeler's research. If complete bubble flooding occurs, the gas volume would become zero. Then the gas pressure would reach infinite, which is not possible. The lower bound tends to underestimate the soil strength because the change of gas volume fraction during compression has not been considered.
- Grozic et al. (2005) have proposed a constitutive model for this soil by considering the gas as part of the pore fluid, which cannot represent the real internal structure of this soil. Meanwhile, the pore gas pressure is equal to the pore water pressure based on the assumption. The difference between these two pore pressures can be significant enough and have a dramatic influence on the strength.
- Pietruszczak and Pande (1996) have developed a method for constitutive modelling of FGS based on micromechanical analysis. Though it can consider the composite structure of FGS, it cannot capture the detrimental effect of gas bubbles on the undrained shear strength.
- Based on extensive laboratory studies, Hong et al. (2020) proposed a constitutive model for FGS by considering the effect of free gas on the dilatancy and yield surface shape. Gao et al. (2020) have developed a composite approach for constitutive modelling of FGS. Both these two recent models are capable of describing the detrimental and beneficial effects of free gas

on the stiffness and strength of FGS. But the two models contain at least two extra parameters in addition to the classic critical state model for saturated clay (i.e., Modified Cam-clay model, or MCC model), some of which may not be easily obtained through conventional triaxial tests. Besides, the gas pressure is employed as an internal variable in Gao et al. (2020), which causes inconvenience for using the model: (i) it is almost impossible to measure the gas pressure in FGS either in the lab or the field; (ii) extra equations for estimating the initial gas pressure and evolution of gas pressure during loading are required; (iii) the elastic bulk modulus of water has to be used to derive the constitutive equations when the gas pressure is employed as a state variable (Gao et al., 2020; Taiebat and Dafalias, 2010; Yin et al., 2013).

2.6 Research Objective

Though some of the proposed constitutive models presented so far can make reasonable predictions on the mechanical behaviour of the FGS, the limitations of these models can make such behaviours hard to predict for most of the problems. The aim of the study is to propose a new constitutive model for both normally consolidated FGS and overconsolidated FGS. To achieve this goal, the new upper and lower bounds of the undrained shear strength for the fine-grained FGS will be investigated to find the terms which can be used to capture the influence of the gas bubbles on the hardening law of the constitutive model. Then the model can be revised by introducing a simple dilatancy relation and bounding surface to make a better prediction of the mechanical behaviour of overconsolidated FGS. The objectives of this study include:

(1) The new upper and lower bounds of the undrained shear strength for the fine-grained soils containing gas bubbles will be proposed. Reasonable assumptions will be made for both upper and lower bounds. For the upper bound, only bubble flooding will be considered, and complete bubble flooding cannot occur. The amount of bubble flooding will depend on the stress path and degree of overconsolidation. The volume change of gas cavities during loading which can reduce the gas volume fraction will be considered in the new lower bound.

(2) A new constitutive model for the normally consolidated fine-grained soils containing gas bubbles will be built. Stress quantities which can be readily measured will be used in the new constitutive model. The soil response in triaxial compression and isotropic compression will be considered in this constitutive model. A new hardening law which can capture the effect

of gas bubbles will be proposed based on the variable found in the new bounds. Volume change due to bubble flooding and gas cavity compression will be considered in the model. Only one parameter will be introduced to describe the effect of gas bubbles on the mechanical behaviour of FGS, which makes the model easier to use and calibrate. More reasonable predictions will be made in this model.

(3) A new constitutive model for the overconsolidated fine-grained soils containing gas bubbles will be presented based on the constitutive model for normally consolidated FGS. With the framework of the normally consolidated constitutive model, the hardening law will be revised to make better predictions for overconsolidated FGS. Meanwhile, a dilatancy relation and a bounding surface will be introduced for overconsolidated condition. The model will be validated with test data from the literature.

Chapter 3: Upper and lower bounds of the undrained shear strength for fine-grained soils containing gas bubbles

This chapter has been published as Gao Z.W., Cai H.J. (2021). “Effect of total stress path and gas volume change on undrained shear strength of FGS.” *Int. J. Geomech.* 21(11). http://doi.org/10.1061/(ASCE) GM.1943-5622. 0002198.

Dr Gao revised the assumptions for the upper and lower bounds. Mr Cai carried out all the detailed derivation, analysis and comparison. Prof. Wheeler made contribution to the development via meetings with Dr Gao and Mr Cai.

3.1 Introduction

There has been extensive research on the undrained shear strength of gassy fine-grained soils. Wheeler (1986) was the first to derive the upper and lower bounds for the undrained shear strength of FGS. The upper bound was derived based on the assumption that the bubbles are completely flooded by the pore water in an undrained test. For the lower bound, it is assumed that the entire saturated soil matrix reaches failure and no bubble flooding occurs. This theory is capable of giving the maximum and minimum possible undrained shear strength of FGS (Wheeler, 1986; Sham, 1989; Hong et al., 2017). However, the upper and lower bounds have limitations in predicting the effect of total stress path on undrained shear strength. As discussed in Chapter 2, the total stress path affects the evolution of pore water pressure, which has a direct influence on the pore gas pressure and undrained shear strength. Specifically, the upper bound tends to overestimate the beneficial effect of gas bubbles on the soil strength because of the assumption of complete bubble flooding, which is not possible if the gas dissolution in pore water is negligible. When the gas cavities were completely flooded, the gas volume would become zero, and the gas pressure would reach infinite if the free gas did not dissolve in the pore water. Since the soil is considered a rigid-perfectly-plastic material, the lower bound can underestimate the soil strength when there is significant compression of gas bubbles during loading (Sultan et al., 2012). Compression of gas bubbles reduces the volume fraction of free gas in the soil. Theoretical analysis has shown that the undrained shear strength of FGS is higher when the gas volume fraction is lower under otherwise identical conditions (Wheeler, 1986; Sham, 1989). Besides, the upper and lower bounds were derived without considering the total stress path. However, the total stress path can affect the change of pore water pressure, which is found to have a dramatic influence on soil strength (Wheeler, 1986; Sham, 1989; Hong et al., 2020; Gao et al., 2020). Some constitutive models have also been proposed for FGS, which can be used to predict the undrained shear strength of this soil (Pietruszczak and Pande, 1996; Grozic et al., 2005; Sultan and Garziglia, 2014; Hong et al., 2020; Gao et al., 2020). But some model parameters which are not easy to determine are needed.

A new study on the upper and lower bounds for the undrained shear strength under specific loading conditions is presented based on the work by Wheeler (1986) and the critical state soil mechanics (Muir Wood, 1990). It is assumed that there is only bubble flooding for the upper bound, but complete bubble flooding does not occur. The amount of bubble flooding is dependent on the stress path and degree of overconsolidation. The lower bound is based on the one in Wheeler (1986), There is no bubble flooding occurs, indicating that the bubbles only have a detrimental effect on soil strength. But the volume change of gas cavities during loading is considered for the lower bound. The effect of overconsolidation and total stress path is accounted for based on the Modified Cam-Clay (MCC) model (Roscoe and Burland, 1968). It should be emphasized that the new upper and lower bounds are not the rigorous upper and lower bounds that consider all the loading conditions (Wheeler, 1986). Instead, they are derived for each specific loading condition and expected to offer a better approximation of the real undrained shear strength than the theory of Wheeler (1986). The new upper and lower bounds have been validated by the test data on three FGS from the literature. Implications for constitutive modelling are discussed. This study only focuses on the behaviour of normally consolidated and lightly overconsolidated FGS, which are frequently seen in the seabed.

3.2 The new upper bound of the undrained shear strength for fine-grained soils containing gas bubbles

FGS is a composite material with a saturated soil matrix and compressible gas cavities. The gas bubbles tend to degrade the soil structure and shear strength when there is no bubble flooding. But they can be flooded by the pore water from the saturated soil matrix in some cases, making the undrained shear strength higher. It is assumed that there is only bubble flooding for the upper bound. The initial stress state is assumed to be isotropic for the derivation below.

In the original work by Wheeler (1988), the upper bound of the undrained shear strength was derived based on complete bubble flooding which can be written as Eq. (3.1).

$$\frac{s_u}{s_u^s} = \frac{3\left\{1-[f_0/(1-f_0)]^{\frac{1}{3}}\right\}}{3-2[f_0/(1-f_0)]^{\frac{1}{4}}} exp\left[\frac{(1+e_{m0})f_0}{\lambda(1-f_0)}\right] \tag{3.1}$$

where e_{m0} is the initial void ratio of matrix.

This is unrealistic and tends to give significant overestimation of the soil strength due to complete bubble flooding is assumed. The following assumptions are made for deriving the new upper bound:

(a) The stress and strain state in the soil is uniform.

(b) There is no gas dissolution in the pore water when the pore pressure increases or more free gas generation when the pore water pressure decreases. Boyle's law can be used to describe the volume change of gas bubbles. The gas pressure remains finite, and the gas volume is not zero at the failure state. Note that gas dissolution in the pore water gives extra volume contraction of the saturated soil matrix, which increases the undrained shear strength. Rigorously speaking, this should be considered in the upper bound. But this is very small in most cases and neglected here.

(c) The gas pressure u_g is always identical to the pore water pressure u_w, which is the condition for bubble flooding (Wheeler, 1986; Sham, 1989). The gas volume change is only due to bubble flooding, which is the same as the volume change of the saturated soil matrix. The volume of the cavity remains the same during bubble flooding.

(d) For the unsaturated soil, the undrained shear strength of the entire soil sample is the same as that of the saturated matrix after bubble flooding. The existence of free gas at the failure state does not damage the soil structure. Note that the derivation of the upper bound in Wheeler (1986) has accounted for this damaging effect by considering the gas volume fraction after bubble flooding is bigger than the initial gas volume fraction ($f_f = f_0/(1 - f_0)$). The volume of cavities thus increases and makes the undrained shear strength lower. But the upper bound can still be very high for some tests. This indicates that proper consideration of the amount of bubble flooding is more important.

Based on the Boyle's law and Assumptions (b) and (c), one can get

$$(u_{w0} + p_a)V_g^0 = \left(u_{wf} + p_a\right)V_g^f \tag{3.2}$$

where V and u denote the specific volume (calculated by assuming that the volume of soil particles is unit) and pressure, respectively; the subscripts 'g' and 'w' denote gas and pore water, respectively; the superscripts '0' and 'f' represent the initial and failure states, respectively; p_a is the atmospheric pressure (101 kPa). At the initial state, the gas volume is

$$V_g^0 = \frac{f_0}{1-f_0} V_m^0 = \frac{f_0}{1-f_0}(1 + e_{m0}) \tag{3.3}$$

where f_0 is the initial gas volume fraction (Wheeler, 1986); V_m^0 is the initial specific volume of the saturated matrix and e_m^0 is the initial matrix void ratio (Wheeler, 1986). If the initial stress state of the soil is isotropic and the stress state is uniform in the soil (Assumption a), the pore water pressure at the failure state can be obtained as below based on the Modified Cam-Clay (MCC) model (Fig. 3.1)

$$u_{wf} = p_0' + u_{w0} + \frac{1}{a} M p_f' - p_f' \tag{3.4}$$

where p_0' ($= p_0 - u_{w0}$) is the initial mean effective stress, p_f' ($= p_f - u_{wf}$) is the mean effective stress at failure, M is the critical state stress ratio and a denotes the slope of the total stress path (Fig. 3.1).

Based on Eqs. (3.2) - (3.4), the volume change of gas during the loading process δV_g can be calculated as below

$$\delta V_g = V_g^0 - V_g^f = \frac{f_0(1+e_{m0})}{1-f_0} \frac{1+b\frac{p_f'}{p_0'}}{1+\frac{u_{w0}+p_a}{p_0'}+b\frac{p_f'}{p_0'}} \quad \text{with} \quad b = \frac{1}{a}M - 1 \tag{3.5}$$

The volume change of the saturated soil matrix during loading δV_m is

$$\delta V_m = V_m^0 - V_m^f = (\mathrm{N} - \Gamma) - (\lambda - \kappa)\ln \mathrm{O}CR + \lambda \ln\left(\frac{p_f'}{p_0'}\right) \tag{3.6}$$

where N and Γ represent the value of V_m on the normal consolidation line (NCL) and critical state line (CSL) at unit mean effective stress, respectively (Fig. 3.1); λ is the slope of NCL and CSL in the $V_m - \ln p'$ plane; OCR is the degree of overconsolidation at the initial state. For the MCC model, $\mathrm{N} - \Gamma = (\lambda - \kappa)\ln 2$, and Eq. (3.6) can be rewritten as

$$\delta V_m = V_m^0 - V_m^f = (\lambda - \kappa)\ln\frac{2}{OCR} + \lambda \ln\left(\frac{p_f'}{p_0'}\right) \tag{3.7}$$

where κ is the slope of the swelling line in the $V_m - \ln p'$ plane. Based on Assumption (c), one can get the following based on Eqs. (3.5) and (3.7)

$$\frac{f_0(1+e_{m0})}{1-f_0} \frac{1+b\frac{p_f'}{p_0'}}{1+\frac{u_{w0}+p_a}{p_0'}+b\frac{p_f'}{p_0'}} - \lambda \ln\left(\frac{p_f'}{p_0'}\right) = (\lambda - \kappa)\ln\left(\frac{2}{OCR}\right) \tag{3.8}$$

The undrained shear strength of the saturated soil s_u^s with p_0' is (Muir Wood, 1990)

$$s_u^s = \frac{1}{2} q_f = \frac{1}{2} M p_0' \Lambda = \frac{1}{2} M p_0' \left(\frac{OCR}{2}\right)^{\frac{\lambda-\kappa}{\lambda}} \tag{3.9}$$

Based Assumption (d), the upper bound for the undrained shear strength of the unsaturated soil is

$$s_u = \frac{1}{2} M p_f' \tag{3.10}$$

Eq. (3.8) can thus be expressed in terms of s_u^s as below based on Eqs. (3.9) and (3.10)

$$\frac{f_0(1+e_{m0})}{1-f_0} \frac{1+\left(\frac{b}{\Lambda}\right)\frac{s_u}{s_u^s}}{1+\frac{u_{w0}+p_a}{p_0'}+\left(\frac{b}{\Lambda}\right)\frac{s_u}{s_u^s}} - \lambda \ln\left(\frac{1}{\Lambda}\frac{s_u}{s_u^s}\right) = (\lambda - \kappa)\ln\left(\frac{2}{OCR}\right) \tag{3.11}$$

While an explicit expression of $\frac{s_u}{s_u^s}$ in terms of f_0 cannot be obtained using Eq. (3.11), the value of f_0 can be easily determined when $\frac{s_u}{s_u^s}$ and other variables are known. Since $\frac{s_u}{s_u^s} \geq 1$ for the upper bound, the relationship between f_0 and s_u^s should be generated starting from $\frac{s_u}{s_u^s} = 1$ based on Eq. (3.11).

The value of f_0 can be obtained by setting a reasonable small increment of $\frac{s_u}{s_u^s}$ from 1. Therefore, the relationship between f_0 and $\frac{s_u}{s_u^s}$ can be drawn as the upper bound. The upper bound expressed by Eq. (3.11) is dependent on the $\frac{u_{w0}+p_a}{p_0'}$ and total stress path described by the different variable a, which is not fully considered by Wheeler (1986). This makes the new upper bound work better for specific loading conditions with different u_{w0}, p_0' and total stress paths. More discussion on this will be given in the section on the validation using existing test data.

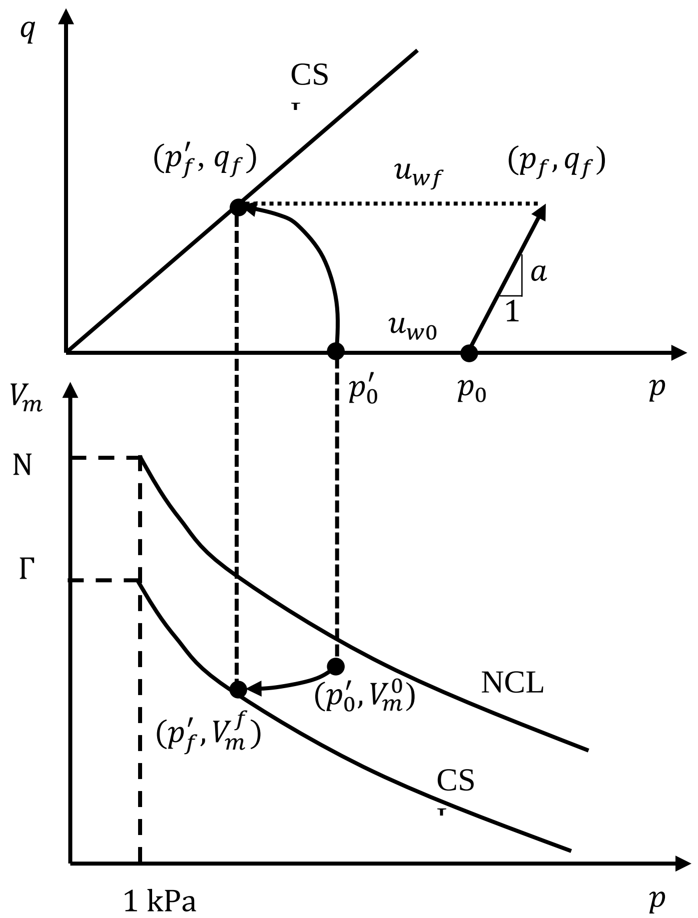

Fig. 3.1 The initial state, failure state and stress paths for the saturated soil matrix

3.3 The lower bound of the undrained shear strength for fine-grained soils containing gas bubbles

By treating the saturated soil matrix as a rigid, perfectly plastic von Mises-type material, Wheeler et al. (1990) showed that the undrained shear strength of FGS can be expressed as

$$4\left[\frac{3-2f_f^{\frac{1}{4}}}{3\left(1-f_f^{\frac{1}{3}}\right)}\right]^2 s_u^2+\left(\frac{3}{2\ln f_f}\right)^2\left(p_f-u_g\right)^2=4(s_u^s)^2 \tag{3.12}$$

where f_f is the gas volume fraction at failure (Wheeler, 1986; Green, 1972). The lower bound in Wheeler (1986) was derived by assuming that there is no change in the gas volume and gas pressure during the loading ($f_f = f_0$ and $u_g = u_{w0}$). It is shown by Sultan et al. (2012) that the lower limit proposed by Wheeler (1986) does offer an absolute lower bound for the test data. But it can be too conservative for tests in which significant contraction of gas bubbles occurs. The reason is that the assumption of $f_f = f_0$ can be too conservative when the gas volume decreases during loading, which makes $f_f < f_0$ and undrained shear strength higher.

In this study, the lower limit is derived by considering the gas volume change. The following assumptions are made:

(a) The stress and strain state in the soil remains uniform but the failure condition can still be expressed by Eq. (3.12). Note that Eq. (3.12) was originally derived based on non-uniform stress distribution in the soil. There is no change of gas volume fraction during shearing in Eq. (3.12) due to the assumption $f_f = f_0$ is made by Wheeler. It means no volume change of gas bubbles under loading condition, which indicates a non-uniform stress distribution in the soil.

(b) The initial gas pressure u_g^0 is the same as the initial pore water pressure u_w^0. The same assumption has been used in the lower bound of Wheeler (1986). Gas dissolution in pore water is neglected.

(c) The change of gas pressure δu_g is the same as the change in total stress δp. This is based on the $u_g = p \pm \frac{4}{3} s_u^m(1-f)$ (Wheeler et al., 1990). s_u^m is the undrained shear strength of saturated soil matrix which is constant. When the gas volume fraction is assumed constant, that equation gives $\delta u_g = \delta p$. In the new lower bound, f is not constant due to the volume change of gas is considered. However, the value of δf can be neglected in $u_g = p \pm \frac{4}{3} s_u^m(1-f)$ (Wheeler et al., 1990) because the change in gas volume fraction is very small and has a limited effect on u_g. Thus, the assumption of $\delta u_g = \delta p$ is reasonable and it is proven to have a better prediction. The cavity volume is the same as the gas volume in the lower bound case.

In a globally undrained test, the δu_g for the lower bound can be obtained based on Fig.3.1 as below

$$\delta u_g = \delta p = \frac{2}{a} s_u^s = \frac{1}{a} M p_0' \Lambda \tag{3.13}$$

In this case, the Boyle's law for the gas is expressed as

$$(u_{w0} + p_a) V_g^0 = \left(u_{w0} + p_a + \frac{1}{a} M p_0' \Lambda\right) V_{gf} \tag{3.14}$$

Eq. (3.14) can be used to get V_g^f as below

$$V_g^f = \frac{u_w 0 + p_a}{u_{w0} + p_a + \frac{1}{a} M p_0' \Lambda} V_g^0 = \frac{\frac{u_{w0}+p_a}{p_0'}}{\frac{u_{w0}+p_a}{p_0'} + \frac{1}{a} M\Lambda} \frac{f_0}{1-f_0} V_m^0 = \beta \frac{f_0}{1-f_0} V_m^0 \tag{3.15}$$

where β is self-evident. Since bubble flooding is not considered in the lower bound, $V_m^0 = V_m^f$ due to the undrained condition. The gas volume fraction at failure f can be expressed as below based on Eqs. (3.3) and (3.15)

$$f_f = \frac{V_g^f}{V_g^f + V_m^0} = \frac{\beta \frac{f_0}{1-f_0}}{\beta \frac{f_0}{1-f_0} + 1} = \frac{\beta f_0}{1 + (\beta - 1) f_0} \tag{3.16}$$

Since $u_g^0 = u_w^0$ and $\delta u_g = \delta p$ (Assumptions b and c above), one can get $p_f - u_g = p_0'$. Therefore, the new lower bound is expressed as

$$4\left[\frac{3 - 2 f_f^{\frac{1}{4}}}{3\left(1 - f_f^{\frac{1}{3}}\right)}\right]^2 s_u^2 + \left(\frac{3}{2 \ln f_f}\right)^2 (p_0')^2 = 4 (s_u^s)^2 \tag{3.17}$$

with s_u^s and f_f being expressed by Eqs. (3.9) and (3.16), respectively. For one specific test, the lower bound can be obtained by giving the value of f_0. Then an f_f can be calculate by using Eq. (3.16) and s_u^s can be calculated by using Eq. (3.9). with a giving u_{w0} and p_0'. The value of s_u is obtained and the lower bound with the ratio of s_u/s_u^s is finally expressed. Similar to the new upper bound, the new lower bound is also dependent on $\frac{u_{w0}+p_a}{p_0'}$ and total stress path, which is described by the variable a (Fig. 3.1). Both variables ($\frac{u_{w0}+p_a}{p_0'}$ and a) appear in the expression of the function of β.

For the new upper and lower bounds of the undrained shear strength of FGS, it can be seen that the volume change of the gas bubble is the same as the volume change of the saturated soil matrix when considering bubble flooding only. It is assumed that the volume of the saturated soil matrix remains constant when the new lower bound is proposed. When the parameter a is unchanged, the upper and lower bounds of the undrained shear strength are influenced by the pore water pressure as Fig. 3.2 shows.

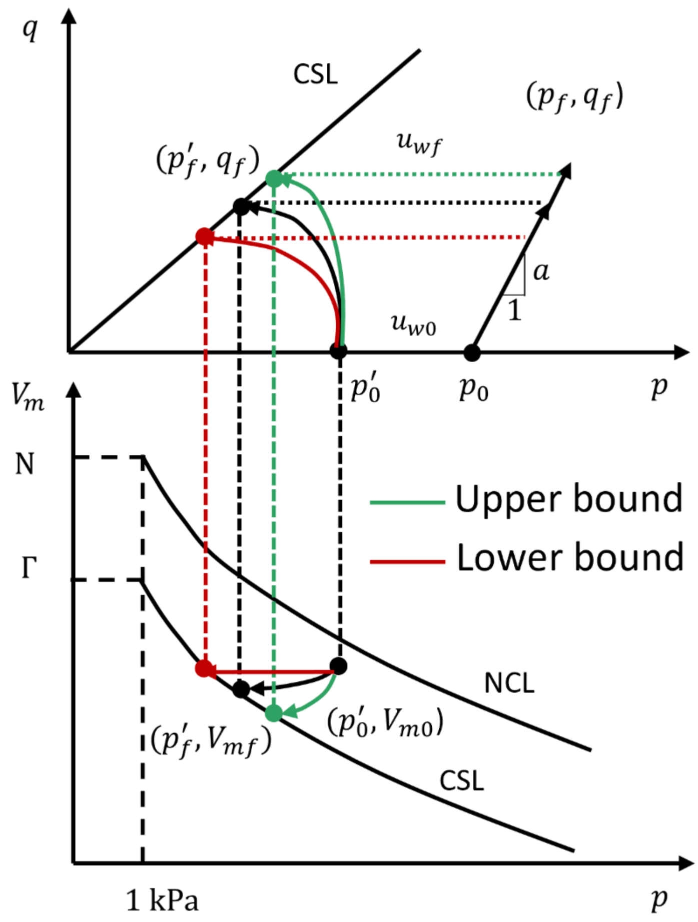

Fig. 3.2 The initial state, failure state and stress paths for the saturated soil matrix considering the new upper and lower bounds

3.4 Model validation

The prediction of the new lower and upper bounds will be compared with the test data on three FGS from literature (Wheeler, 1986, Sham, 1989, Hong et al., 2020). The MCC model parameters for these soils are given in the literatures (Wheeler, 1986, Sham, 1989, Hong et al., 2020) and shown in Table 3.1. All the tests have been done under undrained triaxial compression condition with $\delta q = 3\delta p$ ($a =$

3 in Fig. 3. 1). Most of the samples are normally consolidated and some are lightly overconsolidated. The s_u^s is calculated in different ways for the new and Wheeler's bounds. Eq. (3.9) is used to determine s_u^s for the new bounds. To make it consistent with the work by Wheeler (1986), the s_u^s for Wheeler's (1986) bounds is taken as the measured undrained shear strength for saturated soils.

Table 3.1 MCC model parameters for new bounds

Soil	M	λ	κ	N
Kaolin with helium	0.89	0.23	0.05	3.35
Combwich mud with methane	1.33	0.174	0.0297	3.062
Malaysian kaolin with nitrogen	1.05	0.24	0.05	3.74

3.4.1 Combwich mud with methane

Figs. 3.3 - 3.4 show the prediction of the new upper and lower bounds with the test data on normally consolidated gassy Combwich mud (Wheeler, 1986). The prediction of Wheeler's theory is also included. In most cases, the new upper and lower bounds are closer to the test data. The prediction of the new upper bound is lower than the one in Wheeler (1986) because the new theory does not assume complete bubble flooding. The prediction of the new lower bound is slightly higher than the lower bound of Wheeler (1986). This is due to that the new lower bound considers gas bubble contraction during loading, which makes the undrained shear strength higher.

At the same f_0, the new theory predicts lower shear strength for both the lower and upper bounds as $\frac{u_{w0}+p_a}{p_0'}$ increases (Fig. 3.3). This agrees with the test data, which shows that s_u decreases when $\frac{u_{w0}+p_a}{p_0'}$increases at the same f_0. The reasons are: (a) For the new upper bound, higher $\frac{u_{w0}+p_a}{p_0'}$makes the amount of bubble flooding smaller and undrained shear strength smaller (Eq. 3.5); (b) In the new lower bound, higher $\frac{u_{w0}+p_a}{p_0'}$renders the bubble contraction smaller and f_f bigger at the same f_0, leading to smaller s_u (Eqs. 3.15 and 3.16).

For the tests with $p_0' = 200$kPa and $u_{w0} = 100$kPa, it appears that the new lower bond tends to overestimate the undrained shear strength, while Wheeler's does better. This indicates that the new lower bound may overpredict the undrained shear strength of FGS under certain loading conditions. This overprediction is mainly caused by the Assumption (a) for the new lower bound which neglects the nonuniform stress distribution in FGS that has a negative effect on the soil strength.

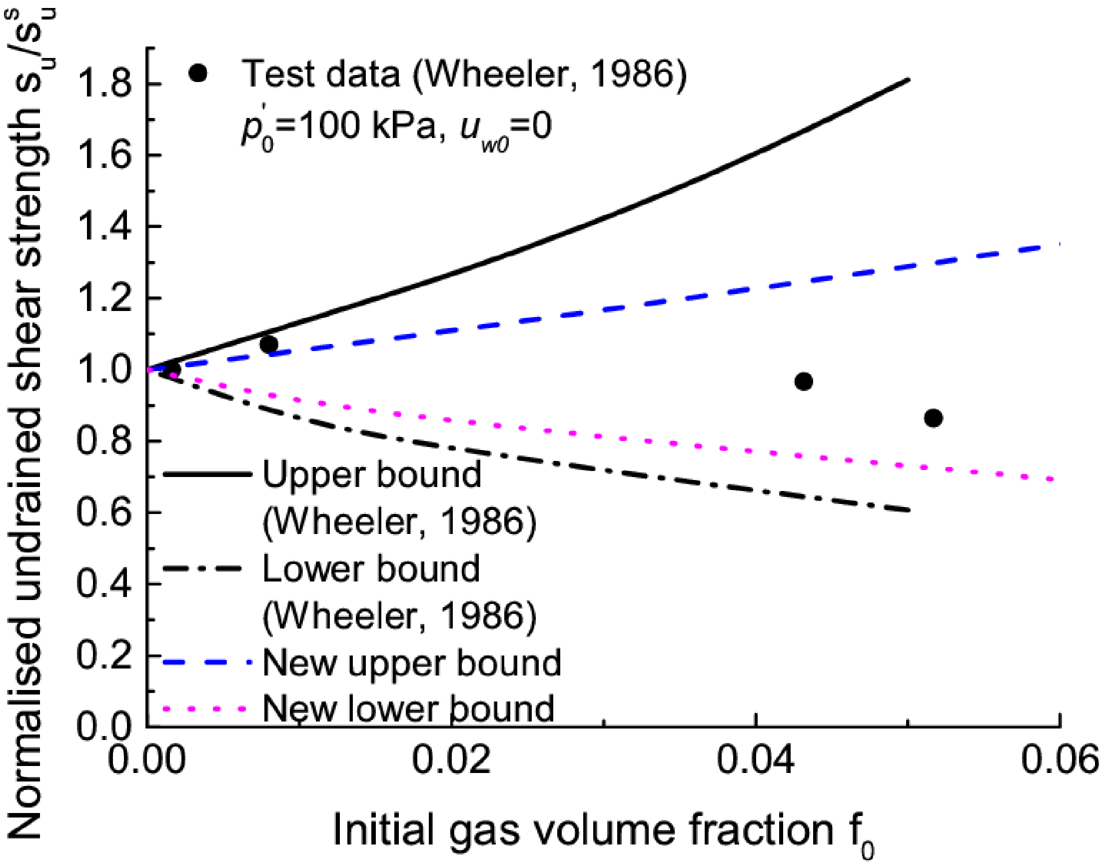

(a)

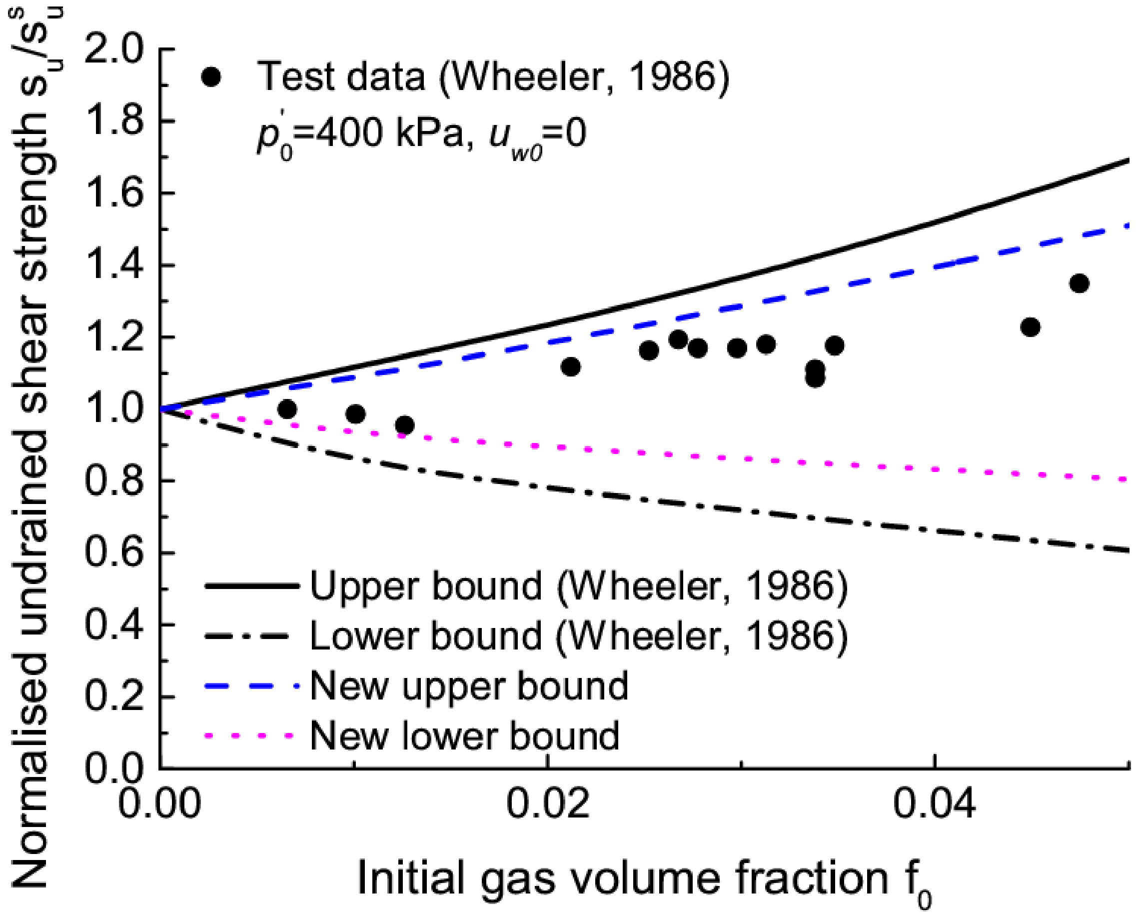

(b)

Fig. 3.3 Prediction of the upper and lower bounds for normally consolidated gassy Combwich mud from Wheeler (1986) with (a) $p'_0 = 100$ kPa and (b) $p'_0 = 400$ kPa

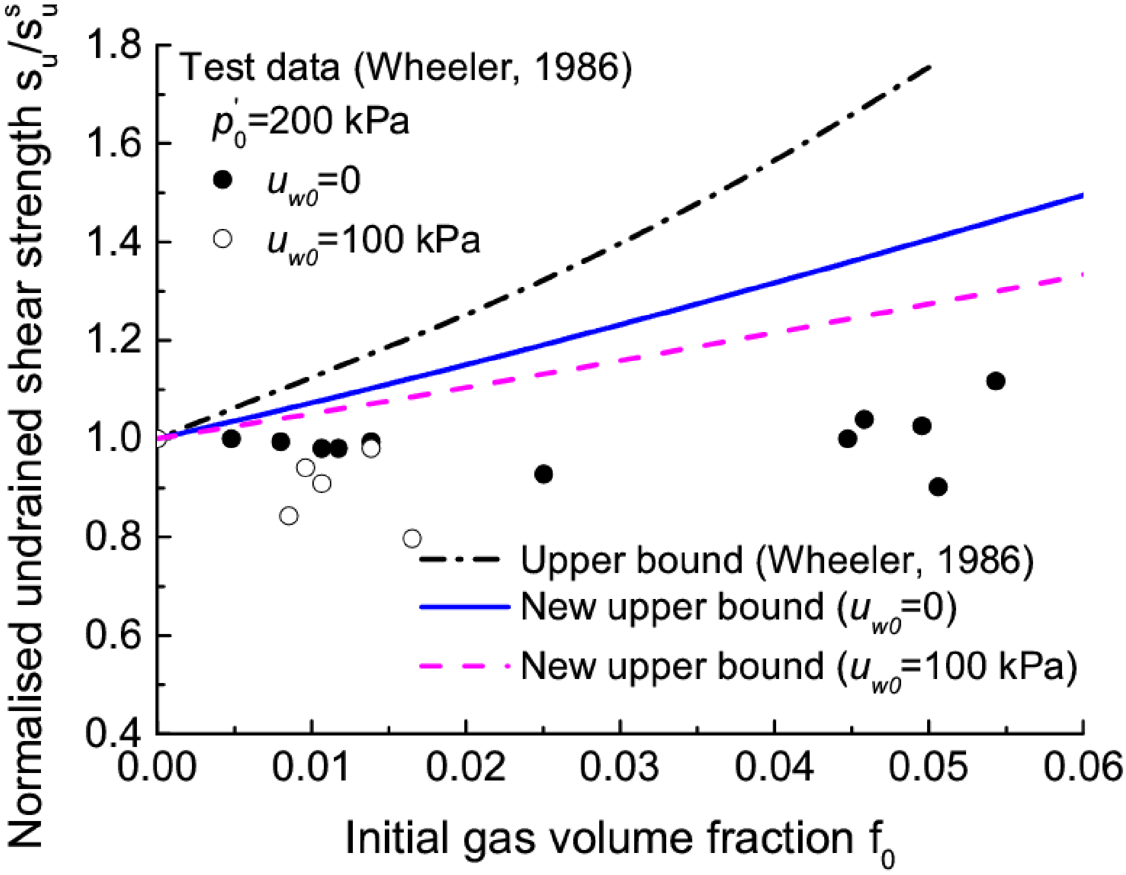

Normalised undrained shear strength s_u/s_u^s
Initial gas volume fraction f_0
Test data (Wheeler, 1986)
p'_0=200 kPa
u_{w0}=0
u_{w0}=100 kPa
Upper bound (Wheeler, 1986)
New upper bound (u_{w0}=0)
New upper bound (u_{w0}=100 kPa)
0.4
0.6
0.8
1.0
1.2
1.4
1.6
1.8
0.00
0.01
0.02
0.03
0.04
0.05
0.06

(a)

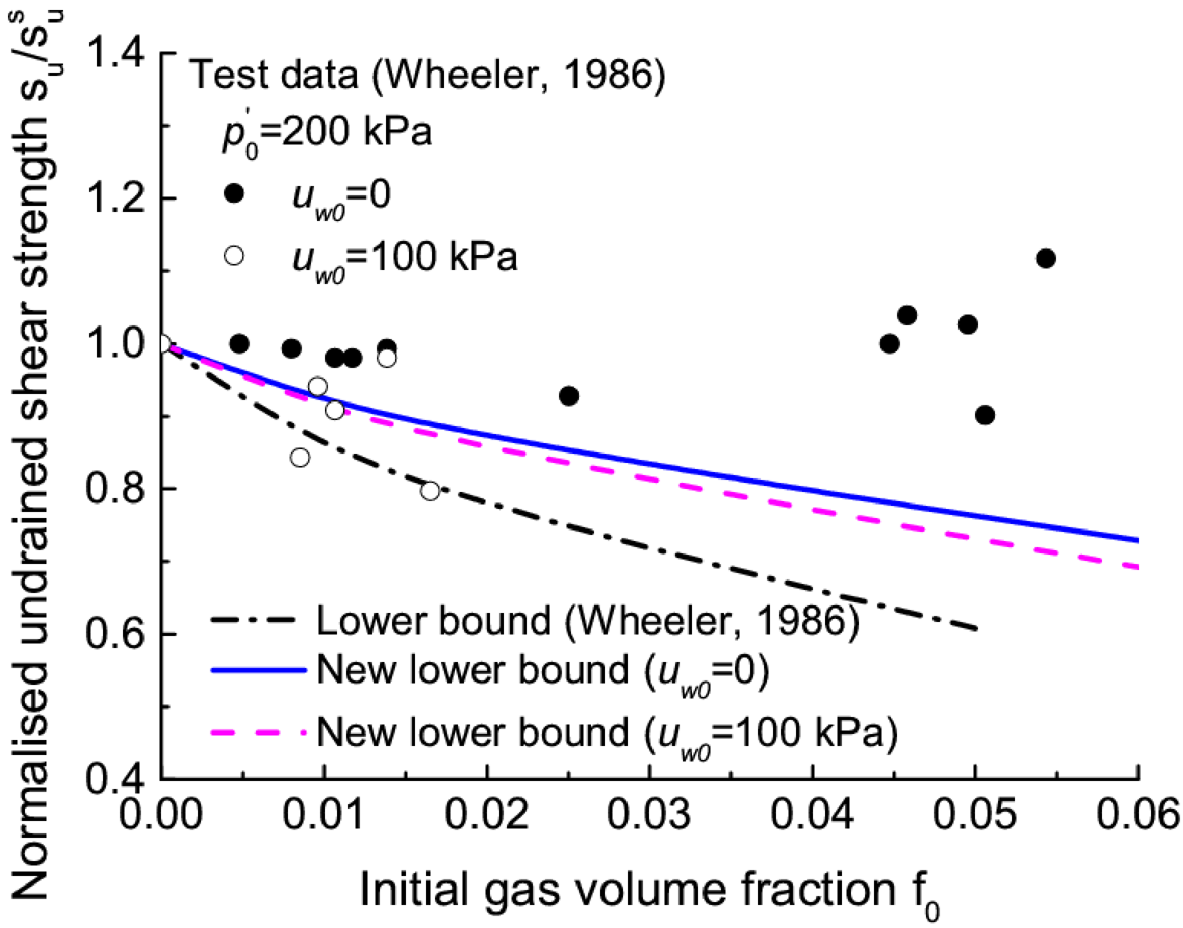

(b)

Fig. 3.4 Prediction of the upper and lower bounds for normally consolidated gassy Combwich mud from Wheeler (1986) with $p'_0 = 200$ kPa: (a) the upper bound prediction and (b) the lower bound prediction

3.4.2 Kaolin with helium (Sham, 1989)

Figs. 3.5 - 3.6 show the comparison between the test data and theoretical predictions for normally consolidated Kaolin with helium (Sham, 1989). The gas bubbles are found to have primarily detrimental effect on the undrained shear strength. The upper bound of Wheeler (1986) gives much higher s_u than the new upper bound, with the latter offering better prediction of the maximum possible s_u for unsaturated soils (Figs. 5a and 6a). At the same p'_0 and f_0, the new upper bound gives lower s_u for unsaturated soils as u_w^0 increases. This is due to smaller amount of bubble flooding at higher u_{w0} or u_{g0} (Eq. 3.5). Wheeler's lower bound predicts zero s_u at f_0 between 0.03 and 0.04, which appears to be very conservative. The new lower bound gives zero s_u at higher f_0 for all the tests, as it considers gas cavity compression during loading. This is closer to the test data. But it is still conservative for tests with $f_0 > 0.2$ (Figs. 3.4b and 3.5b). There could be much more gas cavity compression at higher f_0 in real soil samples than that assumed in Eqs. (3.13) and (3.14).

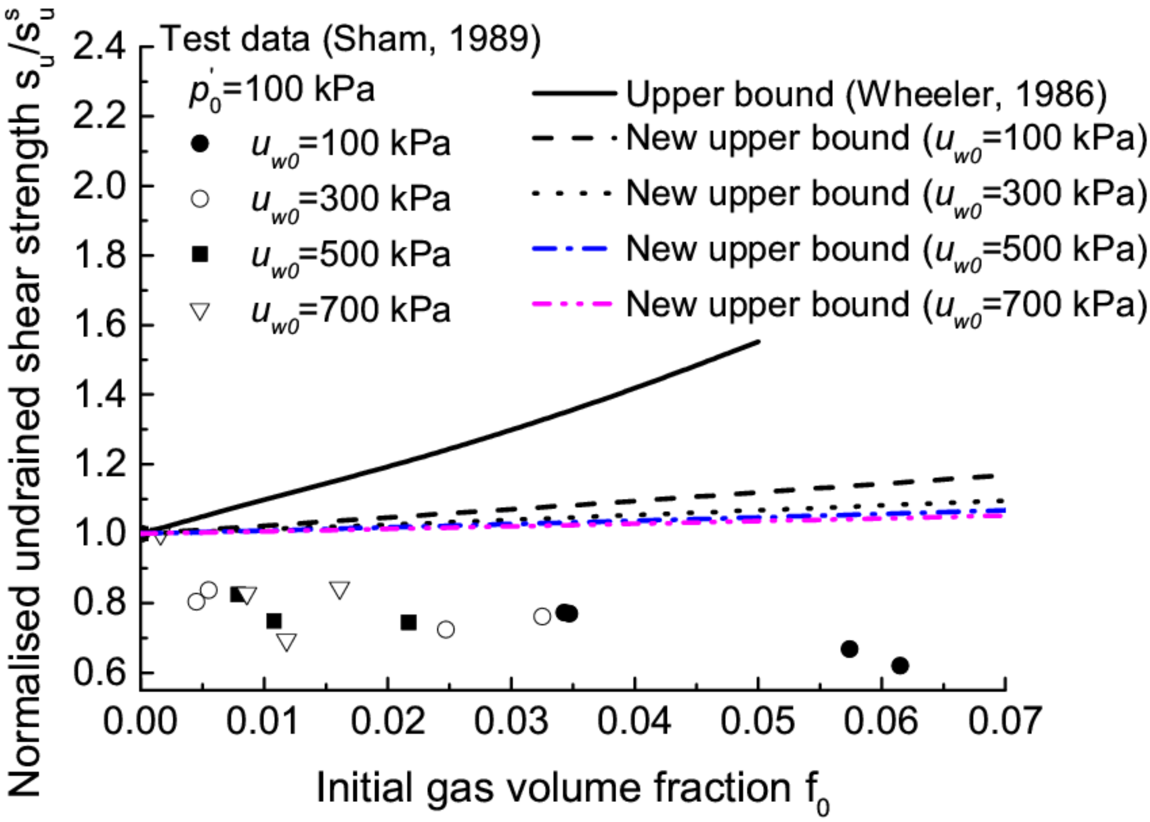

(a)

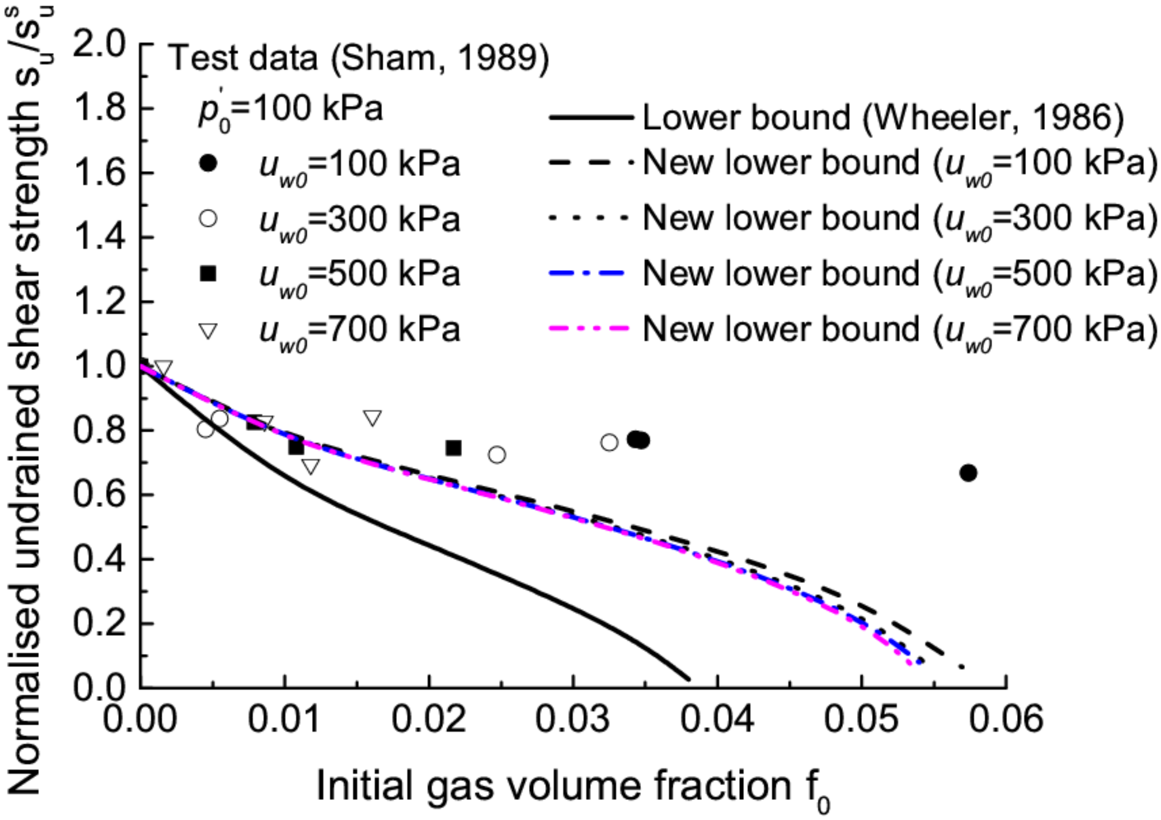

(b)

Fig. 3.5 The upper and lower bounds for normally consolidated Kaolin from Sham (1989) with $p'_0 = 100$ kPa: (a) the upper bound prediction and (b) the lower bound prediction

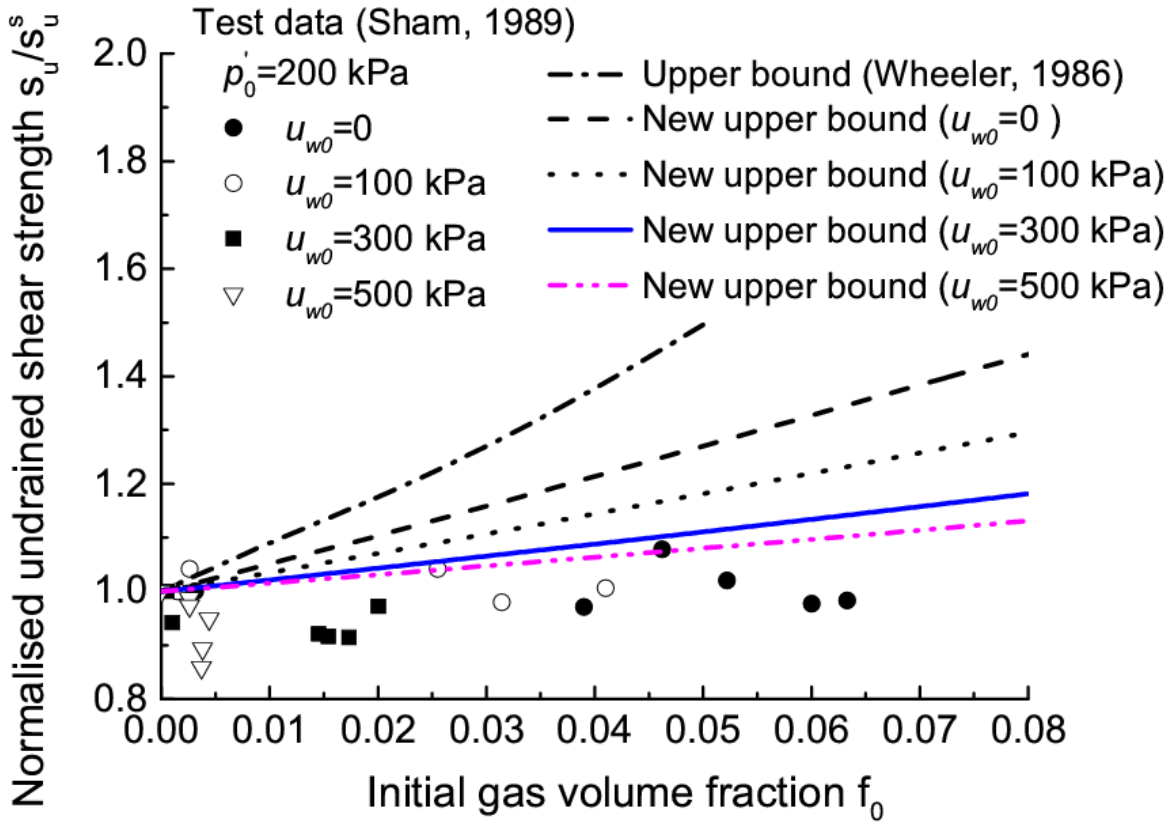

Test data (Sham, 1989)
p_0'=200 kPa
u_{w0}=0
u_{w0}=100 kPa
u_{w0}=300 kPa
u_{w0}=500 kPa
Upper bound (Wheeler, 1986)
New upper bound (u_{w0}=0)
New upper bound (u_{w0}=100 kPa)
New upper bound (u_{w0}=300 kPa)
New upper bound (u_{w0}=500 kPa)
Normalised undrained shear strength s_u/s_u^s
Initial gas volume fraction f_0
0.8
1.0
1.2
1.4
1.6
1.8
2.0
0.00
0.01
0.02
0.03
0.04
0.05
0.06
0.07
0.08

(a)

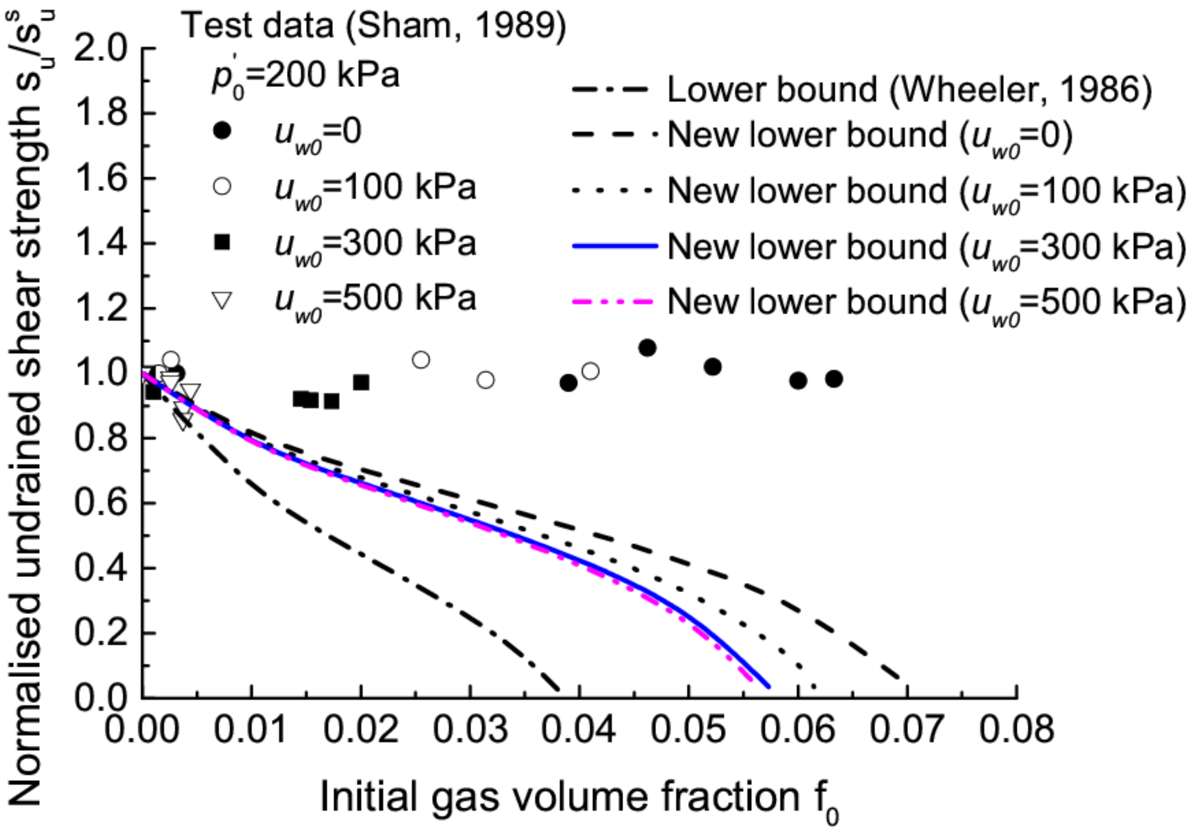

(b)

Fig. 3.6 The upper and lower bounds for normally consolidated Kaolin from Sham (1989) with $p_0' = 200$ kPa: (a) the upper bound prediction and (b) the lower bound prediction

Fig. 3.7 shows the results of overconsolidated Kaolin with $OCR = 2$. Both the new and Wheeler's (1986) lower bounds give higher s_u than the measured value when $f_0 > 0.01$. But the Wheeler's is closer to the test data. One possible reason is that gas bubble expansion during unloading before shearing has caused irreversible damage to the soil structure, leading to lower undrained shear strength (Sultan et al., 2012). The new lower bound does not consider this damage. Meanwhile, it accounts for the bubble compression in triaxial compression after the isotropic unloading, which has beneficial effect on s_u. This makes the new lower bound prediction higher. Similar to the normally consolidated samples, the new upper bound gives smaller s_u than the Wheeler's.

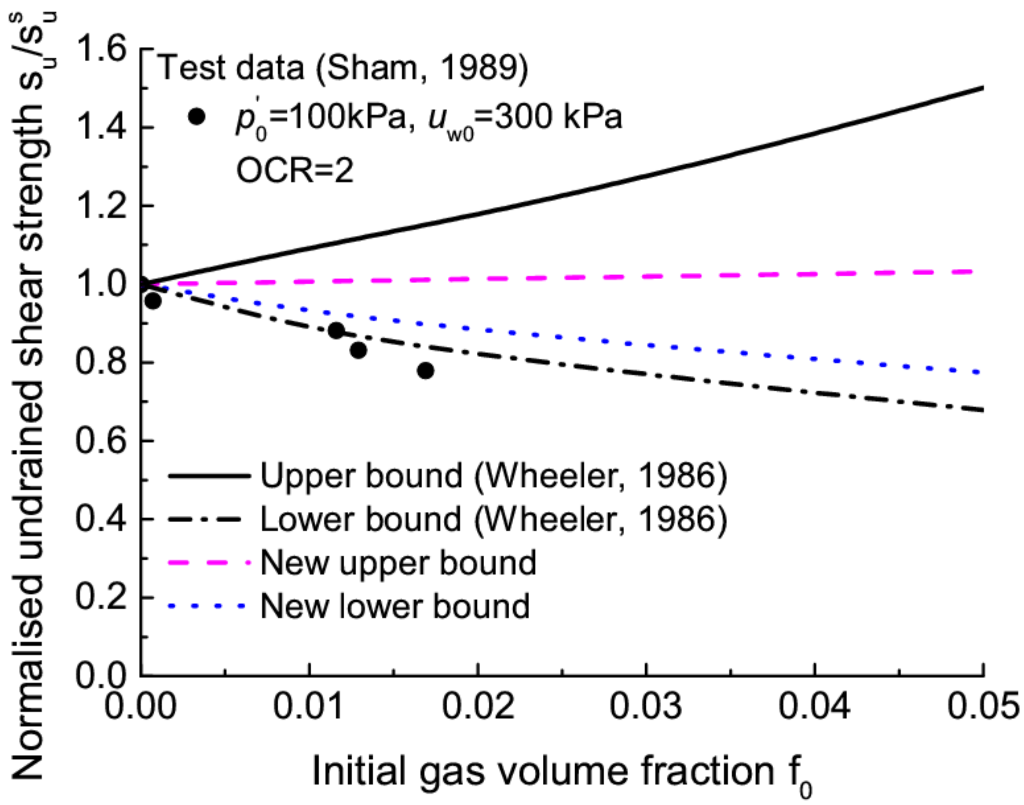

Fig. 3.7 The upper and lower bounds for overconsolidated Kaolin ($OCR = 2$) with $p_0' = 100$ kPa

3.4.3 Malaysian Kaolin silt with nitrogen (Hong et al., 2020)

Fig. 3.8 shows the test results of normally consolidated Malaysian Kaolin silt with different u_{w0} (Hong et al. 2020). p_0' is 200 kPa for all the tests. All the test results lie in the new upper and lower bounds. The new bounds are closer to the test data than the Wheeler's. The results of tests with $u_{w0} = 0$ and $u_{w0} = 50$ kPa lie exactly on the new upper bound, while the test results for $u_{w0} = 600$ kPa are very close to the new lower bound. Compared to the other two clays above, the gas bubbles are found to have less detrimental effect on s_u. Hong et al. (2020) have shown that this is related to the plastic index (I_p) of clays. The Malaysian kaolin silt has the lowest I_p and the least detrimental effect can be observed. The most significant detrimental effect can be seen on Kaolin reported in Sham (1989) which has the highest I_p.

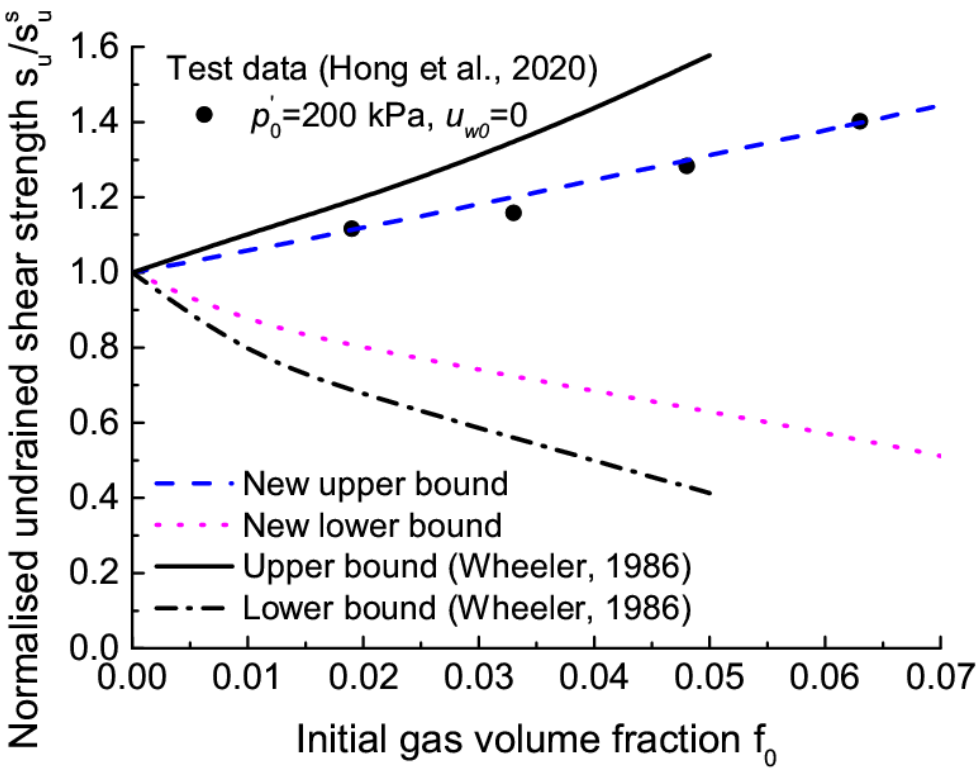

(a)

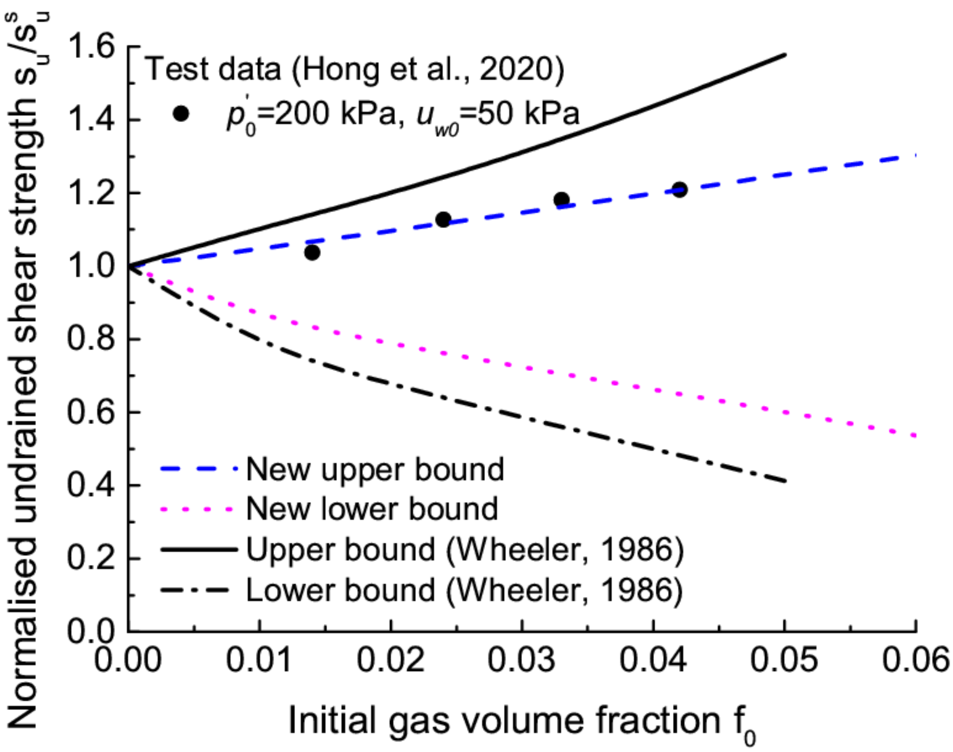
Test data (Hong et al., 2020)
p'0=200 kPa, uw0=50 kPa
New upper bound
New lower bound
Upper bound (Wheeler, 1986)
Lower bound (Wheeler, 1986)
Normalised undrained shear strength su/ssu
Initial gas volume fraction f0
0.0
0.2
0.4
0.6
0.8
1.0
1.2
1.4
1.6
0.00
0.01
0.02
0.03
0.04
0.05
0.06

(b)

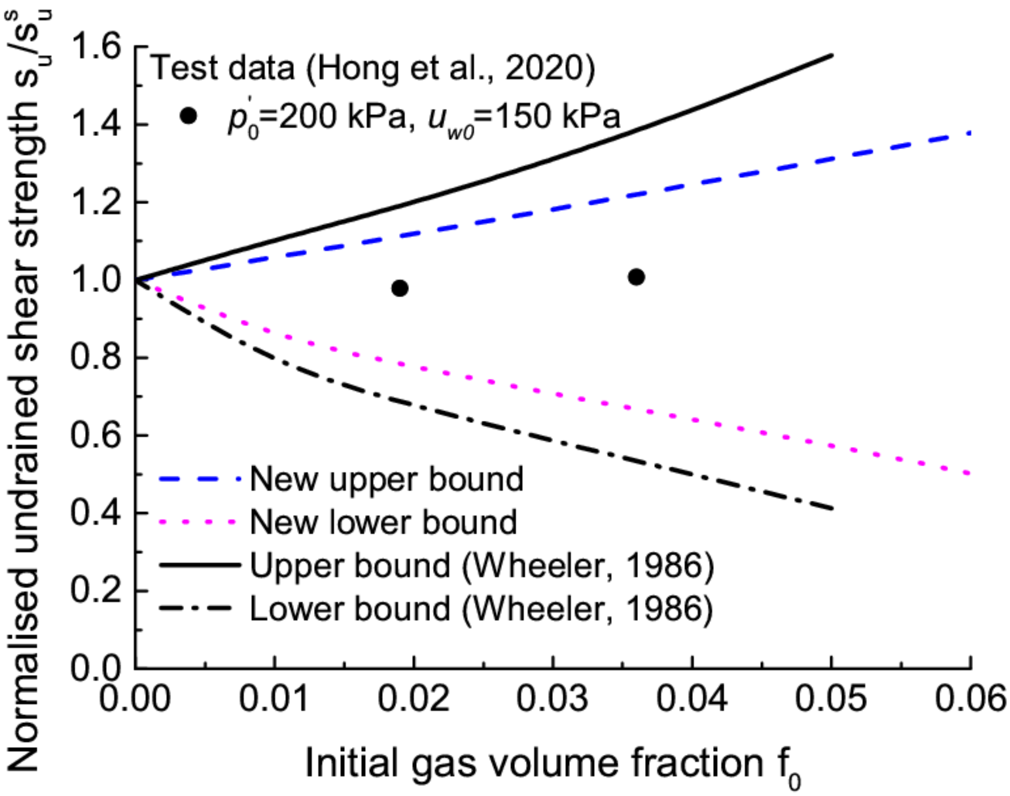
Test data (Hong et al., 2020)
p'0=200 kPa, uw0=150 kPa
New upper bound
New lower bound
Upper bound (Wheeler, 1986)
Lower bound (Wheeler, 1986)
Normalised undrained shear strength su/ssu
Initial gas volume fraction f0
0.0
0.2
0.4
0.6
0.8
1.0
1.2
1.4
1.6
0.00
0.01
0.02
0.03
0.04
0.05
0.06

(c)

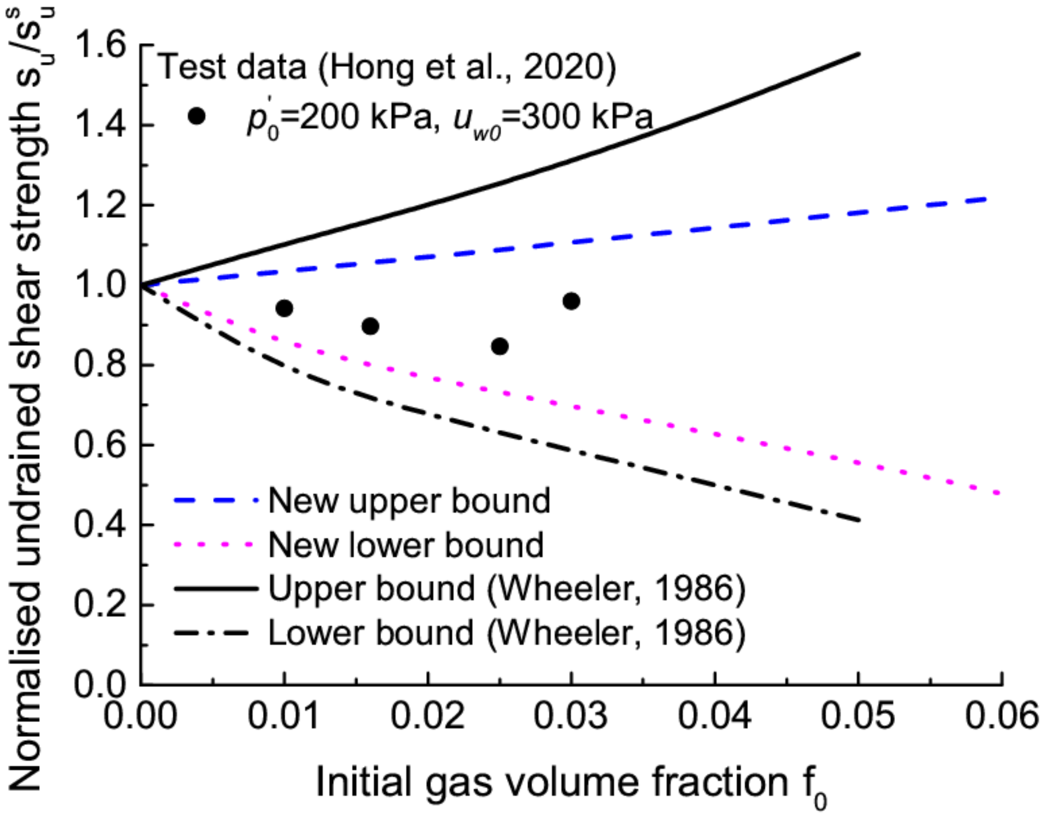

Normalised undrained shear strength s_u/s_u^s
1.6
1.4
1.2
1.0
0.8
0.6
0.4
0.2
0.0
Test data (Hong et al., 2020)
p_0'=200 kPa, u_{w0}=300 kPa
New upper bound
New lower bound
Upper bound (Wheeler, 1986)
Lower bound (Wheeler, 1986)
0.00
0.01
0.02
0.03
0.04
0.05
0.06
Initial gas volume fraction f_0

(d)

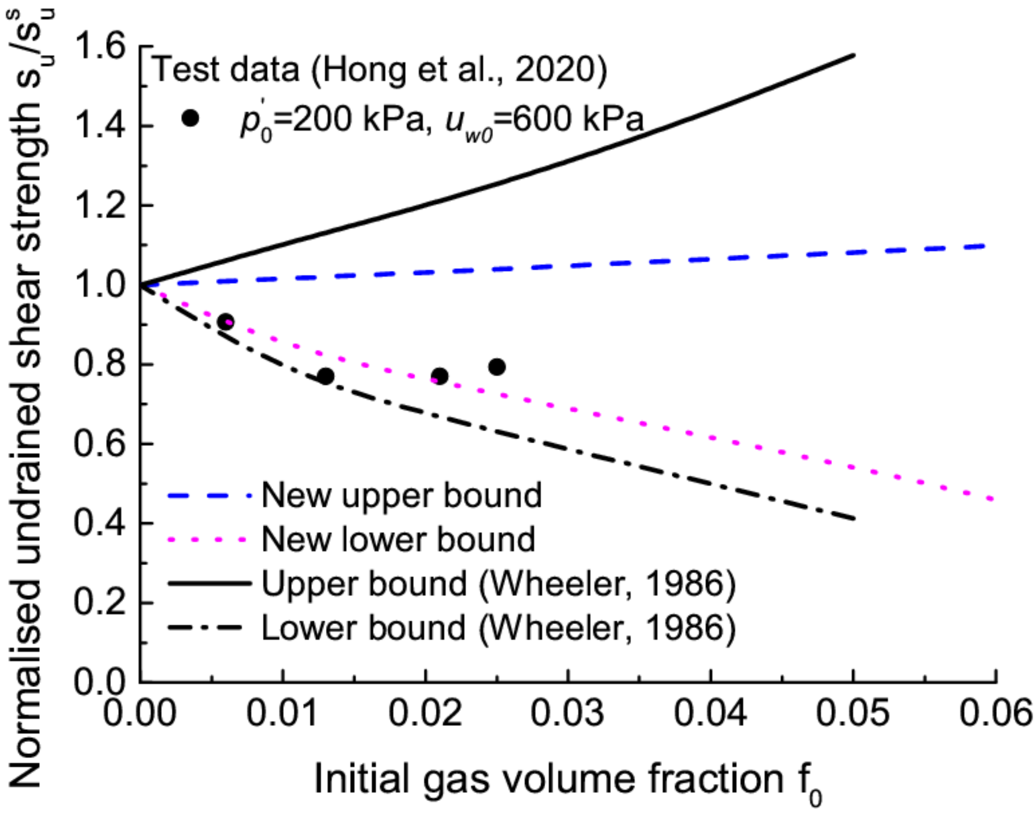

(e)

Fig. 3.8 The upper and lower bounds for normally consolidated Malaysian kaolin with nitrogen from Hong et al. (2020): (a) $u_{w0} = 0$, (b) $u_{w0} = 50$ kPa, (c) $u_{w0} = 150$ kPa, (d) $u_{w0} = 300$ kPa and (e) $u_{w0} = 600$ kPa

Fig. 3.9 shows the results of lightly overconsolidated Malaysian kaolin with different u_{w0} (Hong et al., 2020). All the samples were first consolidated to $p_c' = 200$ kPa and then unloaded to different $p_0' = p_c'/R$. The overconsolidation ratio R varies between 1.05 and 1.67. The undrained shear strength is normalized by the s_u^s at $R = 1$. For each test, the initial gas volume fraction f_0 is different, which can be found in Hong et al. (2020). Some of the test data is above the new upper bound at $u_{w0} = 0$, which means that there could be more bubble flooding than the theoretical prediction. At $u_{w0} = 600$ kPa, the lower bound is higher than the measured results at $R = 1.43$ and $R = 1.67$. Similar to the case for overconsolidated Kaolin in Sham (1989), there could be irreversible soil structure damage during isotropic unloading, which is not accounted for by the new lower bound.

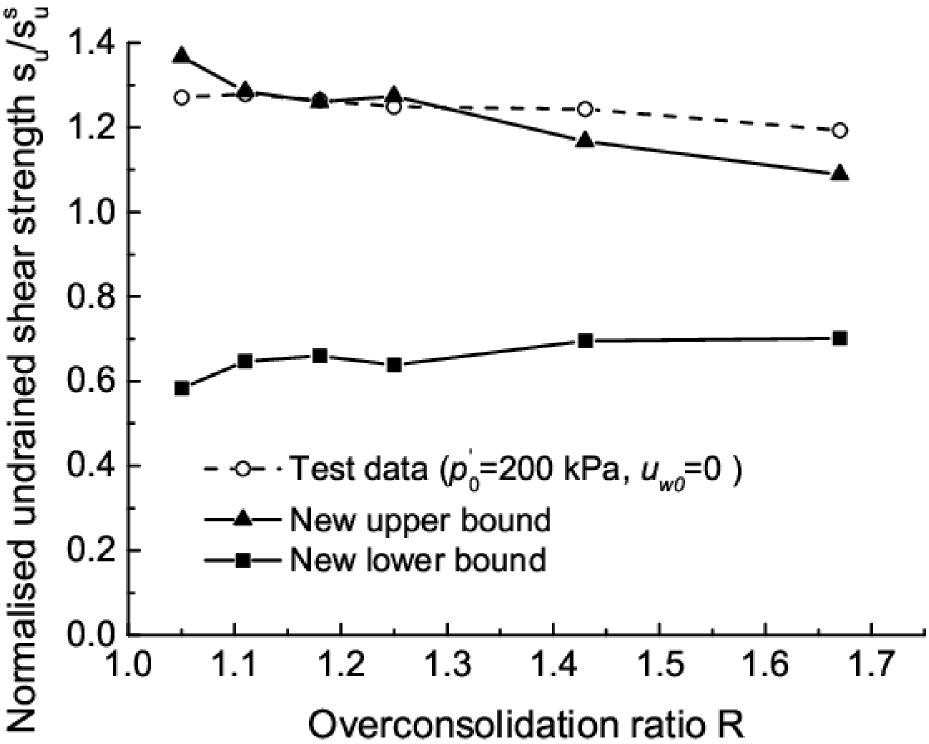

(a)

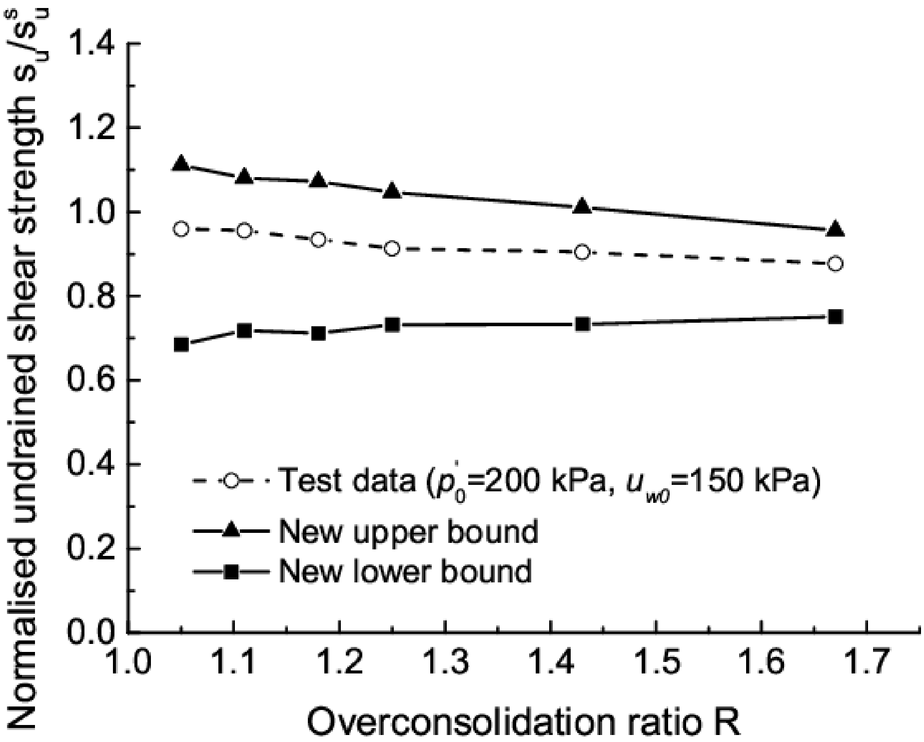

Normalised undrained shear strength s_u/s_u^s
1.4
1.2
1.0
0.8
0.6
0.4
0.2
0.0
1.0
1.1
1.2
1.3
1.4
1.5
1.6
1.7
Overconsolidation ratio R
Test data (p_0'=200 kPa, u_{w0}=150 kPa)
New upper bound
New lower bound

(b)

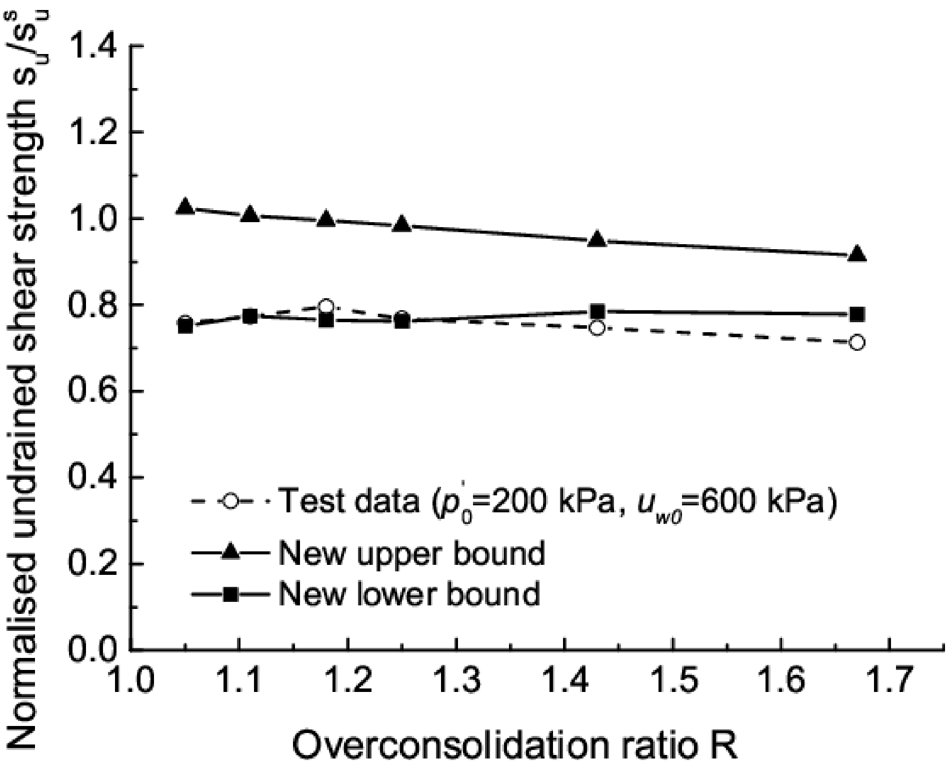

(c)

Fig. 3.9 The new upper and lower bounds for slightly overconsolidated Malaysian Kaolin with nitrogen from Hong et al. (2020): (a) $u_{w0} = 0$, (b) u_{w0} =150 kPa, and (c) $u_{w0} = 600$ kPa

3.4.4 Effect of total stress path

The pore water pressure u_w is found to have dramatic influence on the behaviour of FGS (Wheeler, 1986; Sham, 1989; Hong et al., 2017). Under otherwise identical conditions of f_0 and OCR, FGS has smaller s_u at higher u_w. It is important to realize that u_w changes during loading. In undrained tests, the evolution of u_w is dependent on the total stress path, which means that the s_u of FGS is affected by the total stress path (Sultan et al., 2012). Note that the total stress path does not affect the effective stress path of a saturated clay but does affect that of the FGS because the evolution of gas volume is dependent on the total stress path (Gao et al., 2020).The upper and lower bounds of Wheeler (1986) are independent of the total stress path. Fig. 3.10 shows the prediction of the new upper and lower bounds under total stress paths with different a values (Fig. 3.1). The parameters for Combwich mud are used and the soil is assumed to be normally consolidated. When $a = \infty$, the total stress path is $\delta p = 0$. As a increases from 3 to ∞, both the new upper and lower bounds give smaller s_u. Smaller a leads to smaller change in u_w (Fig. 3.1), which means less bubble flooding and lower s_u for the upper bound. For the lower bound, bigger a causes less bubble compression and higher f_f at the same f_0, which makes the s_u smaller. When $a < 0$, the s_u predicted by the new lower bound is smaller than that of Wheeler's because it considers gas bubble expansion due to reduction in p (Eqs. 3.13-3.15). In this chapter, only triaxial compression condition is considered. When the absolute value of negative a is sufficiently large (which is referring to a triaxial extension test with $p < 0$) which, u_w can decrease during loading, indicating that there can be 'negative' bubble flooding based on Eqs. (3.2) - (3.7), which is water flow from a partially flooded bubble to the saturated matrix. But there is no experimental evidence to show if there is 'negative' bubble flooding at present. For all the simulations presented here, u_w increases and 'negative' bubble flooding does not occur. Unfortunately, there is no test data under loading conditions with $a = \infty$ and $a < 0$. Note that the current theory only works in triaxial compression and cannot be applied in triaxial extension because it is based on the MCC which does not capture the soil response in triaxial extension well.

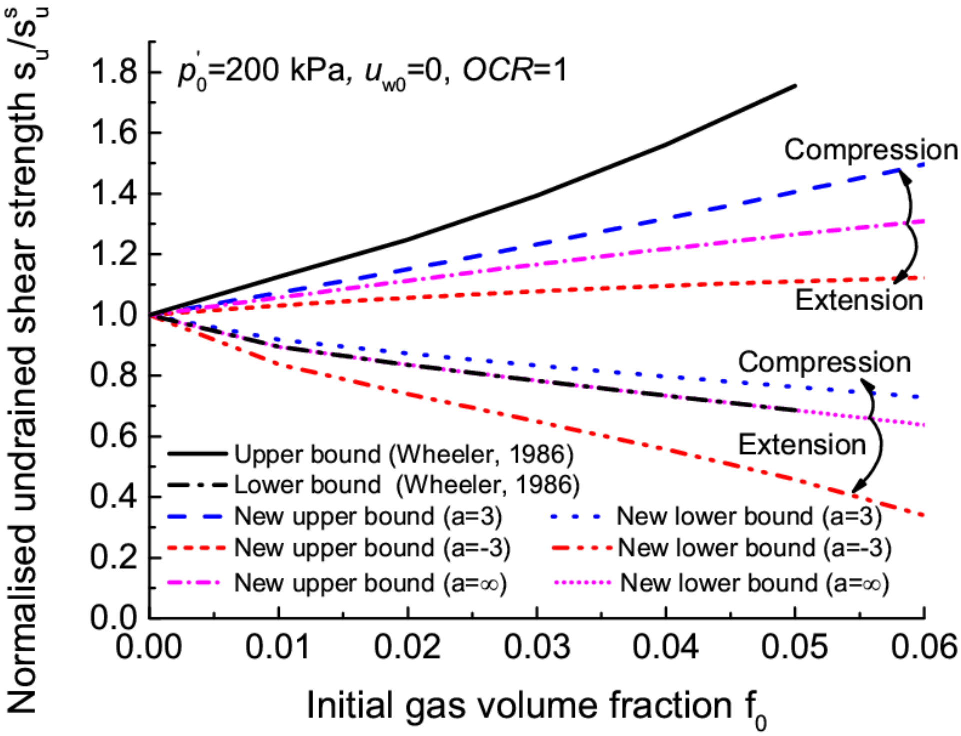

Fig. 3.10 Effect of total stress path on the new upper and lower bounds

3.5 Discussion on the interaction between gas bubbles and saturated soil matrix

The upper and lower bounds of Wheeler (1986) give the maximum and minimum possible s_u for FGS, respectively. They are found to work for all the FGS above. The new bounds are generally closer to the test data because complete bubble flooding is not assumed for the upper bound and gas volume change during loading is considered for the lower bound. The new bounds are also dependent on the stress path. Therefore, the new bounds can be used to get a better prediction of s_u for specific loading conditions.

Some of the test data is very close to the new upper or lower bound, indicating that either bubble flooding or the detrimental effect dominates. But most of the results are within the two bounds. For these tests, some of the gas cavities degrade the soil structure and reduces the undrained shear strength. Meanwhile, some of the bubbles may get flooded by pore water from the saturated matrix, which has beneficial effect on the soil stiffness and strength. As a result, the s_u measured for the entire soil sample lie within the two bounds. The s_u measured for FGS is also dependent on $\frac{u_{w0}+p_a}{p'_0}$.

It has important implications for the constitutive modelling of FGS. First, the theoretical predictions above show that FGS is a composite material with a saturated soil matrix and compressible gas cavities. These bubbles tend to damage the soil structure but could be flooded by pore water. The condition for bubble flooding is $u_g \approx u_w$ for each gas bubble (Wheeler, 1988). For the entire soil, however, some bubbles are flooded while others are not, depending on the microstructure of cavity surface (Wheeler et al., 1990). Complete bubble flooding does not occur, as the measured s_u is well below Wheeler's upper bound. Besides, the variable $\frac{u_{w0}+p_a}{p'_0}$ is appropriate for modelling the effect of free gas on mechanical behaviour of FGS. Higher $\frac{u_{w0}+p_a}{p'_0}$ leads to less bubble flooding and more detrimental effect (Hong et al., 2020; Gao et al., 2020). Note that the variable $\frac{u_{g0}+p_a}{p'_0}$ has been used for FGS, but it is very difficult to measure u_g (Wheeler, 1986; Sham, 1989; Gao et al., 2020)

Chapter 4: A critical state constitutive model of the fine-grained soils containing gas bubbles

This chapter has been published in the Canadian Geotechnical Journal ("Editor's Choice" paper for 2022):

Gao, Z., Cai, H., Hong, Y., Lu, D.C. (2022). "A critical state constitutive model for gassy clay." Canadian Geotechnical Journal, 59(6), pp. 1033-1045. http://doi.org/ 10.1139/cgj-2020-0754.

This work has been done through collaboration among University of Glasgow, Zhejiang University and Beijing University of Technology. Dr Gao developed the basic framework for modelling. Mr Cai made key contributions to the model formulations, validation and manuscript writing, with supervision of Dr Gao. Some test data on gassy clay was provided by Dr Hong at Zhejiang University. Prof. Lu has contributed to the development the ideas and writing.

4.1 Introduction

A new critical state constitutive model for FGS is proposed in this chapter. It is based on the method proposed in Gao et al. (2020), which accounts for the composite internal structure and bubble flooding of FGS. The new model uses stress quantities which can be readily measured and only one parameter is introduced (as compared to the MCC model) to describe the effect of gas bubbles on the mechanical behaviour of clays, making it easy to calibrate and use. The soil response in triaxial compression and isotropic compression is considered in this study. Two stress quantities, the mean effective stress p $[(=\sigma_1 + 2\sigma_3)/3]$ and deviator stress q $(=\sigma_1 - \sigma_3)$ are used, where σ_1 is the total axial stress and σ_3 is the total radial stress. The volumetric strain ε_v $(=\varepsilon_1 + 2\varepsilon_3)$ and shear strain ε_q $[=\frac{2}{3}(\varepsilon_1 - \varepsilon_3)]$ are used in the constitutive equations, where ε_1 is the axial strain and ε_3 is the radial strain.

4.2 Framework of the constitutive model for the fine-grained soils containing gas bubbles

This study focuses on the mechanical behaviour of normally consolidated clay with a fixed amount of free gas. Gas dissolution and exsolution due to the change in mean total stress is not considered, as the two processes can be negligible for the gas types (mainly methane or nitrogen, which has very low solubility) of interests. The following assumptions are made for the new constitutive model based on existing research (Wheeler, 1988; Wheeler et al., 1990; Gao et al., 2020): (a) FGS is a composite material with compressible cavities and saturated soil matrix. The cavities are filled with gas when there is no bubble flooding. Once bubble flooding occurs, there are both gas and water in the cavities (Wheeler, 1988; Gao et al., 2020). Bubble flooding makes the saturated soil matrix partially drained in a globally undrained test, because there is water drainage from the soil, but such water flow is insufficient to make the matrix fully drained. Terzaghi's effective stress principle works for the saturated soil matrix. (b) The volume change of FGS is caused by both water flow at the soil element boundary and bubble flooding (Wheeler, 1988). When there is no bubble flooding, the gas cavities have a detrimental effect on the soil strength only because gas bubbles have no shear stiffness and strength, causing stress concentration (and thus damage) around the cavities. Bubble flooding makes the mean effective stress of the saturated soil matrix increase, which has a beneficial effect on the stiffness and shear strength.

4.3. Stress and strain variables for FGS

As FGS is a composite, the rule of mixtures should be used to get the relationship between total stress and stress state of the saturated soil matrix (Pietruszczak and Pande, 1996; Gao and Diambra, 2020; Gao et al., 2020; Shi et al., 2019). Though the gas bubbles are much larger than the soil particles, the gas volume fraction is small (<0.05 in most cases). Therefore, the following equations are used for stress decomposition (Gao et al., 2020)

$$p_m = p \tag{4.1}$$

$$p'_m = p' = p - u_w \tag{4.2}$$

$$q_m = q \tag{4.3}$$

where p_m and p'_m are total and mean effective stress of the saturated clay matrix, q_m is the deviator stress of the saturated soil matrix, u_w is the pore water pressure. q is only dependent on q_m because the gas has no shear stiffness. Note that the assumption in Eqs. (4.1) and (4.2) is valid when the gas volume fraction is small and the gas pressure is close to the water pressure. As will be shown in the subsequent sections, the model can give reasonable prediction of FGS behaviour with this assumption. It could be due to that the gas pressure and water pressure are close, because the curvature of the air-water interface is small due to big gas bubble size (Wheeler, 1986). The volume fraction of cavities f is expressed as below (Wheeler, 1988)

$$f = \frac{V_c}{V} \tag{4.4}$$

where V_c is the specific volume of cavities and V is the total specific soil volume. When there is no bubble flooding, the cavities are filled with free gas, and one has

$$V_c = V_g = (1 - S_r)e \tag{4.5}$$

$$f = \frac{V_c}{V} = \frac{(1 - S_r)e}{1 + e} \tag{4.6}$$

where S_r $(= \frac{V_w}{V_v})$ is the degree of saturation and e is the global void ratio, with V_w and V_v being the specific volume of pore water and void, respectively. When there is bubble flooding, $V_c > V_g$ and Eq. (4.4) must be used to calculate f (Fig. 2.1). Following Gao et al. (2020), the global shear strain ε_q and volumetric strain of ε_v the FGS can be expressed as below

$$\varepsilon_q = \varepsilon_q^m \tag{4.7}$$

$$\varepsilon_v = (1 - f)\varepsilon_v^m + f\varepsilon_v^c \tag{4.8}$$

where the superscripts ‘m’ and ‘c’ represent the saturated soil matrix and gas cavities, respectively. Eq. (4.7) is assumed because the gas bubbles have no shear stiffness and the distortion of them follows that of the saturated matrix (Gao et al., 2020). But the term $f\varepsilon_v^c$ in Eq. (4.8) cannot be neglected due to bubble flooding and high compressibility of the gas bubbles (Gao et al., 2020). As FGS is considered as a composite, the constitutive equation for the soil needs to be obtained based on the constitutive model for saturated soil matrix and gas cavities, which will be presented in the subsequent sections.

4.4 Constitutive relationship for the saturated soil matrix

4.4.1 Volume change of the saturated soil matrix

The constitutive model for the saturated soil matrix is proposed based on the Modified Cam-Clay (MCC) model (Roscoe and Burland, 1968). The plastic hardening of the MCC is modified to incorporate the effect of gas cavities. Besides, the volumetric strain increment of the matrix $d\varepsilon_v^m$ is dependent on both water flow at the boundary dV_b and bubble flooding dV_f which occurs inside the soil (Wheeler, 1986; Sills et al., 1991). The expression for $d\varepsilon_v^m$ is

$$d\varepsilon_v^m = \frac{dV_b}{V_m} + \frac{dV_f}{V_m} = d\varepsilon_v^b + d\varepsilon_v^f \tag{4.9}$$

where $d\varepsilon_v^b$ and $d\varepsilon_v^f$ denote the volumetric strain increments caused by water flow at the boundary and bubble flooding, respectively.

4.4.2 Constitutive equations for the saturated soil matrix

The yield function F of modified Cam-Clay model is used

$$F = q^2 - M^2 p'(p_0' - p') = 0 \tag{4.10}$$

where p_0' is the size of the current yield surface and M is the critical state stress ratio. The associated plastic flow expressed as below is used

$$d\varepsilon_v^{mp} = \langle L \rangle \frac{\partial F}{\partial p'} \tag{4.11}$$

$$d\varepsilon_q^{mp} = \langle L \rangle \frac{\partial F}{\partial q} \tag{4.12}$$

where $d\varepsilon_v^{mp}$ and $d\varepsilon_q^{mp}$ denote the plastic volumetric and shear strain increment for the saturated soil matrix, respectively; L is the loading index and $\langle \ \rangle$ are the McCauley brackets which make $\langle L \rangle = L$ for $L > 0$ and $\langle L \rangle = 0$ otherwise. The elastic stress-strain relationship is the same as that of the MCC model, with the elastic bulk modulus K_m and shear modulus G_m for the saturated matrix being expressed as

$$d\varepsilon_v^{me} = \frac{dp'}{K_m} \qquad \text{with} \qquad K_m = \frac{1+e_m}{\kappa} p' \tag{4.13}$$

$$d\varepsilon_q^{me} = \frac{dq}{3G_m} \qquad \text{with} \qquad G_m = K_m \frac{3(1-2\nu)}{2(1+\nu)} \tag{4.14}$$

where K_m is the elastic bulk modulus of the saturated soil matrix, G_m is the elastic shear modulus, e_m ($= S_r e$ without bubble flooding) is the void ratio of the saturated soil matrix, $d\varepsilon_v^{me}$ is the elastic volumetric strain increment of the saturated soil matrix, $d\varepsilon_q^{me}$ is the elastic shear strain increment, κ is the swelling index and ν is the Poisson's ratio.

Since the pore gas pressure is not used in the current model, the plastic hardening law and bubble flooding equation are different, which will be discussed in this chapter. In Chapter 3, it is found that the variable $\frac{u_w+p_a}{p_0'}$ is suitable for modelling lower and upper bounds of the shear strength of FGS, where p_a is the atmospheric pressure and p_0' denotes the yield surface size. It will thus be employed in the new model formulations.

The following hardening law is proposed for the saturated soil matrix.

$$dp_0' = \langle L \rangle r_{pc} = \langle L \rangle (r_1 - r_2) = \langle L \rangle \frac{(1+e_0)p_c'}{\lambda-\kappa} \frac{\partial F}{\partial p'} \left[1 - a_H \sqrt{f} \frac{\eta}{\mathrm{M}} \left(1 - \mathrm{e}^{-\frac{u_w+p_a}{p_0'}} \right) \right] \tag{4.15}$$

where p_0' denotes the size of MCC yield surface, L is the loading index, e_0 is the initial value of the saturated matrix void ratio e_m, η ($= q/p'$) is the stress ratio, λ is the compression index, κ is the swelling index, F is the MCC yield function, p_a is the atmospheric pressure, $\langle\ \rangle$ are the McCauley brackets [$\langle L \rangle = L$ for $L > 0$ and $\langle L \rangle = 0$ otherwise].a_H is the new parameter which is used to describe the detrimental effect of gas bubbles on plastic hardening and shear strength, it must be determined using the triaxial compression test data on FGS. $r_1 = \langle L \rangle \frac{(1+e_0)p_0'}{\lambda-\kappa} \frac{\partial F}{\partial p'}$ which is the same as that for the MCC model and the term $r_2 = \langle L \rangle \frac{(1+e_0)p_0'}{\lambda-\kappa} \frac{\partial F}{\partial p'} \left[a_H \sqrt{f} \frac{\eta}{\mathrm{M}} \left(1 - \mathrm{e}^{-\frac{u_w+p_a}{p_0'}} \right) \right]$ is used to model the detrimental effect of gas bubbles on the plastic hardening and shear strength. Higher r_2 indicates more detrimental effect of gas bubbles on plastic hardening and shear strength. $r_2 = 0$ when there is no cavity with $f = 0$. Note that

$\frac{u_w+p_a}{p_0'}$ is used as a state variable here because it is found suitable for modelling lower and upper bounds of the shear strength of FGS in Chapter 3. Existing experimental evidence shows that the gas bubbles merely influence the plastic hardening of saturated soil matrix in isotropic consolidation, and therefore, the term $\frac{\eta}{\mathrm{M}}$ is introduced to make $r_2 = 0$ at $\eta = 0$ (Thomas, 1987; Wheeler, 1986; Hong et al., 2020). When the FGS is subjected to shear (e.g., triaxial compression), the detrimental effect of gas bubbles on plastic hardening is higher as $\frac{u_w+p_a}{p_0'}$ increases, but such detrimental effect is limited (Wheeler, 1988; Hong et al., 2020; Gao et al., 2021). Therefore, the term $1-\mathrm{e}^{-\frac{u_w+p_a}{p_0'}}$ is used to make r_2 increase with $\frac{u_w+p_a}{p_0'}$ and reach the maximum value of 1 when $\frac{u_w+p_a}{p_0'}$ is big enough. The plastic modulus K_p for the saturated matrix is

$$K_p = -\frac{\partial F}{\partial p_c'} r_{pc} \tag{4.16}$$

4.4.3 Bubble flooding

The concept of bubble flooding was first proposed by Wheeler (1986) to explain the beneficial effect of gas bubbles on undrained shear strength of FGS. For each bubble, the condition of bubble flooding is $u_g \approx u_w$, where u_g is the gas pressure (Wheeler, 1986). Since $u_g > u_w$ due to the surface tension of water meniscus, $u_g \approx u_w$ is more likely when u_w increases, which makes the curvature of water meniscus reduce and the difference between u_g and u_w smaller. Therefore, it is assumed that bubble flooding occurs when u_w increases. The following formulation is proposed for $d\varepsilon_v^f$

$$d\varepsilon_v^f = A du_w \tag{4.17}$$

where

$$A = \begin{cases} \frac{(1-s_r)e}{(u_w+p_a)(1+e)} & \text{for } du_w > 0 \\ 0 & \text{for } du_w \leq 0 \end{cases} \tag{4.18}$$

It is evident that there is bubble flooding only when the soil is unsaturated with $s_r < 1$ and $du_w > 0$ (Gao et al., 2020). The rate of bubble flooding is also higher when u_w is smaller, which is supported by the experimental observation that gas cavities have a less beneficial effect on the strength of clay when u_w is higher (Wheeler, 1986; Sham, 1989; Hong et al., 2020). In drained isotropic compression, bubble flooding will not occur based on Eq. (4.17) because u_w is constant. As will be shown in the subsequent sections of this chapter, this assumption is reasonable for modelling the volume change of FGS in drained isotropic compression (Figs. 4.4 and 4.8). However, if we devise an isotropic compression test with partial drainage (e.g., u_w increases), the model will predict some bubble flooding. Note that Eq. (4.12) can predict bubble flooding even when there is a small variation in u_w, which is not realistic because this may not bring u_w close to u_g. This limitation is expected to be addressed in future research.

4.5 Gas and cavity volume change

Since the cavity surface is part of the saturated soil matrix, it is expected that the cavity changes size when the effective stress of saturated soil matrix changes (or there is deformation in the matrix). Therefore, the volumetric strain increment of the cavity $d\varepsilon_v^c$ is assumed to be affected by dp'

$$d\varepsilon_v^c = \frac{dV_c}{V_c} = Bdp' = \frac{1}{p'+u_w+p_a}dp' \tag{4.19}$$

where dV_c is the volume change of the cavity. This equation indicates that the compressibility of the cavity is dependent on the stiffness of saturated soil matrix as p' is included. Higher p' will lead to lower compressibility of both the saturated soil matrix and gas cavity. In addition, the cavity volume change may also depend on other soil properties like the plasticity index and particle size, which means that extra model parameters may be required to describe such influence. But it is found that Eq. (4.14) is suitable for modelling the gas volume change. Therefore, it is unnecessary to use more complex formulations for the gas volume change.

4.6 The constitutive equation and parameter determination

The constitutive equation for the entire FGS can be derived based on the constitutive model for the saturated soil matrix and equations for cavity and gas volume evolution, which is presented in this section. In the present model, the total strain increment is assumed to be the summation of the elastic and plastic parts with $d\varepsilon_v^m = d\varepsilon_v^{me} + d\varepsilon_v^{mp}$ and $d\varepsilon_q^m = d\varepsilon_q^{me} + d\varepsilon_q^{mp}$. Based on Eqs. (4.8) and (4.19), one can get the following

$$d\varepsilon_v = (1-f)d\varepsilon_v^m + fBdp' \tag{4.20}$$

Since $d\varepsilon_v^m = d\varepsilon_v^{me} + d\varepsilon_v^{mp} = \frac{dp'}{K_m} + \langle L\rangle \frac{\partial F}{\partial p'}$, Eq. (4.20) can be rewritten as

$$d\varepsilon_v = (1-f)\left(\frac{dp'}{K_m} + \langle L\rangle \frac{\partial F}{\partial p'}\right) + fBdp' \tag{4.21}$$

The expression of dp' can be obtained based on Eq. (4.21) as below

$$dp' = \frac{d\varepsilon_v - (1-f)\langle L\rangle \frac{\partial F}{\partial p'}}{\frac{1-f}{K_m} + fB} = \frac{d\varepsilon_v}{X} - \langle L\rangle \frac{1-f}{X}\frac{\partial F}{\partial p'} \tag{4.22}$$

where X represents the denominator of Eq. (4.22). Combining Eq. (4.22) and the condition of consistency for the yield function of MCC, one has

$$\frac{\partial F}{\partial p'}\left[\frac{d\varepsilon_v}{X} - \langle L\rangle \frac{1-f}{X}\frac{\partial F}{\partial p'}\right] + 3G_m\frac{\partial F}{\partial q}\left[d\varepsilon_q - \langle L\rangle \frac{\partial F}{\partial q}\right] - \langle L\rangle K_p = 0 \tag{4.23}$$

where L is the loading index and $\langle\ \ \rangle$ are the McCauley brackets which make $\langle L\rangle = L$ for $L > 0$ and $\langle L\rangle = 0$ otherwise. The loading index L can then be determined using Eq. (4.23)

$$\langle L\rangle = \frac{\frac{1}{X}\frac{\partial F}{\partial p'}d\varepsilon_v + 3G_m\frac{\partial F}{\partial q}d\varepsilon_q}{K_p + \frac{1-f}{X}\left(\frac{\partial F}{\partial p'}\right)^2 + 3G_m\left(\frac{\partial F}{\partial q}\right)^2} = \Lambda_p d\varepsilon_v + \Lambda_q d\varepsilon_q \tag{4.24}$$

where $\Lambda_p = \frac{\frac{1}{X}\frac{\partial F}{\partial p'}}{K_p + \frac{1-f}{X}\left(\frac{\partial F}{\partial p'}\right)^2 + 3G_m\left(\frac{\partial F}{\partial q}\right)^2}$ and $\Lambda_q = \frac{3G_m\frac{\partial F}{\partial q}}{K_p + \frac{1-f}{X}\left(\frac{\partial F}{\partial p'}\right)^2 + 3G_m\left(\frac{\partial F}{\partial q}\right)^2}$. The expression of dp' in terms of $d\varepsilon_v$ and $d\varepsilon_q$ can be obtained using Eqs. (4.22) and (4.24)

$$dp' = C_{pp}d\varepsilon_v + C_{pq}d\varepsilon_q \tag{4.25}$$

where

$$C_{pp} = \frac{1}{X} - h(L)\Lambda_p \frac{1-f}{X}\frac{\partial F}{\partial p'} \tag{4.26}$$

$$C_{pq} = -h(L)\Lambda_q \frac{1-f}{X}\frac{\partial F}{\partial p'} \tag{4.27}$$

where $h(L)$ is the Heaviside function with $h(L) = 1$ when $L > 0$ and $h(L) = 0$ otherwise. The increment of the deviator stress dq is

$$dq = 3G_m\left(d\varepsilon_q - d\varepsilon_q^{mp}\right) = 3G_m\left(d\varepsilon_q - \langle L\rangle\frac{\partial F}{\partial q}\right) = C_{qp}d\varepsilon_v + C_{qq}d\varepsilon_q \tag{4.28}$$

where

$$C_{qp} = -h(L)3G_m\Lambda_p\frac{\partial F}{\partial q} \tag{4.29}$$

$$C_{qq} = 3G_m - h(L)3G_m\Lambda_q\frac{\partial F}{\partial q} \tag{4.30}$$

Combining Eqs. (4.8), (4.17), (4.19) and (4.22), the following equation can be got

$$d\varepsilon_v = (1-f)(d\varepsilon_v^b + Adu_w) + fB\left(C_{pp}d\varepsilon_v + C_{pq}d\varepsilon_q\right) \tag{4.31}$$

Eq. (4.31) can then be used to get the expression for du_w

$$du_w = C_{wp}d\varepsilon_v + C_{wq}d\varepsilon_q + C_{wb}d\varepsilon_v^b \tag{4.32}$$

where

$$C_{wp} = \frac{1-fBC_{pp}}{(1-f)A} \tag{4.33}$$

$$C_{wq} = -\frac{fBC_{pq}}{(1-f)A} \tag{4.34}$$

$$C_{wb} = -\frac{1}{A} \tag{4.35}$$

The constitutive equation can be written in a matrix form as below

$$\begin{bmatrix} dp' \\ dq \\ du_w \end{bmatrix} = \begin{bmatrix} C_{pp} & C_{pq} & 0 \\ C_{qp} & C_{qq} & 0 \\ C_{wp} & C_{wq} & C_{wb} \end{bmatrix}\begin{bmatrix} d\varepsilon_v \\ d\varepsilon_q \\ d\varepsilon_v^b \end{bmatrix} \tag{4.36}$$

The constitutive equation requires two volumetric strain quantities ε_v and ε_v^b, which represent the total volume change and volume change due to water flow at the boundary. This is due to the bubble flooding and cavity volume change in the soil, which makes ε_v and ε_v^b different. A code base on the MCC model is used for the model implementation. Both undrained triaxial compression and isotropic consolidation tests are simulated.

In a globally undrained test, $d\varepsilon_v^b = 0$ and a fixed $d\varepsilon_q$ (about 1e-5 is given in the model implementation) du_w can then be calculated based on the total stress path with $dq = 3(dp' + du_w)$. Once du_w is obtained, dp' and dq can be calculated using Equation (4.36). $d\varepsilon_v^c$ can then be calculated using Equation (4.19).

When an isotropic consolidation test is performed, there is no deviator strain ($d\varepsilon_q = 0$ and $d\varepsilon_v$ is given as a fixed value) and $du_w = 0$, which means there is no bubble flooding in isotropic consolidation condition. Equation (4.36) can thus be used to calculate dp' and dq based on this condition.

The volume change of cavity, saturated matrix, and entire soil should be calculated using the following equations:

$$dV_c = V_c d\varepsilon_v^c = V_c\, B dp' = V_c \frac{1}{p' + u_w + p_a} dp' \tag{4.37}$$

$$dV_m = V_m d\varepsilon_v^m = V_c\, (\frac{dV_b}{V_m} + \frac{dV_f}{V_m}) = V_c(d\varepsilon_v^b + d\varepsilon_v^f) \tag{4.38}$$

$$dV = dV_c + dV_m \tag{4.39}$$

The code for this model is provided in the Appendix I.

There are six parameters in the model, five of which are the same as those for the MCC model. Only the parameter a_H in Eq. (4.15) should be determined for FGS. Since a_H is used to describe the detrimental effect of gas bubbles on plastic hardening and shear strength, it must be determined using the triaxial compression test data on FGS. Only one set of test data from the conventional triaxial compression test is needed for determining a_H through best fitting the stress-strain relationship. A test with an initial degree of saturation $S_{r0} \leq 0.95$ where the effect of gas on the soil response is obvious is recommended. Determination of a_H will be presented below using the test data of gassy Combwich mud (Wheeler, 1986).

4.7 Model validation

The model will be validated against the test data on three FGS, including Gassy Combwich mud (Wheeler, 1986), Gassy Kaolin (Sham, 1989) and Gassy Malaysian Kaolin (Hong et al., 2020).

4.7.1 Calibration of model parameter

Both isotropic consolidation and undrained triaxial compression tests have been reported on gassy Combwich mud in Wheeler (1986). The parameters M, λ and N are directly obtained from Wheeler (1986). The elastic parameter $\nu = 0.2$ is assumed as it has a small influence on the model prediction. Finally, a_H is determined using the undrained test data on gassy Combwich mud with initial mean effective stress $p'_0 = 400$ kPa, initial pore water pressure $u_{w0} = 0$ and initial degree of saturation $S_{r0} = 0.95$ (Fig. 4.1). Specifically, a_H is determined by fitting the undrained shear strength of this test visually. The undrained shear strength is higher when a_H is smaller, which describes a less detrimental effect of gas bubbles on the soil stiffness and strength (Fig. 4.1). The best model prediction for the undrained shear strength and effective stress path can be obtained by using $a_H = 14$ for gassy combwich mud (Wheeler, 1986). The calibration of the model parameter a_H for gassy combwich mud is shown in Fig. 4.1 and same method is used for gassy kaolin (Sham, 1989) and gassy Malaysian kaolin (Hong et al., 2020). All the model parameters are listed in Table 4.1.

Table 4.1 Model parameters for Chapter 4

Soil	M	λ	κ	N	ν	a_H
Combwich mud (Wheeler, 1986)	1.33	0.174	0.0297	3.06	0.2	14
Kaolin clay (Sham, 1989)	0.87	0.23	0.014	3.35	0.2	15
Malaysian kaolin silt (Hong et al., 2020)	1.05	0.25	0.06	3.81	0.2	3

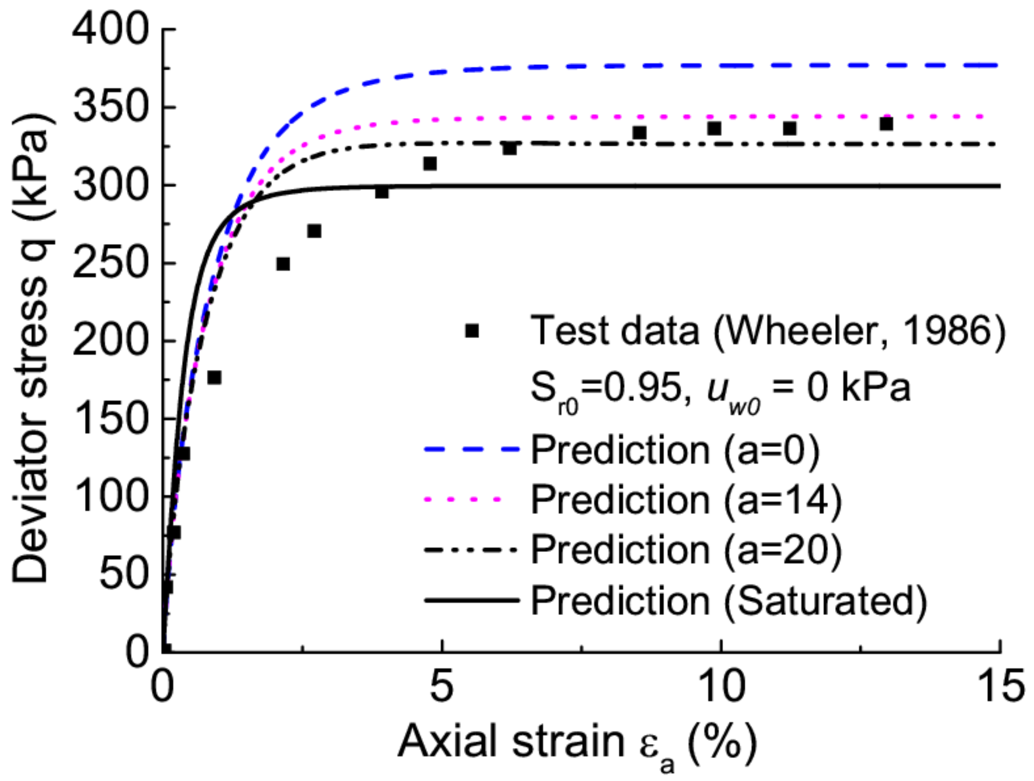

400
350
300
250
200
150
100
50
0
Deviator stress q (kPa)
0
5
10
15
Axial strain εa (%)
Test data (Wheeler, 1986)
Sr0=0.95, uw0 = 0 kPa
Prediction (a=0)
Prediction (a=14)
Prediction (a=20)
Prediction (Saturated)

(a)

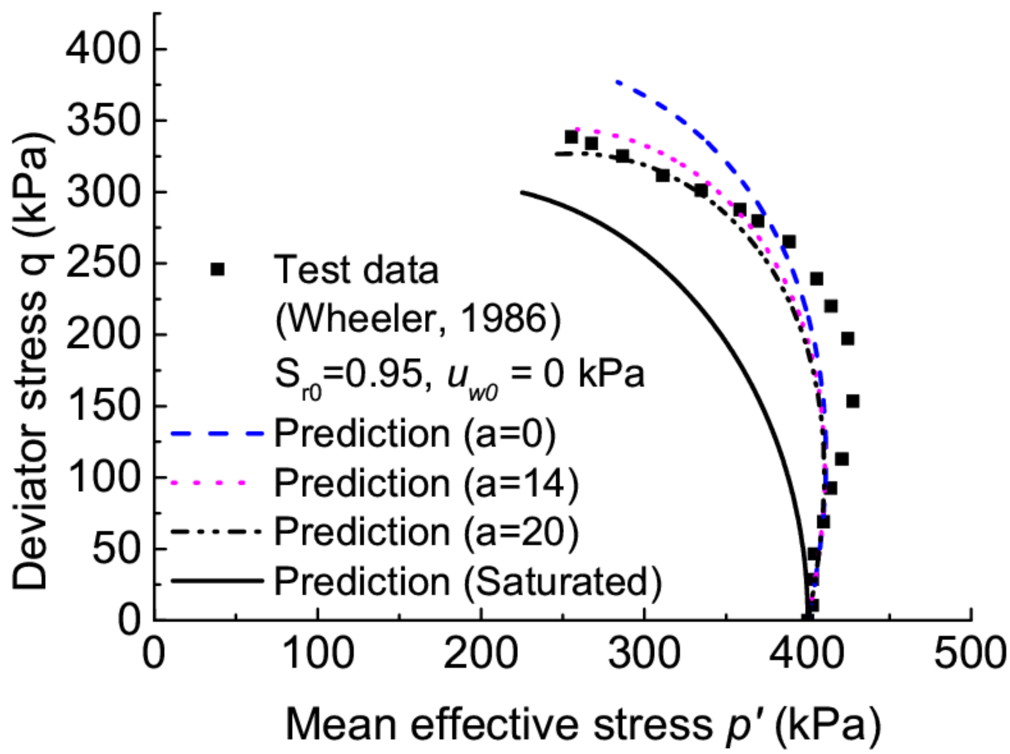

400
350
300
250
200
150
100
50
0
Deviator stress q (kPa)
0
100
200
300
400
500
Mean effective stress p′ (kPa)
Test data
(Wheeler, 1986)
Sr0=0.95, uw0 = 0 kPa
Prediction (a=0)
Prediction (a=14)
Prediction (a=20)
Prediction (Saturated)

(b)

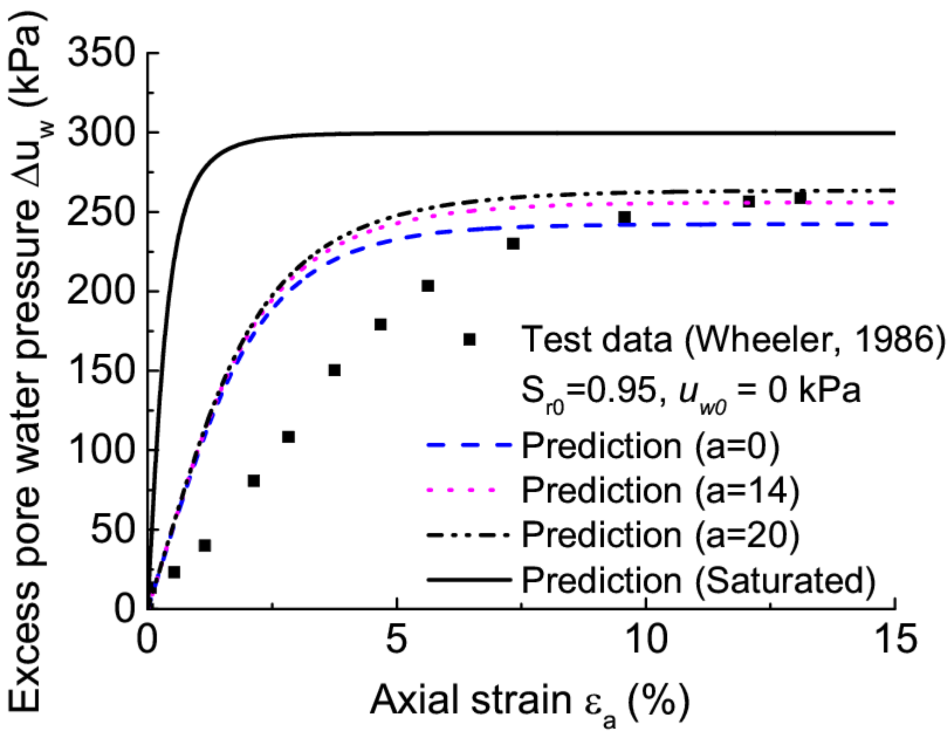

(c)

Fig. 4.1 Model prediction for shear behaviour of gassy Combwich mud (test data from Wheeler, 1986): (a) the $\varepsilon_a - q$ relationship; (b) the effective stress path and (c) the evolution of excess pore water pressure

4.7.2 Gassy Combwich Mud (Wheeler, 1986)

The undrained shear strength of the FGS shown in Fig. 4.1 is higher than that of the saturated soil. This is because of the beneficial effect caused by bubble flooding dominates for the FGS, which is illustrated in Fig. 4.2. The model prediction without bubble flooding is shown in Fig. 4.2 ($A = 0$ in Eq. 4.13). All the model parameters are the same as those in Table 4.1. The undrained shear strength predicted by neglecting bubble flooding is smaller than the saturated one, as bubbles are assumed to have a detrimental effect on the soil stiffness and strength only with $a_H = 14$. Under other conditions of u_{w0}, S_{r0} and p'_0, the overall effect of gas bubbles on undrained shear strength can become detrimental due to a smaller amount of bubble flooding, which has been discussed in the second assumption for the model.

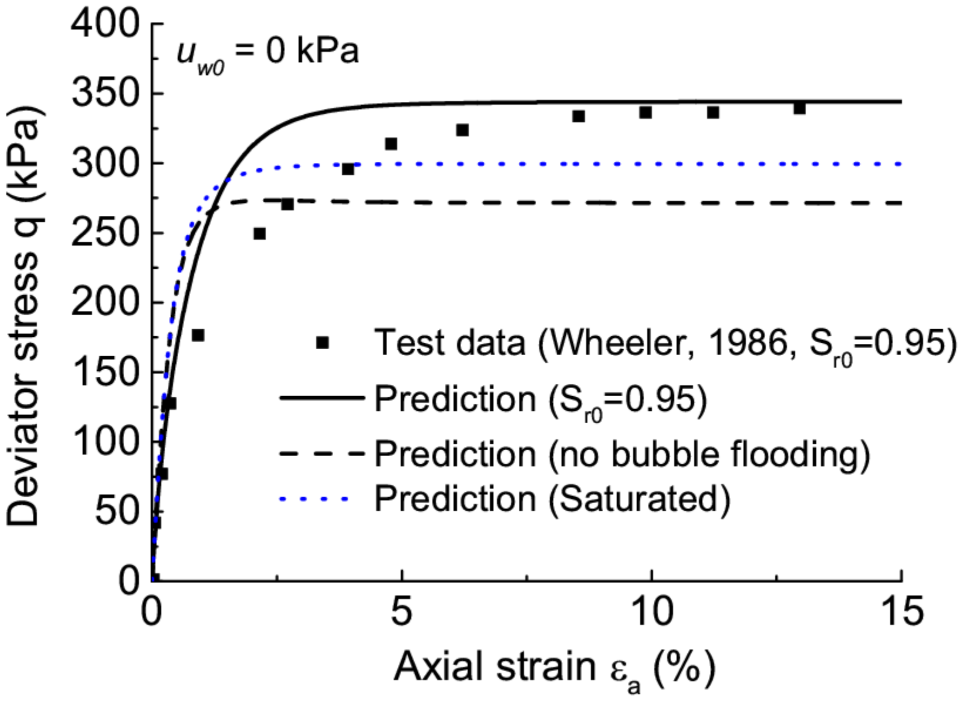

(a)

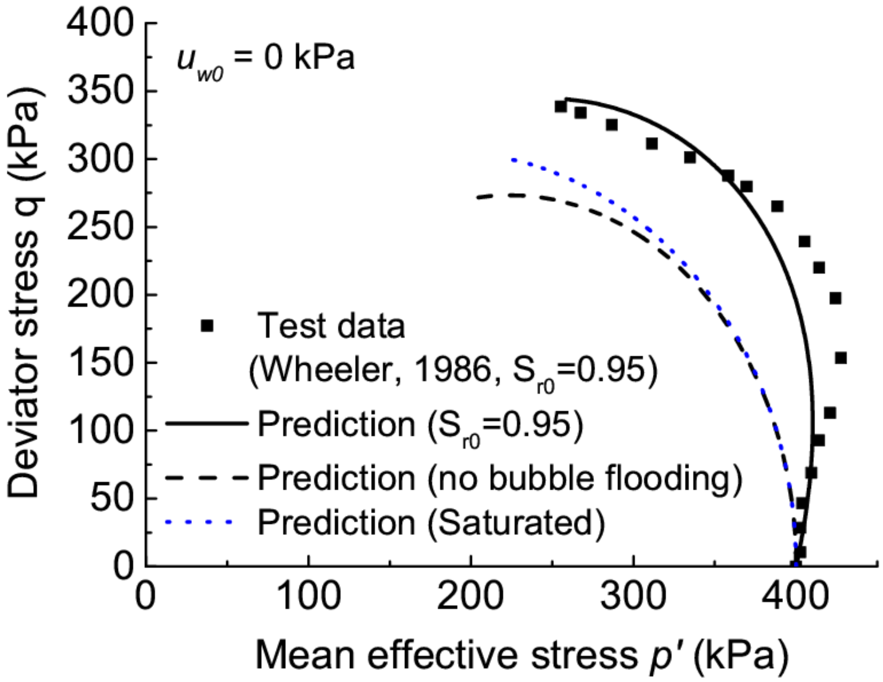

(b)

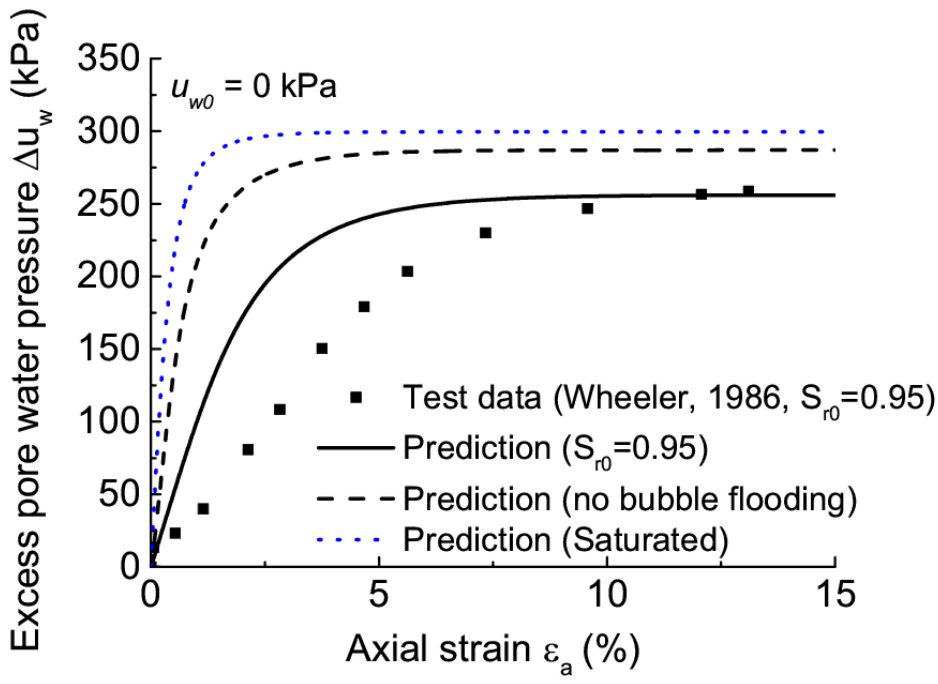

(c)

Fig. 4.2 Effect of bubble flooding on shear behaviour of gassy Combwich mud (test data from Wheeler, 1986): (a) the $\varepsilon_a - q$ relationship; (b) the effective stress path and (c) the evolution of excess pore water pressure

Though many undrained triaxial compression tests have been done by Wheeler (1986), only one complete set of data is available, which includes the effective stress path and shear stress-strain relationship (see Fig. 4.1). For the other tests, only the undrained shear strength s_u is available, which will be used to validate the model prediction. Fig. 4.3 shows the model prediction for the undrained shear strength of gassy Combwich mud with different p'_0 and u_{w0}. The dots and the lines represent the undrained shear strength from test results and the predictions, respectively. The prediction line is obtained by connecting the prediction data points for different S_{r0} values. The model prediction captures the trends of s_u variation with S_{r0} well, including both beneficial and detrimental effects under different circumstances. Obvious overestimation is observed for the tests with $p'_0 = 200$ kPa and $u_{w0} = 100$ kPa (Fig. 4.3b). There are two possible reasons for this discrepancy. First, the s_u for the test with $p'_0 = 400$ kPa,

$u_{w0} = 0$ kPa and $S_{r0} = 0.95$, which has been used for determining the parameter a, lies on the upper bound of the test data in its group (Fig. 4.3a). This indicates that the model prediction tends to give higher s_u for most of the tests. A better model prediction is expected if more results like those in Fig. 4.1 are available for getting more optimum value of a_H. Besides, it is noticed that the data for this group of tests are quite scattered, with two tests ($S_{r0} = 0.97$ and $S_{r0} = 0.984$) showing unexpectedly low s_u (Fig. 4b). The real s_u could be higher and closer to the model prediction.

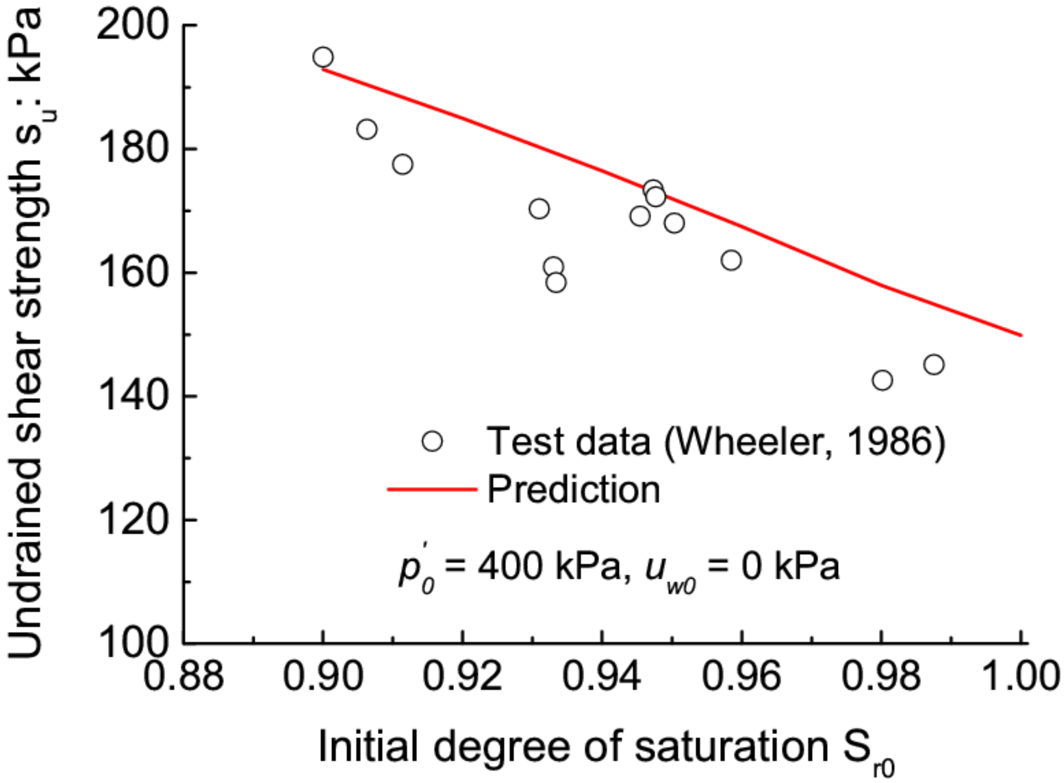

(a)

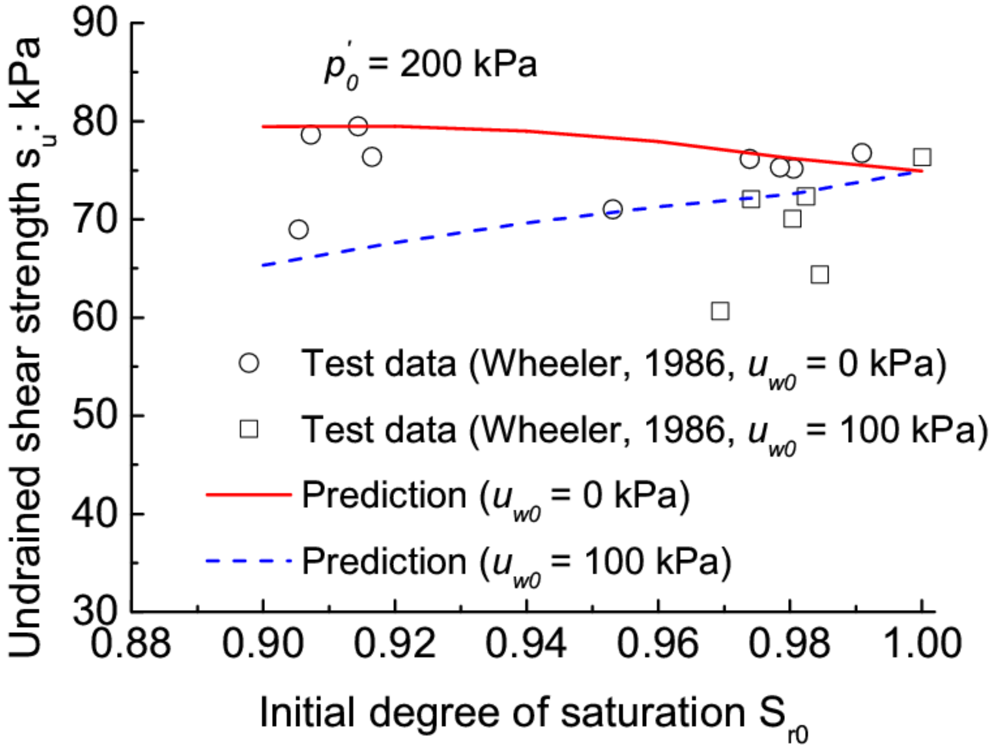

p'_0 = 200 kPa
Test data (Wheeler, 1986, u_{w0} = 0 kPa)
Test data (Wheeler, 1986, u_{w0} = 100 kPa)
Prediction (u_{w0} = 0 kPa)
Prediction (u_{w0} = 100 kPa)
Undrained shear strength s_u: kPa
Initial degree of saturation S_{r0}
90
80
70
60
50
40
30
0.88
0.90
0.92
0.94
0.96
0.98
1.00

(b)

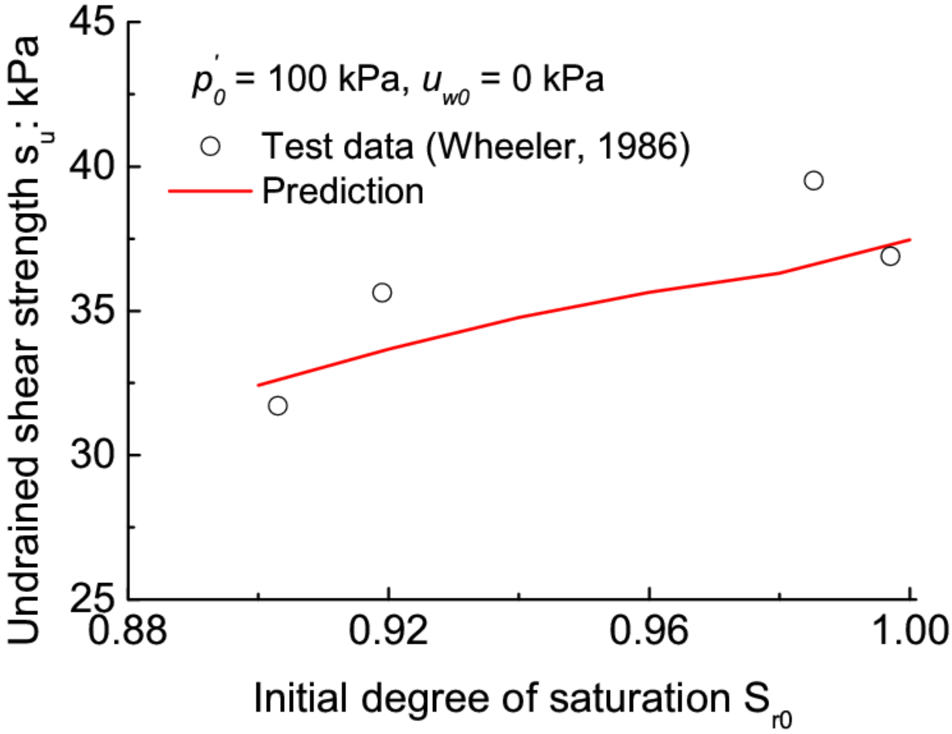

p'_0 = 100 kPa, u_{w0} = 0 kPa
Test data (Wheeler, 1986)
Prediction
Undrained shear strength s_u: kPa
Initial degree of saturation S_{r0}
45
40
35
30
25
0.88
0.92
0.96
1.00

(c)

Fig. 4.3 Model prediction for the undrained shear strength of gassy Combwich mud (test data from Wheeler, 1986): (a) $p'_0 = 400$ kPa; (b) $p'_0 = 200$ kPa and (c) $p'_0 = 100$ kPa

Fig. 4.4 presents the comparison between test data and model prediction of gassy Combwich mud in isotropic compression (Wheeler, 1986). The dots and lines represent the test data and model predictions, respectively. The initial degree of saturation S_{r0} is the one at $p' = 100$ kPa. For the FGS samples, the total volume change is caused by water drainage from the saturated soil matrix and compression of gas bubbles (Eq. 4.14). There is no bubble flooding as u_w is a constant (Eq. 4.12). The model can satisfactorily describe the volume change of FGS with different S_{r0} (Fig. 4.4a), indicating that Eq. (4.14) is suitable for modelling gas cavity compression in FGS. There is a unique relationship between the matrix void ratio e_m and p' for all samples (Fig. 4.4b), because Terzaghi's effective stress principle works in the saturated soil matrix.

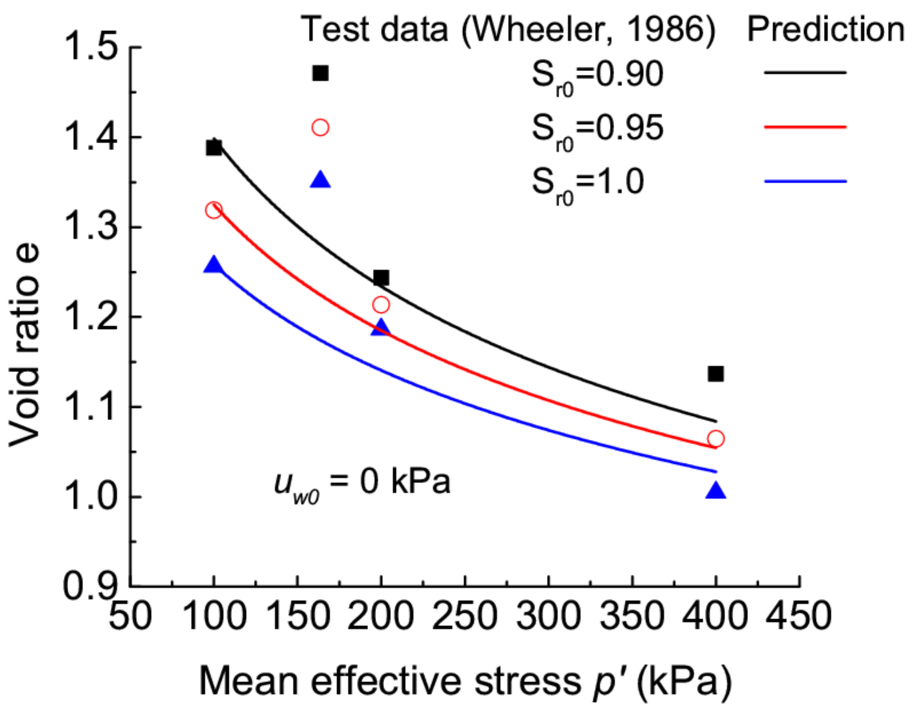

(a)

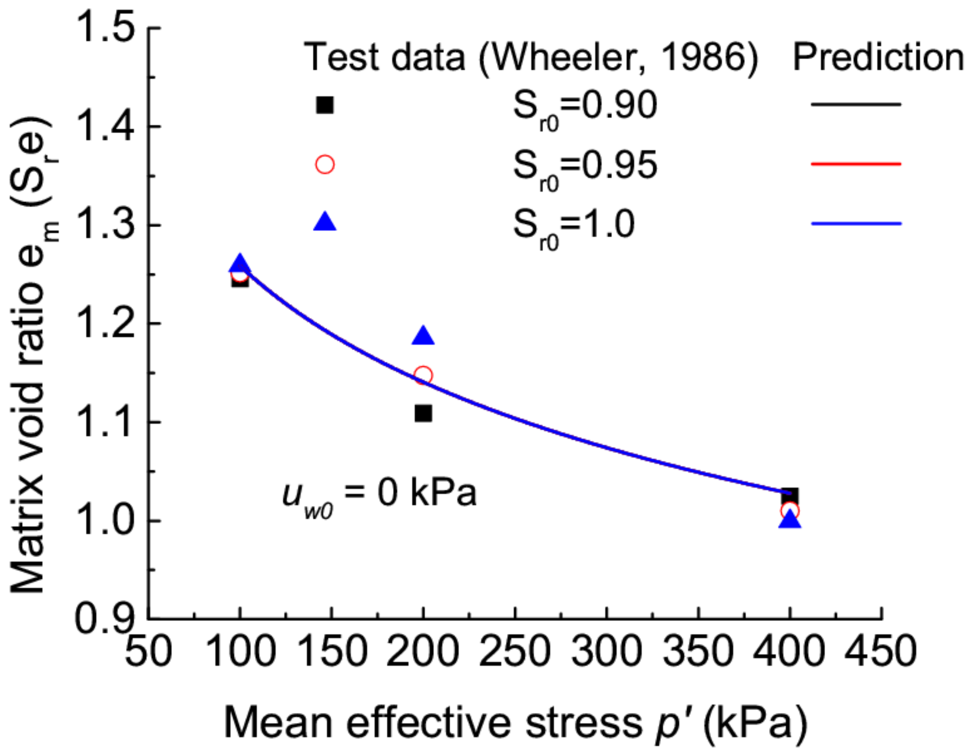

(b)

Fig. 4.4 Model prediction for isotropic consolidation of gassy Combwich mud (test data from Wheeler, 1986): (a) the $e - p'$ relationship and (b) the $e_m - p'$ relationship

4.7.3 Gassy Kaolin (Sham, 1989)

A series of undrained triaxial compression tests have been carried out on Kaolin with helium to investigate the upper and lower bounds for the undrained shear strength of FGS (Sham, 1989). Details of the test procedure can be found in Sham (1989). The MCC parameters are determined using the same method as for Combwich mud. The parameter a_H is determined using the test data shown in Fig. 4.5, which is the only set of data which includes the stress-strain relationship and effective stress path. The model is then used to predict the s_u of all the other gassy Kaolin specimens under different combinations of p_0' and u_{w0} (Fig. 4.6). The predicted s_u is close to the measured value for most cases except those with $p_0' = 100$ kPa and $u_{w0} = 300$ kPa (Fig. 4.7d). Close inspection shows that the initial value of $\frac{u_w+p_a}{p_c'}$ is the maximum for this group of tests. This means that Eq. (4.10) tends to underestimate the detrimental effect of gas bubbles on the shear strength of this soil at higher $\frac{u_w+p_a}{p_c'}$. An improved model prediction can be achieved by introducing more model parameters, which will inevitably make the parameter determination more difficult.

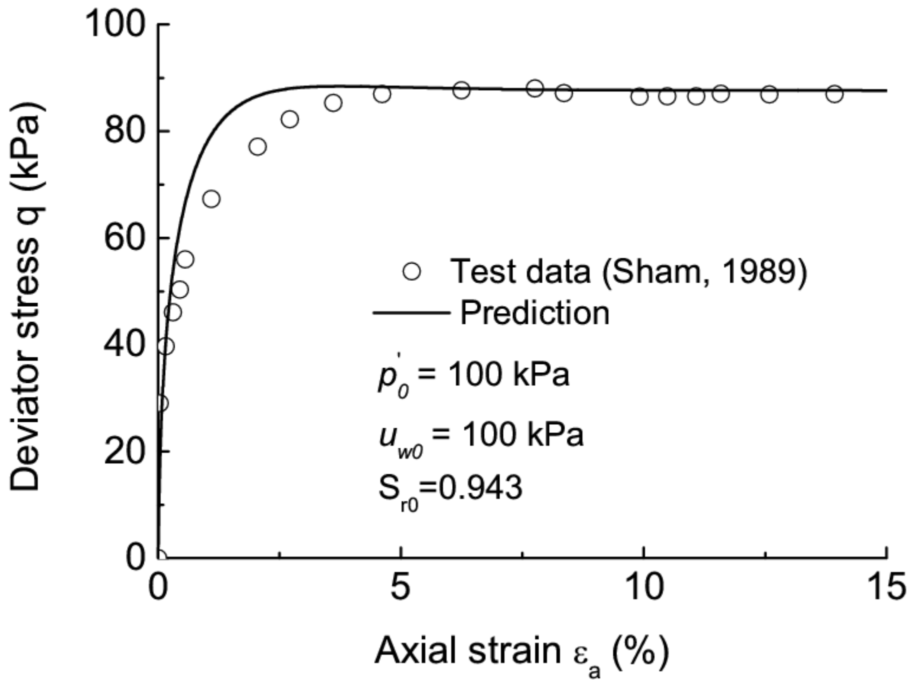

(a)

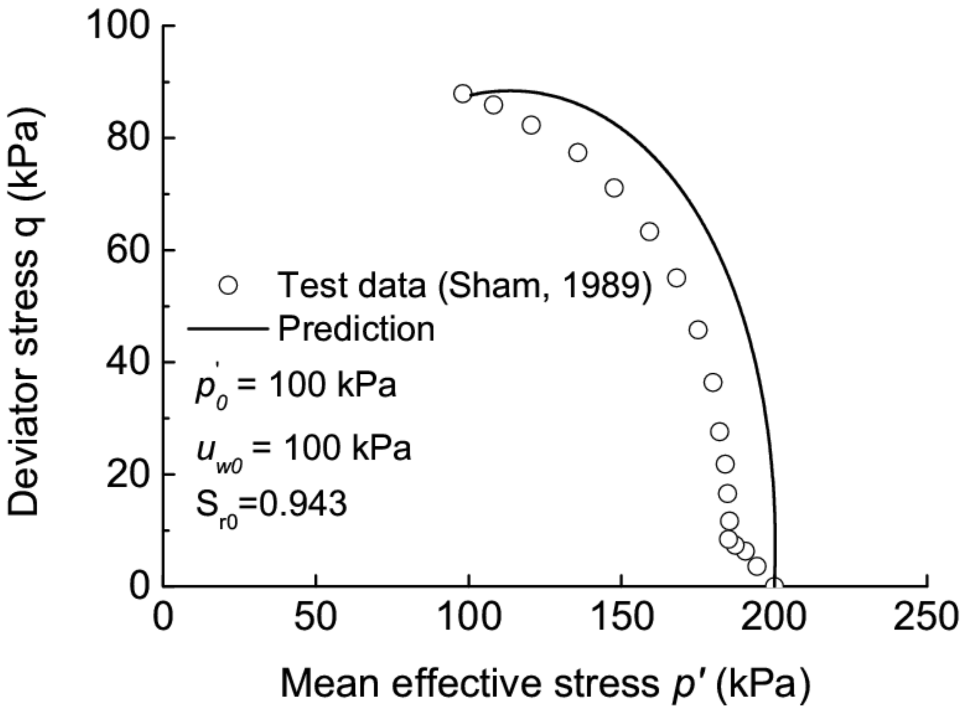

(b)

Fig. 4.5 Model prediction for the shear behaviour of gassy Kaolin (test data from Sham, 1989) with $p_0' = 200$ kPa, $u_{w0} = 100$ kPa and $s_{r0} = 0.943$: (a) the $\varepsilon_a - q$ relationship; (b) the effective stress path

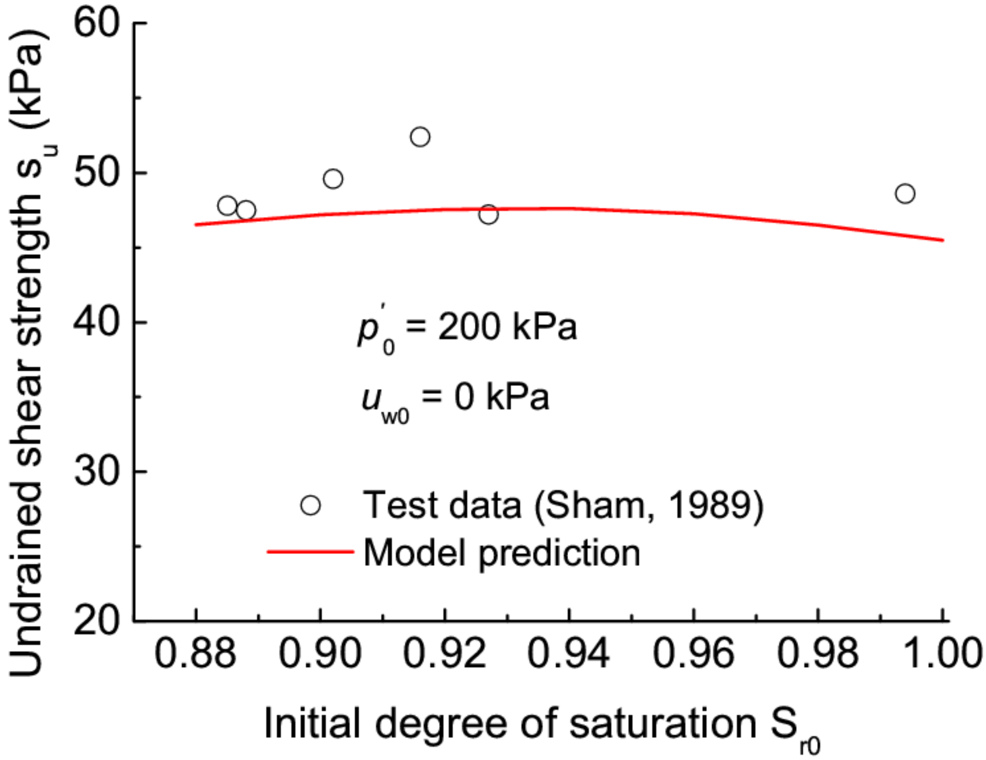

60
50
40
30
20
Undrained shear strength s_u (kPa)
0.88
0.90
0.92
0.94
0.96
0.98
1.00
Initial degree of saturation S_{r0}
p'_0 = 200 kPa
u_{w0} = 0 kPa
Test data (Sham, 1989)
Model prediction

(a)

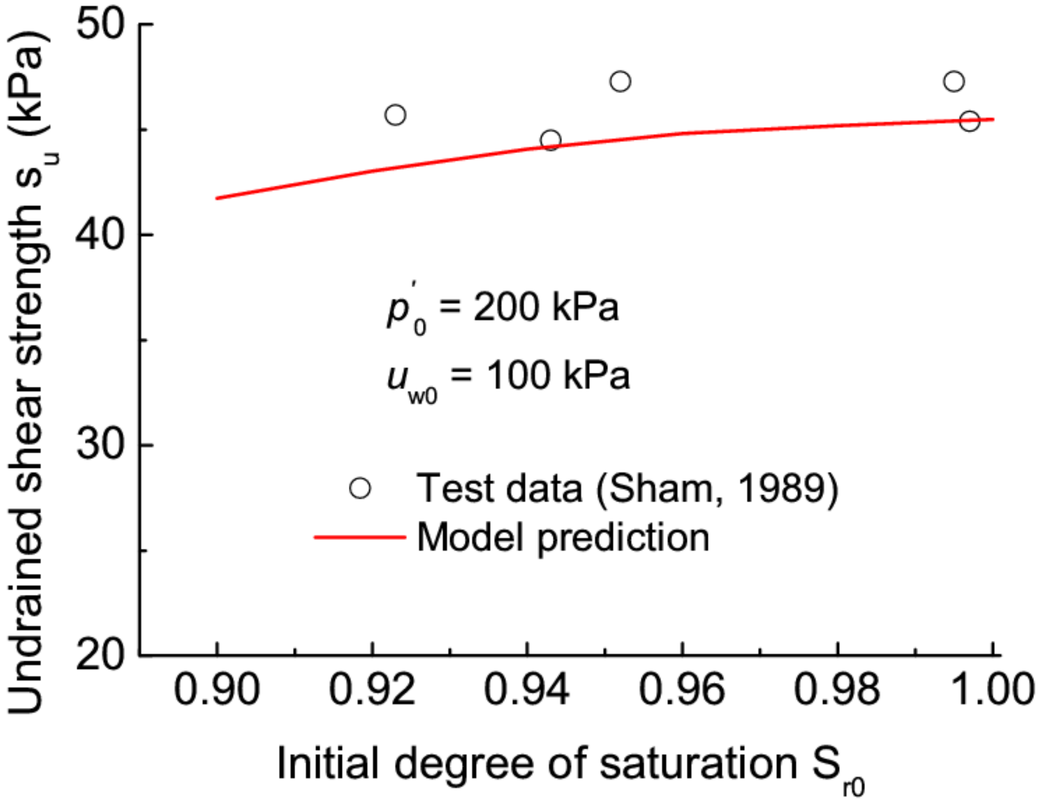

50
40
30
20
Undrained shear strength s_u (kPa)
0.90
0.92
0.94
0.96
0.98
1.00
Initial degree of saturation S_{r0}
p'_0 = 200 kPa
u_{w0} = 100 kPa
Test data (Sham, 1989)
Model prediction

(b)

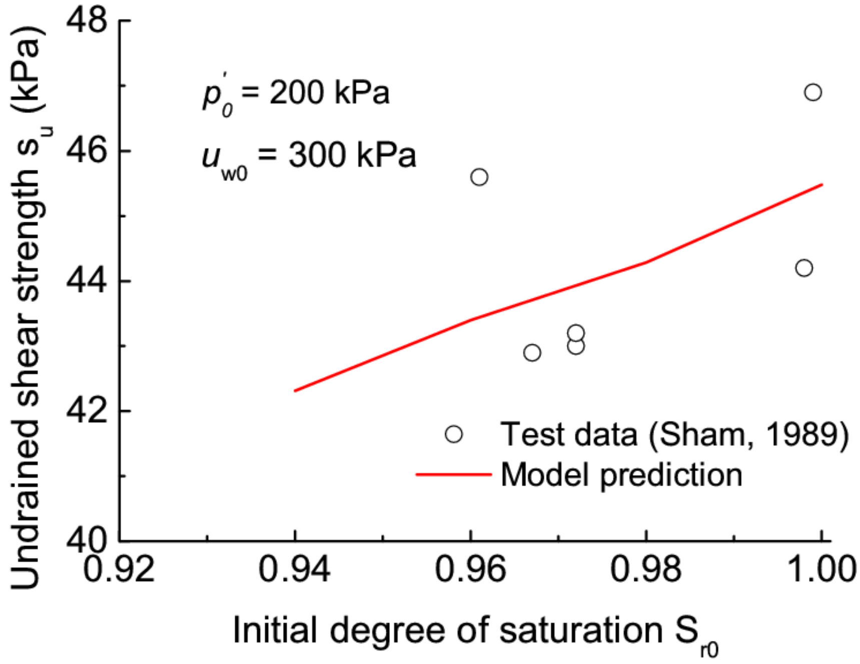

(c)

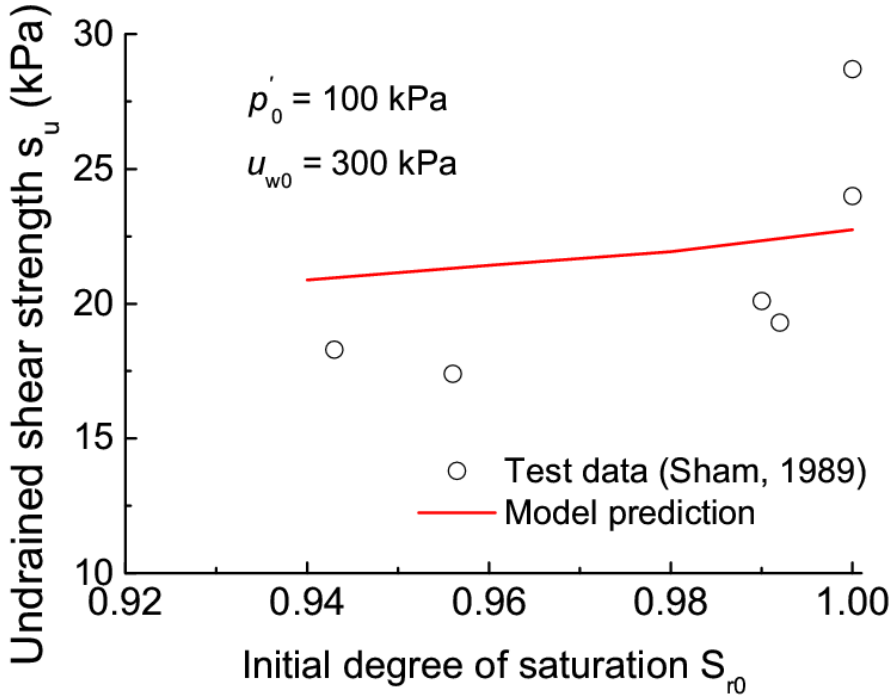

(d)

Fig. 4.6 Model prediction for the undrained shear strength of gassy Kaolin clay (test data from Sham, 1989): (a) $p_0' = 200$ kPa and $u_{w0} = 0$ kPa; (b) $p_0' = 200$ kPa and

$\boldsymbol{u_{w0} = 100}$ **kPa (c)** $\boldsymbol{p'_0 = 200}$ **kPa and** $\boldsymbol{u_{w0} = 300}$ **kPa; (d)** $\boldsymbol{p'_0 = 100}$ **kPa and** $\boldsymbol{u_{w0} = 300}$ **kPa**

4.7.4 Gassy Malaysian kaolin (Hong et al., 2020)

A group of undrained triaxial tests have been carried out on gassy Malaysian kaolin by Dr. Hong to validate the model (Hong et al., 2020). The liquid limit and plastic limit of MK is 65% and 28%, respectively (Hong et al., 2017). According to the plasticity chart (BSI 1999), this soil can be categorized as high plastic silt. The gas used in the tests is nitrogen. To get FGS samples with uniform and repeatable distribution of gas bubbles, the zeolite molecular sieve technique has been used (Nageswaran 1983; Wheeler 1988; Sills et al. 1991; Hong et al., 2020). A more detailed discussion of the sample preparation method can be found in Hong et al. (2017; 2020). The tests have been carried out using the GDS triaxial apparatus with a double-cell (i.e., HKUST cell (Ng et al., 2002)) and a differential pressure transducer (DPT). Before triaxial compression, each specimen was isotropically consolidated to an initial effective mean effective stress of $p'_0 = 200$ kPa with different u_{w0}.

All the MCC parameters are determined using the test results in Figs. 4.7 and 4.8 on the saturated soil. In Fig. 4.7, the dots and lines denote the test results and model predictions, respectively. In isotropic consolidation with constant pore water pressure, there is no bubble flooding and the gas bubbles do not affect plastic hardening (Eq.4. 10). But there is extra gas bubble compression for unsaturated soil samples in isotropic consolidation (Eq. 4.14), which makes the slope of their $e - p'$ curves higher than that of the saturated soil (Fig. 4.8). The model gives a unique $e_m - p'$ relationship, which is identical to the $e - p'$ curve for the saturated soil. The parameter a is determined using the results on FGS in undrained triaxial compression tests with $p'_0 = 200$ kPa and initial pore water pressure $u_{w0} = 150$ kPa (Fig. 4.9). The model predictions for the other undrained triaxial compression tests are shown in Figs. 4.10 and 4.11. In general, the model has reproduced both detrimental and beneficial effect of gas on the soil response with various combinations of u_{w0} and S_{r0}.

It is noticed that gassy Malaysian kaolin silt has a much smaller a_H than gassy Combwich mud and Kaolin (Table 4.1). This indicates that the gas bubbles have a much smaller detrimental effect on the s_u of Malaysian kaolin. Hong et al. (2020) have shown that this is maybe linked with the difference in the plastic index (PI) of the soil. The more detrimental effect of gas on the soil strength is observed when the PI is higher. Among the three clays, the Malaysian kaolin has the lowest PI while the Kaolin in Sham (1989) has the highest. Indeed, the parameter a_H is the biggest for the Kaolin and smallest for the Malaysian kaolin silt (Table 4.1). Therefore, the parameter could be alternatively approximated based on the PI of each soil. But the undrained triaxial tests on Malaysian kaolin silt have been performed with the same p'_0. More tests on Malaysian kaolin with different p'_0 need to be done to confirm the correlation between PI and a_H.

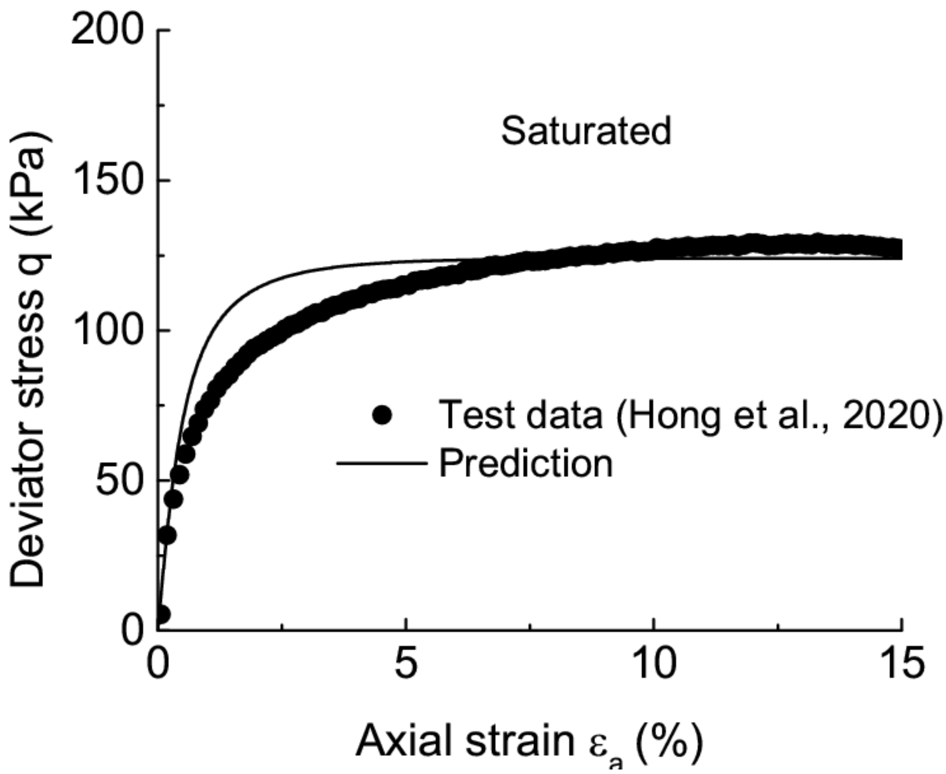

(a)

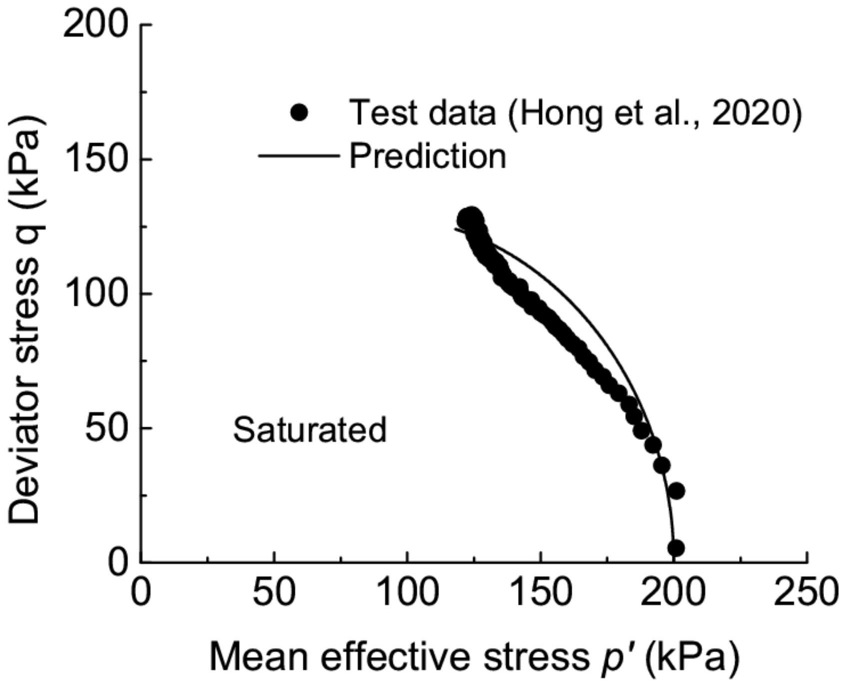
Test data (Hong et al., 2020)
Prediction
Saturated
Deviator stress q (kPa)
Mean effective stress p′ (kPa)

(b)

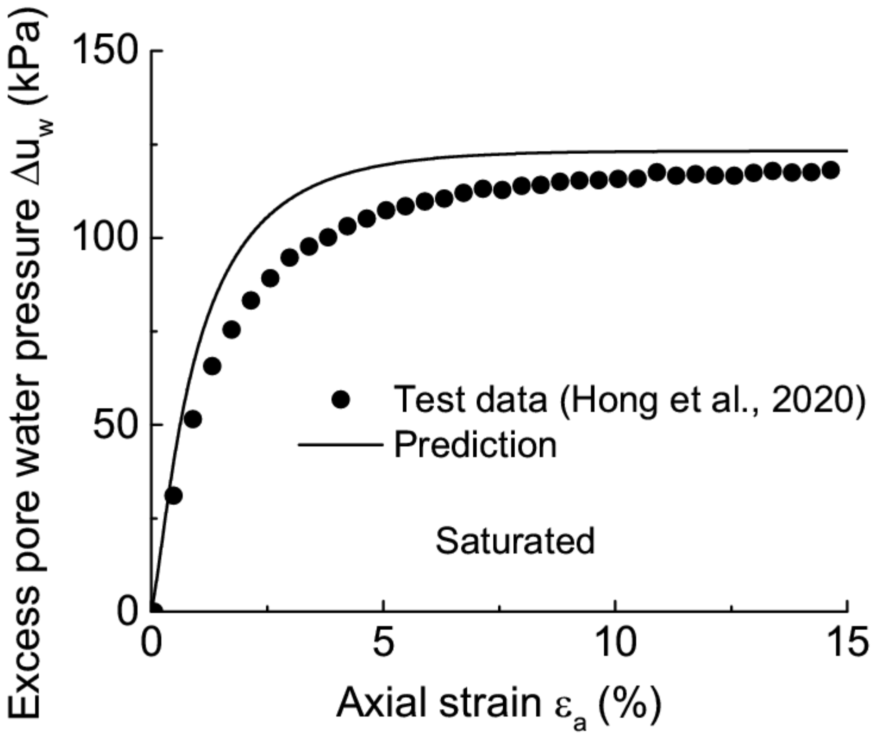
Test data (Hong et al., 2020)
Prediction
Saturated
Excess pore water pressure Δu_w (kPa)
Axial strain ε_a (%)

(c)

Fig. 4.7 Model prediction for the undrained shear behaviour of saturated Malaysian kaolin (test data from Hong et al., 2020): (a) the $\varepsilon_a - q$ relationship; (b) the effective stress path and (c) the evolution of excess pore water pressure

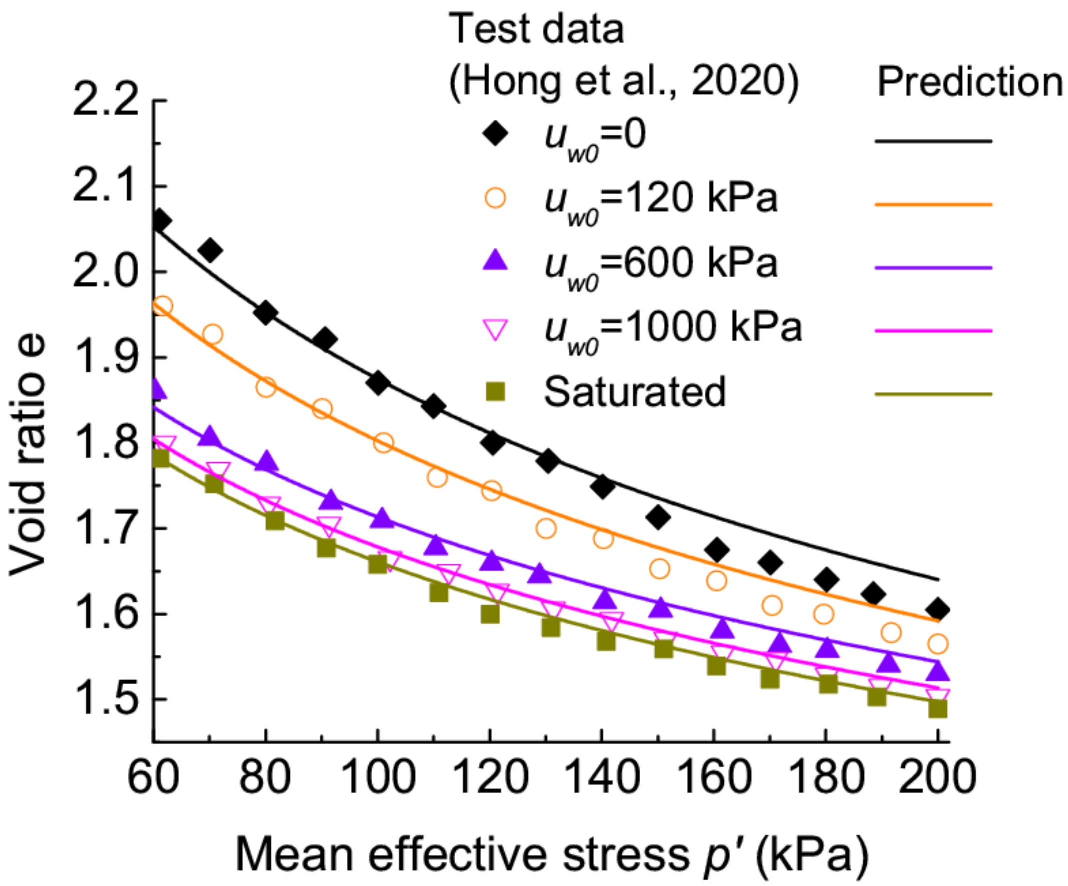

Fig. 4.8 Model prediction for the isotropic consolidation of gassy Malaysian kaolin (test data from Hong et al., 2020)

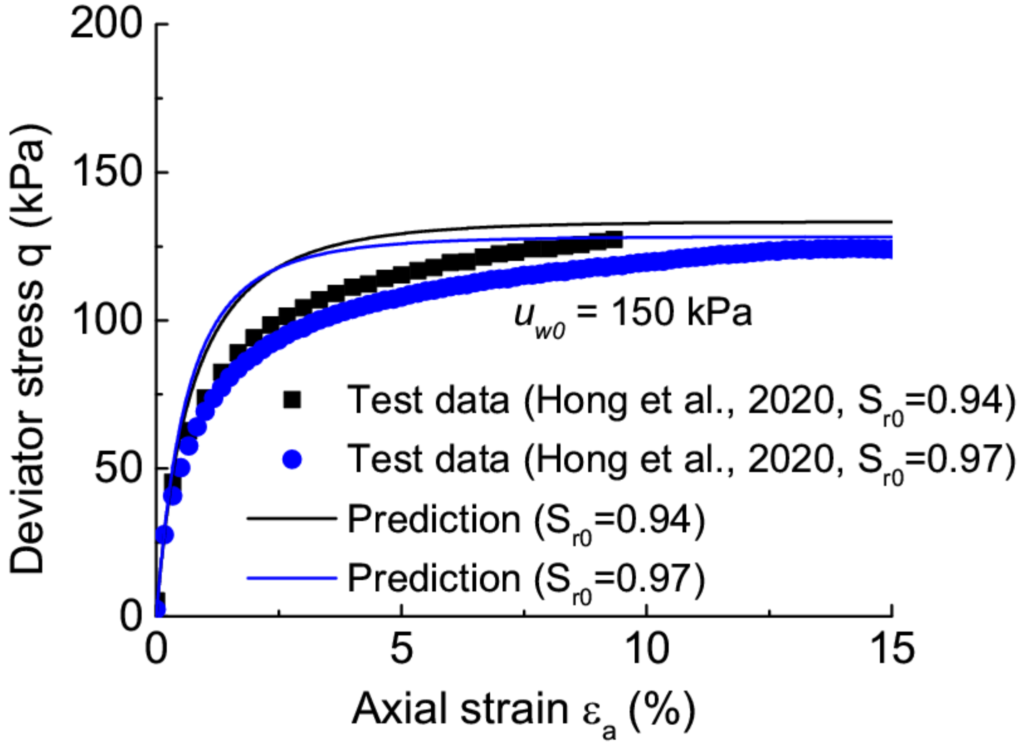
Deviator stress q (kPa)
200
150
100
50
0
0
5
10
15
Axial strain εa (%)
uw0 = 150 kPa
Test data (Hong et al., 2020, Sr0=0.94)
Test data (Hong et al., 2020, Sr0=0.97)
Prediction (Sr0=0.94)
Prediction (Sr0=0.97)

(a)

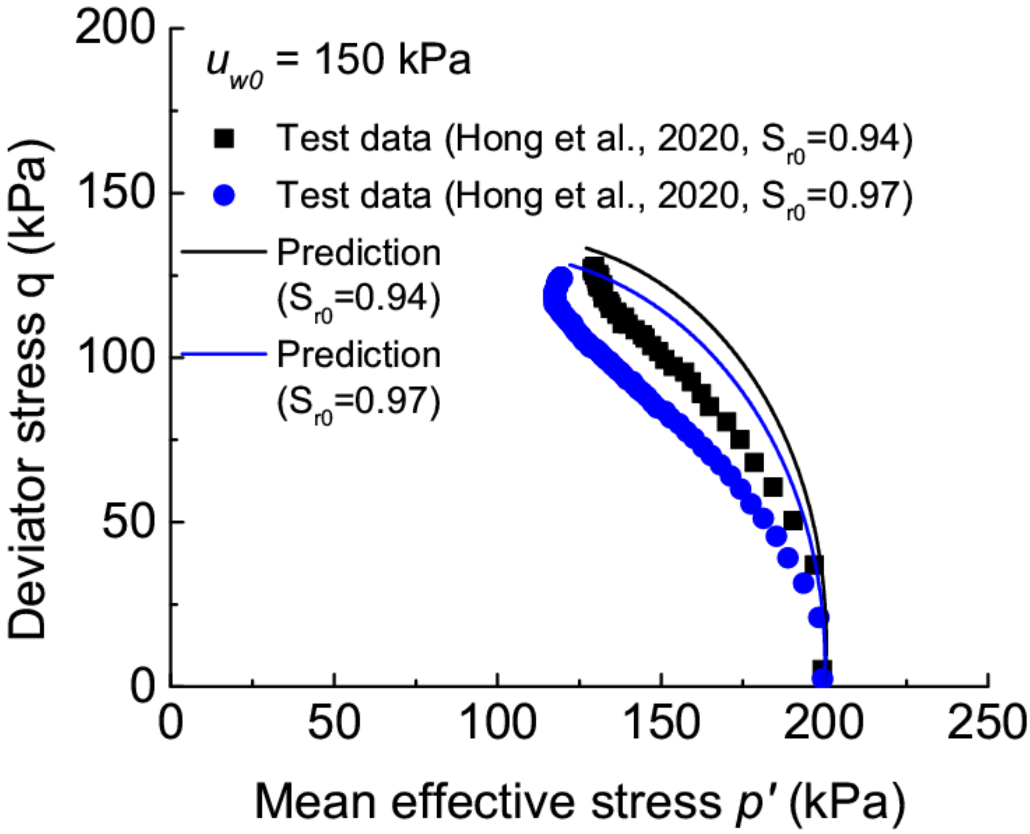
Deviator stress q (kPa)
200
150
100
50
0
0
50
100
150
200
250
Mean effective stress p′ (kPa)
uw0 = 150 kPa
Test data (Hong et al., 2020, Sr0=0.94)
Test data (Hong et al., 2020, Sr0=0.97)
Prediction (Sr0=0.94)
Prediction (Sr0=0.97)

(b)

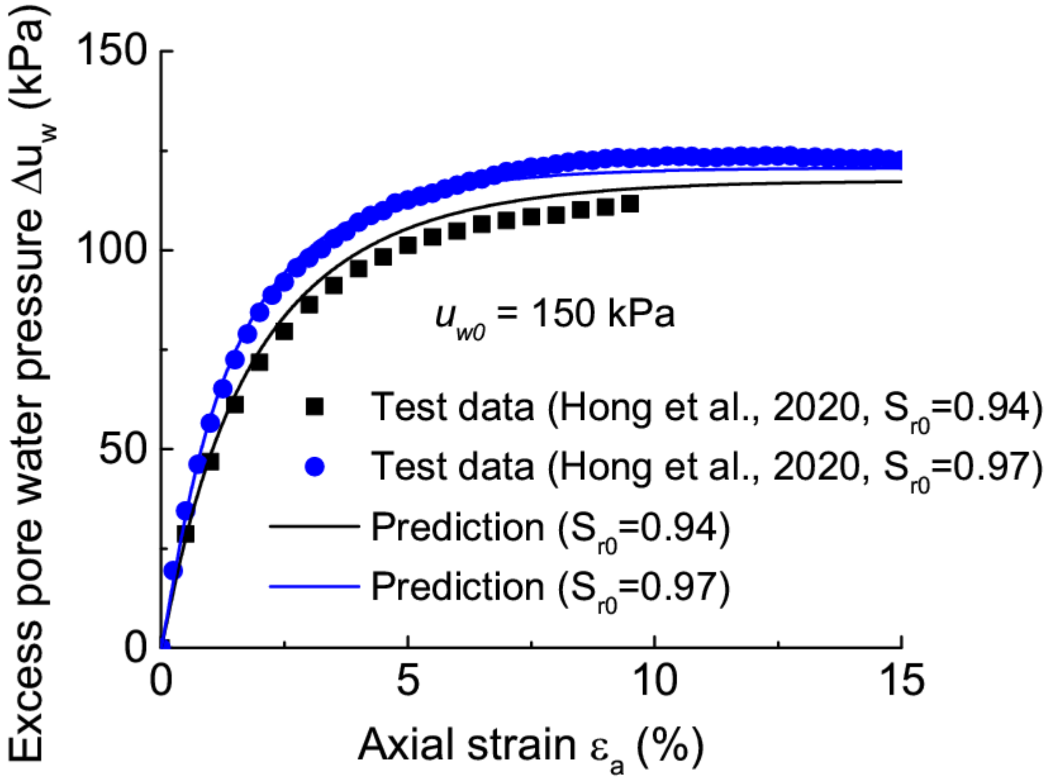

(c)

Fig. 4.9 Model prediction for the stress-strain relationship of gassy Malaysian kaolin (test data from Hong et al., 2020) with $p_0' = 200$ kPa and $u_{w0} = 150$ kPa: (a) the $\varepsilon_a - q$ relationship; (b) the effective stress path and (c) the evolution of excess pore water pressure

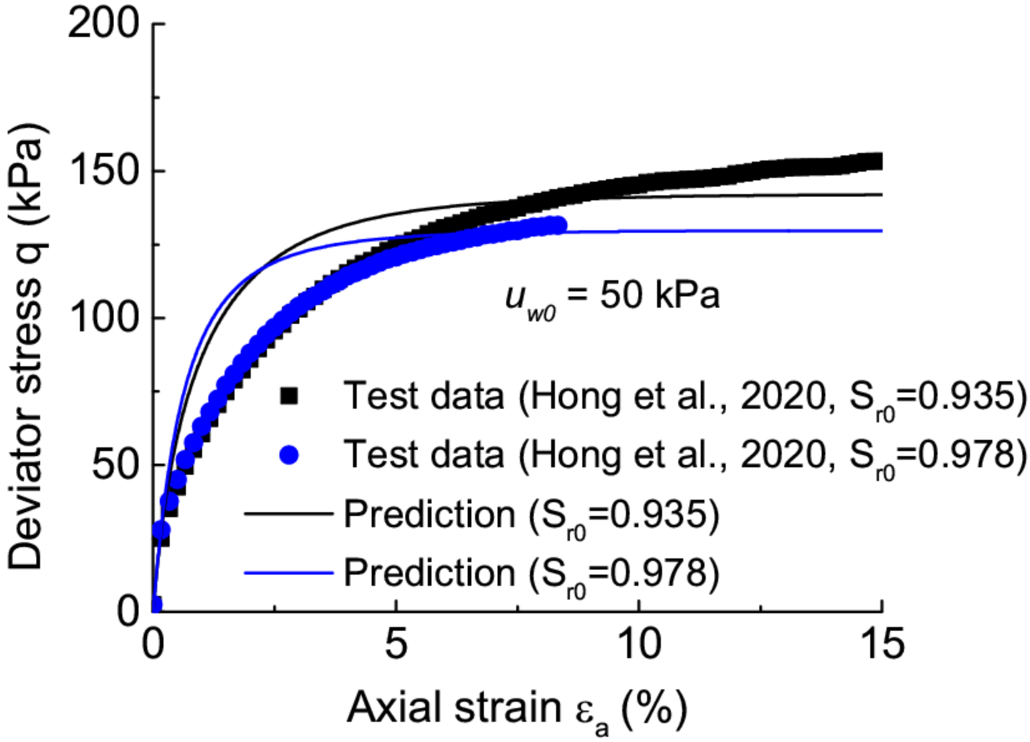
200
150
100
50
0
Deviator stress q (kPa)
0
5
10
15
Axial strain ε_a (%)
u_w0 = 50 kPa
Test data (Hong et al., 2020, S_r0=0.935)
Test data (Hong et al., 2020, S_r0=0.978)
Prediction (S_r0=0.935)
Prediction (S_r0=0.978)

(a)

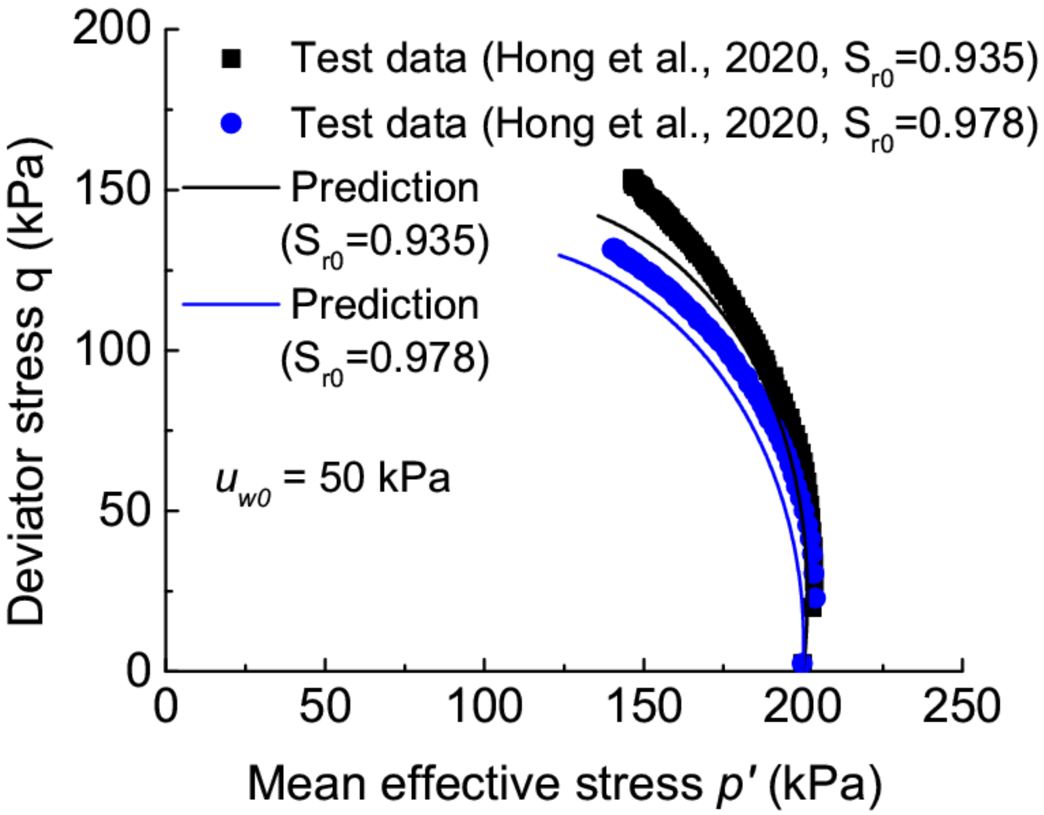
200
150
100
50
0
Deviator stress q (kPa)
0
50
100
150
200
250
Mean effective stress p′ (kPa)
Test data (Hong et al., 2020, S_r0=0.935)
Test data (Hong et al., 2020, S_r0=0.978)
Prediction (S_r0=0.935)
Prediction (S_r0=0.978)
u_w0 = 50 kPa

(b)

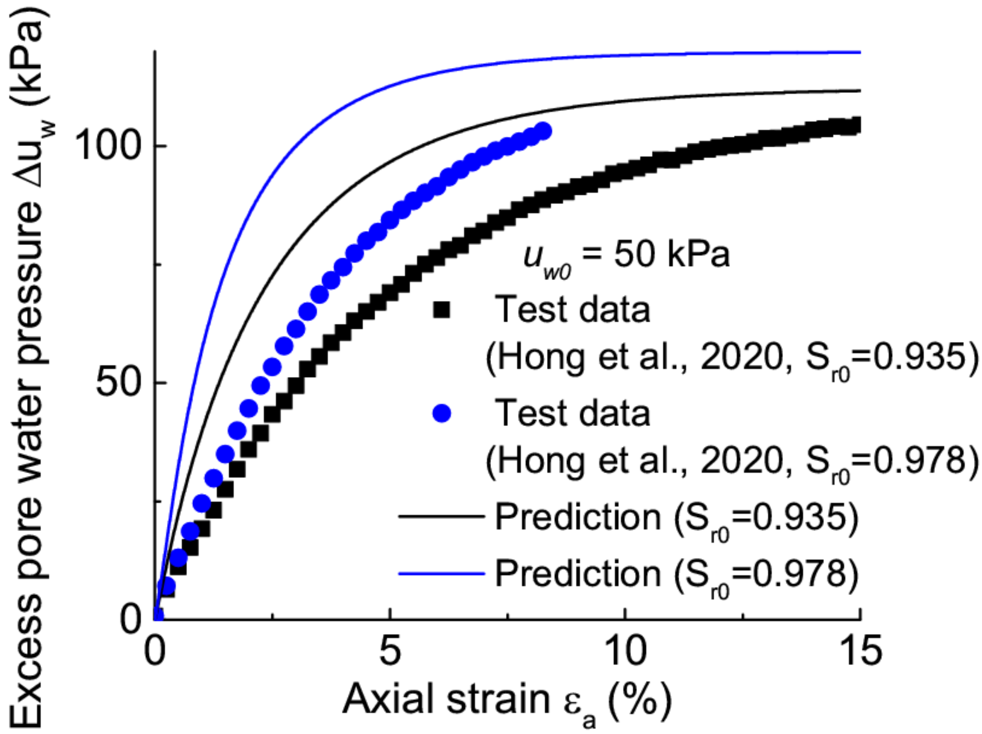

(c)

Fig. 4.10 Model prediction for the stress-strain relationship of gassy Malaysian kaolin (test data from Hong et al., 2020) with $p'_0 = 200$ kPa and $u_{w0} = 50$ kPa: (a) the $\varepsilon_a - q$ relationship; (b) the effective stress path and (c) the evolution of excess pore water pressure

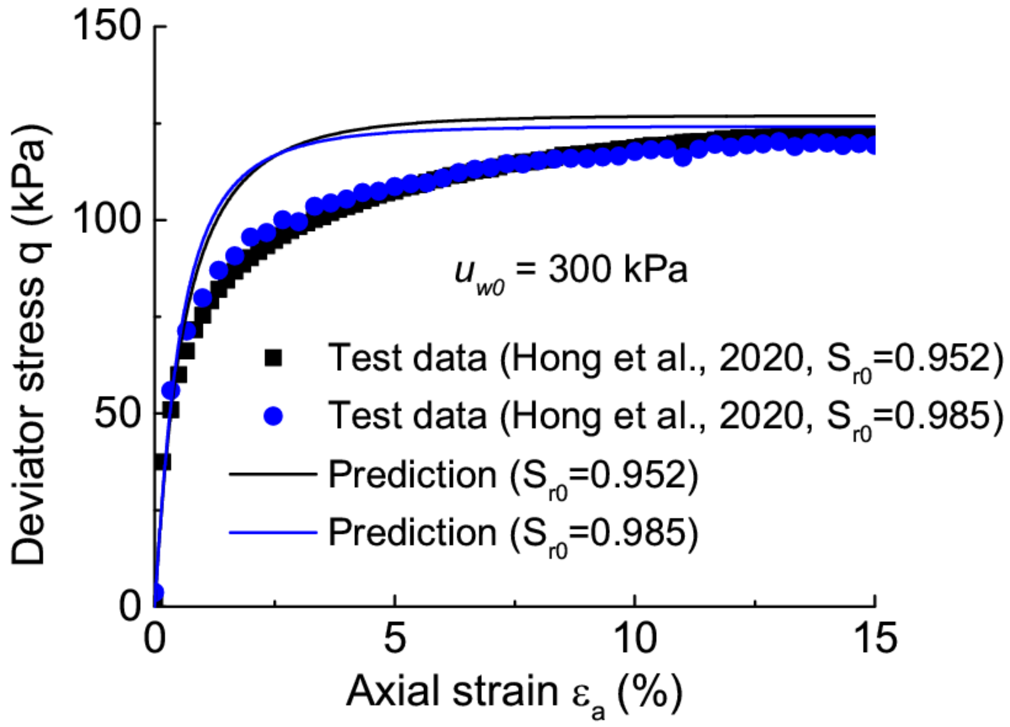

Deviator stress q (kPa)
Axial strain εa (%)
uw0 = 300 kPa
Test data (Hong et al., 2020, Sr0=0.952)
Test data (Hong et al., 2020, Sr0=0.985)
Prediction (Sr0=0.952)
Prediction (Sr0=0.985)
0
50
100
150
0
5
10
15

(a)

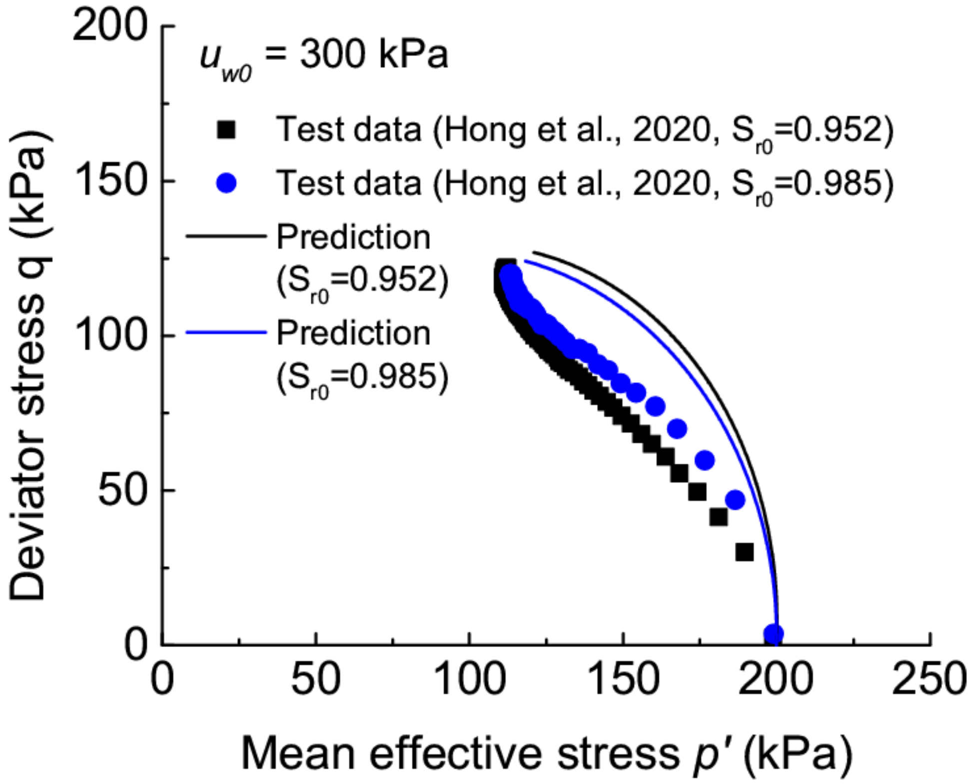

Deviator stress q (kPa)
Mean effective stress p′ (kPa)
uw0 = 300 kPa
Test data (Hong et al., 2020, Sr0=0.952)
Test data (Hong et al., 2020, Sr0=0.985)
Prediction (Sr0=0.952)
Prediction (Sr0=0.985)
0
50
100
150
200
250

(b)

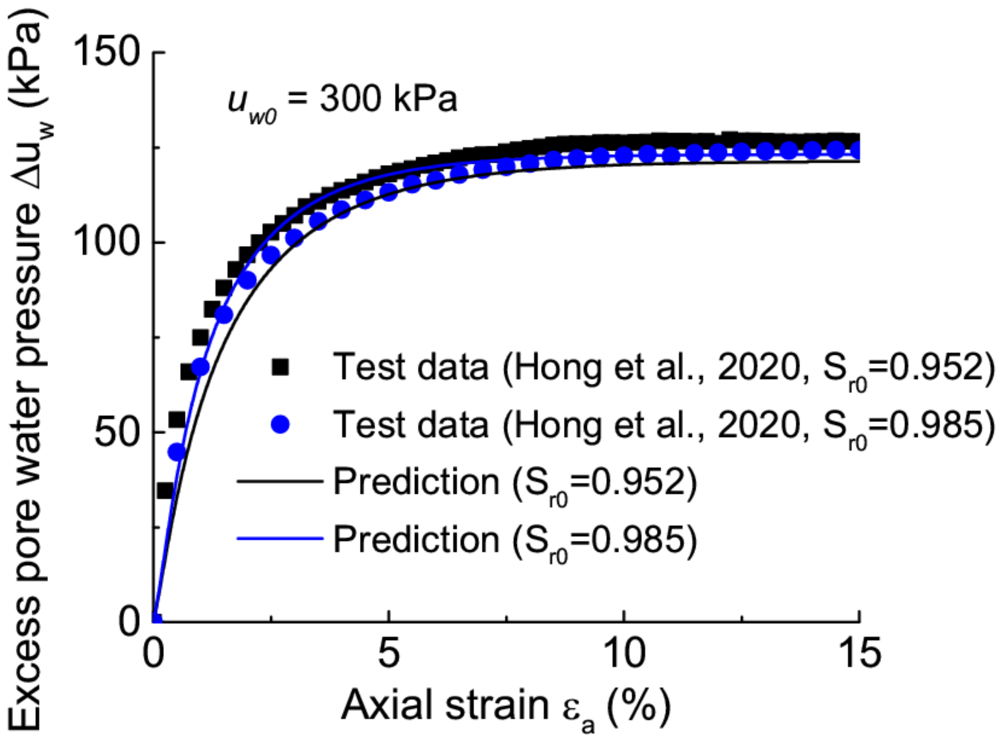

(c)

Fig. 4.11 Model prediction for the undrained shear behaviour of gassy Malaysian kaolin (test data from Hong et al., 2020) with $p'_0 = 200$ kPa and $u_{w0} = 300$ kPa: (a) the $\varepsilon_a - q$ relationship; (b) the effective stress path and (c) the evolution of excess pore water pressure

4.8 Comparison with the new bounds in Chapter 3

Figs. 4.12 and 4.13 show the comparison of the predicted undrained shear strength from the new bounds in Chapter 3 and the constitutive model in Chapter 4 with the test data from Sham (1989) and Hong et al. (2020). It is evident that the model prediction of Chapter 4 is within the two bounds. This shows that the hardening law and bubble flooding equation used in the model are reasonable and the state variable $\frac{u_w+p_a}{p'_0}$ is suitable for constitutive modelling of FGS.

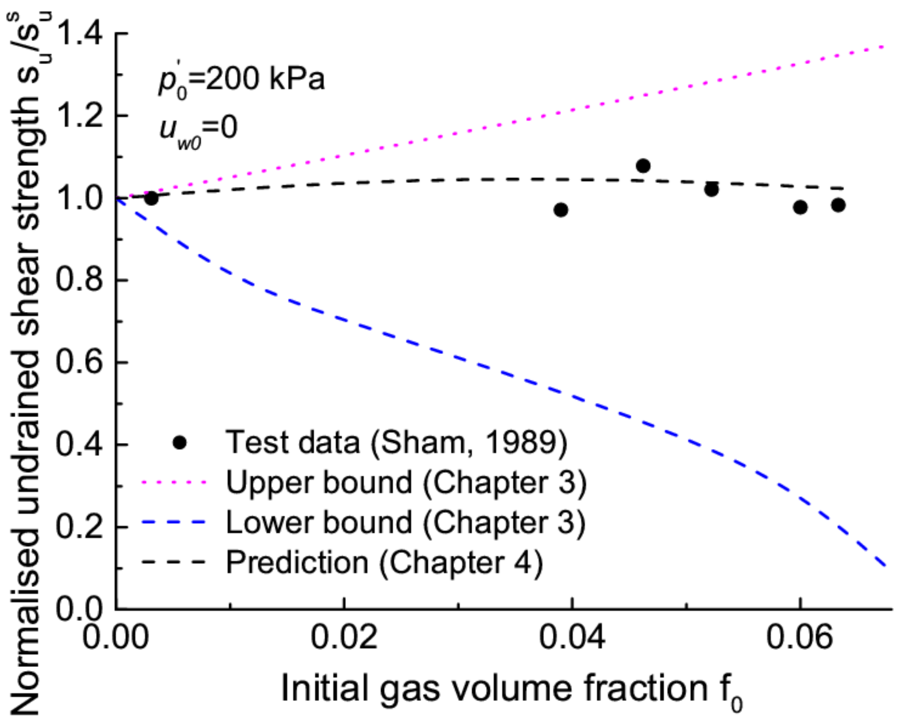
Normalised undrained shear strength s_u/s_u^s
p_0'=200 kPa
u_{w0}=0
Test data (Sham, 1989)
Upper bound (Chapter 3)
Lower bound (Chapter 3)
Prediction (Chapter 4)
Initial gas volume fraction f_0

(a)

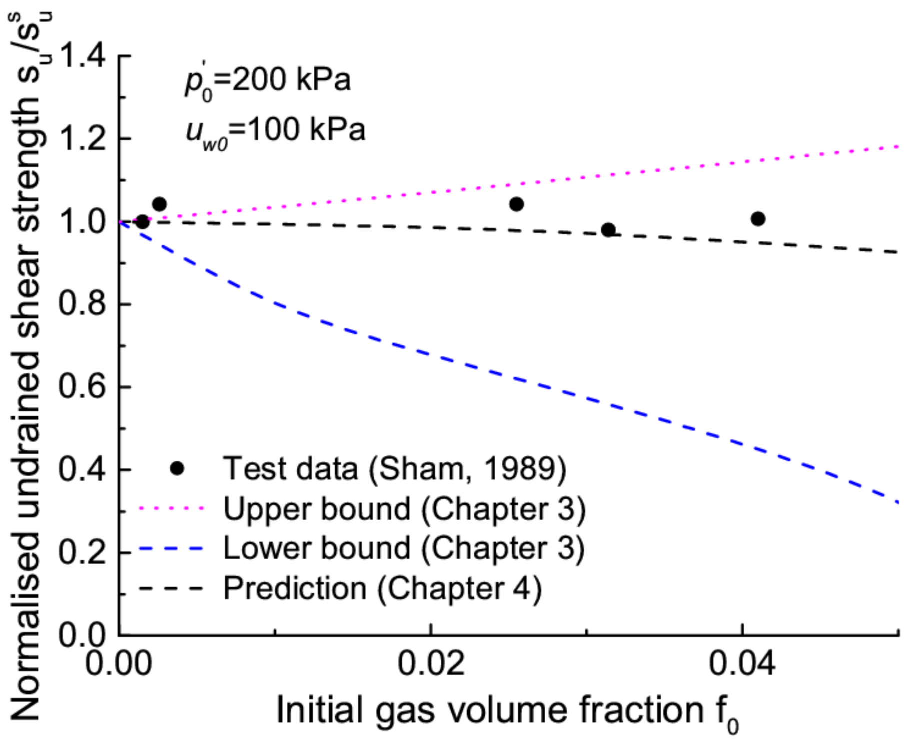
Normalised undrained shear strength s_u/s_u^s
p_0'=200 kPa
u_{w0}=100 kPa
Test data (Sham, 1989)
Upper bound (Chapter 3)
Lower bound (Chapter 3)
Prediction (Chapter 4)
Initial gas volume fraction f_0

(b)

Fig. 4.12 The comparison of predictions between the models in Chapter 3 and Chapter 4 with test data from Sham (1989) with (a) $p_0' = 200$ kPa, $u_{w0} = 0$ and (b) $p_0' = 200$ kPa, $u_{w0} = 100$ kPa

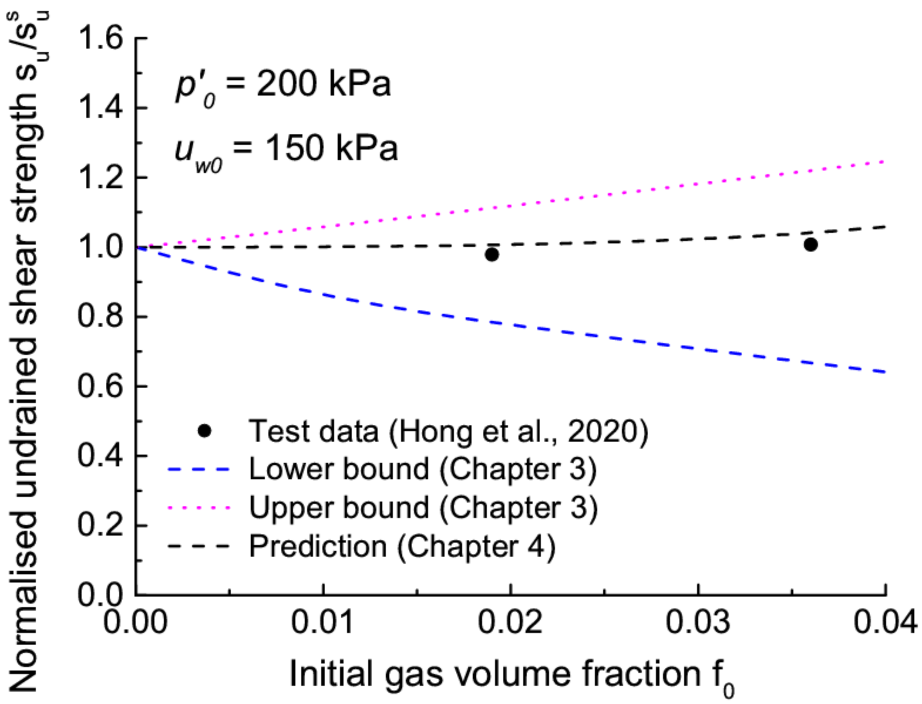

(a)

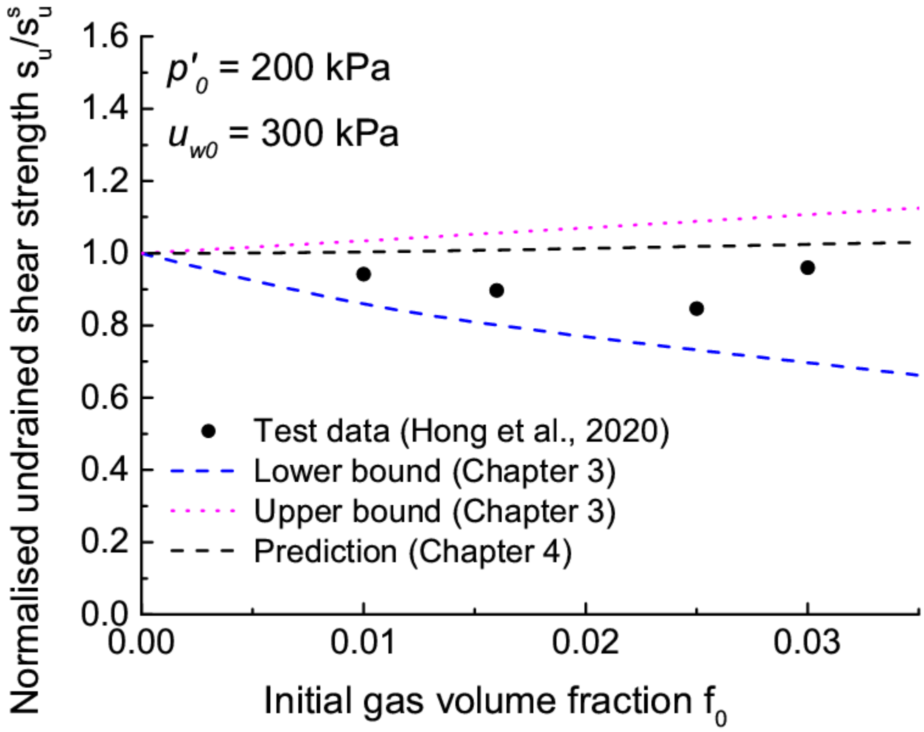

(b)

Fig. 4.13 The comparison of predictions between the models in Chapter 3 and Chapter 4 with test data from Hong et al. (2020) with (a) $p'_0 = 200$ kPa, $u_{w0} = 150$ kPa and (b) $p'_0 = 200$ kPa, $u_{w0} = 300$ kPa

Chapter 5: A bounding surface constitutive model of overconsolidated fine-grained soils containing gas bubbles

This chapter has been submitted to 9th International SUT OSIG Conference "Innovative Geotechnologies for Energy Transition:

Cai H.J., Gao Z.W., Hong .Y, Zhang J.F., Lu D.C. (2023). "Constitutive Modelling of Overconsolidated gassy clay." 9th International SUT OSIG Conference "Innovative Geotechnologies for Energy Transition", London, UK,12-14 September 2023 (under review).

This work has been done through collaboration among University of Glasgow, Zhejiang University and Beijing University of Technology. Mr Cai has made key contributions to the model formulations, validation and manuscript writing, with the supervision of Dr Gao. Some test data on gassy clay was provided by Dr Hong and Mr. Zhang at Zhejiang University. Prof. Lu has contributed to the development the ideas and writing.

5.1 Introduction

The main objective of this chapter is to investigate the mechanical behaviour of overconsolidated FGS and develop a new constitutive model. The constitutive model has been proposed based on the composite material method developed in Chapter 4. The constitutive model for overconsolidated clay proposed by Gao et al. (2017) will be used to describe the response of saturated soil matrix. Undrained triaxial compression tests have been carried out on gassy Malaysian Kaolin by Dr. Yi Hong at Zhejiang University (Hong et al., 2020). The model will be validated by the test data on Malaysian Kaolin (Hong et al., 2020) and Speciwhite Kaolin clay (Sham, 1989).

5.2 Undrained triaxial compression tests on Malaysian Kaolin

A series of undrained triaxial tests have been carried out on reconstituted gassy Malaysian kaolin by Dr. Yi Hong at Zhejiang University. As summarized in Table 5.2, there are three groups of tests. Some of the typical test results are shown in Chapter 2 (Figs. 2.9-2.10), where the initial degree of saturation S_{r0} is the value at the end of isotropic consolidation for normally consolidated FGS or isotropic unloading for overconsolidated FGS.

Table 5.1 Index properties of Malaysian Kaolin silt

Index properties	value
Plasticity index	27
Plastic limit ω_P(%)	38
Liquid limit ω_L(%)	65
Grain size distribution	
Percentage of clay (%)	64.9
Percentage of silt (%)	35.1
Percentage of sand (%)	0

Table 5.2 Programme of test

	Test Group	1						2						3					
	Test number	1-a	1-b	1-c	1-d	1-e	1-f	2-a	2-b	2-c	2-d	2-e	2-f	3-a	3-b	3-c	3-d	3-e	3-f
	u_{w0} (kPa)	0						600						300					
After consolidation	S_r (%)	94.1	93.5	94.2	93.8	94.5	94.0	95.9	96.2	95.7	96.0	96.5	96.1	100					
	f (%)	3.6	3.9	3.5	3.7	3.3	3.6	2.5	2.3	2.6	2.4	2.1	2.3	0					
After unloading	S_r (%)	94.2	93.6	94.2	93.8	94.5	94.0	96.0	96.2	95.7	96.0	96.5	96.1	100					
	OCR	1.67	1.43	1.25	1.18	1.11	1.05	1.67	1.43	1.25	1.18	1.11	1.05	1.67	1.43	1.25	1.18	1.11	1.05

5.3 Constitutive model for overconsolidated soils containing gas bubbles

5.3.1 The stress and strain quantities for the model

The constitutive model in Chapter 4 is based on the MCC model, which gives purely elastic response when the stress state is within the yield surface. But experimental evidence shows that overconsolidated clay always shows elastoplastic response. Therefore, the bounding surface or sub-loading surface concepts have been proposed to model the elastoplastic behaviour of overconsolidated soils (Hashiguchi, 1980; Dafalias et al., 1986). In this chapter, the bounding surface model for overconsolidated clay developed by Gao et al. (2017) will be used. This model employs a bounding surface that is first proposed by Collins (2005) based on the thermodynamics. A new dilatancy relationship for overconsolidated clay is employed. Fig. 5.1 shows the bounding surface used in this model. In this figure, p and q represent the current stress state and $\bar{p}$ and $\bar{q}$ represent the 'image' stress state. The variable r is used to describe the degree of overconsolidation, which evolves during the loading process. At the initial state, $r = 1/OCR$ and it becomes 1 at the critical state. It is shown that this model gives good prediction of overconsolidated FGS.

In addition, the model in Chapter 4 predicts no detrimental effect of gas bubbles on soil strength when the soil behaviour is elastic. As a result, it gives unrealistic prediction of the effective stress path for OC gassy clay (Fig.5.2). The effective stress path shows increasing p before yielding due to bubble flooding. There is no damaging effect of gas bubbles on the soil response because there is no plastic deformation. Therefore, it is desirable to have a bounding surface model that can describe the plastic deformation before yielding, which is the main objective of this chapter.

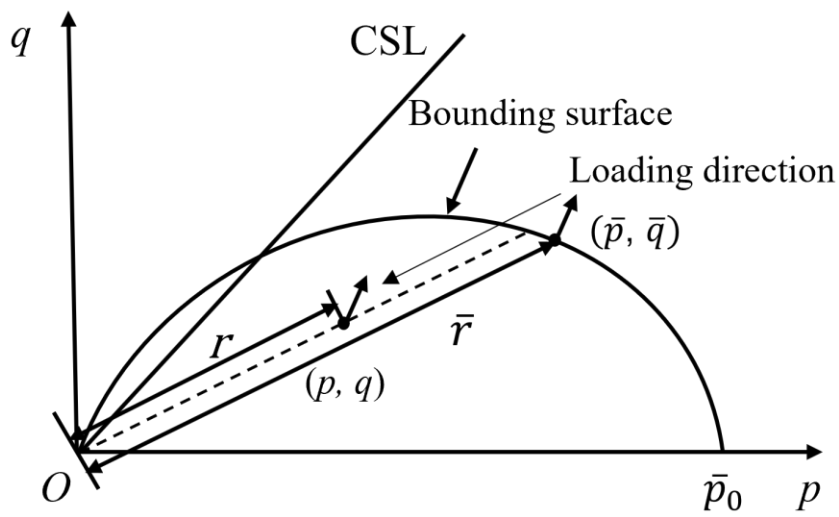

Fig. 5.1 The mapping rule of the model on $p-q$ plane

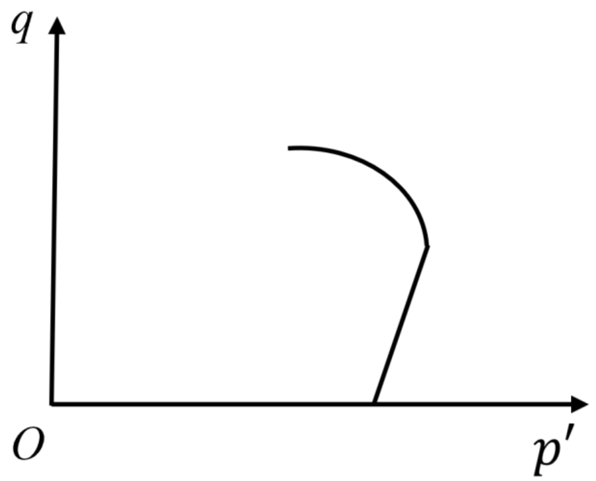

Fig. 5.2 The stress path of prediction by model in Chapter 4 (no plastic deformation and bubble flooding occurs before yielding)

5.3.2 Constitutive relationship for the saturated soil matrix

The bounding surface model with state-dependent dilatancy for overconsolidated clay is used for the saturated soil matrix. The bounding surface is expressed as (Collins, 2005)

$$\bar{F} = \frac{(\bar{p}\prime - \alpha\bar{p}_0/2)^2}{[(1-\alpha)\bar{p}\prime + \alpha\bar{p}_0/2]^2} + \frac{\bar{q}^2}{M_c^2[(1-\alpha)\bar{p}\prime + \alpha\bar{p}_0/2]^2} - 1 = 0 \quad (5.1)$$

where $\bar{p}_0$ is the size of the current yield surface, α is a model parameter and M_c is the critical state stress ratio in triaxial compression. Note that the bounding surface should be expressed in terms of p'_m and q_m, but they are replaced by p' and q according to Eqs. (4.2) and (4.3). The mapping centre for the bounding surface is the origin of the stress space. The following hardening law is employed for modelling the evolution of $\bar{p}_0$:

$$d\bar{p}_0 = \langle L \rangle r_{\bar{p}_0} = \langle L \rangle \frac{(1+e_0)\bar{p}_0}{\lambda-\kappa} \frac{\partial F}{\partial \bar{q}} \frac{M_c^2 - \bar{\eta}^2}{2\bar{\eta}} (1-x) \quad (5.2)$$

where

$$x = \gamma f \frac{1-(1+\bar{\eta}/M_c)^{-20}}{1+\exp\left(-\frac{u_w+p_a}{\bar{p}_0}\right)} \quad (5.3)$$

where L is the loading index, $\langle\ \rangle$ are the McCauley brackets which make $\langle L \rangle = L$ for $L > 0$ and $\langle L \rangle = 0$ otherwise, e_0 is the initial value of the matrix void ratio e_m (Wheeler, 1986), $\bar{\eta}$ $(= \bar{q}/\bar{p}')$ is the stress ratio for the 'image' stress state, p_a is the atmospheric pressure (101 kPa), λ is the compression index, κ is the swelling index and γ is a new model parameter. The term x is used to describe the effect of gas cavities on plastic hardening of the soil. Higher x indicates more detrimental effect of gas bubbles on plastic hardening and shear strength. $x = 0$ when there is no cavity with $f = 0$. Existing experimental evidence shows that the gas bubbles merely influence the plastic hardening of saturated soil matrix in isotropic consolidation, and therefore, the term $(1+\bar{\eta}/M_c)^{-20}$ is introduced to make $x = 0$ at $\bar{\eta} = 0$ (Thomas, 1987; Wheeler, 1986; Hong et al., 2020). Note that $(1+\bar{\eta}/M_c)^{-20} = 0$ where x (no detrimental effect on hardening) approximately equal to 1 when $\bar{\eta} > 0$ (detremiental effected is activated). When the FGS is subjected to shear (e.g., triaxial compression), the detrimental effect of gas bubbles on plastic hardening is higher as $\frac{u_w+p_a}{\bar{p}_0}$ increases, but such detrimental effect is limited (Wheeler, 1988; Hong et al., 2020; Gao et al., 2021). Therefore, the term $1+\exp\left(-\frac{u_w+p_a}{\bar{p}_0}\right)$ is used to make x increase with $\frac{u_w+p_a}{\bar{p}_0}$ and reach the maximum value of 1 when $\frac{u_w+p_a}{\bar{p}_0}$ is big enough.The plastic modulus for the bounding surface is thus expressed as

$$\bar{K}_p = -\frac{\partial F}{\partial \bar{p}_0} r_{\bar{p}_0} = -\frac{\partial F}{\partial \bar{p}_0}\frac{(1+e_0)\bar{p}_0}{\lambda-\kappa}\frac{\partial F}{\partial \bar{q}}\frac{M_c^2-\bar{\eta}^2}{2\bar{\eta}}(1-x) \tag{5.4}$$

Following Gao et al. (2017), the plastic modulus for the current stress state is

$$K_p = -\frac{\partial F}{\partial \bar{p}_0}\frac{(1+e_0)\bar{p}_0}{\lambda-\kappa}\frac{\partial F}{\partial \bar{q}}\frac{M_v^2-\bar{\eta}^2}{2\bar{\eta}}(1-x) \tag{5.5}$$

$$M_v = M_c R^{-n} \tag{5.6}$$

where R is the ratio of the 'image' and current stress state (Gao et al., 2017). M_v is used to model the effect of overconsolidation on the peak shear strength of saturated clay.

The following plastic flow rule is expressed as below is employed

$$d\varepsilon_q^{mp} = \langle L\rangle\frac{\partial \bar{F}}{\partial \bar{q}} \tag{5.7}$$

$$d\varepsilon_v^{mp} = \langle L\rangle\frac{\partial \bar{F}}{\partial \bar{q}} D \tag{5.8}$$

where $d\varepsilon_v^{mp}$ and $d\varepsilon_q^{mp}$ denote the plastic volumetric and shear strain increment for the saturated soil matrix, respectively, D is the dilatancy equation

$$D = \frac{M_d^2-\eta^2}{2\eta} \tag{5.9}$$

$$M_d = M_c R^m \tag{5.10}$$

where m is a model parameter.

The elastic stress-strain relationship is the same as that of the modified Cam-clay (MCC) model, with the elastic bulk modulus K_m and shear modulus G_m for the saturated matrix being expressed in Chapter 4.

$$d\varepsilon_v^{me} = \frac{dp\prime}{K_m} \quad \text{with} \quad K_m = \frac{1+e_m}{\kappa}p' \tag{5.11}$$

$$d\varepsilon_q^{me} = \frac{dq}{3G_m} \quad \text{with} \quad G_m = K_m\frac{3(1-2\nu)}{2(1+\nu)} \tag{5.12}$$

where $d\varepsilon_v^{me}$ is the elastic volumetric strain increment of the saturated soil matrix,

$d\varepsilon_q^{me}$ is the elastic shear strain increment, κ is the swelling index and ν is the Poisson's ratio.

5.3.3 Bubble flooding and cavity volume change

The formulations for modelling the volume change due to bubble flooding $d\varepsilon_v^f$ are the same as the formulations in Chapter 4 (Eq. (4.17) and Eq. (4.18)). The volumetric strain increment of the cavity $d\varepsilon_v^c$ is assumed to be affected by dp' ,and it is shown in Eq. (4.19). The total gas volume change is assumed to be the summation of cavity volume change and bubble flooding

$$dV_g = dV_c + dV_f = V_c d\varepsilon_v^c + V_m d\varepsilon_v^f \tag{5.13}$$

Eq. (4.13) can be used to calculate the evolution of u_g based on Boyle's law. Since u_g is not used in the constitutive equations, and its evolution is not given here. But V_g is updated in each loading step as it has effect on f, which is required in the model. The detailed derivation of the constitutive equations is given as follows.

Since $d\varepsilon_v^m = d\varepsilon_v^{me} + d\varepsilon_v^{mp} = \frac{dp\prime}{K_m} + \langle L\rangle \frac{\partial F}{\partial \bar{q}} D$, The increment of volumetric strain can be rewritten as

$$d\varepsilon_v = (1-f)\left(\frac{dp\prime}{K_m} + \langle L\rangle \frac{\partial F}{\partial \bar{q}} D\right) + fBdp' \tag{5.14}$$

The expression of dp' can be obtained based on Eq. (5.14) as below

$$dp' = \frac{d\varepsilon_v - (1-f)\langle L\rangle \frac{\partial F}{\partial \bar{q}} D}{\frac{1-f}{K_m} + fB} = \frac{d\varepsilon_v}{X} - \langle L\rangle \frac{1-f}{X} \frac{\partial F}{\partial \bar{q}} D \tag{5.15}$$

where X represents the denominator of Eq. (5.15). Based on the bounding surface theory, one has

$$\frac{\partial F}{\partial \bar{p}\prime} dp' + \frac{\partial F}{\partial \bar{q}} dq - \langle L\rangle K_p = 0 \tag{5.16}$$

Combining equations (5.15), (5.16), one can get

$$\frac{\partial F}{\partial \bar{p}\prime}\left[\frac{d\varepsilon_v}{X} - \langle L\rangle \frac{1-f}{X} \frac{\partial F}{\partial \bar{q}} D\right] + 3G_m \frac{\partial F}{\partial \bar{q}}\left[d\varepsilon_q - \langle L\rangle \frac{\partial F}{\partial \bar{q}}\right] - \langle L\rangle K_p = 0 \tag{5.17}$$

The loading index L can then be determined using Eq. (5.17)

$$L = \frac{\frac{1}{X}\frac{\partial F}{\partial \bar{p}'}d\varepsilon_v + 3G_m\frac{\partial F}{\partial \bar{q}}d\varepsilon_q}{K_p + \frac{1-f}{X}\frac{\partial F}{\partial \bar{p}'}\frac{\partial F}{\partial \bar{q}}D + 3G_m\left(\frac{\partial F}{\partial \bar{q}}\right)^2} = \Lambda_p d\varepsilon_v + \Lambda_q d\varepsilon_q \tag{5.18}$$

The expression of dp' in terms of $d\varepsilon_v$ and $d\varepsilon_q$ can be obtained using Eqs. (5.16) and (5.18)

$$dp' = C_{pp}d\varepsilon_v + C_{pq}d\varepsilon_q \tag{5.19}$$

where

$$C_{pp} = \frac{1}{X} - h(L)\Lambda_p\frac{1-f}{X}\frac{\partial F}{\partial \bar{q}}D \tag{5.20}$$

$$C_{pq} = -h(L)\Lambda_q\frac{1-f}{X}\frac{\partial F}{\partial \bar{q}}D \tag{5.21}$$

where $h(L)$ is the Heaviside function with $\mathrm{h(L)} = 1$ when $\mathrm{L} > 0$ and $\mathrm{h(L)} = 0$ otherwise. The increment of the deviator stress dq is

$$dq = 3G_m\left(d\varepsilon_q - d\varepsilon_q^{mp}\right) = 3G_m\left(d\varepsilon_q - \langle L\rangle\frac{\partial F}{\partial \bar{q}}\right) = C_{qp}d\varepsilon_v + C_{qq}d\varepsilon_q \tag{5.22}$$

where

$$C_{qp} = -h(L)3G_m\Lambda_p\frac{\partial F}{\partial \bar{q}} \tag{5.23}$$

$$C_{qq} = 3G_m - h(L)3G_m\Lambda_q\frac{\partial F}{\partial \bar{q}} \tag{5.24}$$

Combining Eqs. (4.8), (4.12), (4.14) and (5.19), the following equation can be got

$$d\varepsilon_v = (1-f)(d\varepsilon_v^b + Adu_w) + fB\left(C_{pp}d\varepsilon_v + C_{pq}d\varepsilon_q\right) \tag{5.25}$$

Eq. (5.25) can then be used to get the expression for du_w

$$du_w = C_{wp}d\varepsilon_v + C_{wq}d\varepsilon_q + C_{wb}d\varepsilon_v^b \tag{5.26}$$

where

$$C_{wp} = \frac{1-fBC_{pp}}{(1-f)A} \tag{5.27}$$

$$C_{wq} = -\frac{fBC_{pq}}{(1-f)A} \tag{5.28}$$

$$C_{wb} = -\frac{1}{A} \tag{5.29}$$

The constitutive equation can be written in a matrix form as below

$$\begin{bmatrix} dp' \\ dq \\ du_w \end{bmatrix} = \begin{bmatrix} C_{pp} & C_{pq} & 0 \\ C_{qp} & C_{qq} & 0 \\ C_{wp} & C_{wq} & C_{wb} \end{bmatrix} \begin{bmatrix} d\varepsilon_v \\ d\varepsilon_q \\ d\varepsilon_v^b \end{bmatrix} \tag{5.30}$$

Note that in a globally undrained test, $d\varepsilon_v^b = 0$. A code base on the MCC model is used for the model implementation. The same framework and calculation procedure as Chapter 4 is used.

In a globally undrained test, $d\varepsilon_v^b = 0$ and a fixed $d\varepsilon_q$ (about 1e-5 is given in the model implementation) du_w can then be calculated based on the total stress path with $dq = 3(dp' + du_w)$. Once du_w is obtained, dp' and dq can be calculated using Equation (4.36). $d\varepsilon_v^c$ can then be calculated using Equation (4.19). The code for this model is provided in the Appendix II.

5.4 Model validation

The tests data on gassy Malaysian Kaolin (Hong et al., 2020) and Speciwhite Kaolin clay reported in Sham (1989) is used for the model validation. The model parameters for the two FGS which can be obtained in the literature are shown in Table 5.3.

All the MCC parameters for Malaysian Kaolin silt are determined using the test results in Fig. 5.4 on the saturated soil. The parameters M_c, λ and N are directly obtained from Hong (2020). $\nu = 0.25$ is assumed as it has negligible influence on the model prediction. κ is determined based on the undrained shear strength of saturated soil. The parameters m, n and γ are determined based on the test results for saturated fine-grained soil (Fig. 5.3). Finally, α is determined using the data for FGS with $p_c' =$ 200 kPa, $u_{w0} = 150$ and $S_{r0} = 0.94$ in normally consolidated conditions (Fig. 5.1) with Eq. (5.31).

$$\frac{p_f}{p_i} = (OCR \times \frac{\alpha}{2})^{(\frac{\lambda-\kappa}{\lambda})} \tag{5.31}$$

where p_f is the mean effective stress at failure and p_i is initial mean effective stress. The relationship between p_f and p_i can be derived based on Fig. 5.3.

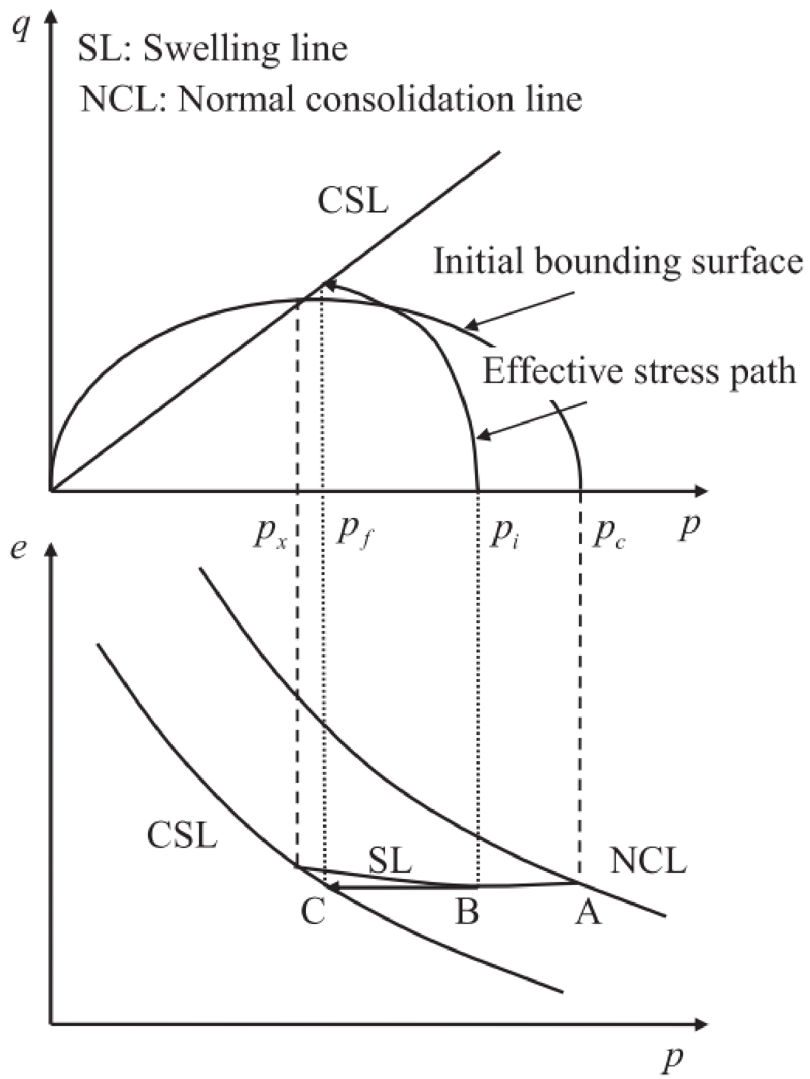

Fig. 5.3 Relationship between p_f and p_i in undrained triaxial compression test (Gao et al., 2017)

Parameters m and n can be determined based on the test results on overconsolidated FGS. It is found that the parameter m has no significant influence on the prediction. Thus, parameter n can be determined by setting $m = 0$ at first. Then m can be determined to fit the test results better.

The model predictions for the undrained triaxial compression tests are shown in Figs. 5.4 to 5.6. The dots and lines represent the test data and model predictions, respectively. Different degree of saturation and OCR are considered in the tests, which includes the effective stress path and shear stress-strain relationship. It is evident that the model can give reasonable prediction of the effective stress path and undrained shear strength. But there is discrepancy in the shear stress-strain relationship when the axial strain is less than 2% and the undrained shear strength for tests with $S_{r0} = 0.96$ (Fig. 5.5). The model gives lower stiffness than the test data. This could be due to that the model does not consider the small-strain stiffness of FGS. The overprediction of the undrained shear strength for the for tests with $S_{r0} = 0.96$ can be improved by using a modified formulation for the term x in the hardening law. But this may require more model parameters.

The validation of gassy kaolin clay with $p_c' = 200$ kPa, $u_{w0} = 100$ kPa and OCR=1 has been shown in Fig. 5.7. It is the only set of data which includes the stress-strain relationship and effective stress path. Fig. 5.8 shows the validation of normalised undrained shear strength on Kaolin (Sham, 1989) with $p_c' = 200$ kPa, $u_{w0} = 300$ and OCR =2. The parameters for the saturated clay are determined based on the test results in Sham (1989). The parameter γ is determined on the undrained shear strength data for unsaturated FGS (Fig. 5.7). All the parameters are listed in Table 5.3. The model prediction is in good agreement with the test data.

Table 5.3 Model parameters for Chapter 5

soil	Malaysian kaolin silt (Hong et al., 2020)	Kaolin clay (Sham, 1989)
M_c	1.04	0.87
λ	0.14	0.23
κ	0.05	0.014
N	3.81	3.35
ν	0.25	0.2
α	1.0	1.0
m	2.0	0.1
n	0.6	0.5
γ	30	46

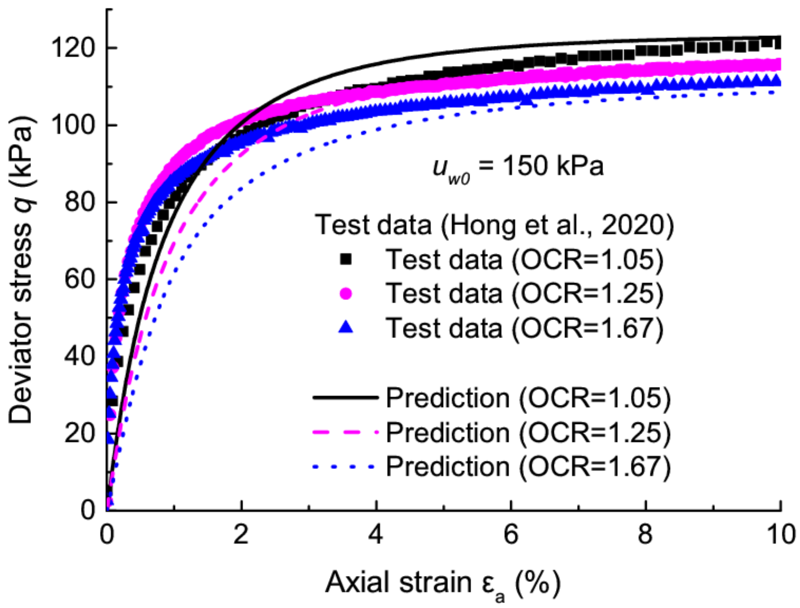

(a)

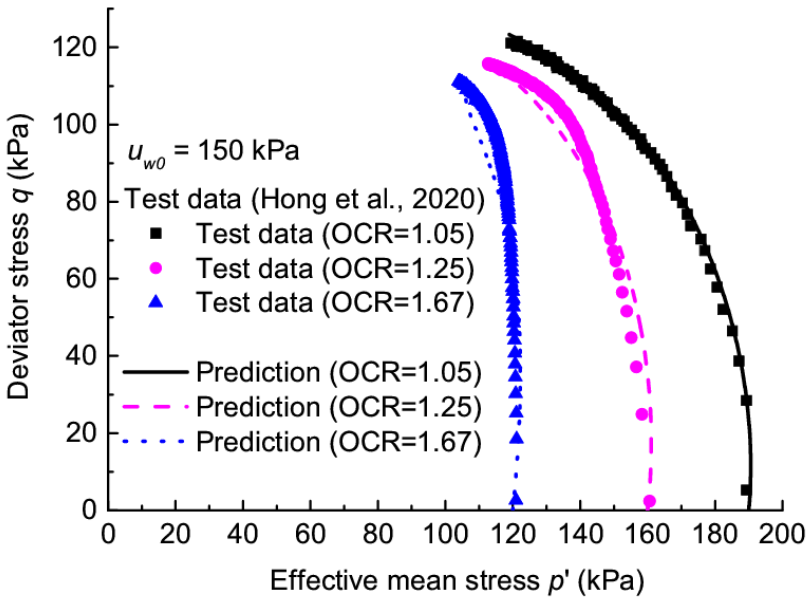

(b)

Fig. 5.4 Model prediction for the stress-strain relationship of gassy Malaysian Kaolin (test data from Hong et al., 2020) with $p_c' = 200$ kPa, $u_{w0} = 150$ kPa, $S_{r0} = 0.94$ and different OCR: (a) the $\varepsilon_a - q$ relationship; (b) the effective stress path

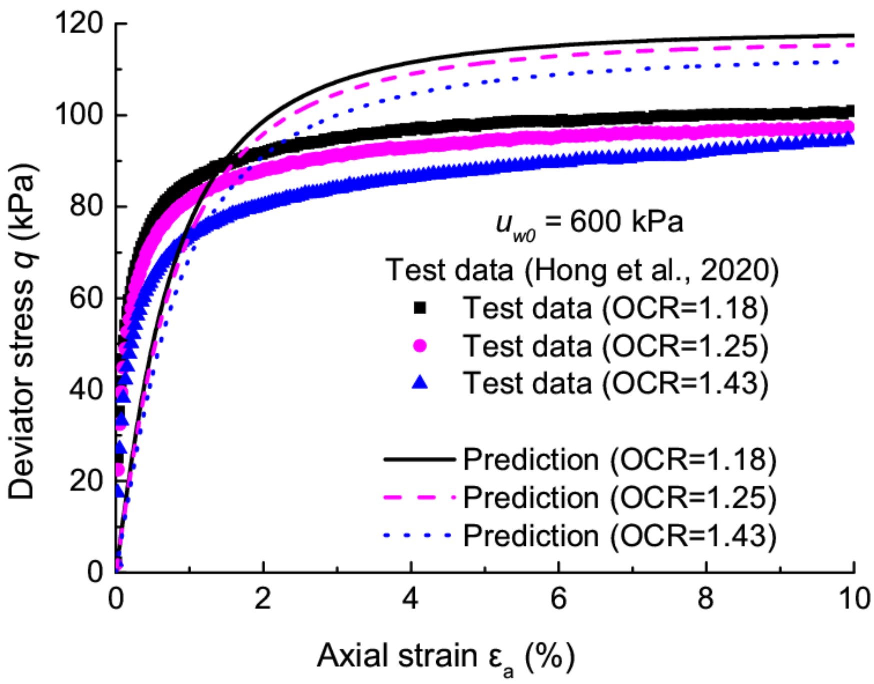

(a)

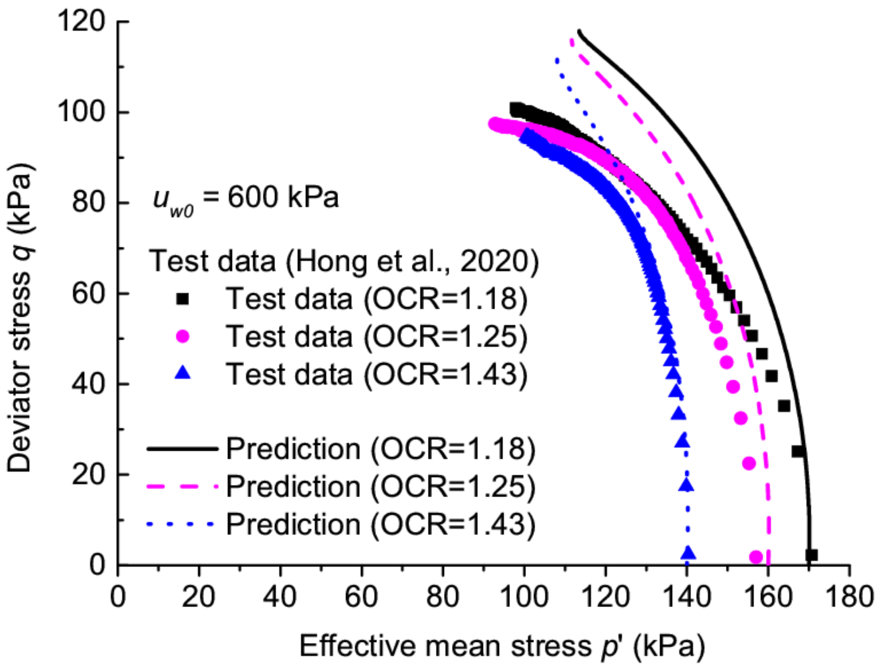

(b)

Fig. 5.5 Model prediction for the stress-strain relationship of gassy Malaysian Kaolin (test data from Hong et al., 2020) with $p_c' = 200$ kPa, $u_{w0} = 600$ kPa, $S_{r0} = 0.96$ and different OCR: (a) the $\varepsilon_a - q$ relationship; (b) the effective stress path

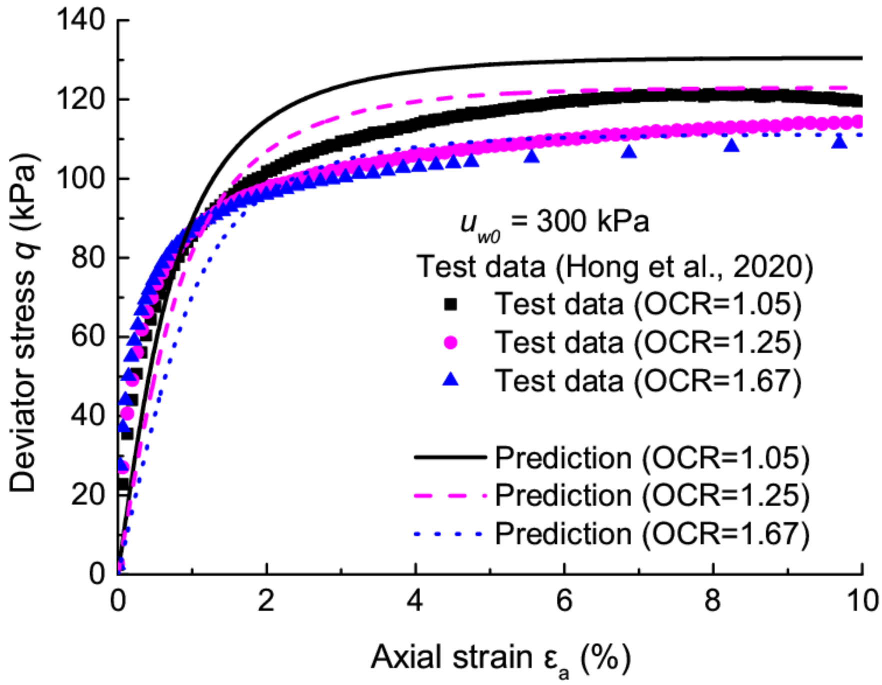

(a)

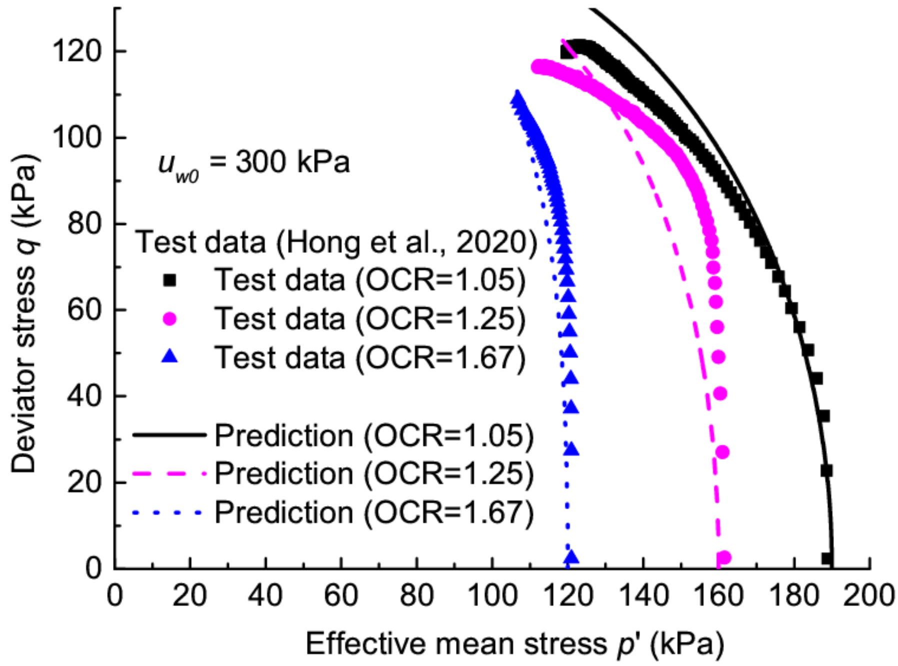

(b)

Fig. 5.6 Model prediction for the stress-strain relationship of gassy Malaysian Kaolin (test data from Hong et al., 2020) with $p'_c = 200$ kPa, $u_{w0} = 300$ kPa, $S_{r0} = 1.00$ and different OCR: (a) the $\varepsilon_a - q$ relationship; (b) the effective stress path

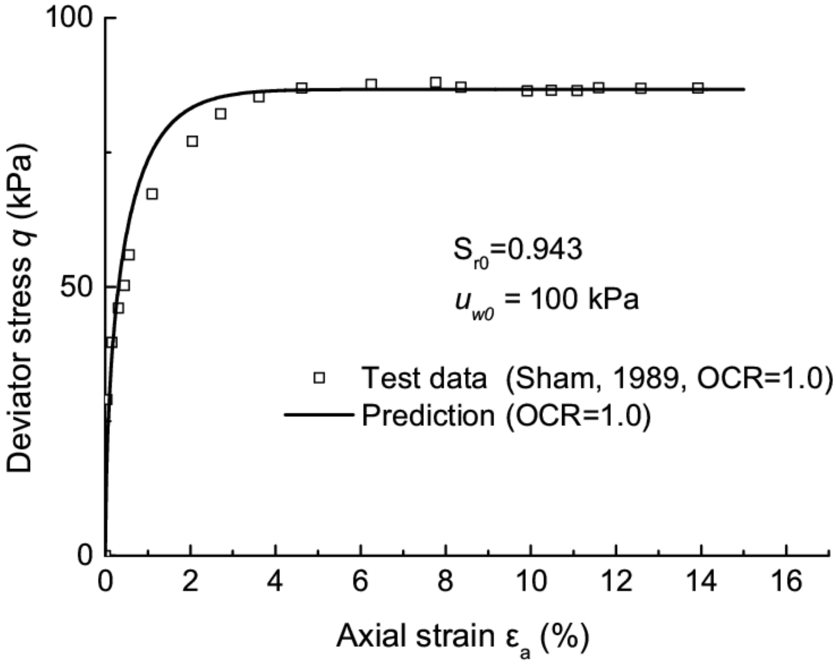
100
50
0
0 2 4 6 8 10 12 14 16
Deviator stress q (kPa)
Axial strain ε_a (%)
S_{r0}=0.943
u_{w0} = 100 kPa
Test data (Sham, 1989, OCR=1.0)
Prediction (OCR=1.0)

(a)

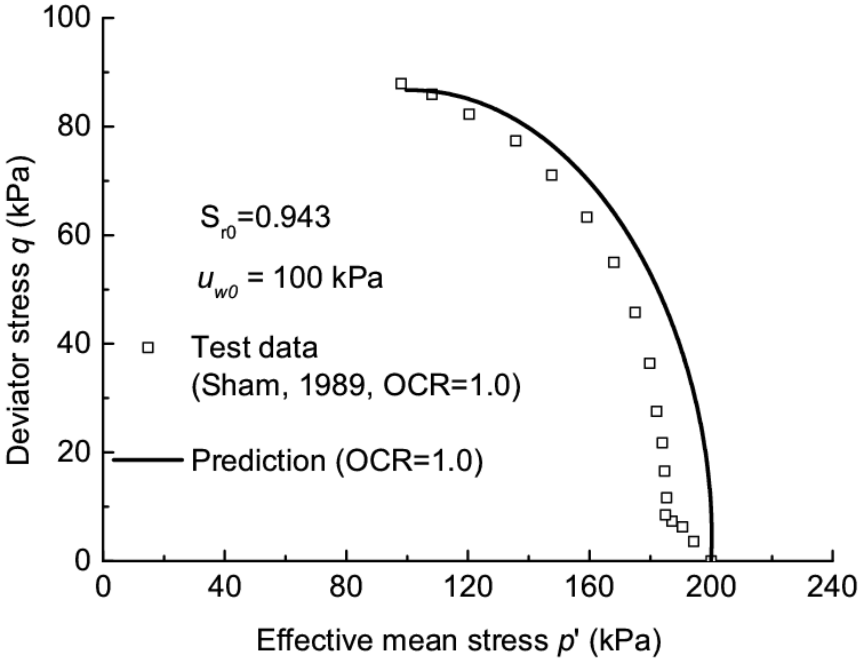
100
80
60
40
20
0
0 40 80 120 160 200 240
Deviator stress q (kPa)
Effective mean stress p' (kPa)
S_{r0}=0.943
u_{w0} = 100 kPa
Test data
(Sham, 1989, OCR=1.0)
Prediction (OCR=1.0)

(b)

Fig. 5.7 Model validation for the stress-strain relationship of gassy Kaolin (test data from Sham, 1989) with $p_c' = 200$ kPa, $u_{w0} = 100$ kPa, $S_{r0} = 0.943$ and $OCR = 1$: (a) the $\varepsilon_a - q$ relationship; (b) the effective stress path

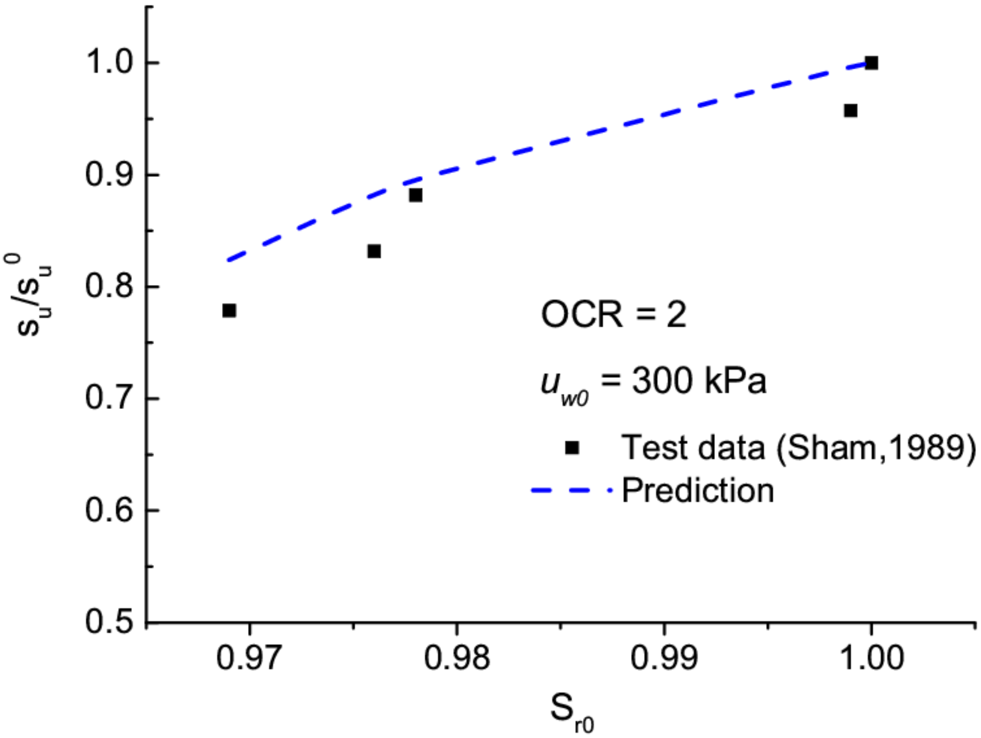

Fig. 5.8 Model validation of normalised undrained shear strength for the different S_r of gassy Malaysian Kaolin (test data from Sham, 1989) with $p_c' = 200$ kPa, $u_{w0} = 300$ kPa and $OCR = 2$

Figs. 5.9 to 5.11 show the calculated results of gassy Malaysian kaolin silt with $p_c' = 200$ kPa, different u_{w0}, S_{r0} and OCR. The stress-strain relationship and effective stress path is included in the figures. The effect of the degree of saturation and OCR can be easily seen in each figure.

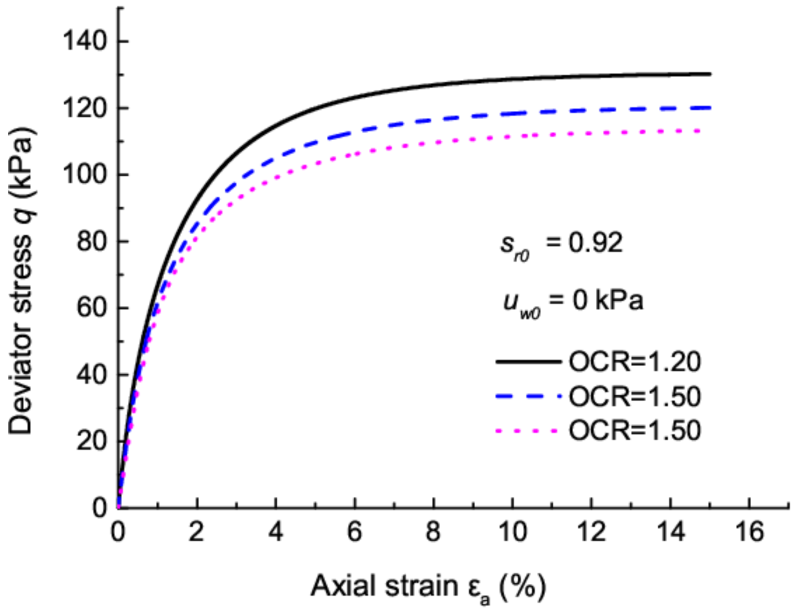

(a)

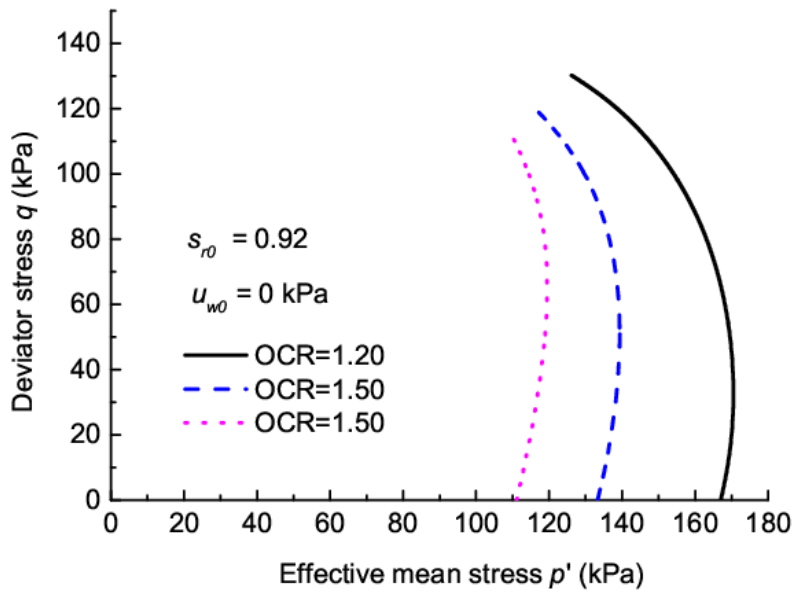

(b)

Fig. 5.9 Model prediction for the stress-strain relationship of gassy Malaysian Kaolin with $p'_c = 200$ kPa, $u_{w0} = 0$ kPa, $S_{r0} = 0.92$ and different OCR: (a) the $\varepsilon_a - q$ relationship; (b) the effective stress path

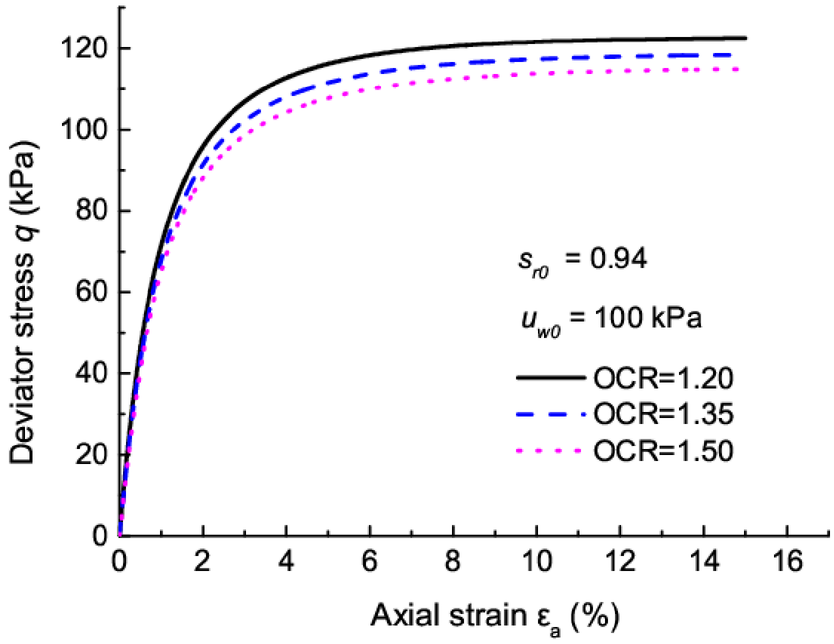

(a)

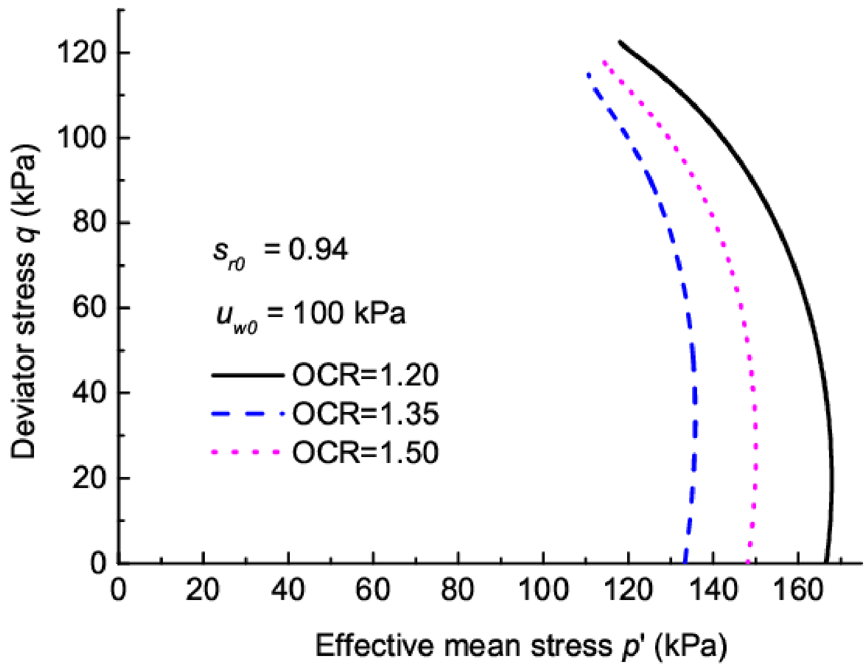

(b)

Fig. 5.10 Model prediction for the stress-strain relationship of gassy Malaysian Kaolin with $p_c' = 200$ kPa, $u_{w0} = 100$ kPa, $S_{r0} = 0.94$ and different OCR: (a) the $\varepsilon_a - q$ relationship; (b) the effective stress path

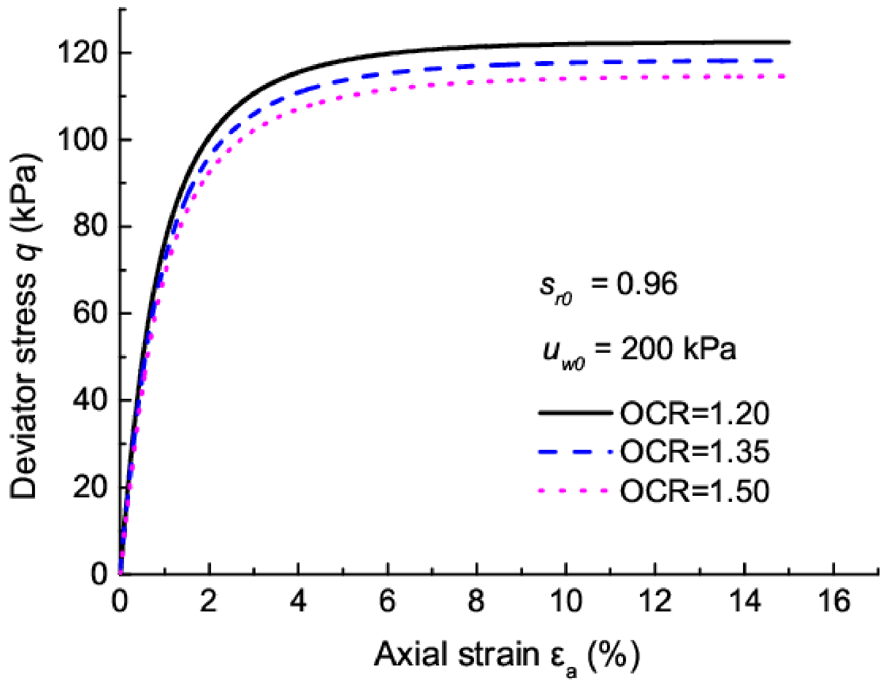

(a)

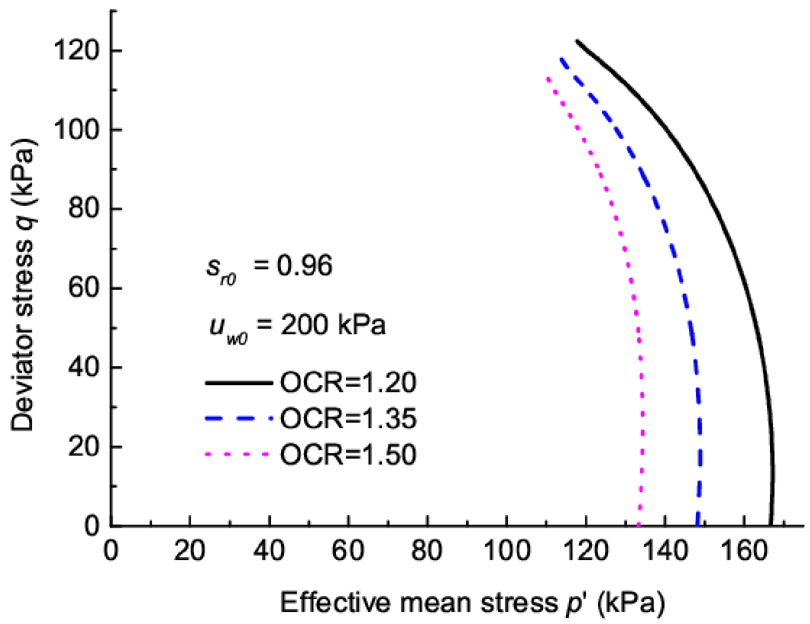

(b)

Fig. 5.11 Model prediction for the stress-strain relationship of gassy Malaysian Kaolin with $p'_c = 200$ kPa, $u_{w0} = 200$ kPa, $S_{r0} = 0.96$ and different OCR: (a) the $\varepsilon_a - q$ relationship; (b) the effective stress path

Figs. 5.12 to 5.14 show the simulation of the normalised undrained shear strength with different degree of saturation and OCR, at different u_w and the same $p_c' = 200\text{kPa}$. s_u^0 is the undrained shear strength of the saturated clay, which varies with the OCR. In Fig. 5.12, the undrained shear strength s_u increases as the degree of saturation S_r decreases, which is related to the 'bubble flooding'. But the increase in s_u becomes less significant as OCR increases. This is due to the dilatancy of overconsolidated clay. As OCR increases, the saturated soil matrix becomes less contractive, which means smaller increase in pore water pressure u_w and less 'bubble flooding' (Eq. 4.17). In Figs. 5.13 and 5.14, s_u decreases as S_r decreases for both the normally consolidated and overconsolidated soils. There is more significant decrease in s_u for normally consolidated soils. This is also due to the detrimental effect of gas cavities on plastic hardening is more significant in normally consolidated soils. There is a specific highest value of the normalised undrained shear strength at $S_r = 0.973$ in Fig. 5.13. One possible reason is that there is more beneficial effect than detrimental effect at a certain value of the degree of saturation. It is found that gas bubbles tend to have less beneficial effect on the undrained shear strength of soil as the OCR increases. This is associated with the dilatancy of overconsolidated FGS. As OCR increases, the saturated soil matrix becomes less contractive, which causes smaller increase in pore water pressure in undrained tests and less bubble flooding. Meanwhile, overconsolidation makes the detrimental effect of gas bubbles on the undrained shear strength less significant.

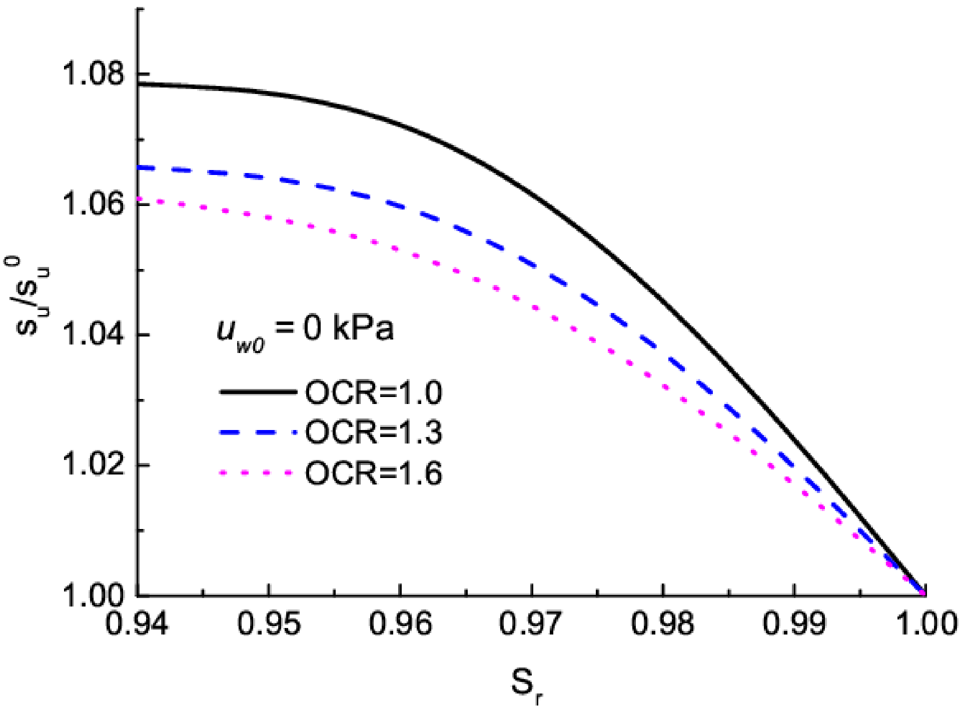

Fig. 5.12 Model prediction of normalised undrained shear strength for gassy Malaysian Kaolin with $p_c' = 200$ kPa, $u_{w0} = 0$ kPa

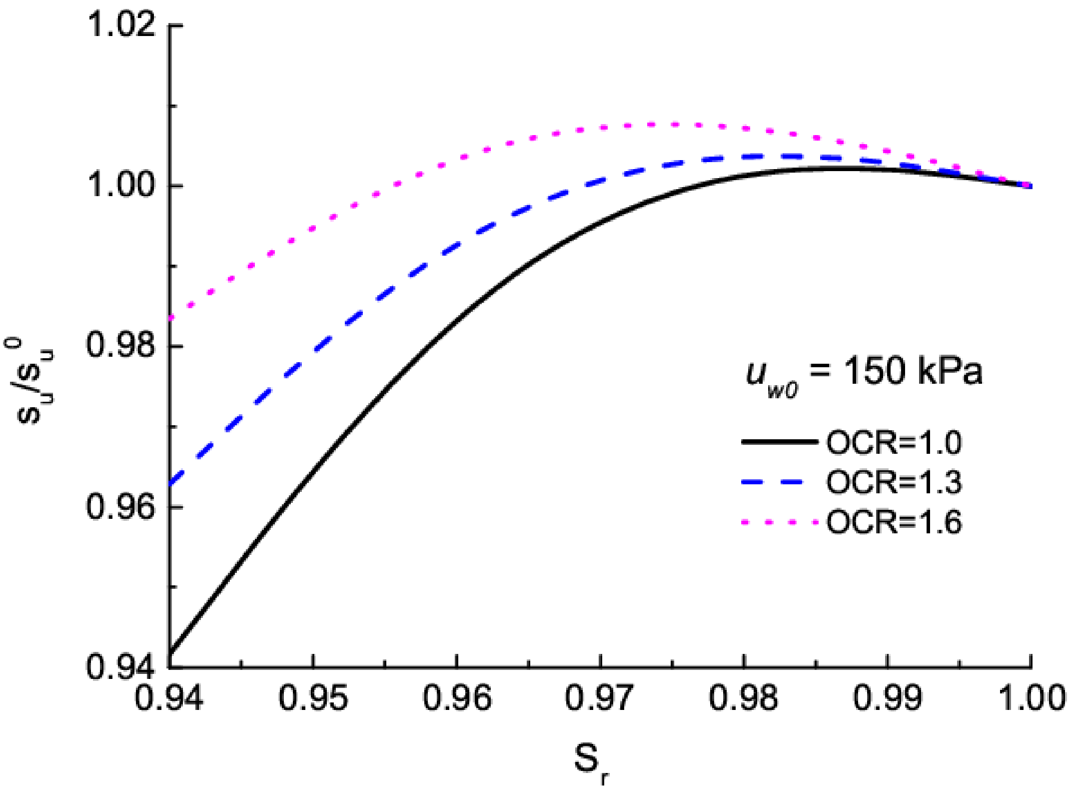

Fig. 5.13 Model prediction of normalised undrained shear strength for gassy Malaysian Kaolin with $p'_c = 200$ kPa, $u_{w0} = 150$ kPa

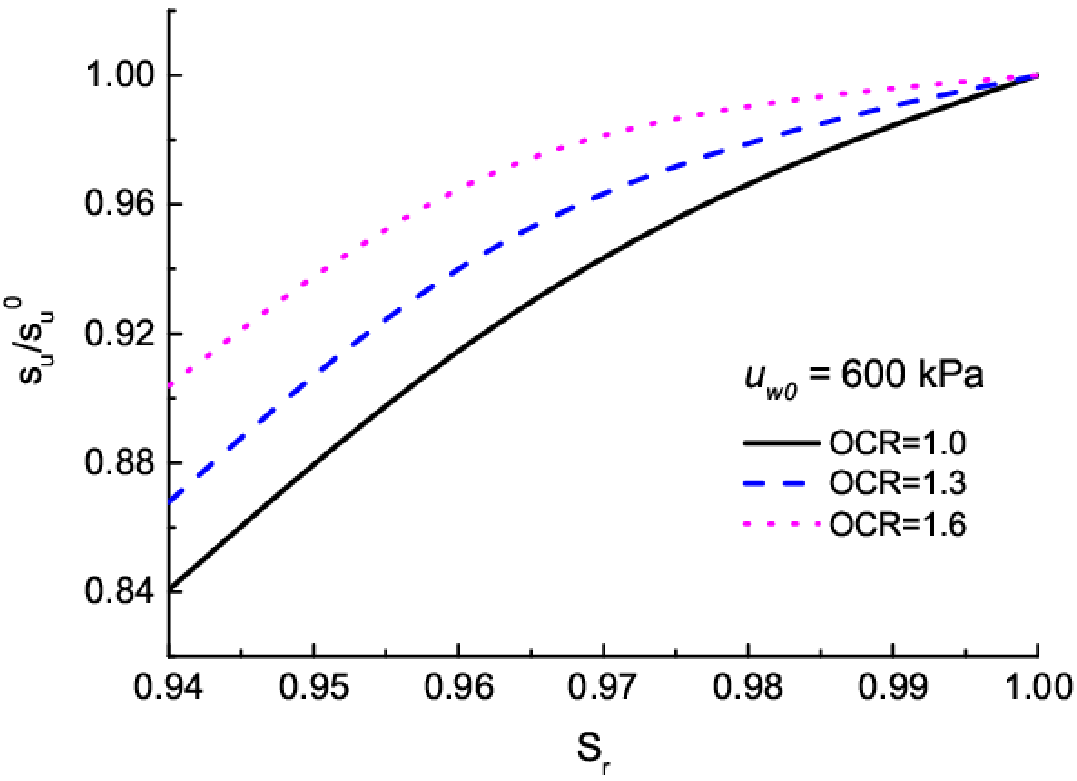

Fig. 5.14 Model calculation of normalised undrained shear strength for the different S_r and OCR of gassy Malaysian Kaolin with $p'_c = 200$ kPa, $u_{w0} = 600$ kPa

5.5 Comparison on new bounds and constitutive models

Fig. 5.15 shows the prediction of the upper and lower bounds and the constitutive model for the overconsolidated FGS with test data. The new upper and lower bounds can simulate the undrained shear strength better in most cases and the model in Chapter 5 can give a closer prediction with test data.

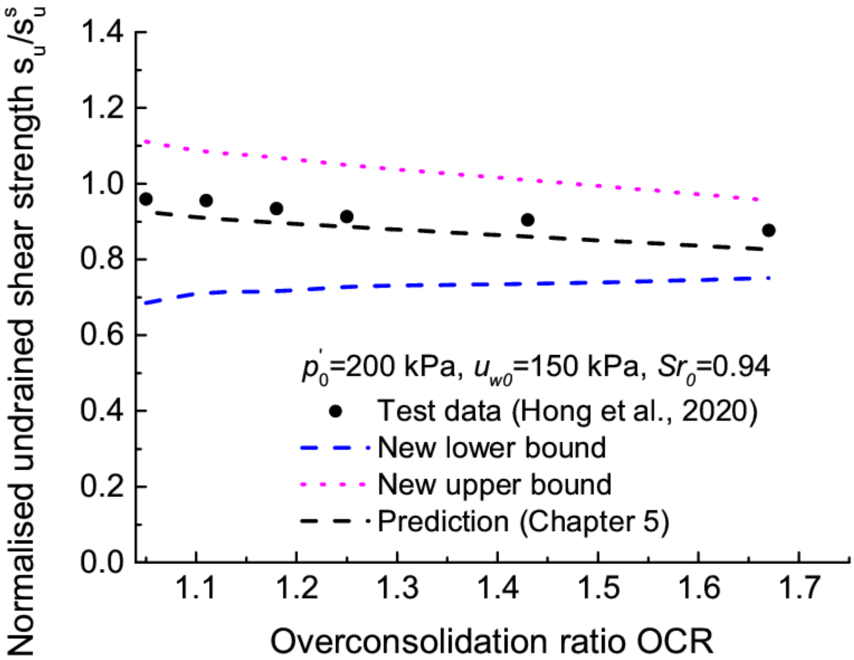

Fig. 5.15 The comparison of predictions between the models in Chapter 3 and Chapter 5 with test data from Hong et al. (2020) with $p_0' = 200$ kPa, $u_{w0} = 150$ kPa and different OCR

Figs. 5.16 and 5.17 show the comparison of the predictions of the constitutive model in Chapters 4 and 5 with test data from Hong et al. (2020). The samples are lightly overconsolidated with $OCR =$ 1.05 and 1.25. Fig. 5.16 indicates that the overconsolidated model gives better prediction for the stress-strain relationship, effective stress path and undrained shear strength. In particular, there is no increase in p' at the initial loading stage when the overconsolidated model is used, because the detrimental effect of gas bubbles on plastic hardening can be captured. The normally consolidated model gives bubble flooding without damaging effect, which leads to the increase of p'.

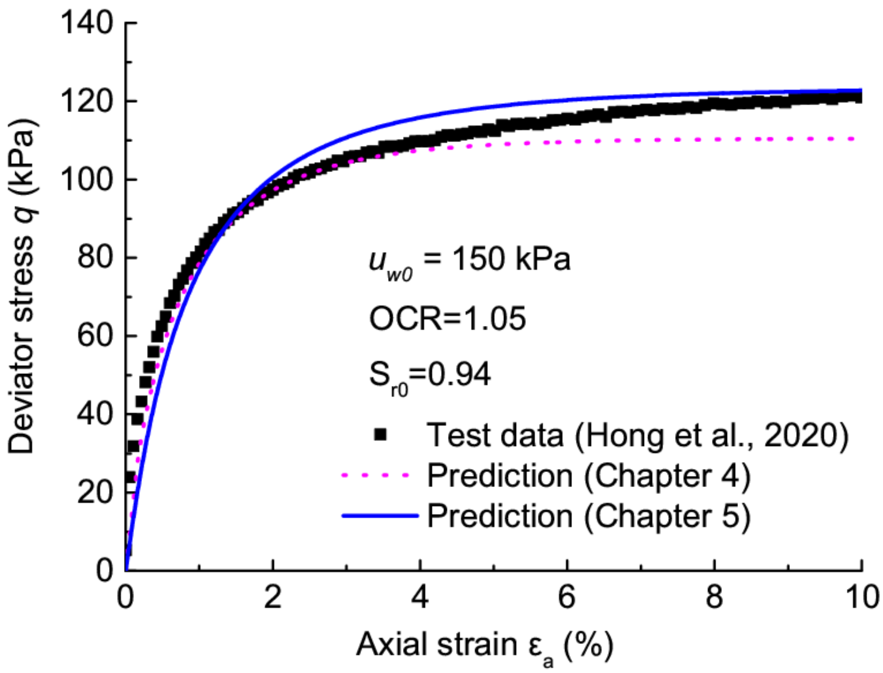

(a)

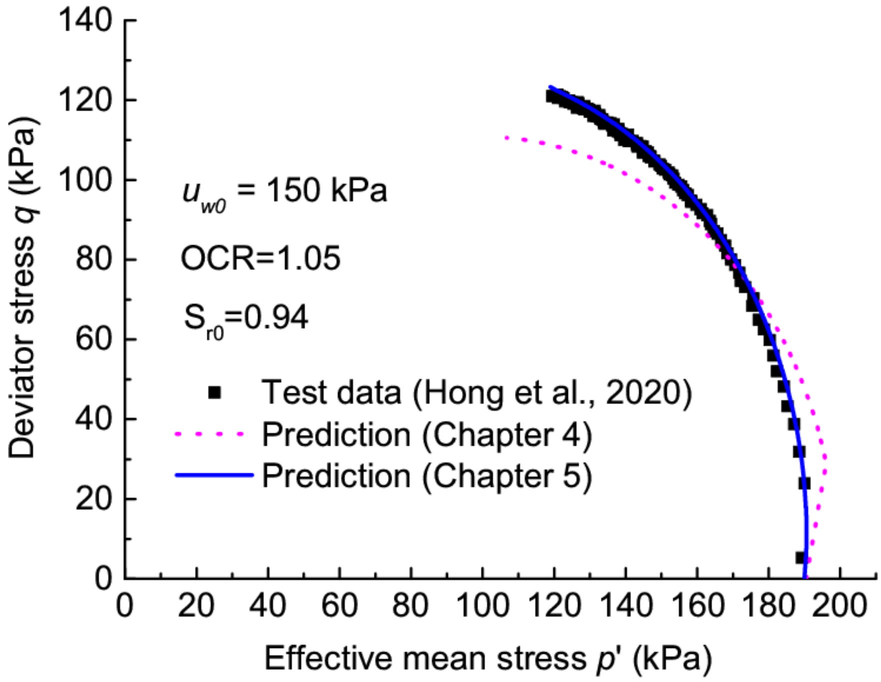

(b)

Fig. 5.16 The comparison of predictions between the models in Chapter 4 and Chapter 5 with test data from Hong et al. (2020) with $p'_c = 200$ kPa, $u_{w0} = 150$ kPa, $s_{r0} = 0.94$ and $OCR = 1.05$: (a) $\varepsilon_a - q$ relationship; (b) the effective stress path

The results in Fig. 5.17 are interesting. The normally consolidated model gives better prediction of the shear stiffness before failure (Fig. 5.17 a) because the model assumes purely elastic response in before q reaches 108 kPa. The overconsolidated model underpredicts the shear stiffness due to the consideration of plastic deformation. Fig. 5.17 b clearly shows that the overconsolidated model overpredicts the p' when q <75 kPa.

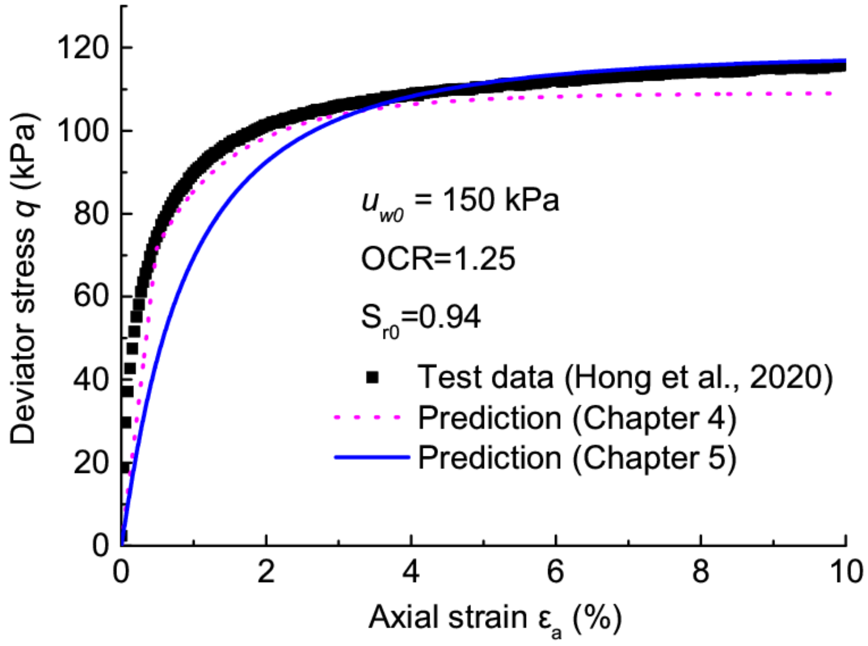

(a)

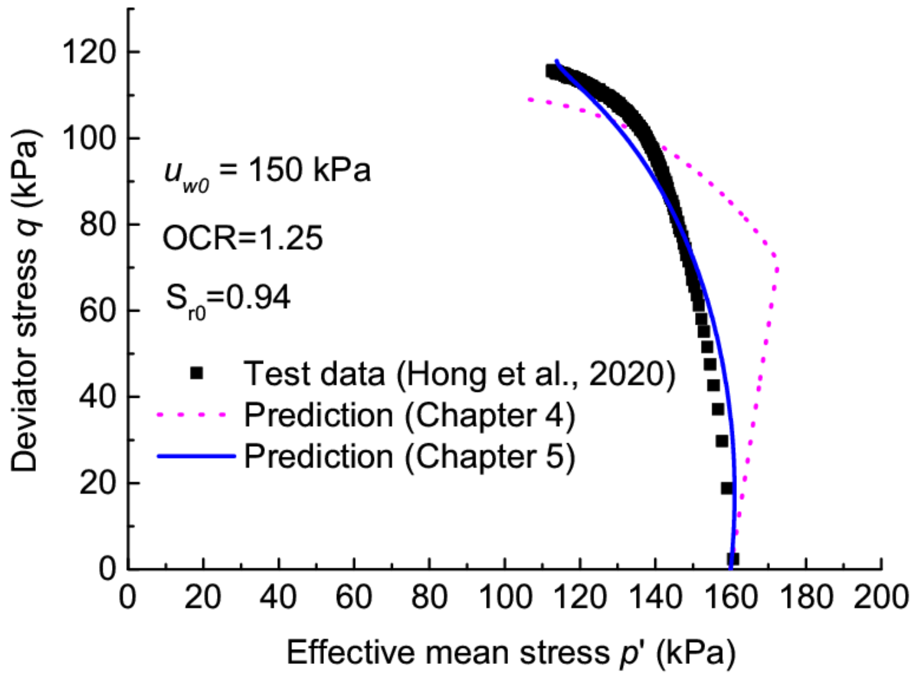

(b)

Fig. 5.17 The comparison of predictions between the models in Chapter 4 and Chapter 5 with test data from Hong et al. (2020) with $p'_c = 200$ kPa, $u_{w0} =$

150 kPa, $s_{r0} = 0.94$ and $OCR = 1.25$: (a) $\varepsilon_a - q$ relationship; (b) the effective stress path

Fig. 5.18 shows the comparison of predicted undrain shear strength by the new bounds and two models. The two models give similar prediction of the undrained shear strength. But it is worth noting that the ooverconsolidation model gives more reasonable prediction of the effective stress path before failure (Figs. 5.16 and 5.17)

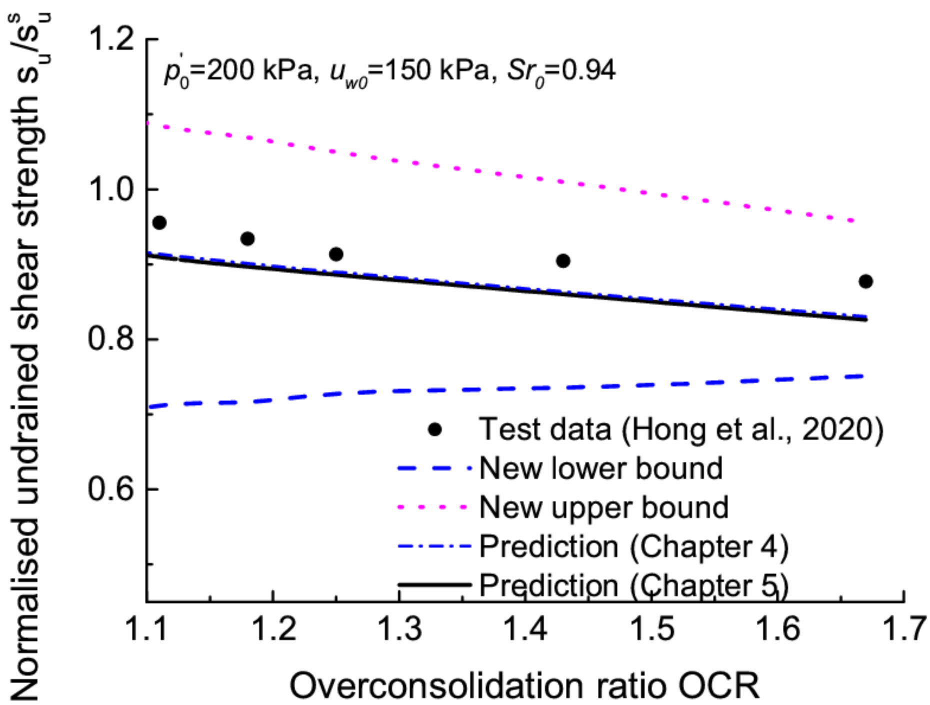

Fig. 5.18 The comparison of predictions of the models in Chapter 3 ,4 and Chapter 5 with test data from Hong et al. (2020) with $p_0' = 200$ kPa, $u_{w0} = 150$ kPa and different OCR

In Fig. 5.19, the lower bound is higher than the model prediction. This shows that the new hardening law used in Chapter 5 is appropriate for overconsolidated FGS. But the assumptions used in Chapter 3 for the lower bound may overestimate the undrained shear strength in some cases. Since there is very limited test data on overconsolidated

FGS, more research is needed to verify this conclusion.

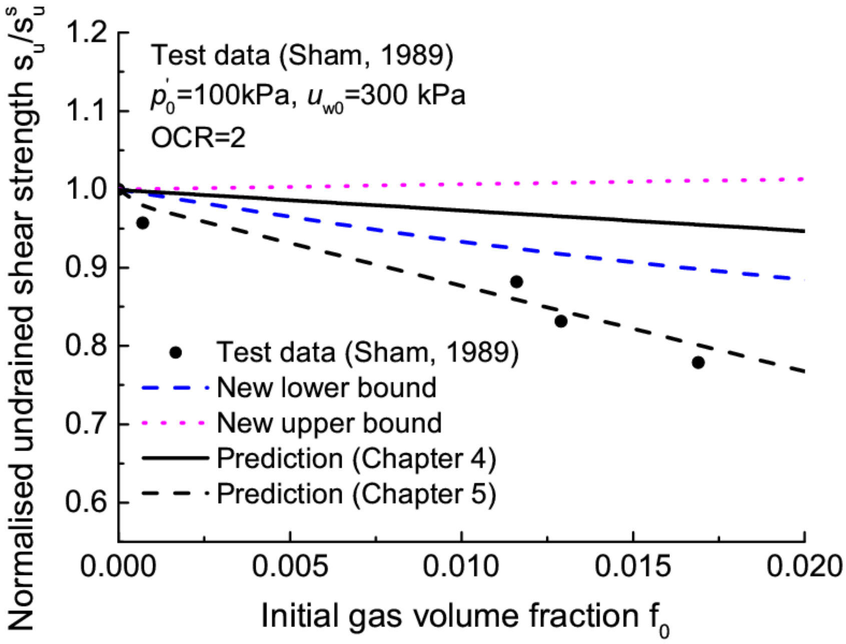

Fig. 5.19 The comparison of predictions between the models in Chapter 3, Chapter 4 and Chapter 5 with test data from Sham (1989) with $p_0' = 200$ kPa, $u_{w0} = 300$ and $OCR = 2$

Chapter 6: Conclusions and Recommendations

This chapter covers the main conclusions of the study in the thesis, with recommendations for future work on the behaviour of fine-grained soils containing gas bubbles.

6.1 Conclusions

Three main parts are included in the thesis. Firstly, a study on the upper and lower bounds for the undrained shear stress of FGS is presented based on the critical state soil mechanics and previous theoretical studies. The variable proposed in the new bounds of the undrained shear strength is then introduced to perform the detrimental effect on the undrained shear strength of FGS. Finally, the constitutive model for overconsolidated FGS is proposed. The constitutive model is validated using the triaxial test data of different FGS.

6.1.1 New lower and upper bounds for the undrained shear strength of FGS

New lower and upper bounds for the undrained shear strength of FGS have been developed based on the critical state soil mechanics and the original work of Wheeler (1986). The new upper bound is derived based on the assumption that the gas volume change is the same as the amount of pore water flowing into the cavities. There is only bubble flooding for the upper bound, but complete bubble flooding does not occur. The amount of bubble flooding is dependent on the stress path and degree of overconsolidation. The MCC model is used to calculate the undrained shear strength after bubble flooding. The lower bound is derived based on the original work of Wheeler (1986), but the volume change of gas cavities during loading is considered.

Both the new and Wheeler's (1986) lower and upper bounds are capable of describing the undrained shear strength of FGS, but the new bounds are closer to the test data of three FGS. Therefore, Wheeler's bounds predict the possible maximum and minimum undrained shear strength for all loading conditions, but the new bounds work better for predicting the undrained shear strength under specific loading conditions. The new bounds can also account for the effect of the total stress path on the undrained shear strength of unsaturated samples. But more experimental work needs to be done to verify the predictions. The new lower bound is found to overestimate the undrained shear strength of lightly overconsolidated FGS. This could be because it does not account for the soil structure damage caused by gas bubble expansion during unloading.

The study of the new bounds has several implications for the constitutive modelling of FGS. The theoretical study shows that the FGS has a unique structure with a saturated soil matrix and compressible cavities. Bubbles damage the soil structure but there could be bubble flooding which increases the soil strength. The variable $\frac{u_{w0}+p_a}{p_0'}$ is proper for characterising the effect of gas on the soil behaviour. Bigger $\frac{u_{w0}+p_a}{p_0'}$ leads to less bubble flooding and more detrimental effect. This variable is introduced to propose the constitutive model in the following section of the thesis.

6.1.2 A critical state constitutive model for FGS

A critical state constitutive model for FGS is then proposed, in which the soil is considered as a composite material with saturated soil matrix and cavities. The cavities tend to have a damaging effect on the soil structure as the gas has high compressibility and zero shear strength. In some cases, the cavities can be flooded by pore water, which makes the saturated soil matrix partially drained in an undrained test. Bubble flooding has a beneficial effect on soil stiffness and strength. The new model has the following features:

(a) Plastic hardening of the saturated soil matrix is assumed to be affected by gas cavities to model the damaging effect of gas cavities on the soil structure. As the gas volume fraction increases, the shear stiffness and strength of the soil decrease.

(b) The beneficial effect of free gas on soil strength and stiffness is modelled by considering bubble flooding. Bubble flooding is assumed to occur in all FGS in shear. But the amount of bubble flooding is dependent on the stress state and pore water pressure change.

(c) There are six parameters (M, λ, κ, N, ν, a_H) in the model, five of which are the same as those for the MCC model. Only one extra parameter (a_H) is introduced to describe the damaging effect of gas bubbles on the plastic hardening of the saturated soil matrix. It can be readily determined using the triaxial compression test data. The model has been validated by the results of over 100 tests on three FGS.

6.1.3 A constitutive model for overconsolidated FGS

A constitutive model for overconsolidated FGS has been proposed based on the model for normally consolidated FGS and the bounding surface model. FGS is considered as a composite with saturated soil matrix and gas cavities. The mechanical behaviour of saturated soil matrix is described by a constitutive model for overconsolidated clay accounting for the effect of overconsolidation on dilatancy. Plastic hardening of the saturated soil matrix is assumed to be affected by gas cavities to model the damaging effect of gas cavities on the stiffness and shear strength. The beneficial effect of free gas on soil behaviour is modelled by considering bubble flooding. The model has been validated by the test data of gassy Malaysian Kaolin. It is found that gas bubbles tend to have a less beneficial effect and more detrimental effect on the undrained shear strength of clay as the OCR increases. This is associated with the dilatancy of overconsolidated clay. As OCR increases, the saturated soil matrix becomes less contractive, which causes a smaller increase in pore water pressure in undrained tests and less 'bubble flooding'.

The model has been validated by the data in undrained triaxial tests from literature (Wheeler, 1986, Sham, 1989, Hong et al., 2020). No drained tests have been performed in this study, and no such data is available in the literature. This is due to that the undrained condition is more important for the geotechnical design in clay. The model may show slight softening behaviour when u_w is very high. The reason is that the evolution law for the bounding surface size can cause contraction of the bounding surface. To improve the model response in this regard, flatter bounding surface with rotational hardening law (for anisotropy) can be used. This will be the future work of this study.

6.2 Recommendations for the future work

Constitutive models are proposed for both normally consolidated and overconsolidated FGS to describe their mechanical behaviour in the thesis. The new upper and lower bounds are firstly derived based on reasonable assumptions. Then a constitutive model for normally consolidated FGS is proposed using the variable which is found in the new upper and lower bounds. Both the effects of bubble flooding and gas bubbles are considered in the new constitutive model. To make further prediction for the mechanical behaviour of overconsolidated FGS, the constitutive model is revised by introducing a dilatancy relation and a bounding surface. Though, the three models can make good prediction with the test data, further research can be promoted. Some future work can be done in the following aspects to improve our understanding of FGS mechanics and constitutive modelling:

Improvement in our understanding of FGS mechanics: There are many studies on both experimental and theoretical aspects. However, it is still worth researching to understand more about FGS mechanics. The gas pressure is hard to measure, and the pore water pressure is then used instead based on reasonable assumptions. A more specific method of measuring gas pressure should be proposed, and related apparatus should be developed. Meanwhile, research on the behaviour of overconsolidated FGS with a higher degree of consolidation is necessary. More parameters may influence the mechanical behaviour of FGS. Even though the prediction will be more complicated with more parameters, they should be introduced to make the prediction well.

Improvement in constitutive modelling:

a) The formulation for describing the plastic hardening, bubble flooding and cavity volume change needs to be further improved to capture FGS behaviour with different properties. The model parameters are performed based on the existing test data, and more extensive laboratory tests on different soils are needed for this work; The model will be implemented in an open-source software package to solve real boundary value problems associated with FGS, enabling the assessment of geo-hazards such as submarine landslides of the gassy seabed. The main code will be modified to account for bubble flooding;

b) When a FGS sample is subjected to unloading, there can be gas exsolution that damages the soil structure. The current model cannot capture the behaviour of FGS under unloading because it gives a purely elastic response. More research will be done to extend the model for such loading conditions.

c) For the constitutive model for the overconsolidated FGS, the data in undrained triaxial tests have validated the model. No drained tests have been performed in this study, and no such data is available in the literature. This is due to that the undrained condition is more important for the geotechnical design in clay. More experimental research on the drained response of FGS is needed in the future. The model may show slight softening behaviour when u_w is very high. The reason is that the evolution law for the bounding surface size can cause contraction of the bounding surface. To improve the model response in this regard, flatter bounding surface with rotational hardening law (for anisotropy) can be used. This will be the future work of this study.

Appendix I

This is the code for constitutive model in Chapter 4. The constitutive equations can be found in Chapter 4.

```
       PROGRAM CONSTITUTIVE MODEL FOR GASSY SOIL
      IMPLICIT REAL*8(A-H,O-Z)
      OPEN (unit=8, file='CM.TXT',status='unknown')
100   FORMAT (f12.6,1x,f12.6,1x,f12.6,1x,f12.6,1x,f12.6,1x,f12.6,
     $              1x,f12.6,1x,f12.6,1x,f12.6)
C
      PRINT*, 'WHAT IS THE SOIL? 1 FOR SHAM AND 2 FOR SIMON, 3 FOR ZJU'
      READ*, ISOIL
      IF (ISOIL .EQ. 1) THEN
      DLA=0.23D0
      DKA=0.014D0
      DNIU=0.2D0
      DM=0.87D0
      EGA=2.350D0
      DMA=15.D0
      ELSE IF (ISOIL .EQ. 2) THEN
         DLA=0.174D0
         DKA=0.0297D0
         DNIU=0.2D0
         DM=1.33D0
         EGA=2.06D0
         DMA=14.0D0
      ELSE IF (ISOIL .EQ. 3) THEN
         DLA=0.25D0
         DKA=0.06D0
         DNIU=0.2D0
         DM=1.05D0
         EGA=2.81D0
         DMA=3.D0
      END IF
C
      PA=101.0D0
C
      PRINT*, ' THE INITIAL EFFECTIVE P'
      READ*, P
      Q=1.0D-6
```

```
C
    PRINT*, 'GIVE THE INITIAL UW'
    READ*, UW
    uw0=uw
    EV=0.0D0
    EQ=0.0D0
    DEQREF=1.0D-5
C
    PC=Q*Q/(DM*DM*P)+P

C*****************************************************

    E0=EGA-DLA*LOG(PC)
    EM=E0
    PRINT*,'give SR initial value'
    READ*, SR
    PRINT*, 'STRESS PATH, 1 FOR CU TEST DQ=3DP, 2 FOR ISO CONS'
    READ*, IPATH

C *************************************************

    VS=1.0D0
    VM=1.D0+EM
    VV=EM/SR
    VG=(1.D0-SR)*EM/SR
    VC=VG
    ETT=VV
    VT=VM+VG
    FV=VG/VT  ! VOLUME FRACTION OF GAS BUBBLES !
C
     IF (IPATH .EQ. 2)THEN
      DSTOP = P
      STOVL = 200.0D0
    ELSE IF (IPATH .EQ. 1)THEN
      DSTOP = EQ
      STOVL = 15.0D-2
    END IF
C
    DO WHILE (DSTOP .LT. STOVL)
       IF (IPATH .EQ. 1)THEN
            WRITE(8,100) p,q, EQ*100.D0,q,EQ*100.D0,UW-uw0
       ELSE IF (IPATH .EQ. 2)THEN
```

```
          WRITE(8,100) ETT, P, EM, P
        END IF
C
      IF (SR .GT. (1.D0-1.D-6)) THEN
        SR=1.D0-1.D-6
      END IF
      ETA=Q/P
      A=(1.D0-SR)/(UW+PA)*ETT/(1.D0+ETT)
      B=(1.D0)/(P+UW+PA)
C
      DK=(1.D0+EM)/DKA*P
      DG=3.D0*(1.D0-2.D0*DNIU)*(1.D0+EM)*P/(2.D0*DKA*(1.D0+DNIU))
C
      PFPQ=2.D0*Q
      PFPP=-DM*DM*PC+DM*DM*2.D0*P
      PFPC=-DM*DM*P
C
      RPC1=PFPP*PC*(1.D0+E0)/(DLA-DKA)
C
      FV=MAX(FV, 0.0D0)
      TRMU=1.D0-EXP(-(UW+PA)/PC)
      TERMF=SQRT(FV)
      TERME=(ETA/DM)
      DAMG=TRMU * TERMF * TERME
      DMG2=PFPP*DMA !
      RPC2=PC*(1.D0+E0)/(DLA-DKA)*DAMG*DMG2
C
      RPC=RPC1-RPC2
C
      PARAX=(1.D0-FV)/DK +FV*B
C
      DKP=-PFPC*RPC
      DNR=DKP+(1.D0-FV)/PARAX*PFPP*PFPP+PFPQ*3.D0*DG*PFPQ
C
      DLP=1.D0/PARAX*PFPP/DNR
      DLQ=PFPQ*3.D0*DG/DNR
C
      CPP = 1.D0/PARAX-DLP*(1.D0-FV)/PARAX*PFPP
      A1 = CPP
      CPQ = -DLQ*(1.D0-FV)/PARAX*PFPP
      A2 = CPQ
      A3=0.0D0
```

```
C
     CQP= -3.D0*DG*DLP*PFPQ
     B1=CQP
     CQQ=3.D0*DG-3.D0*DG*DLQ*PFPQ
     B2=CQQ
     B3=0.0D0
C
     CWP=(1.D0-FV*B*CPP)/((1.D0-FV)*A)
     C1=CWP
     CWQ=-FV*B*CPQ/((1.D0-FV)*A)
     C2=CWQ
     CWB=-1.D0/A
     C3=CWB
C
C=====================================================
C    FOR UNDRAINED TRIAXIAL COMPRESSION TESTS
C=====================================================
C
     IF (IPATH .EQ. 1 ) THEN
        DEQ=DEQREF
        DEV=(B2-3.D0*(A2+C2))/(3.D0*(A1+C1)-B1)*DEQ
        DEVB=0.0D0
     END IF
C
C=====================================================
C    FOR ISOTROPIC CONSOLIDATION TESTS
C=====================================================
C
     IF (IPATH .EQ. 2) THEN
        DEV=DEQREF
        DEQ=0.0D0
        DEVB=-C1*DEV/C3
     END IF
C==================================================
C   STRESS PATH COMPLETED
C==================================================
     DP=A1*DEV+A2*DEQ+A3*DEVB
     DQ=B1*DEV+B2*DEQ+B3*DEVB
     DUW=C1*DEV+C2*DEQ+C3*DEVB
C
     DLIN=DLP*DEV+DLQ*DEQ
     DPC=DLIN*RPC
```

```
C
      DEVC=B*DP
      DEVM=DEVB+A*DUW
      DVM=DEVM*VM
      DVC=VC*DEVC
      DVT=DVC+DVM
      DVG=DVC+A*DUW*VM
C
      VC=VC-DVC
      VT=VT-DVT
      VG=VG-DVG
      VV=VV-DVT
      VM=VM-DVM
C
      SR=1.D0-VG/VV
      FV=VG/VT
      ETT=VV
      EM=VM-VS ! VM-1.0D0
C
      P=P+DP
      Q=Q+DQ
      UW=UW+DUW
C
      PC=PC+DPC
      EV=EV+DEV
      EQ=EQ+DEQ
C
      IF (IPATH .EQ. 2)THEN
        DSTOP = P
        STOVL = 200.0D0
      ELSE IF (IPATH .EQ. 1)THEN
        DSTOP = EQ
        STOVL = 15.0D-2
      END IF
C
      END DO
      END
```

Appendix II

This is the code for constitutive model in Chapter 5. The constitutive equations can be found in Chapter 5.

```
       PROGRAM State_Dependent_Dilatancy_Clay_PQ_Space_Collins_Yield_Surf
       IMPLICIT real*8 (A-H,O-Z)
       IMPLICIT INTEGER (KIND=8) (I-N)
c
      OPEN( UNIT=8,FILE='STATE-DEPD-DLATC-CLAY.TXT', STATUS = 'UNKNOWN')
100   FORMAT (f12.6,1x,f12.6,1x,f12.6,1x,f12.6,1x,f12.6,1x,f12.6)
      ! THE PARAMETERS
      AHARD = 0.5D0
      BDILA = 0.1D0
      DLA = 0.23D0
      DKA = 0.014D0
      DMC = 0.87D0
      DNU = 0.20D0
      DMA = 46.0D0
      DBETA=1.D0
      !
      DAL = 1.0D0
      !GAMA = ALPHA
      !HFGAMA = GAMA / 2.0D0
      !BETA = 1.0D0 - GAMA
    !
! Yield function expression:
!                  F=(P-HFGAMA*PC)**2/(BETA*P+HFGAMA*PC)**2+Q**2/M**2/((1.0D0-
ALPHA)*P+HFGAMA*ALPHA*PC)**2

C     PRINT*, 'WHAT IS THE OCR VALUE ? '
C     READ*, OCR
      OCR=2.0d0

      P = 100.0D0
      PC = P * OCR
      P0B = PC
      PINI = P
      Q = 1.0D-16
      UW=300.0D0
```

```
      UW0=UW
      DEQREF = 1.0D-6
      VOIDR0 = 1.13D0
      VOIDR = VOIDR0

      EPSV = 0.0D0
      EPSQ = 0.0D0
      RPAST = 1.0D0 / OCR
      PA=101.0D0

C===================================================================
==========
  !  DO WHILE (EPSQ .LT. 0.102D0)
  !  IF(EPSQ .lt. 0.01d0)then
  !  DEPSQ = 1.D-6
  !  ELSE
  !  DEPSQ = 1.D-5
  !  END IF
C===================================================================
==========
C     PRINT*,'give SR initial value'
C     READ*, SR
C     SR=1.0d0-1.0D-6
      SR=0.969D0
C     PRINT*, 'STRESS PATH, 1 FOR CU TEST DQ=3DP, 2 FOR ISO CONS'
C     READ*, IPATH
      IPATH=1
C ************************************************
      VS=1.0D0
      VM=1.D0+VOIDR
C     WRITE(*,*),'VM=',VM
      VV=VOIDR/SR
      VG=(1.D0-SR)*VOIDR/SR
C     WRITE(*,*),'VG=',VG
      VC=VG
      ETT=VV
      VT=VM+VG
C     WRITE(*,*),'VT=',VT

      FV=VG/VT
C
      IF (IPATH .EQ. 2)THEN
```

```
        DSTOP = P
        STOVL = 200.0D0
      ELSE IF (IPATH .EQ. 1)THEN
        DSTOP = EPSQ
        STOVL = 15.0D-2
      END IF
C
      DO WHILE (DSTOP .LT. STOVL)
         IF (IPATH .EQ. 1)THEN
             WRITE(8,100) P,Q,EPSQ*100.D0,Q,EPSQ*100.D0,UW-UW0
         ELSE IF (IPATH .EQ. 2)THEN
           WRITE(8,100) ETT, P, VOIDR, P
         END IF
C
      IF (SR .GT. 1.D0) THEN
         SR=1.D0-1.D-6
      END IF
      A=(1.D0-SR)/(UW+PA)*ETT/(1.D0+ETT)
C     WRITE(*,*),'A=',A
C     READ*,SJDF
      B=(1.D0)/(P+UW+PA)
C     WRITE(*,*),'B=',B
C     READ*,SJDF
C     print*, sr,uw,ett
C     read*, sttrr
C     WRITE(*,*),'UW=',UW
  !
      ETA=Q/P
      R=RPAST
c     print*,p,q
c     read*,ccs

911   PB=P/R
      QB=Q/R
      DF1=((PB-DAL*P0B/2.D0)**2.D0)/(((1.D0-DAL)*PB+DAL*P0B/2.D0)**2.D0)
      DF2=(QB*QB)/(DMC**2.D0)/(((1.D0-DAL)*PB+DAL*DAL*P0B/2.D0)**2.D0)
      FCHECK=DF1+DF2-1.D0
      IF ( FCHECK .GT. 1.0D-5 ) THEN
         R = R * 1.001D0
         GO TO 911
         ELSE IF  ( FCHECK .LT. -1.0D-5 ) THEN
           R = R * 0.999D0
```

```
        GO TO 911
    END IF
c
    IF (R .GT. 1.0D0)  R = 1.0D0
    RPAST = R
c           print*, R,RPAST
c   ! PRINT*, R
c

    FQ=2.D0*QB/(DMC*DMC*((1.D0-DAL)*PB+DAL*DAL/2.D0*P0B)**2.D0)
C     WRITE(*,*),'FQ=',FQ
C     READ*,SDJF
    DC1=2.D0*(PB-DAL/2.D0*P0B)/(((1.D0-DAL)*PB+DAL/2.D0*P0B)**2.D0)
    DC2=(PB-DAL/2.D0*P0B)**2.D0
    DC3=(-2.D0)*((1.D0-DAL)*PB+DAL/2.D0*P0B)**(-3.D0)*(1.D0-DAL)
    DC4=QB*QB/(DMC*DMC)*(-2)*(((1.D0-DAL)*PB+DAL*DAL/2*P0B)**(-3.D0))
    FP=DC1+DC2*DC3+DC4*(1.D0-DAL)
C     WRITE(*,*),'FP=',FP
C     READ*,SDJF
    DC5=DC1*(-DAL/2.D0)
    DC6=(-2.D0)*(((1.D0-DAL)*PB+DAL/2.D0*P0B)**(-3.D0))*(DAL/2.D0)
    FP0B=DC5+DC2*DC6+DC4*(DAL*DAL/2.D0)
C     WRITE(*,*),'FP0B=',FP0B
C     READ*,SDJF
    IF (FP0B .GT. 0.0D0) then
       PRINT*, 'ERROR'
    end if

c
    DKPB=-FP0B*(1.D0+VOIDR)*P0B/(DLA-DKA)*FQ*(DMC**2-ETA**2)/2.0D0/ETA
C    print*, dkpb
C    WRITE(*,*),'DKPB=',DKPB
C    READ*,SFES



c
    DMVP=DMC/(R**AHARD)    !  EXP ( AHARD * (1.D0 - R) )!  POWER LAW..
C    WRITE(*,*),'DMVP=',DMVP
    DMDIL=DMC*(R**BDILA)       !  EXP (BDILA * (-1.0D0 + R) )! POWER LAW..
C    WRITE(*,*),'DMDIL=',DMDIL
c
    DMVPP=(DMVP**2-ETA**2)/2.0D0/ETA
```

```
C    WRITE(*,*),'DMVPP=',DMVPP
C    READ*,SDJF
     DPLA=(DMDIL**2-ETA**2)/2.0D0/ETA
C    WRITE(*,*),'DPLA=',DPLA
C    READ*,SJDF

     DKELA=P*(1.D0+VOIDR)/DKA
C    WRITE(*,*),'DKELA=',DKELA
C    READ*,SDJF
     G=3.0D0*(1.0D0-2.0D0*DNU)/2.0D0/(1.0D0+DNU)*DKELA
C    WRITE(*,*),'G=',G
C    READ*,SDJF
c
     RPC1=FQ*DPLA*P0B*(1.D0+VOIDR)/(DLA-DKA)  !FP=FQ*D
C    WRITE(*,*),'RPC1=',RPC1
C    READ*,SDJF
     FV=MAX(FV, 0.0D0)
     TRMU=1.D0+EXP(-DBETA*(UW+PA)/P0B)
C    TERMF=SQRT(FV)
     TERME=1.D0-(1.D0+(ETA/DMC))**(-20.D0)   ! DMC OR DMVP ???
     DAMG=FV*TERME/TRMU                    !TRMU * TERMF * TERME (ORIGINAL)
     DMG2=FQ*DPLA*DMA !
     RPC2=P0B*(1.D0+VOIDR)/(DLA-DKA)*DAMG*DMG2
C     JLK;;KJ
     RPC=RPC1-RPC2
C    WRITE(*,*),'RPC=',RPC
C    READ*,SDJF
C
     RPC3=FQ*DMVPP*P0B*(1.D0+VOIDR)/(DLA-DKA)  !FP=FQ*D
C    WRITE(*,*),'RPC1=',RPC1
C    READ*,SDJF
     DMG3=FQ*DMVPP*DMA !
     RPC4=P0B*(1.D0+VOIDR)/(DLA-DKA)*DAMG*DMG3
C     JLK;;KJ
     RPC5=RPC3-RPC4
C    WRITE(*,*),'RPC=',RPC
C    READ*,SDJF
     PARAX=(1.D0-FV)/DKELA +FV*B
C    WRITE(*,*),'PARAX=',PARAX
C    READ*,SDJF
C
     DKP=-FP0B*RPC5
```

```
C    WRITE(*,*),'DKP=',DKP
C    READ*,SDJF
     DNR=DKP+(1.D0-FV)/PARAX*FP*FQ*DPLA+FQ*3.D0*G*FQ
C    WRITE(*,*),'DNR=',DNR
C    READ*,SDJF
C    PRINT*,DKP

C
     DLP=1.D0/PARAX*FP/DNR
C    WRITE(*,*),'DLP=',DLP
C    READ*,SDJF
     DLQ=FQ*3.D0*G/DNR
C    WRITE(*,*),'DLQ=',DLQ
C    READ*,SDJF
C
     CPP = 1.D0/PARAX-DLP*(1.D0-FV)/PARAX*FQ*DPLA
     A1 = CPP
C    WRITE(*,*),'A1=',A1
C    READ*,SDJF
     CPQ = -DLQ*(1.D0-FV)/PARAX*FQ*DPLA
     A2 = CPQ
C    WRITE(*,*),'A2=',A2
C    READ*,SDJF
     A3=0.0D0
C
     CQP= -3.D0*G*DLP*FQ
     B1=CQP
C     WRITE(*,*),'B1=',B1
C     READ*,SDJF
     CQQ=3.D0* G-3.D0*G*DLQ*FQ
     B2=CQQ
C     WRITE(*,*),'B2=',B2
C     READ*,SJDF
     B3=0.0D0
C
     CWP=(1.D0-FV*B*CPP)/((1.D0-FV)*A)
     C1=CWP
C     WRITE(*,*),'C1=',C1
C     READ*,SJDF
     CWQ=-FV*B*CPQ/((1.D0-FV)*A)
     C2=CWQ
C     WRITE(*,*),'C2=',C2
```

```
C     READ*,SJDF
      CWB=-1.D0/A
      C3=CWB
C     WRITE(*,*),'C3=',C3
C     READ*,SJDF
C=========================================================
C    FOR UNDRAINED TRIAXIAL COMPRESSION TESTS
C=========================================================
C
      IF (IPATH .EQ. 1 ) THEN
         DEPSQ=DEQREF
C          DEPSV=0.0D0
         DEPSV=(B2-3.D0*(A2+C2))/(3.D0*(A1+C1)-B1)*DEPSQ
C          WRITE(*,*),'DEPSV=',DEPSV
C          READ*,SDJF
         DEVB=0.0D0
      END IF
C
C=========================================================
C   FOR ISOTROPIC CONSOLIDATION TESTS
C=========================================================
C
      IF (IPATH .EQ. 2) THEN
         DEPSV=DEQREF
         DEPSQ=0.0D0
         DEVB=-C1*DEV/C3
      END IF
C======================================================
C   STRESS PATH COMPLETED

C======================================================
      DP=A1*DEPSV+A2*DEPSQ+A3*DEVB
C    WRITE(*,*),'DP=',DP
C    READ*,SJDF
      DQ=B1*DEPSV+B2*DEPSQ+B3*DEVB
C    WRITE(*,*),'DQ=',DQ
C    READ*,SJDF
      DUW=C1*DEPSV+C2*DEPSQ+C3*DEVB
C    WRITE(*,*),'DUW=',DUW
C    READ*,SJDF
      !DP0B=P0B*(1.0D0+VOIDR)/(DLA-DKA)*HDL*DLINDEX*FQ*DPLA
C    DVOID=(1.0D0+VOIDR)*DEPSV        !
```

```
C
C    DLIN=DLP*DEPSV+DLQ*DEPSQ    ! THIS IS IMPORTANT, PAY ATTENTION TO THE
CHANGES MADE
      DLIN=DLP*DEPSV+DLQ*DEPSQ
C      WRITE(*,*),'DLIN=',DLIN
C      READ*,SJDF!
C      DP=DKELA*(DEPSV-DLIN*FQ*DPLA)
C      WRITE(*,*),'DP=',DP
C      READ*,SJDF
C      DQ=3.D0*G*(DEPSQ-DLIN*FQ)
C      WRITE(*,*),'DQ=',DQ
C      READ*,SJDF
      DP0B=DLIN*RPC
C      WRITE(*,*),'DP0B=',DP0B
C      READ*,SJDF
C
      DEVC=B*DP
      DEVM=DEVB+A*DUW
C      WRITE(*,*),'DEVM=',DEVM
C      READ*,SJDF
      DVM=DEVM*VM
C      WRITE(*,*),'DVM=',DVM
C      READ*,SJDF
      DVC=VC*DEVC
      DVT=DVC+DVM
      DVG=DVC+A*DUW*VM
C
      VC=VC-DVC
      VT=VT-DVT
      VG=VG-DVG
      VV=VV-DVT
      VM=VM-DVM
C      WRITE(*,*),'VM=',VM
C      READ*,SDJF
C
      SR=1.D0-VG/VV
      FV=VG/VT
      ETT=VV
C      VOIDR=VOIDR-DVOID
      VOIDR=VM-VS ! VM-1.0D0
C      WRITE(*,*),'VOIDR=',VOIDR
C      READ*,SJDF
```

```
C
    P=P+DP
    Q=Q+DQ
    UW=UW+DUW
C
    P0B=P0B+DP0B
    EPSV=EPSV+DEPSV
    EPSQ=EPSQ+DEPSQ
C
    IF (IPATH .EQ. 2)THEN
      DSTOP = P
      STOVL = 200.0D0
    ELSE IF (IPATH .EQ. 1)THEN
      DSTOP = EPSQ
      STOVL = 15.0D-2
    END IF
c
    END DO
c
    END
```

References

Amaratunga, A., and J. L. H. Grozic. (2009). "On the undrained unloading behaviour of gassy sands." Canadian Geotechnical Journal. 46.11.1267-1276. https://doi.org/10.1139/T09-056.

Anderson, A. L. and Hampton, L. D. (1980). "Acoustics of gas-bearing sediments." The Journal of the Acoustical Society of America 67.6: 1865-1889. https://doi.org/ 10.1121/1.384453.

Atigh, E., and Byrne, P. M. (2004). “Liquefaction flow of submarine slopes under partially undrained conditions: an effective stress approach.” Canadian geotechnical journal, 41(1), 154-165. https://doi.org/10.1139/t03-079.

Barden, L. and Sides, G. R. (1970). “Engineering behaviour and structure of compacted clay.” Journal of the Soil Mechanics and Foundations Division 96.4. 1171-1200. https://doi.org/10.1061/JSFEAQ.0001434.

Bea, R. G., and Arnold, P. G. (1973). “Movements and forces developed by wave-induced slides in soft clays.” Offshore Technology Conference. OnePetro. https://doi.org/10.4043/1899-MS.

Bishop, A.W, Donald, I.B. (1961). “The experimental study of partly saturated soil in the triaxial apparatus-Bishop.” 5th International Conference on Soil Mechanics and Foundation Engineering (Paris).13-21.

Boudreau, B. P., Algar, C., Johnson, B. D., Croudace, I., Reed, A., Furukawa, Y., Dorgan, K.M., Jumars, P.A., Grader, A.S. and Gardiner, B.S. (2005). Bubble growth and rise in soft sediments. Geology, 33(6), 517-520. https://doi.org/10.1130/ G21259.1.

Boudreau, B. P., Algar, C., Johnson, B. D., Croudace, I., Reed, A., Furukawa, Y., Gardiner,

B. S. (2005). “Bubble growth and rise in soft sediments.” Geology, 33(6), 517-520. https://doi.org/10.1130/G21259.1.

Chang, C. S., and J. M. Duncan. (1983). "Consolidation analysis for partly saturated clay by using an elastic–plastic effective stress–strain model." International Journal for Numerical and Analytical Methods in Geomechanics 7.1: 39-55. https://doi.org/10.1002/nag.1610070106.

Coleman, J. M., Prior, D. B., Garrison, L. E. (1978). “Submarine landslides in the Mississippi River delta.” In Offshore Technology Conference. 1067-1074. https://doi.org/10.4043/3170-MS.

Collins, I. F. (2005). “Elastic/plastic models for soils and sands.” *Int. J. Mech. Sci*. 47(4–5), 493–508. http://doi.org/10.1016/j.ijmecsci.2004.12.016.

Dafalias, Y. F. (1986). “Bounding surface plasticity. I: Mathematical foundation and hypoplasticity.” Journal of Engineering Mechanics, 112(9), 966-987. https://doi.org/10.1061/(ASCE)0733-9399(1986)112:9(966).

Dafalias, Y., and Herrmann, L. (1986). “Bounding surface plasticity II: Application to isotropic cohesive soils.” J. Eng. Mech., 112(12). 1263–1291. https://doi.org/10.1061/(ASCE)0733-9399(1986)112:12(1263).

de Boer, R. (2003). “Reflections on the development of the theory of porous media.” Applied Mechanics Reviews,56(6),R27-R42. https://doi.org/10.1115/1.1614815.

Diambra, A., Ibraim, E., Wood, D. M., Russell, A. R. (2010). “Fibre reinforced sands: experiments and modelling.” Geotextiles and geomembranes, 28, No. 3, 238–250. https://doi.org/10.1016/j.geotexmem.2009.09.010.

Dittrich, P. D. P., Rowe, K. R. K., Becker, D. E. B. E., Lo, K. Y. L. Y. (2010). “Influence of exsolved gases on slope performance at the sarnia approach." Revue Canadienne De Géotechnique, 47, No. 9, 971–984. https://doi.org/10.1139/ T10-008.

Ehlers, W. and Blome, P. (2003). "A triphasic model for unsaturated soil based on the theory of porous media." Mathematical and computer modelling, 37(5-6), 507-513. https://doi.org/10.1016/S0895-7177(03)00043-8.

Ehlers, W., Graf, T., Ammann, M. (2004). "Deformation and localization analysis of partially saturated soil." Computer methods in applied mechanics and engineering,193(27-29),2885-2910. https://doi.org/10.1016/j.cma.2003.09.026.

Esrig, M. I. and Kirby, R. C. (1977). "Implications of gas content for predicting the stability of submarine slopes." Marine Georesources & Geotechnology, 2(1-4), 81-100. https://doi.org/10.1080/10641197709379771.

Fleischer, P., Orsi, T., Richardson, M., Anderson, A. (2001). "Distribution of free gas in marine sediments: a global overview." Geo-Marine Letters 21(2):103-122. https://doi.org/10.1007/s003670100072.

Fredlund, DG, Rahardjo, H. (1993). "Soil mechanics for unsaturated soils." https://doi.org/10.1002/9780470172759.

Gao, Z.W., Cai, H.J., Hong, Y., Lu, D.C. (2021). "Constitutive modelling of fine-grained gassy soils." *Canadian Geotechnical Journal.* http://doi.org/ 10.1139/cgj-2020-0754.

Gao, Z.W., Cai, H.J. (2021). "Effect of total stress path and gas volume change on undrained shear strength of gassy clay." *Int. J. Geomech.* 21(11). http://doi.org/10.1061/(ASCE) GM.1943-5622. 0002198.

Gao, Z.W., Diambra, A. (2020). "A multiaxial constitutive model for fibre-reinforced sand.” Géotechnique.1-13.DOI: 10.1680/jgeot.19.p.250.

Gao, Z.W., Hong, Y., Wang, L.Z. 2020. “Constitutive modelling of fine-grained gassy soil: A composite approach. Numerical and Analytical Methods in Geomechnics.” 44:1350-1368. https://doi.org/10.1002/nag.3065.

Gao, Z.W., Zhao, J.D., Yin, Z.Y. (2017). Dilatancy relation for overconsolidated clay. International Journal of Geomechanics, 17(5), 06016035. https://doi.org/ 10.1061/(ASCE)GM.1943-5622.0000793.

Green, R.J. 1972. “A plasticity theory for porous solids.” International Journal of Mechanical Sciences. 14(4): 214-224. https://doi.org/10.1016/0020-7403(72)90063-X.

Grozic, J.L., Nadim, F., Kvalstad, T.J. 2005. “On the undrained shear strength of fine-grained gassy soils.” Computers and Geotechnics. 32(7): 483–490. https://doi.org/10.1016/j. compgeo.2005.10.002.

Grozic, J. L., Imam, S. M., Robertson, P. K., Morgenstern, N. R. (2005). “Constitutive modeling of gassy sand behaviour.” Canadian Geotechnical Journal, 42(3), 812-829. https://doi.org/10.1139/t05-015.

Hashiguchi, K. (1980). “Constitutive equations of elastoplastic materials with elastic-plastic transition.” J. Appl. Mech., 47(2), 266–272.

Hight, D. W., Leroueil, S. 2003. “Characterisation of soils for engineering purposes.” In Characterisation and engineering properties of natural soils (eds T. S Tan, K. K. Phoon, D. W. Hight and S. Leroueil), pp. 255–362. Lisse, the Netherlands: Balkema.

Hong, Y., Wang, L.Z., N,g C.W., Yang, B. (2017). “Effect of initial pore pressure on undrained shear behaviour of fine-grained gassy soil." *Canadian Geotechnical Journal.* 4(11): 1592–1600. http://doi.org/10.1139/cgj-2017-0015.

Hong, Y., Wang, L.Z., Zhang, J.F., Gao, Z.W. (2020). "3D elastoplastic model for fine-grained gassy soil considering the gas-dependent yield surface shape and stress-dilatancy." *Journal of Engineering Mechanics*. 146(5): 04020037. http://doi.org/10.1061/(ASCE)EM.1943-7889. 0001760.

Houslby, G.T., Byrne, B.W. (2005). Design procedures for installation of suction caissons in clay and other materials. Proceeding of the Institution of Civil Engineers-Geotechnical Engineering. 2005;158(2):75-82. DOI:10.1680/geng.2005.158.2. 75.

Hovland, M., Judd, Alan. (1988). Seabed pockmarks and seepages: Impact on geology, biology and the marine environment. 10.13140/RG.2.1.1414.1286.

Jommi, C., Muraro, S., Trivellato, E., Zwaneburg, C. 2019. "Experimental results on the influence of gas on the mechanical response of peats." Géotechnique. 69(9):753-766. https://doi.org/10.1680/jgeot.17.p.148.

Kvenvolden, K. A. (1988). "Methane hydrate—A major reservoir of carbon in the shallow geosphere?" Chemical Geology, 71, No. 1–3, 41–51. https://doi.org/10.1016/0009-2541(88)90104-0.

Lewis, H. K., Brian, M. (1970). Pockmarks on the Scotian Shelf. GSA Bulletin. 81(10):3141-3148. https://doi.org/10.1130/00167606(1970)81[3141:POTSS]2.0.CO;2

Locat, J., Lee, H.J. (2002). "Submarine landslides: advances and challenges." *Canadian Geotechnical Journal.* 39(1): 193–212. http://doi.org/10.1139/t01-089.

Lunne, T., Berre, T., Stranvik, S., Andersen, K.H., Tjelta, T.I. (2001). “Deepwater sample disturbance due to stress relief.” *In Proc., OTRC 2001 Int. Conf.* 64–85. Houston: Offshore Technology Conference.

Mabrouk, A., R. Kerry, R. (2011). "Effect of gassy sand lenses on a deep excavation in a clayey soil." Engineering Geology 122.3-4. 292-302. https://doi.org/10.1016/j.enggeo.2011.06.009.

Mihalache, C., Buscarnera, G. (2016). “Controllability criteria for soils saturated by a compressible fluid.” Journal of Engineering Mechanics, 142(10), 04016076. https://doi.org/10.1061/(ASCE)EM.1943-7889.0001137.

Milich, L. (1999). The role of methane in global warming: where might mitigation strategies be focused? Global Environmental Change. 9(3): 179–201.DOI: 10.1016/s0959-3780(98)00037-5.

Mita, K., Dasari,G., and Lo, K. (2004). “Performance of a three-dimensional Hvorslev–Modified Cam Clay model for overconsolidated clay.” Int. J. Geomech.4(4). 296–309. https://doi.org/10.1061/(ASCE)1532-3641(2004)4:4(296).

Wood, M. D. 1990. “Critical state soil mechanics.” Cambridge University Press, Cambridge, UK.

Nageswaran, S. (1983). Effect of gas bubbles on the sea-bed behaviour. PhD thesis, 1983; Oxford University.

Nakai, T., Hinokio, M. (2004). “A simple elastoplastic model for normally and overconsolidated soils with unified material parameters.” Soils Found., 44(2), 53–70. https://doi.org/10.3208/sandf.44.2_53.

Ng, C. W., Zhan, L. T., Cui, Y. J. (2002). A new simple system for measuring volume changes in unsaturated soils. Canadian geotechnical journal, 39(3), 757-764.

Nisbet, E. G., Piper, D. J. (1998). “Giant submarine landslides.” Nature, 392, No. 6674, 329. https://doi.org/10.1038/32765.

Okusa, S. (1985). “Wave-induced stresses in unsaturated submarine sediments.” Geotechnique, 35(4), 517-532. https://doi.org/10.1680/geot.1985.35.4.517.

Pestana, J. M., and Whittle, A. J. (1999). “Formulation of a unified constitutive model for clays and sands.” Int. J. Numer. Anal. Methods Geomech., 23(12), 1215–1243.https://doi.org/10.1002/(SICI)1096-9853(199910)23:12<1215::AID-NAG29>3.0.CO;2-F.

Pietruszczak S, Pande GN. 1996. “Constitutive relationships for partially saturated soils containing gas inclusions.” Journal of Engineering Mechanics. 122(1): 50–59. https://doi.org/10.1061/(ASCE)0733-9410(1996)122:1(50).

Prior, D. B., Suhayda, J. N. (1979). “Application of infinite slope analysis to subaqueous sediment instability,” Mississippi Delta. Engineering Geology, 14(1), 1-10. https://doi.org/10.1016/0013-7952(79)90059-0.

Puzrin, A.M., Tront, J., Schmid, A., Hugues, J.B. (2011). “Engineered use of microbial gas production to decrease primary consolidation settlement in clayey soils.” Géotechnique. 61(9):785-794. https://doi.org/10.1680/geot.9.T.023.

Rebata-Landa, V., Santamarina, J. (2012). "Mechanical effects of biogenic nitrogen gas bubbles in soils." Journal of Geotechnical and Geoenvironmental Engineering 138.2.128-137. https://doi.org/10.1061/(ASCE) GT.1943-5606.0000571.

Roscoe, K.H., Burland, J.B. 1968. “On the generalized stress-strain behaviour of ‘wet’ clay. “Engineering plasticity (eds. J. Heyman and F. A. Leckie), Cambridge University Press, Cambridge, UK, 535–609.

Rowe, R. K. and Mabrouk, A. (2012). “Forensic numerical analysis of gas venting in Southwestern Ontario.” Engineering Geology, 151, No. 4, 47–55. https://doi.org/10.1016/j.enggeo.2012.09.005.

Sham, W.K. (1989). The undrained shear strength of soils containing large gas bubbles. PhD thesis. The Queen’s University of Belfast.

Shi, X.S., Zhao, J.D., Yin J.H., Yu, Z.J. (2019). An elastoplastic model for gap-graded soils based on homogenization theory. International Journal of Solids and Structures. 163: 1-14.DOI: 10.1016/j.ijsolstr.2018.12.017.

Sills, G.C., Wheeler, S.J., Thomas, S.D., Gardner TN. 1991. “Behaviour of offshore soils containing gas bubbles.” Géotechnique. 41(2):227–241. https://doi.org/10.1680/geot.1991.41. 2.227.

Sills, G.C., Wheeler, S.J. 1992. “The significance of gas from offshore operations.” Continental Shelf Research. 12(10): 1239–1250. https://doi.org/10.1016/0278-4343(92)90083-v.

Sills, G. C., Thomas, S. D. (2018). “Pore pressures in soils containing gas.” In Chemo-Mechanical Coupling in Clays (pp. 211-222). Routledge

Sills, G.C., Gonzalez, R. (2001). "Consolidation of naturally gassy soft soil." Geotechnique 51.7. 629-639. https://doi.org/10.1680/geot.2001.51.7.629.

Sparks, A. D. W. (1965). “Theoretical considerations of stress equations for partly saturated soils.” Civil Eng Bull, Capetown Univ/S Afr/.

Sultan, N., De Gennaro, V., Puech, A. 2012. “Mechanical behavior of gas-charged marine plastic sediments.” Géotechnique. 62(9): 751–766. https://doi.org/10.1680/geot.12.og.002.

Sultan, N., Garziglia, S. 2014. “Mechanical behaviour of gas-charged fine sediments: model formulation and calibration.” Géotechnique. 64(11): 851-864. https://doi.org/10.1680/ geot.13.p.125.

Taiebat, M., Dafalias, Y. F. (2010). “Simple Yield Surface Expressions Appropriate for Soil Plasticity.” Int. J. Geomech. 10(4):161-169. https://doi.org/10.1061/ (ASCE)GM.1943-5622.0000059.

Thomas, S.D. 1987. “The consolidation behaviour of gassy soil.” PhD thesis, Oxford University.

Tjelta, T. I., Svanø, G., Strout, J. M., Forsberg, C. F., Johansen, H., Planke, S. (2007). “Shallow gas and its multiple impact on a North Sea production platform.” Proceedings of the 6th international offshore site investigation and geotechnics conference, London, 205–220. London, UK: Society for Underwater Technology.

Tsai, S. W., Hahn, H. T. (1980). “Introduction to Composite Materials.” Technomic. https://doi.org/10.1201/9780203750148.

van Kessel, T., van Kesteren, W. (2002). “Gas production and transport in artificial sludge depots.” Waste Management, 22(1), 19-28. https://doi.org/10.1016/S0956-053X(01)00021-6.

van Kesteren, W., van Kessel, T. (2002). "Gas bubble nucleation and growth in cohesive sediments." Proceedings in Marine Science. Vol. 5. Elsevier. 329-341. https://doi.org/10.1016/S1568-2692(02)80025-0.

Vega-Posada, C. A., Finno, R. J., Zapata-Medina, D. G. (2014). “Effect of gas on the mechanical behavior of medium-dense sands.” Journal of Geotechnical and Geoenvironmental Engineering, 140(11), 04014063. https://doi.org/10.1061/(ASCE)GT.1943-5606.0001163.

Wheeler, S.J., Gardner, T.N. 1989. “Elastic-moduli of soils containing large gas-bubbles.” Géotechnique. 39(2): 333–342. https://doi.org/ 10.1680/geot.1989.39.2.333.

Wheeler, S.J., Sham, W.K., Thomas, S.D. 1990. “Gas pressure in unsaturated offshore soils.” Canadian Geotechnical Journal. 27(1): 79–89. https://doi.org/10.1139/t90-008.

Wheeler, S.J. 1986. “The stress-strain behaviour of soils containing gas bubbles.” PhD thesis, Oxford University.

Wheeler, S.J. 1988a. “A conceptual model for soils containing large gas bubbles.” Géotechnique. 38(3): 389–397. https://doi.org/10.1680/geot.1988.38.3.389.

Wheeler, S.J. 1988b. “The undrained shear strength of soils containing large gas bubbles.” Géotechnique. 38(3):399-413.https://doi.org/10.1680/geot.1988.38.3.399.

Whelan III, T., Coleman, J. M., Suhayda, J. N., Roberts, H. H. (1977). “Acoustical penetration and shear strength in gas-charged sediment.” Marine Georesources & Geotechnology, 2 (1-4), 147-159. https://doi.org/10.1080/106411977093797-76.

Whelan III, T., JM, C., Roberts, H. H., Suhayda, J. N. (1976). “The occurrence of methane in recent deltaic sediments and its effect on soil stability.” Bulletin of the International Association of Engineering Geology-Bulletin de l'Association

Internationale de Géologie de l'Ingénieur, 13(1), 55-64. https://doi.org/10.1007/BF02634759.

Wroth, C. P., Houlsby, G. T. (1985). "Soil mechanics: property characterization and analysis procedures." Proc. 11th Int. Conf. Soil Mech. Fdn Engng, San Francisco 1, l-55.

Wu, S., Jeng, D.S. (2019). "Effects of dynamic soil permeability on the wave-induced seabed response around a buried pipeline." Ocean Engineering 186: 106132. https://doi.org/10.1016/j.oceaneng.2019.106132.

Yao, Y. P., Gao, Z. W., Zhao, J. D., Wan, Z. (2012). "Modified UH model: Constitutive modeling of overconsolidated clays based on a parabolic Hvorslev envelope." Journal of Geotechnical and Geoenvironmental Engineering, 138(7), 860-868. https://doi.org/10.1061/(ASCE)GT.1943-5606.0000649.

Yao, Y. P., Hou,W., Zhou, A. N. (2009). "UH model: three-dimensional unified hardening model for overconsolidated clays." Geotechnique, 59(5), 451–469. https://doi.org/10.1680/geot.2007.00029.

Yin, Z., Xu, Q., Hicher, P. Y. (2013). "A simple critical state based double-yield-surface model for clay behavior under complex loading." Acta Geotechnica, 8, No. 5, 509-523. https://doi.org/10.1007/s11440-013-0206-y.

Zervoyanis, C. (1982). "Etude synth_etique des propri_et_es m_ecaniques des argiles et des sables sur chemin oedom_etrique et triaxial de revolution." Thèse de Docteur-Ing_enieur, Ecole Centrale de Paris, Paris (in French).